

UNIwersytet KAZIMIERZA WIELKIEGO W BYDGOSZCZY
RADA DZIEDZINY NAUK ŚCISŁYCH I PRZYRODNICZYCH

Anna Shakhno

**Correlation of structural and optical properties of white light emitting
diode converters based on doped mixed garnets
with micro- and nano-ceramic, and epitaxial structure**

Korelacja właściwości strukturalnych i optycznych konwerterów diod białych
na bazie domieszkowanych granatów mieszanych
o mikro- i nano- ceramicznej oraz epitaksjalnej strukturze

Dysertacja na stopień doktora

Promotor:

prof. dr. hab. Yuriy Zorenko

Drugi promotor:

dr. hab. inż. Mieczysław Cieszek, prof. uczelni

Bydgoszcz 2025

Preface

This doctoral dissertation was carried out within the framework of the Doctoral School in Mechanical Engineering at the Department of Mechatronics and the Department of Physics of Kazimierz Wielki University in Bydgoszcz.

The research presented in this dissertation was conducted as part of investigations performed in the framework of projects funded by the National Science Centre (Narodowe Centrum Nauki) of Poland:

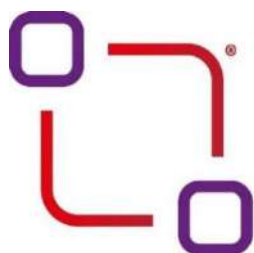
- No 2017/25/B/ST8/02932 project;
- No 2019/33/B/ST3/00406 project;
- No 2022/45/B/ST8/01757 project;
- No 2018/31/B/ST8/03390 project.

Additionally, this work was supported by internal regional initiatives in frame of the RID (Regionalna Inicjatywa Doskonałości) project No. RID/SP/0048/2024/01, conducted at the Department of Physics of Kazimierz Wielki University.

As a project researcher and scholarship recipient, the doctoral candidate conducted this research at both the Department of Mechatronics and the Department of Physics of Kazimierz Wielki University in Bydgoszcz.



Uniwersytet
Kazimierza
Wielkiego
w Bydgoszczy



Regionalna
Inicjatywa
Doskonałości

"One never notices what has been done; one can only see what remains to be done. It is this awareness of the unfinished nature of knowledge that pushes every researcher forward and makes the pursuit of science a lifelong endeavor."

Marie Skłodowska-Curie

I would like to express my profound gratitude to **Professor Dr. habil. Dr. Sc. Yuriy Zorenko** for his scientific supervision, invaluable guidance, and continuous support throughout the entire course of my doctoral studies. His expertise, insightful advice, and encouragement significantly contributed to the conception, development, and finalization of this dissertation.

I extend my sincere thanks to **Dr. habil. Eng. Mieczysław Cieszko, Associate Professor**, auxiliary supervisor, for his prudent guidance, patience, and essential assistance in the execution of the experimental components of this work.

I am grateful to the academic staff of the **Faculty of Physics** and the **Faculty of Mechatronics at Kazimierz Wielki University in Bydgoszcz** for their shared knowledge, technical assistance, and for fostering a professional and stimulating scientific environment conducive to the realization of this research.

My appreciation is further extended to **Dr. Vitalii Gorbenko** for his indispensable contribution, commitment, and expertise in the preparation and analysis of samples, as well as for his readiness to provide support at every stage of the research process.

I would particularly like to thank **Mgr. Tetiana Zorenko** for her assistance in performing measurements and for her consistent support and collegiality during the experimental work.

I also wish to acknowledge **Mgr. Zbigniew Szczepański** for his constructive comments, academic support, and for granting access to research facilities, which substantially facilitated the experimental aspects of this study.

Furthermore, I acknowledge the research group of **Priv.-Doz. Dr. Mirosław Batentschuk** from i-MEET at Friedrich-Alexander University Erlangen–Nuremberg in Erlangen, Germany for their support in the synthesis of samples and the analysis of epitaxial structures.

Finally, I extend my deepest gratitude to my **family and friends** for their patience, understanding, and steadfast confidence in my abilities. Their unwavering support was indispensable throughout the course of this work.

"Nie zauważa się nigdy tego, co zostało już dokonane; widzi się jedynie to, co pozostaje do zrobienia. To właśnie świadomość nieukończonych natury wiedzy popycha każdego badacza do przodu i sprawia, że poszukiwanie naukowe staje się przedsięwzięciem na całe życie."

Maria Skłodowska-Curie

Chciałabym wyrazić szczerą wdzięczność Panu **prof. dr hab. Yuriyowi Zorenko** za opiekę naukową, inspirację do badań oraz cenne wskazówki, które towarzyszyły mi przez cały okres studiów doktoranckich i znacząco wpłynęły na kształt niniejszej rozprawy.

Serdecznie dziękuję **dr hab. inż. Mieczysławowi Cieszko, prof. uczelni**, promotorowi pomocniczemu, za jego życzliwość, cierpliwość oraz wsparcie w realizacji części eksperymentalnej pracy.

Dziękuję pracownikom **Wydziału Fizyki** oraz **Wydziału Mechatroniki UKW** za przekazaną wiedzę, wsparcie techniczne i przyjazną atmosferę pracy badawczej.

Składam podziękowania **dr Vitaliyowi Gorbenko** za jego nieocenioną pomoc w przygotowaniu i analizie próbek, a także za gotowość do współpracy na każdym etapie badań.

W szczególności pragnę podziękować **mgr Tetianie Zorenko** za pomoc w wykonywaniu pomiarów oraz okazaną życzliwość.

Wyrazy wdzięczności kieruję także do **mgr. Zbigniewa Szczepańskiego** za merytoryczne wskazówki i możliwość korzystania z zaplecza badawczego.

Składam również podziękowania grupie **Prywat-Docenta dr. hab. Mirosława Batentschuka** z i-MEET Uniwersytetu Friedricha-Aleksandra w Erlangenie, Niemcy za pomoc w syntezie próbek i analizie struktur epitaksjalnych.

Na koniec kieruję moją najgłębszą wdzięczność do **rodziny i przyjaciół** za ich cierpliwość, zrozumienie i wiarę w moje możliwości. Bez Waszej obecności, otuchy i wsparcia ta droga byłaby znacznie trudniejsza. Jestem wdzięczna, że mogłam dzielić tę podróż z tak niezwykłymi ludźmi.

Abbreviations

CCT	– Correlated color temperature
CL	– Cathodoluminescence
CRI	– Color rendering index
CSSG	– $\text{Ca}_3\text{Sc}_2\text{Si}_3\text{O}_{12}$ garnet
CYMSSG	– $\text{Ca}_2\text{YMgScSi}_3\text{O}_{12}$ garnet
GAGG	– $\text{Gd}_3\text{Al}_{2.5}\text{Ga}_{2.5}\text{O}_{12}$ Gadolinium Aluminium Gallium Garnet
LED	– Light-emitting diode
LPE	– Liquid phase epitaxy
MP	– Micropowder
HDC	– Horizontal directional crystallization
PC	– Phosphor converter
PCLC	– Planar chip level conversion
WLED	– White LED
PL	– Photoluminescence
RE	– Rare-earth elements
RGB	– Red, green, and blue
RT	– Room Temperature
SC	– Single crystal
SCF	– Single crystalline films
SEM	– Scanning Electron Microscopy
T_g	– Growth temperature
T_s	– Saturation temperature
VCC	– Volume casting conversion
XRD	– X-ray diffraction
YAG	– $\text{Y}_3\text{Al}_5\text{O}_{12}$ garnet
μCT	– Microcomputer tomography
μPD	– Micro pulling down

Contents

1. INTRODUCTION	7
2. STRUCTURE OF THE DOCTORAL THESIS AND THE DOKTORAL STUDENT CONTRIBUTION TO PUBLICATIONS	9
2.1. Structure of the Doctoral Thesis	9
2.2. Doctoral student's contribution to publications	11
3. CHARACTERISATION OF GROWTH METHODS FOR MATERIALS PREPARATION AND EXPERIMENTAL TECHNIQUES	11
3.1. Materials Preparation	11
3.1.1. Crystallization of (Al ₂ O ₃ -YAG):Ce Eutectic using the HDC Method [C1.1]	11
3.1.2. Preparation of CSSG:Ce and CYMSSG:Ce Micropowders Using the Solid-State Phase Synthesis [C2.1, C2.2, C2.3]	13
3.1.3 Growth of CSSG:Ce Crystals Using the MPD Method [C3.1]	16
3.1.4. Growth of CSSG:Ce and CYMSSG:Ce SCFs on GAGG and YAG Substrates using LPE Method [C4.1, C4.2]	18
3.2. Experimental Techniques	21
3.2.1. X-ray Diffraction Analysis	21
3.2.2. Scanning Electron Microscopy	22
3.2.3. Micro-Computed Tomography	23
3.2.4. Absorption Spectroscopy	24
3.2.5. Luminescence Spectroscopy	25
3.2.6. Colorimetry	25
4. OPTICAL AND PHOTOCONVERSION PROPERTIES OF WLED CONVERTERS BASED ON THE DIFFERENT CRYSTALLINE FORMS OF GARNET COMPOUNDS	27
4.1. Ce ³⁺ -Doped Al ₂ O ₃ -YAG Eutectic: Synthesis, Structural Characterization, and Luminescent Properties for White LED Applications [C1.1]	27
4.2. Ce ³⁺ and Mn ²⁺ Doped Ca ₃ Sc ₂ Si ₃ O ₁₂ and Ca ₂ YMgScSi ₃ O ₁₂ Micropowders as Efficient Light Converters for White LEDs [C2.1, C2.2, C2.3]	30
4.3. Ce ³⁺ -Doped Ca ₃ Sc ₂ Si ₃ O ₁₂ Crystal: Luminescence and Photoconversion Properties for White LED Applications	37
4.4 Ce ³⁺ -Doped Ca ₃ Sc ₂ Si ₃ O ₁₂ Single Crystalline Films: Luminescence and Color Conversion Properties for White LED Applications	40
4.5. Ce ³⁺ -Doped Ca ₂ YMgScSi ₃ O ₁₂ Single Crystalline Films: Luminescence and Color Conversion Properties for White LED Applications	45
5. MAIN CONCLUSIONS OF THE DOCTORAL DISSERTATION	49
REFERENCES	51
Other Scientific Achievements of Author	54

1. INTRODUCTION

Nowadays white light-emitting diode (WLED) have emerged as the dominant technology in solid-state lighting applications due to their superior energy efficiency, extended operational lifetime, environmental compatibility, and compact form compared to conventional incandescent and fluorescent lighting systems [1-4]. The fundamental operating principle of WLEDs relies on phosphor-conversion mechanisms, where blue or near-ultraviolet LED chips are coupled with luminescent materials that partially convert the primary emission to longer wavelengths, generating white light through spectral combination [5-7].

The phosphor-conversion method widely relies on cerium-doped yttrium aluminum garnet ($\text{Y}_3\text{Al}_5\text{O}_{12}:\text{Ce}^{3+}$, or YAG:Ce) as the standard material, thanks to its high quantum efficiency and impressive chemical and thermal stability [8-12]. Despite these advantages, YAG:Ce phosphor has drawbacks that limit the WLED performance. The characteristic broad yellow emission band of the YAG:Ce results in significant red spectral deficiency, leading to poor color rendering capabilities and elevated correlated color temperatures [13-16]. Additionally, thermal quenching effects at high operating temperatures limit spectral tunability and reduce efficiency in high-power applications [17]. These limitations have motivated extensive research into *alternative phosphor-converter materials* capable of addressing the spectral and thermal constraints while maintaining or exceeding established performance standards [18-20].

The first approach involves the use of eutectic crystalline structures, particularly Ce^{3+} -doped alumina–YAG composites ($(\text{Al}_2\text{O}_3\text{--YAG}):\text{Ce}$), grown from the high-temperature melt using Czochralski method, or Horizontal-Direct Crystallization (HDC) as variation of horizontal Bridgman method. Such eutectic offers unique opportunities to combine the advantageous properties of multiple phases while enabling novel optical behaviours through interfacial interactions and carefully controlled microstructural features [21-26].

Among the most promising alternative strategies for next-generation WLED converters is the development of mixed garnet systems featuring modified cation compositions and tailored crystal structures to optimize emission characteristics. These materials aim to overcome the inherent limitations of conventional YAG:Ce by offering superior colour rendering and improved thermal performance. In particular, Ce^{3+} doped calcium scandium silicate garnets $\text{Ca}_3\text{Sc}_2\text{Si}_3\text{O}_{12}:\text{Ce}$ (CSSG:Ce) [27-30] and their compositionally tuned compounds, such as $(\text{Ca},\text{Y})_3(\text{Mg},\text{Sc})_2\text{Si}_3\text{O}_{12}:\text{Ce}$ (CYMSSG:Ce) [31-33], demonstrate significant potential due to their improved thermal stability and enhanced red emission components, respectively. Consequently, the present work focuses on systematically exploring such alternative phosphor materials for advanced WLED applications.

The correlation between structural characteristics and optical performance in these advanced phosphor materials represents a fundamental aspect that requires comprehensive

investigation. The local coordination environment of activator ions, crystal field effects, electron-phonon interactions, and defect structures all directly influence the luminescence properties, including emission wavelength, quantum efficiency, thermal stability, and spectral bandwidth [34,35]. Understanding these structure-property relationships is essential for the rational design and optimization of phosphor-converter materials [36].

The structural diversity achieved through different synthesis approaches adds a critical dimension to the correlation between material structure and optical behaviour. Eutectic crystalline structures, grown by direct crystallization from high-temperature melts, offer a unique combination of multiple phases, enabling the development of composites with novel optical properties through interfacial interactions and precisely controlled microstructural features. In contrast, micropowders synthesized via solid-state reactions result in polycrystalline materials where grain boundaries and surface effects significantly influence optical performance compared to bulk single crystals (SC). Single-crystal growth techniques, such as the micro-pulling-down (μ PD) method [37, 38], yield materials with well-defined crystallographic orientations and low defect concentrations, providing insights into their intrinsic optical properties. Meanwhile, single-crystalline films (SCFs) and composite epitaxial structures grown by liquid-phase epitaxy (LPE) method [39, 40, 41] introduce additional factors such as substrate interactions, epitaxial strain, and thickness-dependent effects, that can further modulate luminescence characteristics.

The systematic evaluation of these diverse structural forms, from eutectic composites and nano- or micropowders to single crystals and single crystalline films, and finally epitaxially grown composite film-crystal converters provides a comprehensive framework for understanding how material architecture influences phosphor performance. This understanding is crucial for optimizing photoconversion efficiency, color quality parameters including color coordinates, correlated color temperature, and color rendering index, which ultimately determine the suitability of these materials for specific WLED applications.

The present research addresses the need for advanced phosphor-converter materials through a systematic investigation of the correlation between structural and optical properties in doped mixed garnet systems. By examining materials prepared through various synthesis methodologies and characterized using complementary optical spectroscopy techniques, this work aims to establish fundamental relationships that guide the development of efficient WLED converters. The comprehensive analysis of absorption, photoluminescence (PL), and cathodoluminescence (CL) properties, combined with detailed structural characterization, provides the foundation for understanding how material design parameters influence the ultimate performance in WLED applications.

This work contributes to the goal of developing phosphor-converter technologies that overcome the limitations of current YAG:Ce phosphor while providing enhanced color quality, improved thermal performance, and expanded spectral tunability for next-generation solid-state lighting devices. Achieving this goal requires solving the following scientific tasks:

1. The controlled crystallization of (Al₂O₃-YAG):Ce eutectic through the HDC method by optimizing composition, fine-tuning growth parameters, and ensuring superior structural, optical, and mechanical properties for advanced applications.
2. The synthesis of CSSG:Ce and CYMSSG:Ce micropowders using the solid-state phase method to achieve controlled composition, phase purity, and optimal luminescent properties.
3. The growth of CSSG:Ce crystals using the μ PD method to achieve high-quality crystal formation with precise control over composition and structure.
4. The growth of CSSG:Ce and CYMSSG:Ce SCFs on GAGG and YAG substrates, respectively, using the LPE method to ensure high-quality film formation with optimal crystalline structure and luminescent properties.
5. A comprehensive analysis of the structural properties of the fabricated materials to evaluate the crystal structure, identify defects, and gain a deeper understanding of their crystallographic characteristics.
6. An analysis of the spectroscopic properties of the obtained materials to evaluate their luminescent characteristics and assess their suitability for use in manufacturing phosphor converters for LEDs.
7. The development of prototype WLEDs using the obtained materials in different crystalline forms, as well as the evaluation of their chromaticity parameters to assess colour quality and performance for potential lighting applications.

2. STRUCTURE OF THE DOCTORAL THESIS AND THE DOKTORAL STUDENT CONTRIBUTION TO PUBLICATIONS

2.1. Structure of the Doctoral Thesis

The doctoral thesis *"Correlation of Structural, Mechanical, and Optical Properties of White Light-Emitting Diode Converters Based on Doped Mixed Garnets with Micro- and Nano-Ceramic and Epitaxial Structures"* is based on a review of seven articles published in peer-reviewed scientific journals and is divided into *four thematic parts*.

Part I: Ce³⁺-Doped Al₂O₃-YAG Eutectic: Synthesis, Structural Characterization, and Luminescent Properties for White LED Applications

C1.1. A. Shakhno, T. Zorenko, S. Witkiewicz-Lukaszek, M. Cieszko, Z. Szczepański, O. Vovk, S. Nizhankovskyi, Y. Siryk, Y. Zorenko, Ce³⁺ Doped Al₂O₃-YAG Eutectic as an Efficient

Light Converter for White LEDs, Materials 16 (2023) 2701.
<https://doi.org/10.3390/ma16072701>.

This part of work focuses on the development, structural analysis, and luminescence properties of Ce^{3+} -doped Al_2O_3 -YAG eutectic materials, highlighting their potential as efficient light converters for WLEDs.

Part II: Ce^{3+} and Mn^{2+} Doped $\text{Ca}_3\text{Sc}_2\text{Si}_3\text{O}_{12}$ and $\text{Ca}_2\text{YMgScSi}_3\text{O}_{12}$ Silicate Garnet Micropowders as Efficient Light Converters for White LEDs

C2.1. I. Levchuk, A. Osvet, C.J. Brabec, M. Batentschuk, **A. Shakhno**, T. Zorenko, Y. Zorenko, Micro-powder $\text{Ca}_3\text{Sc}_2\text{Si}_3\text{O}_{12}:\text{Ce}$ silicate garnets as efficient light converters for WLEDs, Optical Materials 107 (2020) 109978. <https://doi.org/10.1016/j.optmat.2020.109978> .

C2.2. **A. Shakhno**, A. Markovskiy, T. Zorenko, S. Witkiewicz-Łukaszek, Y. Vlasyuk, A. Osvet, J. Elia, C.J. Brabec, M. Batentschuk, Y. Zorenko, Micropowder $\text{Ca}_2\text{YMgScSi}_3\text{O}_{12}:\text{Ce}$ Silicate Garnet as an Efficient Light Converter for White LEDs, Materials 15 (2022) 3942. <https://doi.org/10.3390/ma15113942> .

C2.3. **A. Shakhno**, S. Witkiewicz-Łukaszek, V. Gorbenko, T. Zorenko, Y. Zorenko, Luminescence and photoconversion properties of micro-powder phosphors based on the Ce^{3+} and Mn^{2+} doped $\text{Ca}_2\text{YMgScSi}_3\text{O}_{12}$ silicate garnets, Optical Materials: X 16 (2022) 100187. <https://doi.org/10.1016/j.omx.2022.100187> .

This part of dissertation explores the synthesis, structural properties, and photoluminescence behavior of Ce^{3+} -doped and Mn^{2+} -doped silicate garnet micropowders, evaluating their efficiency as phosphor materials for white LED applications.

Part III: Ce^{3+} -Doped $\text{Ca}_3\text{Sc}_2\text{Si}_3\text{O}_{12}$ Crystal: Luminescence and Photoconversion Properties for White LED Applications

C3.1. **A. Shakhno**, W. Gieszczyk, P. Bilski, S. Witkiewicz-Łukaszek, T. Zorenko, M. Cieszko, Z. Szczepański, A. Kotlov, Y. Zorenko, Luminescence and photoconversion properties of Ce-doped $\text{Ca}_3\text{Sc}_2\text{Si}_3\text{O}_{12}$ crystal, Journal of Luminescence 266 (2024) 120311. <https://doi.org/10.1016/j.jlumin.2023.120311>.

This section investigates the luminescence and photoconversion properties of Ce^{3+} -doped $\text{Ca}_3\text{Sc}_2\text{Si}_3\text{O}_{12}$ crystals, assessing their performance as light-converting materials in WLED technologies.

Part IV: Single crystalline film and composite film-crystal converters on the base of the Ce^{3+} -Doped $\text{Ca}_3\text{Sc}_2\text{Si}_3\text{O}_{12}$ and $\text{Ca}_2\text{YMgScSi}_3\text{O}_{12}$ garnets: Luminescence and Color Conversion Properties for White LED Applications.

C4.1. **A. Shakhno**, S. Witkiewicz-Łukaszek, V. Gorbenko, T. Zorenko, Yu. Zorenko, Composite color converters based on the $\text{Ca}_3\text{Sc}_2\text{Si}_3\text{O}_{12}:\text{Ce}$ single crystalline films,

Optical Materials: X 22 (2024) 100328. <https://doi.org/10.1016/j.omx.2024.100328>.

C4.2. A. Shakhno, V. Gorbenko, T. Zorenko, A. Fedorov, Y. Zorenko, Optical and Photoconversion Properties of Ce^{3+} -Doped $(\text{Ca}, \text{Y})_3(\text{Mg}, \text{Sc})_2\text{Si}_3\text{O}_{12}$ Films Grown via LPE Method onto YAG and YAG:Ce Substrates, Materials 18 (2025) 3590. <https://doi.org/10.3390/ma18153590>.

This section examines the fabrication, luminescence behavior, and color conversion efficiency of Ce^{3+} -doped CSSG SCFs grown onto GAGG and GAGG:Ce substrates as well as describes the luminescence properties, and color conversion efficiency of CSSG:Ce and CYMSSG:Ce single crystalline films, grown onto YAG and YAG:Ce substrates.

2.2. Doctoral student's contribution to publications

The Author made important contributions to all of the publications listed above. In **C1.1**, the Author collected and analyzed the complete set of experimental results, prepared the figures and tables, developed the WLED prototypes, measured their photoconversion properties, and participated in drafting and revising the paper. In **C2.1**, the Author's contribution focused on analyzing the whole experimental material, preparing the publication figures, and assisting with writing, drafting and revising the paper. For **C2.2**, the Author was responsible for collecting and analyzing the data, preparing the figures and tables, taking part in photoluminescence measurements, assembling the WLED prototypes, testing their photoconversion performance, and contributing to the manuscript. In **C2.3**, the Author's contribution included synthesizing the micropowders, analyzing the results, preparing the figures and tables, participating in the optical and structural studies, creating and testing the prototypes, and co-authoring the paper. In **C3.1**, the Author collected and analyzed the existing literature, performed structural, optical, and photoconversion measurements, prepared the prototype, and contributed to the manuscript. For **C4.1**, the Author's role again included analyzing experimental data, preparing the figures, participating in the optical and photoconversion studies, developing the WLED prototypes, and contributing to the writing. Finally, in **C4.2**, the Author collected and analyzed the experimental results, prepared the publication materials, created the WLED prototypes, carried out the structural and optical measurements, and participated in drafting and revising the paper.

3. CHARACTERISATION OF GROWTH METHODS FOR MATERIALS PREPARATION AND EXPERIMENTAL TECHNIQUES

3.1. Materials Preparation

3.1.1. Crystallization of $(\text{Al}_2\text{O}_3\text{-YAG})\text{:Ce}$ Eutectic using the HDC Method [C1.1]

Ce-doped $\text{Al}_2\text{O}_3\text{-YAG}$ eutectic samples were crystallized at the Institute for Single Crystals,

National Academy of Sciences of Ukraine in Kharkiv, Ukraine (ISC Kharkiv), a leading research center in Eastern Europe specializing in crystal growth technologies.

The crystallization process was performed using the HDC method using the Horizont-3M setup (Fig.1a). For the preparation of the initial eutectic charge, an *equimolar mixture* of Y_2O_3 + CeO_2 (5N purity) and Al_2O_3 (4N purity) oxides was used. These powders were thoroughly mixed in a drum for several hours, and the resulting mixture was compressed into tablets. The tablets were annealed at 1200 °C for several hours, and the annealed tablets served as a “green body” for crystallization. The YAG- Al_2O_3 melt was solidified in molybdenum crucibles under a controlled atmosphere of Ar, CO, and H_2 at a total pressure of 1.3×10^5 Pa. The crystallization process took place in the setup's hot zone, where the temperature was 1835 °C, with a temperature gradient of 30 °C/cm at the solidification front. The crucible's pulling speed varied between 1 and 8 mm/h, allowing precise control over the growth conditions.

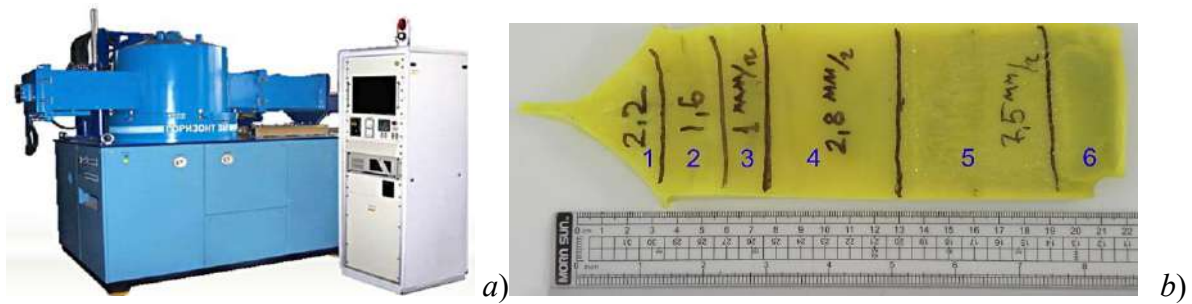


Fig. 1. The Horizont-3M installation used for HDC crystallization (a) [42] and $(Al_2O_3-YAG):Ce$ eutectic ingot (b). Different parts of the ingot grown at different crystallization rates (Table 1).

Table 1. Modes of crystallization of $(Al_2O_3-YAG):Ce$ eutectics.

Sample	Rate of crystallization, mm/h	Melt Temperature, °C	Gradient, °C /cm	Al_2O_3 , Surf. %	YAG, Surf. %
2	1.6	1835	30	47.1 ± 2.4	52.9 ± 2.4
3	1	1835	30	46.1 ± 1.3	54.0 ± 1.3
4	2.8	1835	30	44.7 ± 1.3	55.3 ± 0.7
5	7.5	1835	30	45.2 ± 0.7	54.8 ± 0.7

The values listed as “Surf. %” represent the surface fraction percentages of the phases, determined from SEM image analysis. Specifically, Al_2O_3 , Surf. % corresponds to the fraction of the sample’s surface area occupied by Al_2O_3 , while YAG, Surf. % corresponds to the fraction occupied by the YAG phase. Together, these values sum to ~100%, providing a quantitative measure of the relative distribution of phases in the eutectic composite. However, small amount of other phases, mostly $YAlO_3:Ce$ (YAP:Ce) perovskite, can be present in eutectic samples in amount below of detectable level of SEM analysis.

During solidification, the boat-like crucible containing the melt was gradually pulled from the hot zone through the temperature gradient into the cold zone. This movement was controlled by a

specialized mechanism designed to maintain a stable pulling speed. The mechanism also allowed for abrupt adjustments in the pulling rate, which directly influenced the crystallization dynamics.

As a result of the solidification process, a composite ingot with dimensions of $240 \times 75 \times 35$ mm³ was successfully grown (Fig. 1b). To analyze its morphology and microstructure, the ingot was sectioned into pieces corresponding to different pulling rates. Samples for further investigation were prepared from these sections in the form of rectangular plates (1×1 mm²) with a thickness of 0.5 mm. The normal vectors of the sample surfaces were oriented either perpendicular or parallel to the ingot's growth direction. The surfaces were meticulously polished using a diamond abrasive, gradually decreasing the grain size to achieve a smooth finish suitable for analysis.

The HDC method was chosen for the crystallization of Ce-doped Al₂O₃-YAG eutectic samples due to its ability to produce high-quality, large-scale eutectic crystals with controlled microstructures [42]. This technique allows for precise regulation of the solidification process, enabling the formation of a well-aligned composite microstructure with minimized defects. The use of a molybdenum crucible and a controlled atmosphere (Ar, CO, and H₂) help prevent unwanted oxidation, ensuring the purity of the crystal. Additionally, the HDC method provides a stable temperature gradient and controlled growth rates, which are crucial for optimizing the luminescent and structural properties of the material. These factors make HDC an effective approach for fabricating eutectic materials for advanced optical and phosphor applications.

3.1.2. Preparation of CSSG:Ce and CYMSSG:Ce Micropowders Using the Solid-State Phase Synthesis [C2.1, C2.2, C2.3]

The synthesis of CSSG:Ce phosphors was performed using two complementary approaches for *nano-* and *micro-* particles (NP and MP) [C2.1]. Micro-size particle samples were produced via a modified solid-state reaction, where stoichiometric blends of CaCO₃, Sc₂O₃, and SiO₂ oxides were pre-synthesized in air, then subjected to high-temperature calcination at 1300–1400 °C in a reducing atmosphere of 95% nitrogen and 5% hydrogen. A small amount of CaF₂ (1 wt. %) was added as a flux to enhance crystallinity and luminescent properties. This process yielded cubic microparticles with sizes ranging from 3 to 10 μm and a PL quantum yield of about 70%.

For CSSG:Ce NPs production, a fatty acid-assisted co-precipitation method was employed [C2.1]. Metal nitrates of calcium, scandium, and cerium were dissolved in water and combined with a silica source, either SiO₂ nanoparticles or tetraethyl orthosilicate (TEOS). Sodium oleate was added dropwise to induce precipitation of metal oleates, which were subsequently centrifuged, dried, and calcined sequentially—first in air at 850 °C for 3 hours, then in a reducing N₂/H₂ atmosphere at 1200 °C for 2 hours. This produced NPs in size 80–300 nm with high photoluminescence quantum yield (50–55%) and enhanced thermal stability, making them

suitable for WLED applications. Both methods yield highly luminescent CSSG:Ce materials with superior thermal performance compared to conventional YAG:Ce phosphors [C2.1].

CYMSSG:Ce and CYMSSG:Ce,Mn MPs, studied in the articles [C2.2, C2.3], were produced using conventional solid-state synthesis. This method relies on a solid-state reaction, specifically between microcrystalline grains. Diffusion plays a crucial role in the process, directly influencing the reaction rate. The reaction progresses isothermally in this context, as the diffusion of ions and atoms occurs very slowly. For this reason, flux components like B_2O_3 , were used to accelerate the solid-state reaction and increase the so-called "*depth of synthesis*", e.g. the ratio of the quantity of the resulting compounds to the quantity of the initial charge. At the end of the production process, the resulting powder is an oxide ceramic, with oxides serving as the reactants in the reaction.

Preparation of CSSG:Ce powder samples was performed using both one-step and two-step technological methods (Fig.2). In the one-step method, after calculating the required amounts of individual oxides according to their stoichiometric proportions, the components were mixed and ground in an agate mortar for 20 minutes to achieve maximum powder homogeneity. The resulting phosphor mixture was then annealed in an Al_2O_3 crucible at a heating rate of $20\text{ }^{\circ}C/min$, up to $1300\text{ }^{\circ}C$, for 10 hours in a forming gas atmosphere ($95\% N_2 + 5\% H_2$) (see Fig. 2, left table).

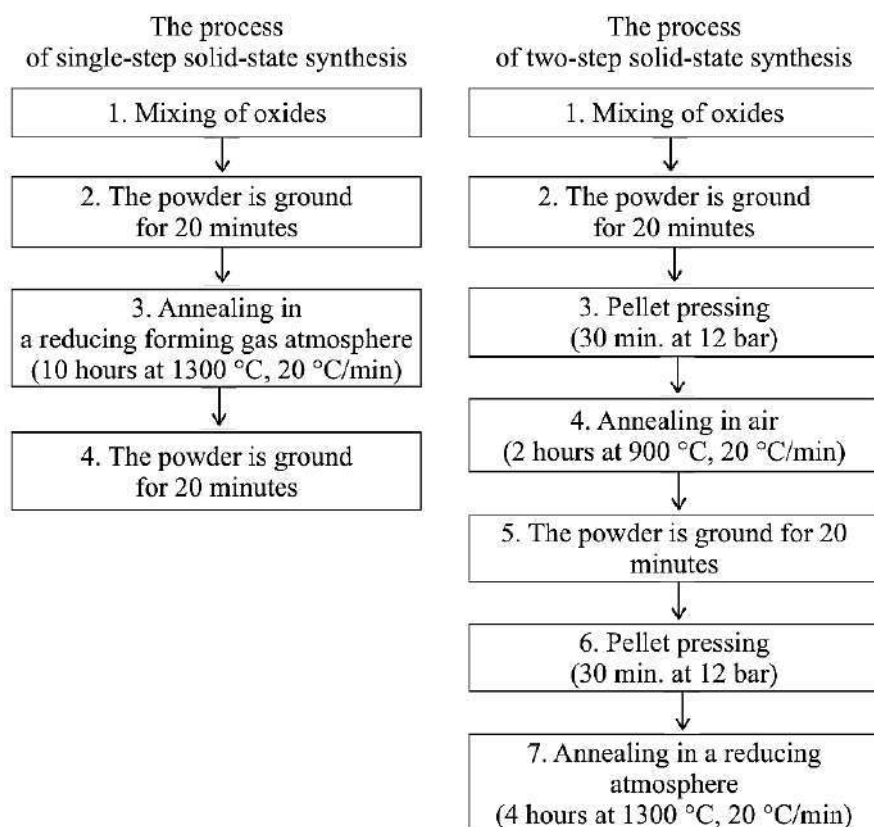


Fig.2. Diagram of the single-step and two-step solid-state synthesis process of micropowders.

In the second method used for synthesizing CYMSSG:Ce powder (Fig. 2, right table). The ground powder was first pressed into pellets using a press for 30 minutes under a pressure of 12

bar. This step increased the contact area between particles. A single-phase powder structure was obtained during the initial annealing stage, in which the pellets were heated in air at a rate of 20 °C/min to 900 °C and held for two hours. The sample was then ground again in a mortar, repressed into pellets, and annealed in a reducing atmosphere (95% N₂ + 5% H₂ forming gas) at 1300 °C for 4 hours, with the same heating rate (20 °C/min). This two-step annealing process, combined with intermediate grinding, promoted the formation of a highly homogeneous powder.

The annealing furnace is shown in Fig.3. It essentially consists of an Al₂O₃ tube surrounded by a silicon carbide heating element. To ensure even heat distribution, the crucible with the powder is placed inside the tube, and additional insulation surrounds the heating element. Gas supply and exhaust flow through the Al₂O₃ tube.

In both synthesis routes, the process was carried out in a reducing forming gas atmosphere (95% N₂ + 5% H₂). The annealing in the forming gas reduces Ce⁴⁺ ions from CeO₂ to Ce³⁺. The gas outlet entered the water reservoir, which allowed for a good estimation of the flow intensity. The flow rate of the gas has a significant impact on calcination. For this synthesis, one or two air bubbles within 10 seconds were sufficient.

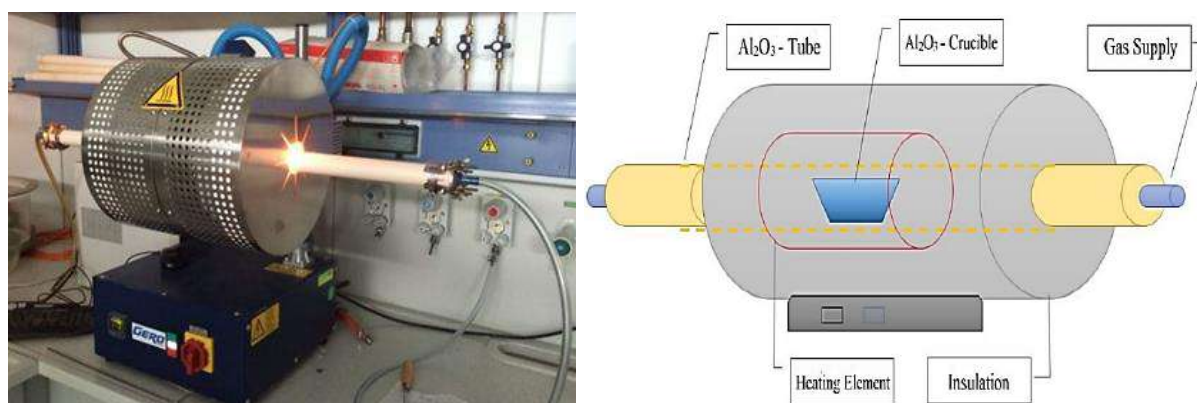


Fig. 3. Photo and diagram of the furnace for MP preparation.

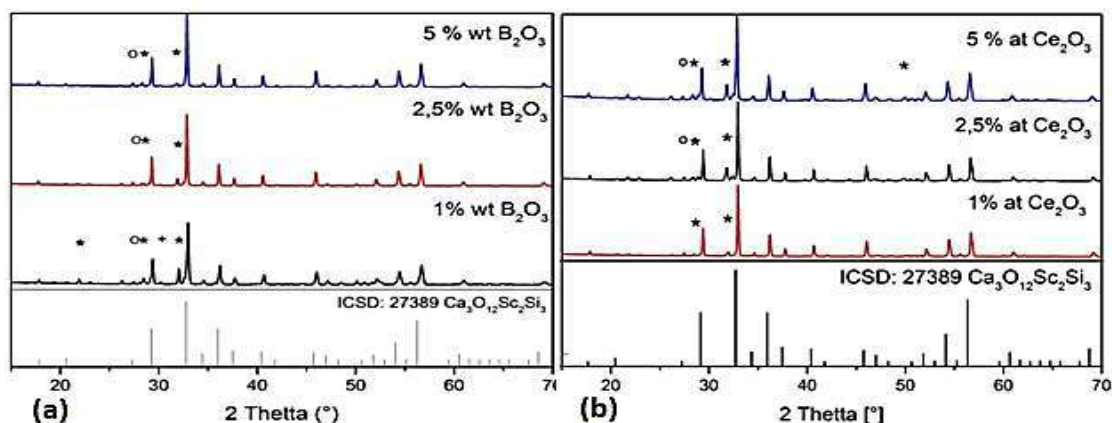


Fig. 4. XRD patterns of CYMSSG:Ce MPs samples sintering with different flux (a) and activator content (b), where * is Ca₂Ce₈O₂₆Si₆, + is SiO₂, and o is YBO₃.

X-ray diffraction (XRD) analysis was used to determine the phase composition of the MPs. The XRD results (Fig.4) indicate that under optimal sintering conditions, the material primarily consists of a nearly pure $\text{Ca}_3\text{Sc}_2\text{Si}_3\text{O}_{12}$ (CSSG) garnet phase, which closely matches the ICSD-27389 reference pattern. Minor amounts of unreacted SiO_2 and secondary phases, such as $\text{Ca}_2\text{Ce}_8\text{O}_{26}\text{Si}_6$ and YBO_3 , were also detected. The highest garnet phase content (80–82%) was observed in samples sintered with 2.5–5 at.% B_2O_3 flux and 1–2.5 at.% Ce^{3+} dopant. The optimal composition, yielding a maximum garnet content of 82%, was achieved with 2.5 wt.% B_2O_3 flux and 2.5 at.% Ce^{3+} concentration (see Table 2).

Table 2. The garnet phase content of CYMSSG:Ce MPs
(depth of synthesis) sintering with different flux and activator content

Nominal chemical composition $\text{Ca}_2\text{MgYScSi}_3\text{O}_{12}:\text{Ce}$	Garnet content %
1 at.% Ce + 1 wt.% B_2O_3	49.5
1 at.% Ce + 2.5 wt.% B_2O_3	80
1 at. % Ce + 5 wt.% B_2O_3	80
1 at.% Ce + 2.5 wt.% B_2O_3	81
2.5 at.% Ce + 2.5 wt.% B_2O_3	82
5 at.% Ce + 2.5 wt. % B_2O_3	62

3.1.3 Growth of CSSG:Ce Crystals Using the MPD Method [C3.1]

The μPD method was selected for the crystallization of Ce^{3+} -doped $\text{Ca}_3\text{Sc}_2\text{Si}_3\text{O}_{12}$ garnet due to its ability to produce small-volume, rod-shaped crystals with a diameter of 2–3 mm and a length of up to several decimetres. This crystal form is very useful for producing WLED converters using cutting and polishing operations. In general, the μPD method is considered a low-cost growth technique with precise control over growth parameters such as pulling rate, temperature gradient, and gas atmosphere, ensuring optimal crystal quality and consistent dopant incorporation, both essential for producing high-quality single crystals [43]. Furthermore, the μPD technique minimizes thermal gradients, which helps achieve uniform crystals with low defect concentrations. All these factors make the μPD method the optimal choice for growing crystals of Ce^{3+} -doped garnets for optical applications, including WLED converter production.

$\text{Ca}_3\text{Sc}_2\text{Si}_3\text{O}_{12}:\text{Ce}$ crystals were grown from the melt using the μPD method at the Institute of Nuclear Physics, Polish Academy of Sciences, Cracow, Poland (INP Cracow) (Fig. 5). The charge material was prepared by thoroughly mixing stoichiometric amounts of CaO , Sc_2O_3 , and SiO_2 in an agate mortar. CeO_2 was added as a dopant oxide to achieve a 1 mole % Ce^{3+} concentration in the final crystal. A 1.5 g portion of the prepared mixture was placed in a Mo crucible, which was mounted on graphite immediately downstream of the heating zone.

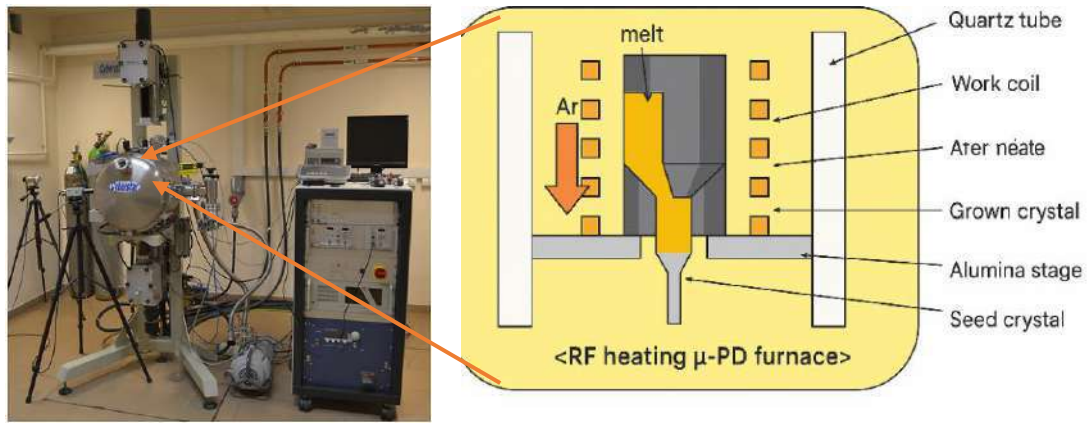


Fig. 5. Photo and diagram of the μ PD equipment used for the growth of CSSG:Ce crystals [44].

To establish a stable temperature gradient suitable for crystal growth, three layers of ceramic insulation, comprising alumina and magnesium-stabilized zirconia, were used. The μ PD furnace chamber was initially evacuated to a pressure of approximately 3.1 μ bar and then filled with argon to atmospheric pressure. Crystal growth was carried out at a constant pulling rate of 1.5 mm/min, using an Al_2O_3 seed crystal. Throughout the growth process, the argon gas flow rate was maintained at approximately 20 L/min.

Table 3. The nominal composition (in oxide powders) and the actual compositions in the CSSG:Ce crystals grown via the MPD method.

No of measurements	Radial position	Nominal crystal content	Actual crystal content
1	Center	$\text{Ca}_3\text{Sc}_2\text{Si}_3\text{O}_{12}:\text{Ce}$	$\text{Ca}_{3.45}\text{Sc}_{1.37}\text{Si}_{3.18}\text{O}_{12}:\text{Ce}$
2	Edge – Top	$\text{Ca}_3\text{Sc}_2\text{Si}_3\text{O}_{12}:\text{Ce}$	$\text{Ca}_{3.37}\text{Sc}_{1.43}\text{Si}_{3.2}\text{O}_{12}:\text{Ce}$
3	Edge – Bottom	$\text{Ca}_3\text{Sc}_2\text{Si}_3\text{O}_{12}:\text{Ce}$	$\text{Ca}_{2.97}\text{Sc}_{1.21}\text{Si}_{3.82}\text{O}_{12}:\text{Ce}$
4	Edge – Left	$\text{Ca}_3\text{Sc}_2\text{Si}_3\text{O}_{12}:\text{Ce}$	$\text{Ca}_{2.92}\text{Sc}_{1.12}\text{Si}_{3.96}\text{O}_{12}:\text{Ce}$
5	Edge – Right	$\text{Ca}_3\text{Sc}_2\text{Si}_3\text{O}_{12}:\text{Ce}$	$\text{Ca}_{2.49}\text{Sc}_{1.25}\text{Si}_{4.26}\text{O}_{12}:\text{Ce}$

The radial deviation of the CSSG:Ce crystal content was established using a KEYENCE Digital Microscope VHX-7000, with a Laser-based Elemental Analyzer with $\pm 5\%$ deviation. (Table 3). The analysis was taken at five different points on the crystal sample, with ensuing averaging of the results to enhance accuracy of the content determination. The obtained results in the center of crystal show some advance of Ca^{2+} and Si^{4+} cations and deficit of Sc^{3+} ions in comparison with stoichiometric content of the $\text{Ca}_3\text{Sc}_2\text{Si}_3\text{O}_{12}$ garnet. For compensation of the charge excess, the cation vacancies V_{Sc} and Ca_{Sc} antisite defects can be created. However, such an assumption needs the detailed confirmation using EPR, NMR or other sensitive methods. Some advancement of Si^{3+} at the crystal edges can be explained by the formation of secondary phases at the crystal–crucible interface, most likely unreacted SiO_2 (see XRD image in Fig. 12b).

3.1.4. Growth of CSSG:Ce and CYMSSG:Ce SCFs on GAGG and YAG Substrates using LPE Method [C4.1, C4.2]

The SCFs and composite film-crystal samples under study were grown using the LPE method in the Chair for Optoelectronic Materials (COM) at the Department of Physics, Kazimierz Wielki University, Bydgoszcz (UKW Bydgoszcz) (Fig. 6). This method enables the crystallization of SCFs of various oxide compounds with precise control of thickness and high structural and optical quality. The process involves creating super saturation in a solution of the crystallizing material within a molten flux, allowing film growth at relatively low temperatures (around 1000 °C), compared to traditional melt crystallization methods that require temperatures above 2000 °C [45, 46].

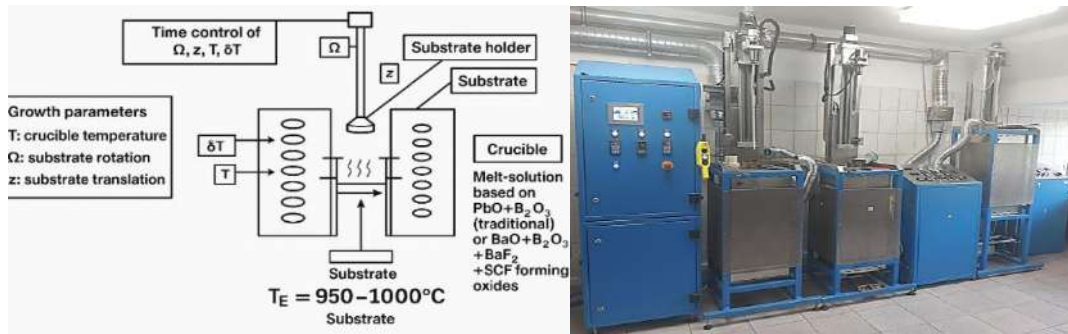


Fig. 6. Diagram (left) and photo (right) of the equipment used for SCF growth by the LPE method.

The formation of an SCF on the substrate is primarily governed by the super cooling process of the solution. To achieve this, the crucible is placed in a furnace (Fig. 6) heated to 1050–1100 °C. At this temperature, the molten materials form an unsaturated solution, characterized by a specific saturation temperature (T_s – *temperature of solidus*). When the solution cools below T_s to the growth temperature (T_g), within the range of 950–1050 °C, it reaches a *supercooled state*, causing the excess dissolved material to deposit onto the rotating substrate introduced into the crucible.

The substrate's dimensions should not exceed half the crucible diameter (15-20 mm). The growth rate of the SCFs is influenced by several factors, primarily the relationship between T_g and T_s . In general, the SCF thickness is proportional to the degree of supercooling ($\Delta T = T_g - T_s$) and the square root of the substrate's rotation speed (ω).

A conventional flux based on the mixture of lead oxide (PbO) and boron oxide (B_2O_3) was used to achieve the necessary liquid molten state of many oxide compounds, with a molar concentration of 95–97% with respect to the total content of the melt-solution (100%). The charge material for film growth was prepared by mixing specific molar amounts of CaO, Sc_2O_3 , Y_2O_3 , MgO, SiO_2 , and CeO_2 oxides, as film constituents, according to the stoichiometric formulas $Ca_3Sc_2Si_3O_{12}$ and $Ca_2YMgScSi_3O_{12}$, and PbO and B_2O_3 oxides as components of the flux. The purity of all raw materials was required to be above 99.99%.

During the charge preparation, the Blank Nielsen coefficients (R_1 , R_2 , R_3 , and R_4) were calculated to ensure optimal film growth:

$$R_1 = \frac{P_{flux_{PbO}}}{P_{flux_{B_2O_3}}}; \quad R_2 = \frac{\sum P_{garnet(dot)}}{\sum P_{garnet(oct+tet)}}; \quad R_3 = \frac{\sum P_{garnet}}{\sum P_{garnet} + \sum P_{flux}}; \quad R_4 = \frac{\sum P_{dopant}}{\sum P_{garnet}}$$

where P represents the molar masses of the flux components (PbO and B₂O₃), the SCF host cations and the activator (Ce), which occupy the dodecahedral (dod), octahedral (oct), and tetrahedral (tet) positions in the garnet lattice.

These coefficients influence the solubility of raw material oxides, the kinetic properties of the melt-solution, the garnet phase formation during LPE crystallization, as well as the luminescent (lighting) characteristics of the SCF. Namely, the coefficient $R_1=11-12$, e.g., the PbO/B₂O₃ molar ratio, defines the kinetic characteristics of the solution and the solubility of the oxides forming the films. The coefficient $R_2=0.6$, e.g., the CaO + Y₂O₃ / Sc₂O₃ + MgO + SiO₂ molar ratio, determines the garnet phase as the primary phase during SCF crystallization.

Meanwhile, selecting the molar ratios R_3 and R_4 within the ranges of 0.025–0.035 and 0.1–0.15, respectively, is crucial mainly for optimizing the luminescence efficiency of the films. Indeed, the R_3 “garnet/flux” coefficient directly determines the temperature range of SCF growth (T_g) and influences the segregation coefficients of the activator (Ce ions) and flux-related dopants (Pb²⁺ and Pb⁴⁺ ions). Specifically, the Ce and Pb content increases with decreasing T_g range and vice versa, but the slopes of these dependencies are different. For this reason, the Ce/Pb ratio increases when R_3 increases up to the optimal values of 0.025–0.035 and drops at higher values due to a decrease in the total Ce concentration in the films. The choice of a very high molar coefficient $R_4=0.1-0.15$, e.g., relative CeO₂ content in the melt-solution, is caused by the very low Ce³⁺ segregation coefficients (usually below 0.01) at low-temperature SCF crystallization of different garnets and other oxide compounds [47, 48].

In frame research in this work, three different sets of SCFs with nominal compositions of Ca₃Sc₂Si₃O₁₂:Ce (CSSG:Ce), with thicknesses ranging from 6 to 30 μm, were prepared using the LPE method [C4.1] (Table 4). The films were crystallized within a temperature range of 975–990 °C from a supercooling melt-solution based on PbO–B₂O₃ flux. The growth of CSSG:Ce SCFs were performed onto undoped GAGG (2.5) substrate (serie A) and two Ce³⁺ doped GAGG:Ce (2.5) substrates (serie B) and GAGG:Ce (3) substrates (serie C) with orientation close to (100). The thickness of GAGG and GAGG:Ce substrates was equal to 0.9 mm. The Ce content both in CSSG:Ce SCFs and GAGG:Ce substrates was about of 0.09–1 at. %.

The real composition of the CSSG:Ce SCF samples was determined using a Laser-based Elemental Analyzer at Keyence VHX-7000 Digital Microscope, providing content measurements with ±5% deviation. The results showed minor variations in Ca, Sc, and Si cation content compared to the stoichiometric formula Ca₃Sc₂Si₃O₁₂, with deviations of less than ±0.15 formula units (Table 4).

Table 4. The nominal composition (in melt-solution) and the real content of LPE grown CSSG:Ce SCFs of A, B and C series [C4.1], h - SCF thickness.

Sample	Nominal content	Real SCF content	h, μm
A1	$\text{Ca}_3\text{Sc}_2\text{Si}_3\text{O}_{12}:\text{Ce}$	$\text{Ca}_{3.12}\text{Sc}_{1.8}\text{Si}_{3.08}\text{O}_{12}:\text{Ce}$	6
A2	$\text{Ca}_3\text{Sc}_2\text{Si}_3\text{O}_{12}:\text{Ce}$	$\text{Ca}_{3.1}\text{Sc}_{1.87}\text{Si}_{3.07}\text{O}_{12}:\text{Ce}$	10
A3	$\text{Ca}_3\text{Sc}_2\text{Si}_3\text{O}_{12}:\text{Ce}$	$\text{Ca}_{3.05}\text{Sc}_{1.94}\text{Si}_{3.01}\text{O}_{12}:\text{Ce}$	30
B1	$\text{Ca}_3\text{Sc}_2\text{Si}_3\text{O}_{12}:\text{Ce}$	$\text{Ca}_{2.95}\text{Sc}_{2.13}\text{Si}_{2.92}\text{O}_{12}:\text{Ce}$	17
B2	$\text{Ca}_3\text{Sc}_2\text{Si}_3\text{O}_{12}:\text{Ce}$	$\text{Ca}_{2.97}\text{Sc}_{2.08}\text{Si}_{2.95}\text{O}_{12}:\text{Ce}$	18
B3	$\text{Ca}_3\text{Sc}_2\text{Si}_3\text{O}_{12}:\text{Ce}$	$\text{Ca}_{2.98}\text{Sc}_{2.06}\text{Si}_{2.96}\text{O}_{12}:\text{Ce}$	32
C1	$\text{Ca}_3\text{Sc}_2\text{Si}_3\text{O}_{12}:\text{Ce}$	$\text{Ca}_{3.01}\text{Sc}_{1.99}\text{Si}_{2.98}\text{O}_{12}:\text{Ce}$	7
C2	$\text{Ca}_3\text{Sc}_2\text{Si}_3\text{O}_{12}:\text{Ce}$	$\text{Ca}_{3.03}\text{Sc}_{1.95}\text{Si}_{3.02}\text{O}_{12}:\text{Ce}$	19
C3	$\text{Ca}_3\text{Sc}_2\text{Si}_3\text{O}_{12}:\text{Ce}$	$\text{Ca}_{3.05}\text{Sc}_{1.93}\text{Si}_{3.02}\text{O}_{12}:\text{Ce}$	22

In this work, two other sets of SCFs with nominal compositions of $\text{Ca}_2\text{YMgScSi}_3\text{O}_{12}:\text{Ce}$ and $\text{Ca}_{1.75}\text{Y}_{1.25}\text{Mg}_{1.25}\text{Sc}_{0.75}\text{Si}_3\text{O}_{12}:\text{Ce}$ (Series A and B, respectively), with thicknesses h ranging from 10 μm to 67 μm , were fabricated using the LPE method [C4.2] (Table 5). The films were crystallized within a temperature range of 975–990 $^{\circ}\text{C}$ from a supercooled melt-solution using conventional $\text{PbO}:\text{B}_2\text{O}_3$ flux. The CYMSSG SCFs were grown on undoped YAG substrates for Series A and on Ce^{3+} -doped YAG substrates for Series B, with orientations close to the (111) crystallographic plane. The YAG and YAG:Ce substrates used in these experiments had a thickness of 0.5 mm. The nominal Ce concentration in the CYMSSG:Ce SCFs and YAG:Ce substrates was approximately 0.05-0.15 at. % and 0.05-0.06 at.%, respectively (Table 5).

Table 5. The nominal composition (in melt-solution) and the real content of LPE grown CYMSSG:Ce/YAG SCFs and CYMSSG:Ce/YAG:Ce SCFs (Series A and B, respectively) and YAG:Ce substrates (Series C) [C4.2].

Sample	Nominal content	Real SCF content	h, μm
A1	$\text{Ca}_2\text{YMgScSi}_3\text{O}_{12}:\text{Ce}$	$\text{Ca}_{1.88}\text{Y}_{1.09}\text{Ce}_{0.01}\text{Mg}_{0.9}\text{Sc}_{1.42}\text{Si}_{2.73}\text{O}_{12}$	19
A2	$\text{Ca}_2\text{YMgScSi}_3\text{O}_{12}:\text{Ce}$	$\text{Ca}_{1.83}\text{Y}_{1.08}\text{Ce}_{0.03}\text{Mg}_{0.9}\text{Sc}_{1.51}\text{Si}_{2.68}\text{O}_{12}$	34
A3	$\text{Ca}_2\text{YMgScSi}_3\text{O}_{12}:\text{Ce}$	$\text{Ca}_{1.81}\text{Y}_{1.12}\text{Ce}_{0.03}\text{Mg}_{0.93}\text{Sc}_{1.48}\text{Si}_{2.67}\text{O}_{12}$	49
A4	$\text{Ca}_{1.75}\text{Y}_{1.25}\text{Mg}_{1.25}\text{Sc}_{0.75}\text{Si}_3\text{O}_{12}:\text{Ce}$	$\text{Ca}_{1.63}\text{Y}_{1.27}\text{Ce}_{0.03}\text{Mg}_{1.19}\text{Sc}_{1.27}\text{Si}_{2.72}\text{O}_{12}$	67
B1	$\text{Ca}_2\text{YMgScSi}_3\text{O}_{12}:\text{Ce}$	$\text{Ca}_{1.92}\text{Y}_{1.08}\text{Ce}_{0.02}\text{Mg}_{0.95}\text{Sc}_{1.27}\text{Si}_{2.78}\text{O}_{12}$	10
B2	$\text{Ca}_{1.75}\text{Y}_{1.25}\text{Mg}_{1.25}\text{Sc}_{0.75}\text{Si}_3\text{O}_{12}:\text{Ce}$	$\text{Ca}_{1.65}\text{Y}_{1.35}\text{Ce}_{0.03}\text{Mg}_{1.18}\text{Sc}_{0.61}\text{Si}_{3.21}\text{O}_{12}$	11
B3	$\text{Ca}_{1.75}\text{Y}_{1.25}\text{Mg}_{1.25}\text{Sc}_{0.75}\text{Si}_3\text{O}_{12}:\text{Ce}$	$\text{Ca}_{1.68}\text{Y}_{1.32}\text{Ce}_{0.03}\text{Mg}_{1.28}\text{Sc}_{0.71}\text{Si}_{3.01}\text{O}_{12}$	22
C1	$\text{Y}_3\text{Al}_5\text{O}_{12}:\text{Ce}$	$\text{Y}_{2.99}\text{Ce}_{0.01}\text{Al}_5\text{O}_{12}$	500
C2	$\text{Y}_3\text{Al}_5\text{O}_{12}:\text{Ce}$	$\text{Y}_{2.99}\text{Ce}_{0.01}\text{Al}_5\text{O}_{12}$	500
C3	$\text{Y}_3\text{Al}_5\text{O}_{12}:\text{Ce}$	$\text{Y}_{2.988}\text{Ce}_{0.012}\text{Al}_5\text{O}_{12}$	500

The content of YAG:Ce substrates and CYMSSG:Ce films were analyzed using a JEOL JSM-820 electron microscope with an IXRF 500i EDX detector, offering $\pm 1\%$ accuracy. This analysis revealed slight deviations in Ca, Mg, Sc, and Si concentrations compared to the nominal formulas, consistently under ± 0.2 formula units (Table 5). For consistency, the nominal composition of the SCFs is used throughout the study to standardize comparisons.

3.2. Experimental Techniques

A variety of experimental techniques were employed to gain a deeper understanding of the interrelation between structural and optical properties of the materials under study. These methods were essential for characterizing the materials and obtaining the key results presented in this work.

3.2.1. X-ray Diffraction Analysis

X-ray diffraction was primarily conducted at the ISC Kharkiv, and partly at the Institute of Materials for Electronic and Energetic (i-MEET), Friedrich-Alexander-Universität (FAU) Erlangen-Nürnberg, Germany (i-MEET Erlangen). XRD analysis was used to determine the real phase composition of various samples, including nano- and micro-powders, eutectics, single crystals, and SCFs.

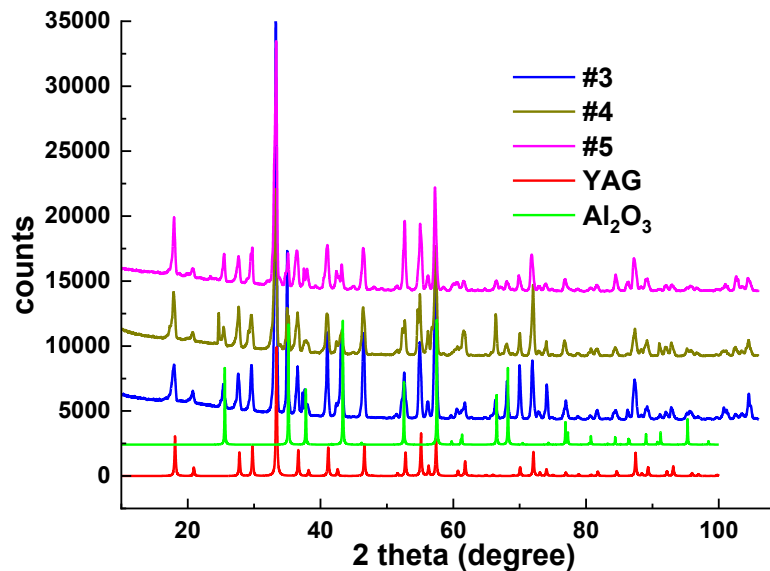


Fig. 7. XRD patterns of $(\text{Al}_2\text{O}_3\text{-YAG})\text{:Ce}$ eutectic samples (2–5) in comparison with Al_2O_3 (ICSD#63,647) and YAG (ICSD #23,848) reference phases [C1.1].

The obtained XRD patterns allowed us to identify the dominant and secondary phases present in each material. In particular, Fig. 7 present the XRD patterns of selected eutectic samples under study compared with standard patterns of Al_2O_3 (ICSD #63,647) and YAG (ICSD #23, 848) phases, providing clear insight into their crystalline structure and phase purity [C1.1].

3.2.2. Scanning Electron Microscopy

SEM was used to analyze the surface morphology of the eutectic samples (Fig. 8) [C1.1] and examine the structure of synthesized CSSG:Ce and CYMSSG:Ce micropowders (Fig. 9 - Fig. 11) [C2.1, C2.2, C2.3]. SEM analysis of eutectic samples was conducted at both the Kharkiv Institute for Single Crystals (Ukraine) using conventional SEM JEOL JSM-6390LV. Microscopic images of the synthesized powder samples were obtained at the i-MEET Erlangen using a Field Emission SEM (FESEM) JEOL JSM-7610F. Due to the poor conductivity of the powder samples, they were coated with carbon.

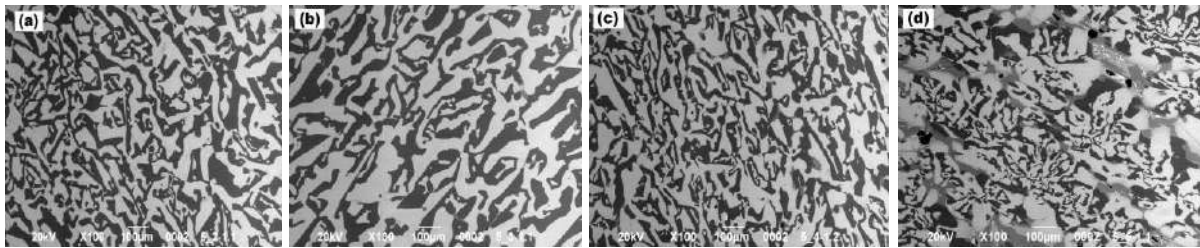


Fig. 8. The garnet (white) and sapphire (gray) phases distribution in SEM images of the (Al₂O₃-YAG):Ce eutectics: (a) sample 2, (b) sample 3, (c) sample 4, and (d) sample 5 [C1.1].

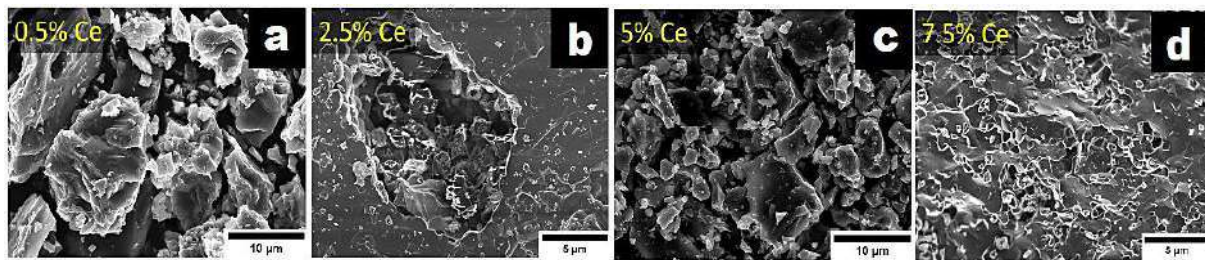


Fig. 9. SEM images of CSSG:Ce MPs samples with different Ce content (samples containing a nominal Ce³⁺ concentration of 0.5 (a), 2.5 (b), 5 (c) and 7.5 (d) at. %) [C2.1].

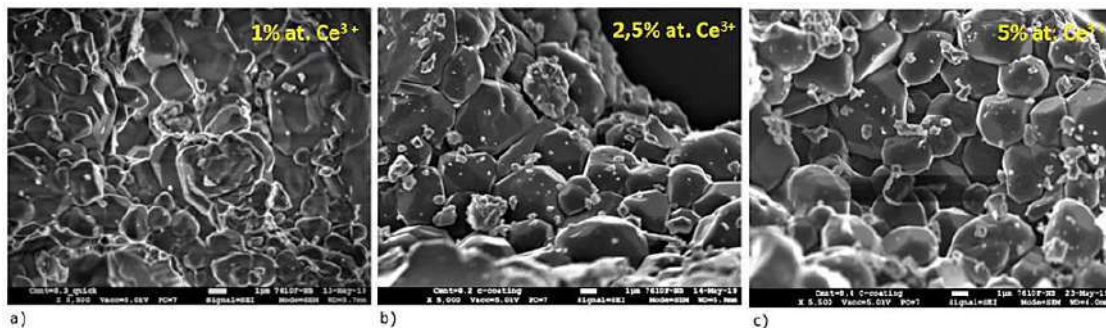


Fig. 10. SEM images of CYMSSG:Ce MPs samples with different Ce content: (a) – 1 at. % Ce³⁺, (b) – 2.5 at. % Ce³⁺, (c) – 5 at. % Ce³⁺ [C2.2].

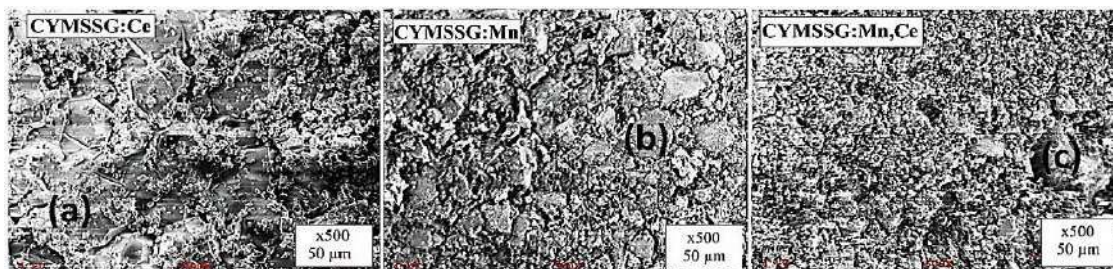


Fig. 11. SEM images, at the magnification (x500) of micro powder samples of CYMSSG garnets, doped with Ce³⁺ (a), Mn²⁺ (b) and Ce³⁺-Mn²⁺ (c) ions [C2.3].

3.2.3. Micro-Computed Tomography

Micro-Computed Tomography (μ CT) was used in this study due to its ability to provide high-resolution, non-destructive 3D imaging of the internal structure of materials. This technique is particularly valuable for analysing the morphology, density variations, and structural integrity of synthesized samples without requiring complex sample preparation. These investigations were performed at the Department of Mechatronics, UKW Bydgoszcz.

μ CT operates on the principle of X-ray attenuation, where a focused X-ray beam passes through the sample and a detector records the transmitted intensity at different angles. By acquiring multiple projections, a detailed 3D reconstruction of the sample is generated using computational algorithms. The resulting images allow for precise visualization and quantification of internal features such as porosity, grain distribution, and defects at the micrometer scale. This technique is especially beneficial for studying *composite and crystalline materials*, as it provides insights into their homogeneity, phase distribution, and potential structural imperfections. Moreover, the non-destructive nature of μ CT enables repeated analysis of the same sample under different conditions, making it an essential tool for material characterization.

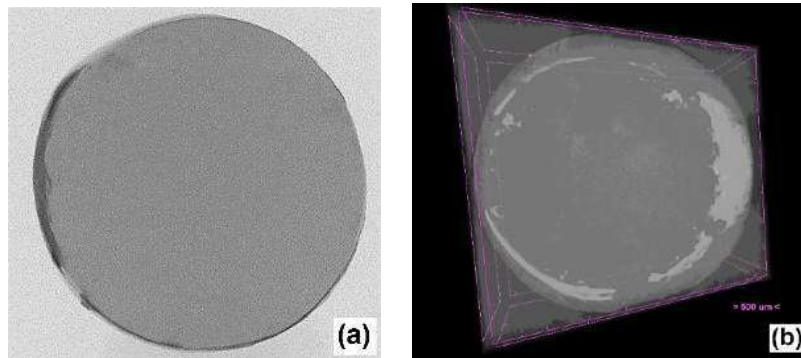


Fig. 12. The radiograph of the CSSG:Ce crystal acquired through X-ray μ CT (a) and the reconstructed three-dimensional image of this crystal structure (b).

μ CT was used to examine the internal structure of the CSSG:Ce crystal, revealing a dominant CSSG garnet phase in the center, with a secondary phase (most likely unreacted SiO_2 , Table 3) observed at the edges (Fig. 12b). This secondary phase is likely due to the specific growth conditions of the μ PD method, including thermal gradients, impurity concentration, and segregation effects during solidification. Due to the presence of a secondary phase along the crystal's edges, optical investigations were focused on the central part of the crystal (Table 3).

X-ray μ CT analysis (Fig. 13) of the eutectic samples shows that the $(\text{Al}_2\text{O}_3\text{-YAG})\text{:Ce}$ eutectic structure exhibits a random spatial distribution of stripes corresponding to the main garnet (white) and sapphire (gray) phases. A histogram analysis, based on the mixture model, determined the volume fractions of both phases in the eutectic samples (Table 6).

Table 6. The sapphire and garnet phase proportions of the eutectic samples.

Sample	Al ₂ O ₃ Phase content, %	YAG Phase Content, %
2	54.39	46.61
3	50.02	49.98
4	45.58	54.42
5	46.60	53.4

The gray level distribution graphs for both phases in the image of sample two, corresponding to their content (Fig. 13, left side). The difference in the position of the observed peaks is attributed to the varying X-ray absorption abilities of the YAG and sapphire phases. This variation is governed by $\mu \sim \rho * Z_{\text{eff}}^4$, where ρ is the density and Z_{eff} is the effective atomic number, with values of 35 for YAG and 11.2 for sapphire.

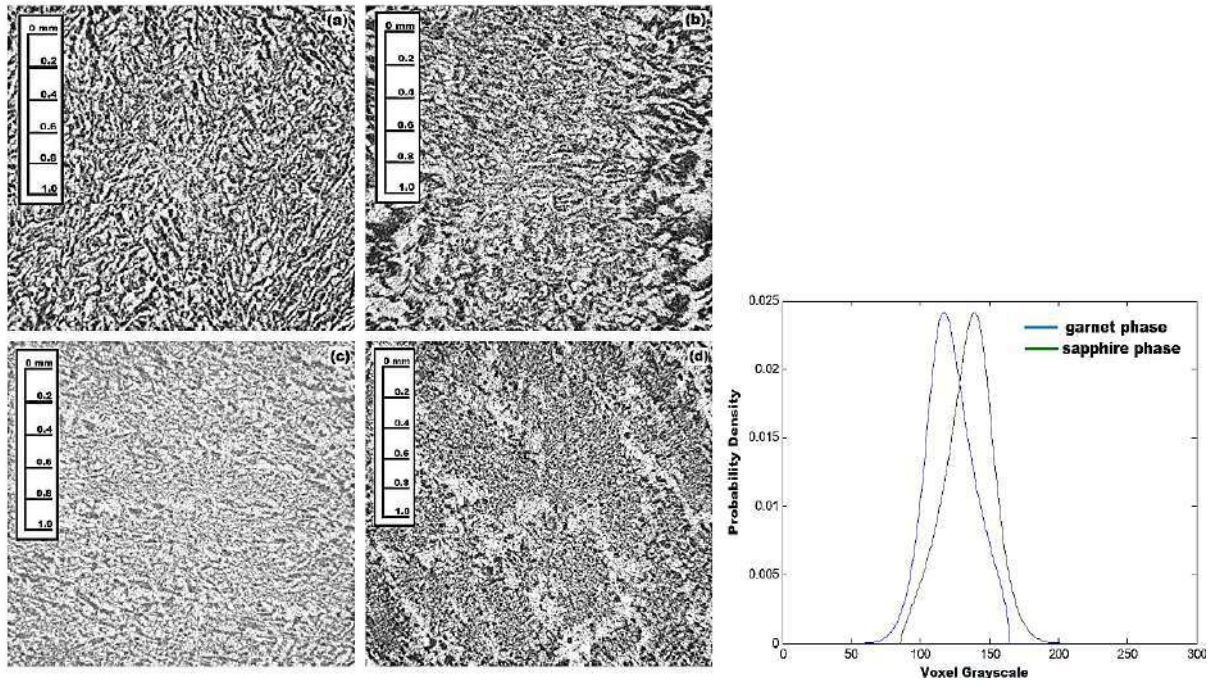


Fig. 13. Left - X-ray μ CT of the (Al₂O₃-YAG):Ce eutectic: garnet (white) and sapphire (gray) phases distribution for samples 2 (a), 3 (b), 4 (c), and 5 (d). Right bottom - graphs of the calculated density function in two subsets of voxels, corresponding to YAG (white) and sapphire (gray) phases in the μ CT image presented in Fig.13a for sample 2.

3.2.4. Absorption Spectroscopy

Absorption spectroscopy was conducted at the COM, UKW Bydgoszcz. Absorption spectra were measured using the Jasco V-760 UV-Visible/NIR spectrophotometer (Fig. 14). The instrument employs a deuterium lamp for the UV region and a tungsten lamp for the visible/IR range. Light is directed through a monochromator to isolate specific wavelengths, passes through the sample, and is detected by a light detector (UV-Vis photomultiplier; IR SPb cell).



Fig. 14. Absorption spectroscopy setup using the Jasco V-760 UV-Visible/NIR spectrophotometer.

The V-760 features a double monochromator for high resolution and extremely low stray light (0.00008%). Its adjustable bandwidth, down to 0.1 nm, enables precise measurements across 200–1000 nm. Data acquisition and control are managed using the Spectra Manager™ software [49]. The measurement results obtained with this equipment are presented in Fig. 28 and Fig. 31.

3.2.5. Luminescence Spectroscopy

Photoluminescence (PL), PL excitation spectra (PLE), and PL decay kinetics were measured using an Edinburgh FS5 spectrofluorometer (Fig. 15).

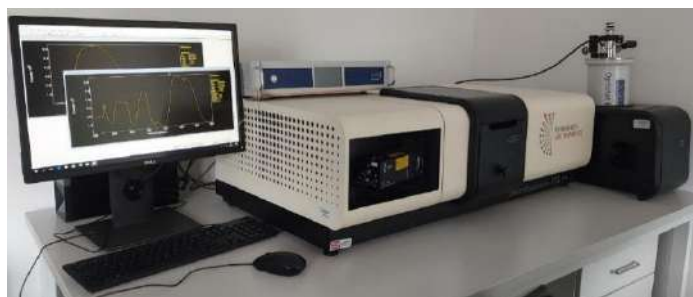


Fig. 15. Edinburgh FS5 spectrofluorometer used for PL emission, excitation spectra, and decay kinetics measurements.

The instrument features a cooled photomultiplier and an optimized mirror-based optical system (flat, spherical, toroidal, and elliptical mirrors) to provide high sensitivity and resolution. Data are automatically corrected for the spectral response of the system and changes in excitation power using factory correction files and a reference silicon detector. A Xenon lamp is used for PL emission and excitation measurements, while a pulsed microsecond lamp or tunable lasers are used for decay kinetics, enabling measurements over excitation and emission ranges of 250–820 nm and 250–820 nm, respectively. The measurement results obtained with this equipment are presented in Fig. 17, Fig. 19 - Fig. 21, Fig. 26, Fig. 32.

3.2.6. Colorimetry

Colorimetry is a branch of spectroscopy that focuses on measuring, analyzing, and describing colors based on their wavelength, intensity, and perception. Colorimetry is essential in LED development for analyzing and optimizing light emission to achieve the desired color

quality and efficiency. It helps determine the exact chromaticity coordinates of LEDs, ensuring color consistency and accuracy. By measuring the CCT, colorimetry defines whether an LED emits warm or cool light, which is crucial for applications like indoor lighting and display technologies. Additionally, it assesses the CRI to evaluate how accurately an LED reproduces colors compared to natural light. In phosphor-converted LEDs, such as WLEDs using YAG:Ce phosphors, colorimetry is used to fine-tune phosphor compositions to achieve the ideal spectral balance, brightness, and efficiency. This process ensures that LEDs meet industry standards for color performance and application-specific requirements.

Fig. 16 illustrates the setup for measuring the color characteristics of phosphor-converters. The test sample is placed on a blue LED (1) as the excitation source, while an integrating sphere (2) collects and evenly distributes the emitted light through multiple diffuse reflections. The sphere's highly reflective inner surface (>96%) ensures uniform illumination across a broad wavelength range (180-1200 nm). A fiber optic cable (3), positioned at a 90-degree angle to the input port, transmits the collected light to the AvaSpec-ULS2048-LTEC spectrometer (4), which operates across 200-1100 nm with ultra-low light scattering. To enhance performance, the spectrometer's CCD detector is cooled by a Peltier element, reducing thermal noise and increasing the dynamic range. The AvaSoft software processes the spectral data, recording intensity in absolute units ($\mu\text{W}/\text{cm}^2/\text{nm}$) and generating CIE chromatic diagrams to determine dominant wavelength as well as correlated color coordinates (CCC), correlated color temperature (CCT), and correlated rendering index (CRI). An Osram LBE 6SG blue LED (450 nm, 30 mA, 2.5V) serves as the excitation source for chromaticity measurements. A YAG:Ce crystal sample with a known luminous efficiency (LE) of approximately 100 lm/W is used as the reference sample. The results of measurements obtained with this equipment are presented in Figs. 18, 22, 24, 27, 30, and 33.

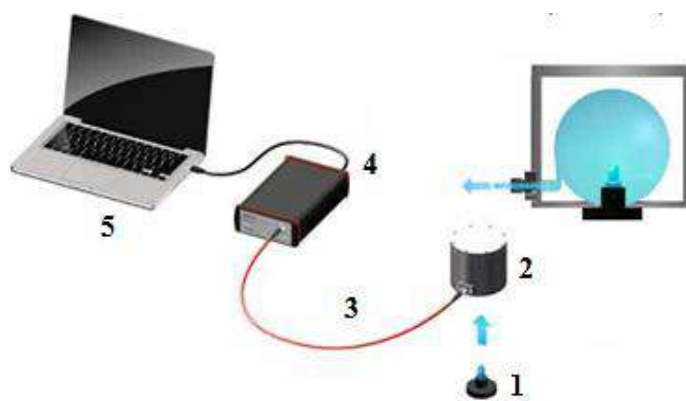


Fig.16. Standard Avaspec equipment setup for measuring the photoconversion properties of phosphors:1-blue LED chip, 2-integrating sphere, 3-fiber optic cable, 4-the AvaSpec-ULS2048-LTEC spectrometer, 5 - laptop.

4. OPTICAL AND PHOTOCONVERSION PROPERTIES OF WLED CONVERTERS BASED ON THE DIFFERENT CRYSTALLINE FORMS OF GARNET COMPOUNDS

4.1. Ce³⁺-Doped Al₂O₃-YAG Eutectic: Synthesis, Structural Characterization, and Luminescent Properties for White LED Applications [C1.1]

This part of the dissertation focuses on the detailed analysis of the optical properties of Ce³⁺ doped Al₂O₃-YAG Eutectics. This eutectic system is regarded as a promising material for light conversion in WLEDs due to its outstanding luminescent characteristics, including high quantum yield and efficient light emission. Additionally, the material's excellent thermal stability makes it particularly well-suited for high-power WLED applications, where heat resistance and long-term reliability are essential. The findings presented in this part of the study represent a significant step toward optimizing materials for enhanced WLED performance and contribute to the advancement of more efficient and durable light-conversion systems.

The structural properties of Ce³⁺-doped Al₂O₃-YAG eutectic samples were characterized using a combination of SEM, XRD, and high-resolution μ CT (see Chapter 4.1.1). Optical characterization of this material included CL, PL and PLE spectra, as well as PL decay kinetics and photoconversion measurements. The photoconversion behavior of the (Al₂O₃-YAG):Ce eutectic samples was evaluated under blue LED excitation, with particular attention paid to the determination of CCC on CIE diagram, CCT, and CRI values.

The PL and PLE spectra of the Ce³⁺-doped Al₂O₃-YAG eutectic, exemplified by sample 4 (Table 1), are shown in Fig. 17a and Fig. 17b, respectively. Excitation at the characteristic maxima of the PLE spectra at 340 and 450 nm results in a dominant yellow-green PL emission band peaking in the 547–556 nm range, corresponding to the 4f–5d transitions of Ce³⁺ ions in the YAG:Ce garnet phase. The spin–orbit splitting of the ground state causes the emission band under 450 nm excitation to resolve into two components at 539 and 584 nm, related to the Ce³⁺ 5d₁ → ²F_{5/2} and 5d₁ → ²F_{7/2} transitions, respectively.

The shift in the Ce³⁺ emission band at other excitation wavelengths is likely due to differences in the 5d₁ → ²F_{5/2} and ²F_{7/2} transition probabilities and energy transfer processes between the sapphire and garnet phases. Furthermore, under excitation at 265 nm, corresponding to the sapphire phase, PL from Ce³⁺ ions in the sapphire host is observed as a band peaking at 398 nm (Fig. 17a). This band is strongly distorted by the Ce³⁺ absorption band at 340 nm in garnet phase, as well as by an emission band at 363 nm, which most likely corresponds to a small amount (less than 1 wt.%) of YAlO₃ perovskite phase in the Al₂O₃-YAG eutectic, undetectable by XRD method.

The decay kinetics of Ce³⁺ luminescence in the (Al₂O₃-YAG):Ce eutectic, measured at 560 nm under 460 nm excitation (Fig.17c, curve 1), exhibit a strong single-exponential behavior

with a decay time of 66 ns, typical for Ce^{3+} in garnet hosts. However, under high-energy and UV excitation (e.g., at 260 nm), effective energy transfer from Ce^{3+} ions in the Al_2O_3 phase to the garnet phase is observed. This is supported by the non-exponential decay kinetics of Ce^{3+} luminescence in $\text{Al}_2\text{O}_3:\text{Ce}$ (Fig.17c, curve 2), which reveals two components with decay times of 31 and 38 ns. An average decay time of 35 ns was used to describe the overall behavior, which is lower but consistent with the 42 ns lifetime observed in $\text{Al}_2\text{O}_3:\text{Ce}$ SCF [50].

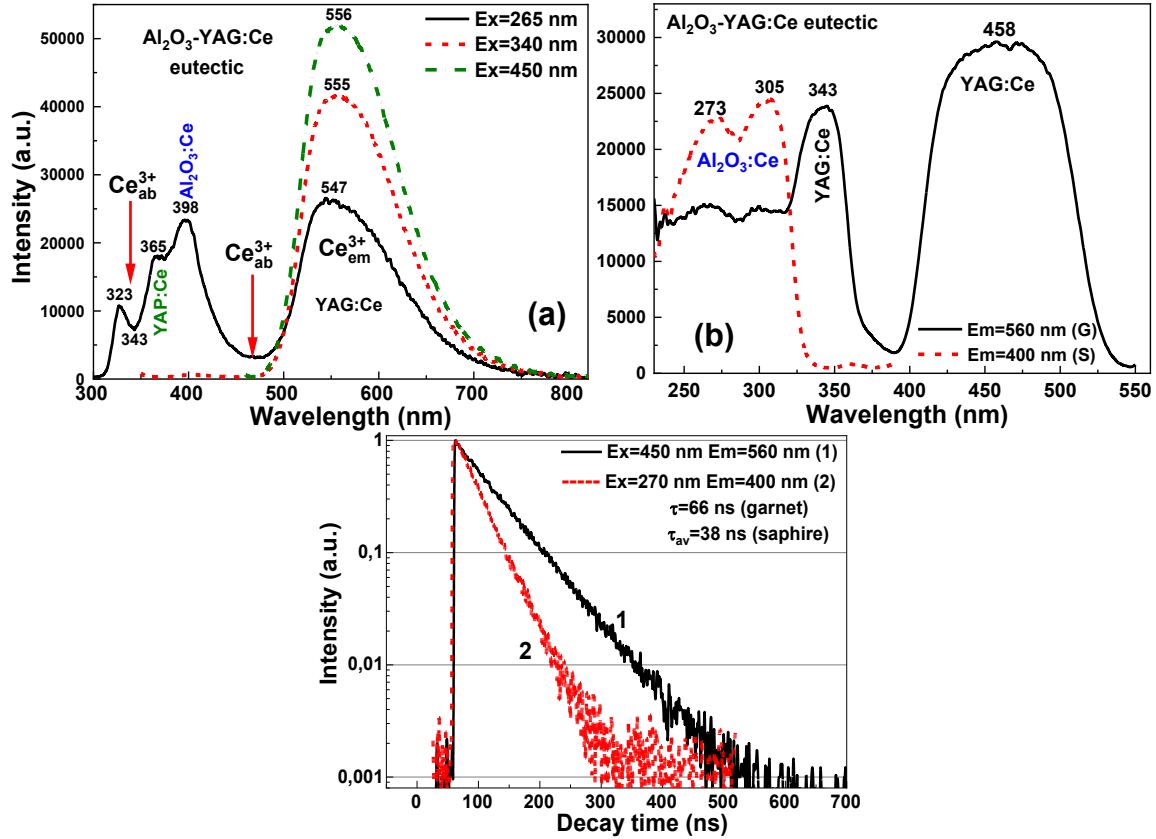


Fig. 17. PL (a) and PLE spectra (b) of $(\text{Al}_2\text{O}_3\text{-YAG})\text{:Ce}$ eutectic (sample 4) under excitation at different wavelengths (a) and registration of Ce^{3+} luminescence in the garnet ((b), curve 1) and sapphire phase ((b), curve 2). Decay kinetics (c) of $(\text{Al}_2\text{O}_3\text{-YAG})\text{:Ce}$ eutectic (sample 4) corresponding to the Ce^{3+} luminescence in the YAG:Ce (1) and $\text{Al}_2\text{O}_3\text{:Ce}$ (2) phases under excitation in the respective PLE bands at 450 nm (1) and 270 nm (2).

Photoconversion prototypes of WLEDs were tested using a blue 450 nm LED chip and $(\text{Al}_2\text{O}_3\text{-YAG})\text{:Ce}$ eutectic photoconverters with thicknesses ranging from 0.15 to 1 mm (Fig.18). The results were promising, as the emission spectrum of the $\text{Al}_2\text{O}_3\text{-YAG}:\text{Ce}$ eutectic converter spanned the visible range from 460 to 820 nm, producing warmer light compared to the standard YAG:Ce photoconverter. As the eutectic thickness increased, the intensity of the blue LED emission decreased, while the yellow emission intensity increased, peaking at a thickness of approximately 1.0 mm, where nearly all the blue light was absorbed.

The CIE 1931 chromaticity diagram in Fig.18b illustrates the variation in colour coordinates (x, y) of the $(\text{Al}_2\text{O}_3\text{-YAG})\text{:Ce}$ eutectic converter as the thickness increases from

0.15 mm to 1.0 mm. The coordinates exhibit a nonlinear trend, with both x and y values increasing as thickness grows. By adjusting the eutectic thickness between 0.15 mm and 0.4 mm, it is possible to fine-tune the CCT of the emitted white light. The CIE coordinates of the WLED prototypes are summarized in Table 7, showing that eutectic thicknesses in this range can produce white light hues from warm white (CCT = 3810 K) to warm/daylight white (CCT \approx 5120 K). These findings indicate that an optimal white light colour can be achieved with a eutectic thickness of approximately 0.1–0.15 mm under 450 nm LED excitation. This optimal thickness is notably smaller than that of the YAG:Ce crystal counterpart (0.5–0.55 mm for 1 mol% Ce) [51], owing to reduced light-guiding and reflection losses.

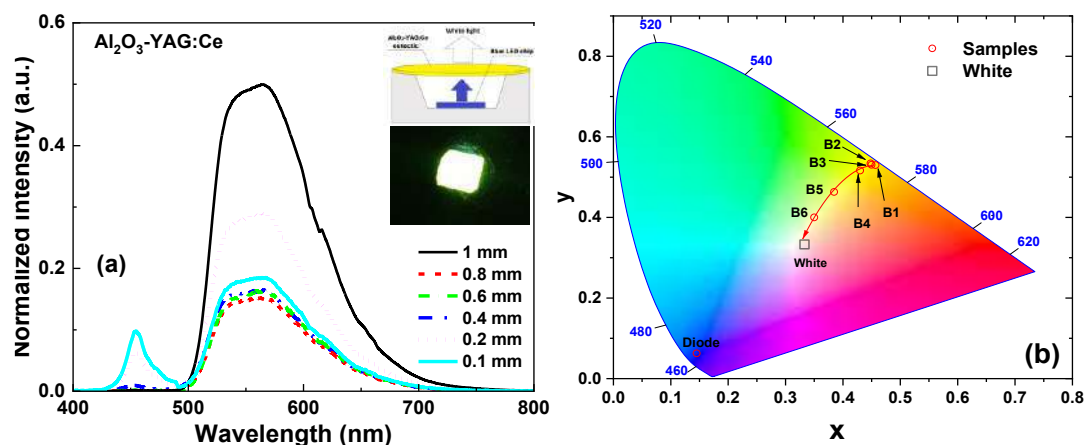


Fig. 18. The spectral performance of (Al₂O₃-YAG):Ce eutectic samples under 450 nm blue LED excitation (a); color coordinates of (Al₂O₃-YAG):Ce eutectic-based LEDs in CIE-1931 color space chromaticity diagram (b).

Table 7. CIE coordinates, CTT and LE of a WLED lamp fabricated on the base of 450 nm LED chip and (Al₂O₃-YAG):Ce eutectic converters (sample 4) with different thicknesses.

Thicknesses of the sample, mm	CIE Coordinates		CCT, K	CRI	LE, lm/W
	x	y			
1 (B1)	0.4567	0.5299	3489	39.7	68
0.8 (B2)	0.4498	0.5306	3580	46.1	81
0.6 (B3)	0.4483	0.5341	3620	42.3	107
0.4 (B4)	0.4300	0.5165	3810	55.9	120.4
0.2 (B5)	0.4047	0.4633	4530	67.4	132
0.15 (B6)	0.3500	0.4000	5120	72.5	142.5

In conclusion, the main achievements regarding the eutectic (Al₂O₃-YAG):Ce converter can be summarized as follows:

1. Successful preparation of eutectic samples using HDC method, yielding a stable and well-structured material for WLED applications.

2. Characterization of the structural and optical properties, including XRD and SEM analyses, confirming the presence of Ce^{3+} doped YAG and corundum phases, with undetectable by XRD amount of YAP contamination.

3. PL studies of the $(\text{Al}_2\text{O}_3\text{--YAG})\text{:Ce}$ converter reveal the presence of efficient Ce^{3+} energy transfer from the sapphire to the garnet host, with dominant Ce^{3+} luminescence in the garnet phase within the green-yellow range. The spectral position of the Ce^{3+} emission band in the $(\text{Al}_2\text{O}_3\text{--YAG})\text{:Ce}$ eutectic depends on the excitation wavelength and the interactions between the sapphire and garnet phases.

4. Investigation of the photoconversion properties of WLEDs prototypes with $(\text{Al}_2\text{O}_3\text{--YAG})\text{:Ce}$ colour converter, showing the ability to adjust the emitted color of white light by modifying the eutectic thickness, achieving white light with various CCT from 3810 to 5120 K under 450 nm blue excitation.

5. Demonstration that an $(\text{Al}_2\text{O}_3\text{--YAG})\text{:Ce}$ eutectic with a thickness of 0.1–0.15 mm can provide optimal white light colour under 450 nm LED excitation, outperforming the YAG:Ce crystal counterpart in terms of both thickness and light conversion efficiency.

4.2. Ce^{3+} and Mn^{2+} Doped $\text{Ca}_3\text{Sc}_2\text{Si}_3\text{O}_{12}$ and $\text{Ca}_2\text{YMgScSi}_3\text{O}_{12}$ Micropowders as Efficient Light Converters for White LEDs [C2.1, C2.2, C2.3]

This part of the work is dedicated to the investigation of Ce^{3+} and Mn^{2+} co-doped mixed silicate garnets, specifically $\text{Ca}_3\text{Sc}_2\text{Si}_3\text{O}_{12}$ (CSSG) and $\text{Ca}_2\text{YMgScSi}_3\text{O}_{12}$ (CYMSSG), synthesized in the NP and MP forms. These materials were prepared using different solid-state synthesis methods, and their structural properties of these MPs were analyzed using SEM and XRD (see Chapter 3.2), which allow for a high degree of phase formation and precise control over particle morphology. Exploring the properties of such mixed garnets is crucial for optimizing light-converting MP materials, as they offer broader tunability of optical properties compared to conventional YAG:Ce phosphors. This makes them a promising alternative for the development of WLEDs with improved colour rendering and luminous efficiency.

The luminescent properties of CSSG:Ce MP, CYMSSG:Ce and CYMSSG:Ce,Mn MP samples reveal distinct spectral behaviours, excitation characteristics, and decay kinetics (Fig. 19, Fig. 20, and Fig. 21, respectively), indicating differences in the site distribution of Ce^{3+} and Mn^{2+} ions, as well as in the energy transfer processes from host lattices to activator ions. These peculiarities can be utilized to tune the conversion properties of WLEDs based on the MP of these materials (Figs. 22, Fig. 23, and Fig. 24, respectively).

The CSSG:Ce MPs exhibit a complex, non-monotonic shift in their PL spectra, initially blue-shifting from 501.5 to 495 nm and then red-shifting to 505 nm with increasing excitation wavelength in the 236–450 nm range (insert of Fig. 19a). This behavior suggests the presence of

at least two distinct Ce^{3+} centers, Ce1 and Ce2, which occupy different local environments within the crystal lattice. The PLE spectra (Fig. 19b) confirms this multicenter formation, showing multiple excitation bands at 437, 339, and 256 nm for Ce1 center, and 449, 311, and 256 nm for Ce2 center. Additionally, an excitation peak at 280 nm is associated with defect-related centers, likely F-centers, which may play a role in energy transfer processes to Ce1 and Ce2 centers.

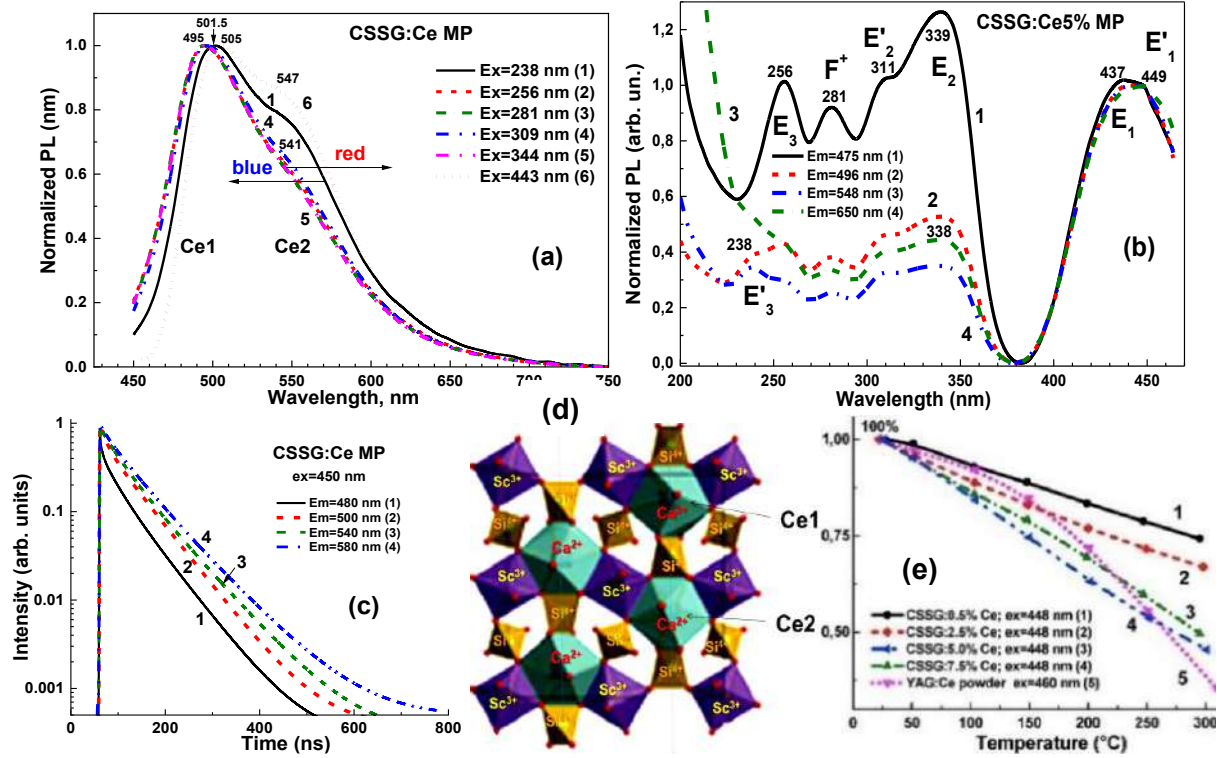


Fig. 19. Luminescent properties of CSSG:Ce:5% Ce MPs at RT. Emission (a) and excitation (b) recorded in different parts of the respective spectra. PL decay kinetics (c) at RT recorded under blue light (450 nm) excitation in different parts of Ce^{3+} emission band; (d) - visualization of possible multicenters in structures of $\text{Ca}_3\text{Sc}_2\text{Si}_3\text{O}_{12}:\text{Ce}$ garnet; (e) - temperature dependence of integral emission in 450–700 nm spectral range for CSSG:Ce MPs with different Ce^{3+} concentrations in comparison with commercial YAG:Ce powder.

In contrast, CYMSSG:Ce MPs exhibit a significant redshift in their PL spectra (Fig. 20a), shifting from 564 to 587 nm with increasing excitation wavelength in the 420–480 nm range. The redshifted and slightly narrowed emission bands suggest a stronger crystal field effect and a distinct Ce^{3+} site distribution compared to CSSG:Ce. The PLE spectra (Fig. 20b) of CYMSSG:Ce powders include two main Ce^{3+} -related bands at 454 and 353 nm, as well as additional peaks at 306 and 274 nm, which are likely linked to defect centers or flux-related impurities, indicating the presence of alternative excitation pathways.

The luminescence decay kinetics of both materials (Fig. 19c and Fig. 20c) confirm the existence of multiple Ce^{3+} centers and energy transfer processes between them. CSSG:Ce powder exhibits strongly non-exponential decay, best described using a three-component exponential

model, with decay times increasing from 4.7 ns, 27.2 ns, and 63.5 ns at 480 nm excitation to 14.6 ns, 59.1 ns, and 83.6 ns at 580 nm excitation (Fig.19c). This variation suggests energy transfer from higher-energy to lower-energy Ce^{3+} centers, influenced by the surrounding Sc^{3+} and Si^{4+} cations in octahedral and tetrahedral positions. Similarly, PL decay profiles for CYMSSG:Ce powder also follows a three-component decay model, but its redshifted emission and slightly longer decay times indicate a different Ce^{3+} environment, with additional contributions from Ca^{2+} and Y^{3+} in dodecahedral positions.

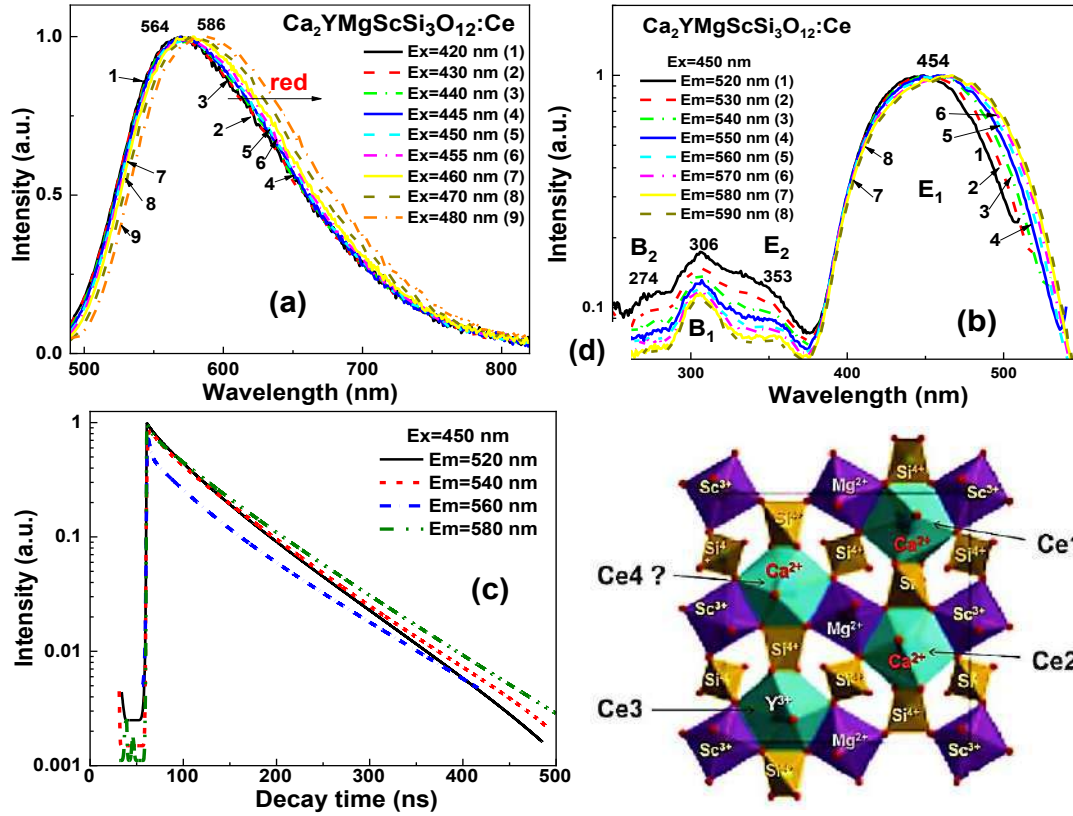


Fig. 20. Luminescent properties of $\text{Ca}_2\text{YMgScSi}_3\text{O}_{12}:\text{Ce}5\%$ MPs at RT. Emission (a) and excitation (b) recorded in different parts of the respective spectra. (c) - PL decay kinetics at RT recorded under blue light (450 nm) excitation in different parts of the Ce^{3+} emission band, (d) - visualization of possible multicenters in structures of $\text{Ca}_2\text{YMgScSi}_3\text{O}_{12}:\text{Ce}$ garnet.

Both CSSG:Ce and CYMSSG:Ce phosphors exhibit the formation of Ce^{3+} multicenters with distinct local environments, as evidenced by their non-monotonic PL shifts and varying PLE spectra. CSSG:Ce displays of Ce^{3+} radiative transitions with PL band primarily in the green-yellow region, while CYMSSG:Ce shows a much broader and redshifted PL emission band. The visualization of these multicenters (two in CSSG:Ce and four in CYMSSG:Ce) and their spatial structure is presented in Figs.19d and Fig. 20d, respectively.

While both materials exhibit Ce^{3+} multicenters behaviour and energy transfer effects, the stronger redshift and altered PL decay dynamics of CYMSSG:Ce powder make it a promising candidate for use as a WLED converter in applications requiring warm-white emission.

The phosphors used as colour conversion materials in WLEDs must exhibit low thermal quenching behaviour, at least up to 150 °C. For this reason, the temperature-dependent quenching characteristics of GSSG:Ce and CYMGGG:Ce MPs were investigated and compared with those of the commercial OSRAM YAG:Ce phosphor (Fig. 19e). The PL of CSSG:Ce phosphors is less quenched at lower Ce doping concentrations (0.5–2.5%) than that of the commercial YAG:Ce phosphor, even at elevated temperatures (>200 °C). Therefore, this phosphor is a suitable colour conversion material for high-power LEDs. However, at higher doping levels (5–7.5%), the thermal quenching of PL becomes more significant. The CYMGGG:Ce MP phosphors also exhibit lower thermal stability, with quenching of the Ce^{3+} luminescence occurring at lower temperatures than in the YAG:Ce and CSSG:Ce samples.

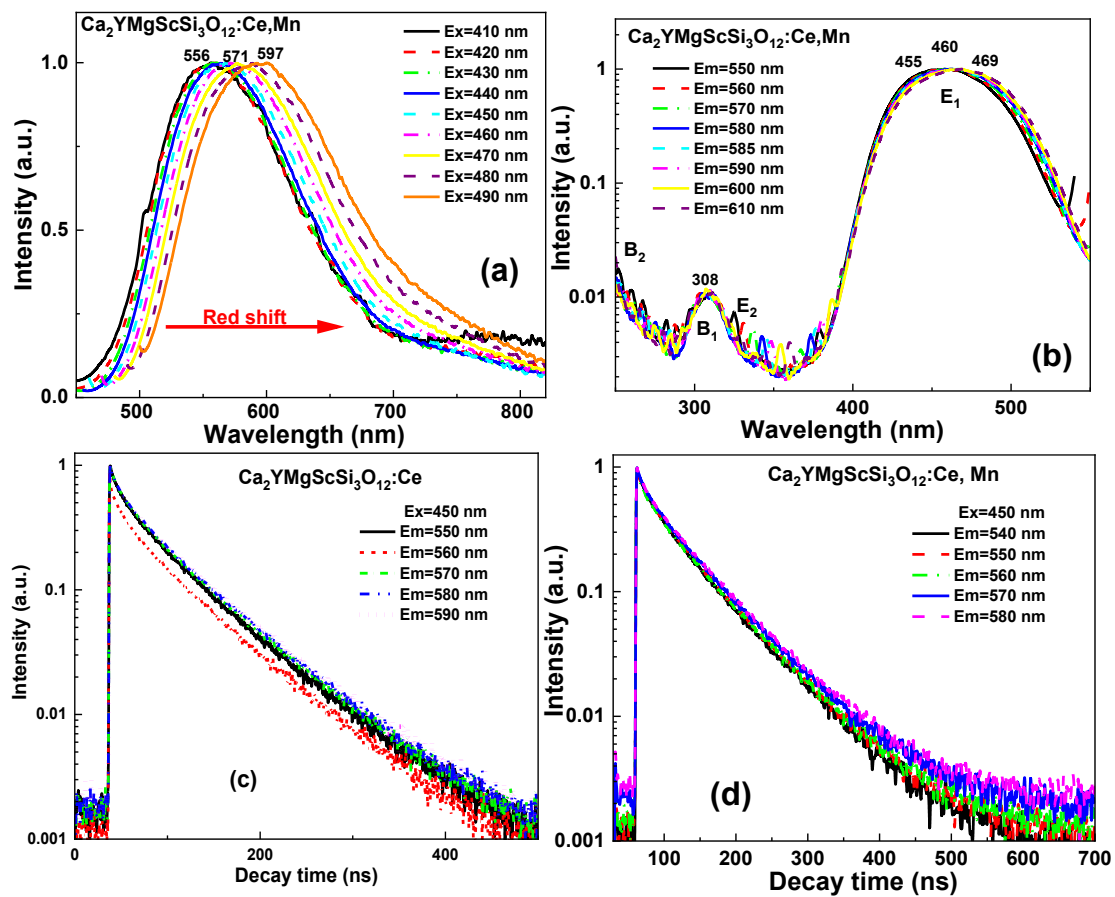


Fig. 21. (a) – normalized PL emission spectra of CYMSSG:Ce,Mn MP under excitation in the 410–490 nm range, corresponding to the different parts of Ce^{3+} related absorption band; (b) – PL excitation spectra of CYMSSG:Ce,Mn MP, recorded in 550–610 nm in different parts of the Ce^{3+} and Mn^{2+} emission bands; (c) – PL decay kinetics of CYMSSG:Ce MP, recorded in the different parts of the Ce^{3+} emission band in the 550–590 nm range under excitation at 450 nm; (d) – PL decay kinetics of CYMSSG:Ce,Mn MP, recorded in the different parts of the $\text{Mn}^{2+}, \text{Ce}^{3+}$ emission band in the 540–580 nm range under excitation at 450 nm.

Significant differences in the PL emission and PLE spectra of CYMSSG:Ce,Mn MP (Fig.21a) are observed in comparison with CYMSSG:Ce MP (Fig.20). Notably, a redshift in the main emission band from 556 nm to 597 nm is observed in the PL spectra of CYMSSG:Ce,Mn MP as

the excitation wavelength increases from 410 to 490 nm. This emission region is substantially red-shifted relative to that of CYMSSG:Ce MP due to the simultaneous contributions of both Ce^{3+} and Mn^{2+} luminescence (Fig. 21a). Specifically, compared to CYMSSG:Ce MP under the same excitation conditions, the PL spectra of CYMSSG:Ce,Mn MP exhibit a redshift of approximately 10 nm, indicating energy transfer from Ce^{3+} to Mn^{2+} ions. Furthermore, differences are also observed in the wavelength-dependent shift of the PL peak maximum between CYMSSG:Ce and CYMSSG:Ce,Mn MPs as the excitation wavelength increases (Fig.21c).

In CYMSSG:Ce micropowders, the PL decay is dominated by the fast 5d–4f transition of Ce^{3+} with lifetimes on the order of tens to hundreds of nanoseconds. When Mn is co-doped (CYMSSG:Ce,Mn), the decay becomes multi-exponential: the fast Ce^{3+} component shortens due to energy transfer to Mn, while a slower microsecond–millisecond component appears from Mn emission. As a result, Ce-only samples show clean, fast decay, while Ce,Mn samples display reduced Ce intensity and a pronounced slow tail, reflecting efficient Ce→Mn energy transfer that enhances red emission but lowers the intrinsic speed of the Ce channel.

Ce^{3+} and Mn^{2+} -doped silicate garnet phosphors have been successfully implemented in WLED prototypes, as shown in Figs. 22 - 24. The emission spectra and chromaticity diagrams for each prototype are presented in Fig.22 (WLED based on a bulb-bulk CSSG:Ce phosphor converter), Fig.23 (WLED using a multilayered film CYMSSG:Ce converter), and Fig. 24 – WLED incorporating a multilayered films CYMSSG:Ce,Mn converter. All studied phosphors exhibit promising potential for various lighting applications. However, they differ significantly in their lighting figure of merit, highlighting the importance of phosphor composition and structure in optimizing WLED performance.

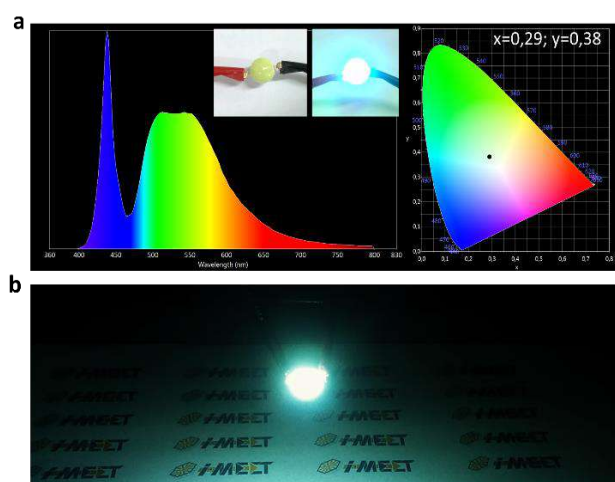


Fig. 22. (a) - CIE chromaticity coordinates and emission spectrum of a WLED lamp fabricated on the base of 432 nm LED chip, operating at 130 mA and 3.5 V, and CSSG:5%Ce phosphor embedded in the epoxy resin. In set it shows appearance of a well-packaged LED lamp in operation. (b) - demonstration of the white LED in dark room.

The first WLED prototype was fabricated using a conventional GaN 432 nm blue LED chip, operating at 130 mA and 3.5 V, and coated with CSSG:Ce5% phosphor embedded in a bulb-like epoxy resin. This prototype provides a broad emission spectrum that spans the entire visible range (from 400 to 780 nm), with CIE coordinates of $x = 0.29$ and $y = 0.38$ (Fig. 22), making it suitable for both indoor and outdoor lighting. This phosphor also exhibit outstanding thermal stability of Ce^{3+} luminescence (Fig. 19e), particularly at lower (1%) Ce concentrations.

The second WLED prototype (Fig. 23), based on a multilayered CYMSSG:Ce MP converter embedded in epoxy resin and combined with a 450 nm blue LED chip, exhibits a nearly linear redshift in colour coordinates as the thickness of the photoconversion layer increases. Table 8 presents the changes in CIE coordinates for this WLED with CYMSSG:Ce MP at each photoconversion layer, with a thickness of approximately 0.1–0.12 mm. Finally, the WLED prototype based on a six-layered CYMSSG:Ce 1% MP converter produces emission close to the standard white light, with CIE coordinates of $x=0.315$ and $y=0.31$, and a CCT of 6930 K.

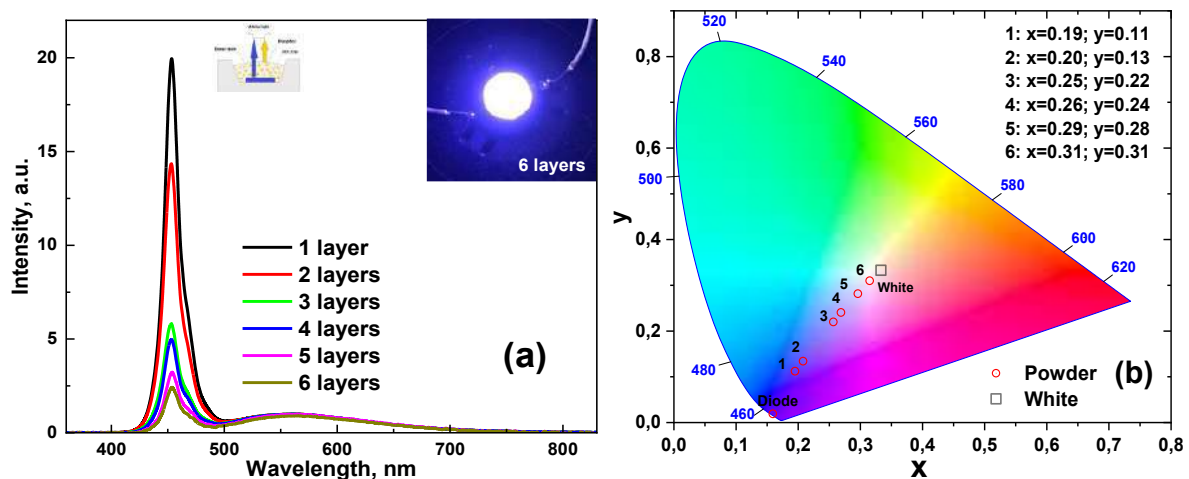


Fig. 23. Emission spectrum (a) and chromaticity diagram (b) of a WLED lamp fabricated on the base of 450 nm LED chip and CYMSSG:1% Ce phosphor.

Table 8. CIE chromaticity coordinates of a WLED lamp fabricated using a 450 nm LED chip and a multilayered CYMSSG:1%Ce phosphor embedded in epoxy resin, with each layer having a thickness of approximately 100–120 μm .

Samples	Unpolished samples	
	CIE coordinates	
	x	y
1 layer	0.195	0.112
2 layer	0.208	0.134
3 layer	0.257	0.220
4 layer	0.269	0.241
5 layer	0.296	0.282
6 layer	0.315	0.31

Furthermore, for the third WLED prototype (Fig.24), based on a five-layered CYMSSG:Ce,Mn MP converter, a warmer white emission was achieved, with colour coordinates of $x = 0.30$ and $y = 0.29$, a CCT of 7607 K, and a CRI of 87, in comparison to the WLED counterpart based on a five-layered CYMSSG:Ce MP converter, which showed chromaticity coordinates of $x = 0.29$ and $y = 0.28$, a CCT of 8699 K, and a CRI of 86.

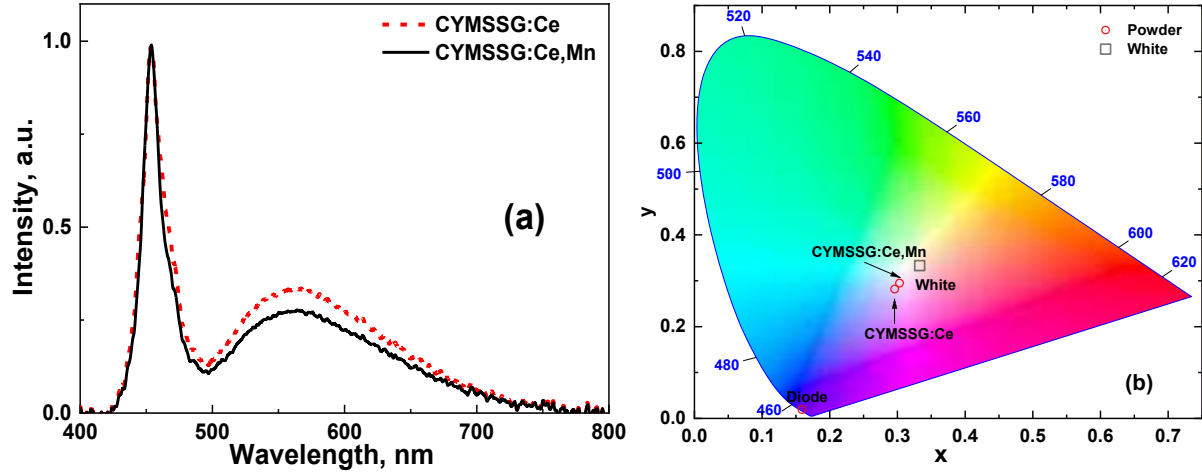


Fig. 24. Emission spectrum (a) and chromaticity diagram (b) of a WLED lamp fabricated on the base of 450 nm LED chip and CYMSSG:Ce and CYMSSG:Ce,Mn MP phosphor.

These results confirm that double doping of the CYMSSG garnet host with Ce and Mn can lead to the development of effective photoconverters for WLEDs, enabling tuneable white light emission. However, both CSSG:Ce and CYMSSG:Ce,Mn-based WLEDs exhibit limited conversion efficiency at a 1 at.% Ce^{3+} concentration, suggesting that higher Ce^{3+} concentrations may be necessary to achieve improved performance.

To conclude, the main achievements regarding the CSSG:Ce and CYMSSG:Ce MP converter include:

1. Both Ce^{3+} -doped MP phosphors exhibit broad emission spectra covering the visible range, attributed to Ce^{3+} ion transitions in CSSG and CYMSSG hosts.
2. CSSG:Ce MP phosphor shows non-monotonic shifts in emission maxima with varying excitation wavelengths, indicating multiple Ce^{3+} centers formation. At least two centers, Ce1 and Ce2, were detected CSSG:Ce phosphors, based on their PL and PLE spectra.
3. CYMSSG:Ce MP phosphor displays a more complicated redshift in Ce^{3+} emission maxima with increasing excitation wavelength, suggesting similar multicenter behavior with more reach structure. Four different Ce^{3+} centers were detected in CYMSSG:Ce phosphors.
4. The effective Ce^{3+} to Mn^{2+} energy transfer process is observed in CYMSSG:Ce,Mn MP samples resulting in the redshift of the emission spectra to 590 nm in comparison with CYMSSG:Ce counterpart.

5. The decay kinetics of the Ce^{3+} emission in CSSG:Ce, CYMSSG:Ce and CYMSSG:Ce,Mn MPs are strongly non-exponential due to the energy transfer processes from high-energy to low energy Ce^{3+} centers, as well as Ce^{3+} to Mn^{2+} energy transfer. These behaviors are linked to the unique structural environments within the garnet lattice.

6. WLEDs based on CSSG:Ce (5%) phosphor provide relatively cool and thermally stable white emission, suitable for lighting applications, with CIE coordinates of $x=0.29$; $y = 0.38$. In contrast, the WLED prototype utilizing a six-layered CYMSSG:Ce micropowder photoconverter with a total thickness of approximately 0.6–0.7 mm achieves a nearly standard white emission, with chromaticity coordinates of $x=0.315$; $y = 0.31$, a CCT of 6930 K, and a CRI of 86. Meanwhile, the WLED prototype using a five-layered CYMSSG:Ce,Mn photoconverter with a total thickness of 0.5–0.6 mm exhibits a noticeably warmer white emission, with CIE coordinates of $x=0.30$; $y = 0.29$, a CCT of 7607 K, and CRI of 87.

7. Tuning of the Ce and Mn content in the CSSG:Ce, CYMSSG:Ce and CYMSSG:Ce,Mn MP phosphors, gives the possibility to fabricate WLED with “color-on demand” photoconversion properties related to the color temperature of white light.

4.3. Ce^{3+} -Doped $\text{Ca}_3\text{Sc}_2\text{Si}_3\text{O}_{12}$ Crystal: Luminescence and Photoconversion Properties for White LED Applications

This part of the thesis presents the main results of a comprehensive investigation of optical properties of Ce^{3+} -doped CSSG garnet crystals grown using the μ -PD method (see Section 3.1.2 for details). The structural properties of these crystals were examined using high-resolution X-ray microtomography with 0.5 μm resolution (Fig.12). The composition of the crystal samples was determined by laser microscopy combined with elemental analysis (Table 3). The luminescent characteristics of the crystals were studied using CL, PL, PLE spectra, and PL decay kinetics (Figs. 25 and 26), as well as photoconversion measurements (Fig.27 and Table 9).

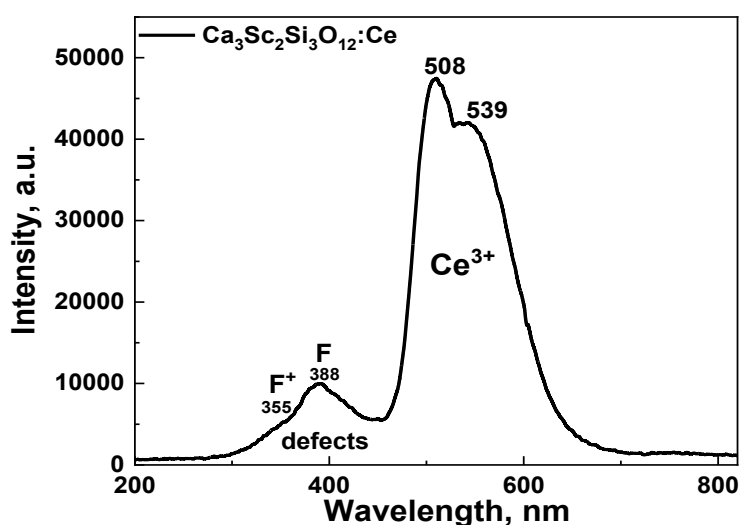


Fig. 25. RT CL spectrum of the CSSG:Ce crystal sample.

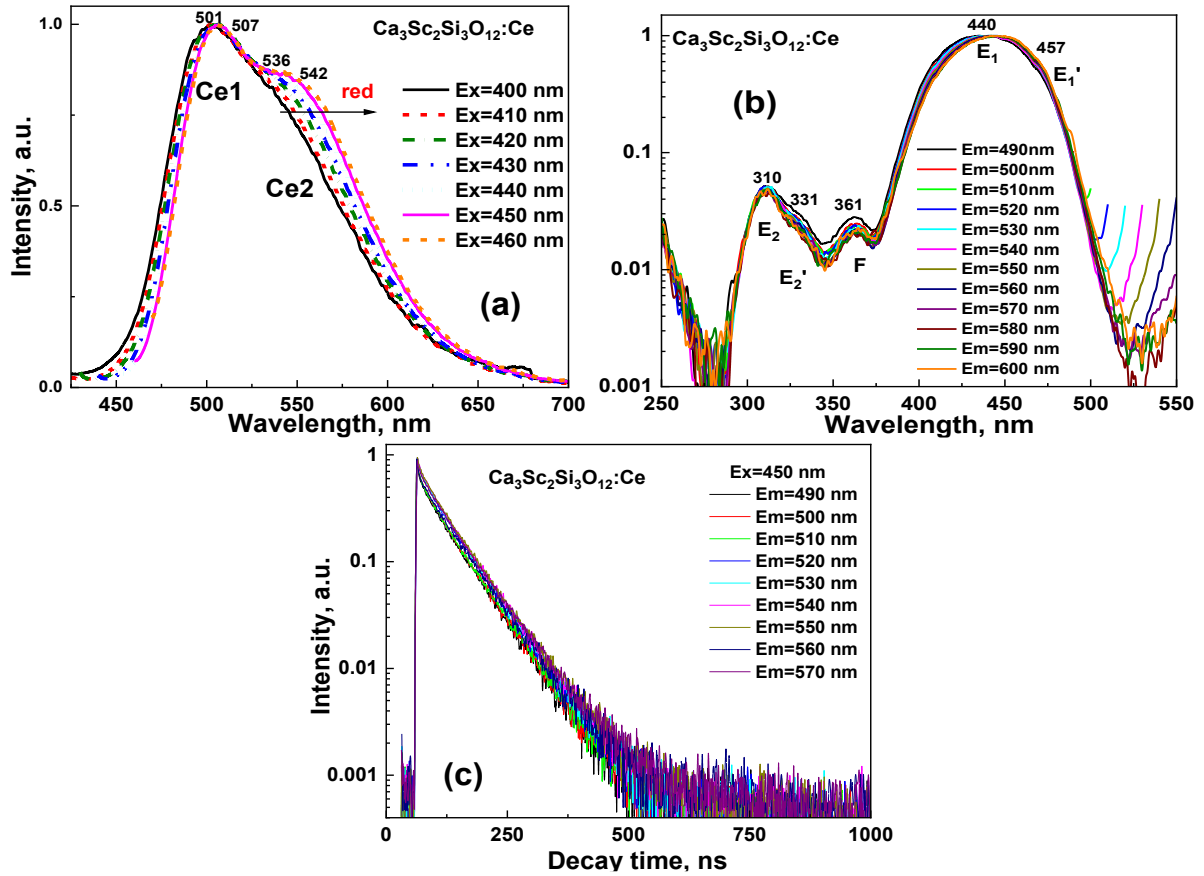


Fig. 26. Details of the luminescent properties of CSSG:Ce crystal at RT. PL (a) and PLE (b) spectra were recorded in different parts of the respective Ce^{3+} emission/excitation bands, PL decay kinetics (c) at RT were recorded in different parts of the complex Ce^{3+} emission band under blue light (450 nm) excitation.

The room-temperature CL spectrum of the CSSG:Ce crystal is shown in Fig. 25. The spectrum contains two main emission bands at 508 and 539 nm, which originate from the $5d \rightarrow 4f$ ($^2F_{5/2,7/2}$) transitions of Ce^{3+} ions occupying dodecahedral sites in the garnet lattice. Compared with the typical emission of Ce^{3+} in YAG, the Ce^{3+} band in CSSG:Ce is shifted toward the blue range. This shift results from the replacement of Y^{3+} and Al^{3+} ions by Ca^{2+} , Sc^{3+} and Si^{4+} ions in the different crystallographic sites, which modifies the local crystal field around the Ce^{3+} centers.

Besides the Ce^{3+} emission, the spectrum also shows two broad ultraviolet bands with maxima peaked at 355 and 388 nm. These features are commonly associated with defect-related centers, most likely involving oxygen vacancies created during crystal growth or arising from slight deviations in the concentrations of Ca^{2+} and Si^{4+} ions. Such defects may form F- and F'-type centers, which contribute to the observed UV luminescence.

The PL spectrum of the CSSG:Ce crystal under 400 nm excitation (Fig. 26a) exhibits typical double Ce^{3+} $5d-4f$ emission bands, peaking at 501 and 536 nm, which correspond to transitions from the $5d_1$ excited level to the $^2F_{5/2}$ and $^2F_{7/2}$ ground states. With excitation wavelengths between 400 and 450 nm, these PL bands shift toward the red. Specifically, under 460 nm excitation, the bands peak at 507 and 542 nm. The mentioned sets of PL bands are

associated with Ce1 and Ce2 centers in the CSSG host, respectively (Fig. 19d). The PLE spectra of the CSSG:Ce crystal (Fig. 26b) reveals broad excitation bands, with strong peaks at 440 nm and a weaker peak at 310 nm for the Ce1 center, peaks at 457 nm and 331 nm for the Ce2 center, along with a peak at 361 nm that may correspond to a defect center.

The PL decay kinetics of the C1 and Ce2 centers in CSSG:Ce crystal show non-exponential behavior (Fig. 26c). Using a three-exponential fit, the decay times for Ce1 center emission (at 490 nm under 450 nm excitation) are 3.7 ns, 21.7 ns, and 64.0 ns, while for Ce2 center emission (at 570 nm), the decay times are 5 ns, 44.8 ns, and 76.5 ns. The varying decay times suggest possible energy transfer between high-energy and low-energy Ce^{3+} centers. The differences in decay times may also reflect the different local environments of Ce^{3+} centers in the CSSG garnet, influenced by the localization of Sc^{3+} and Si^{4+} ions in octahedral and tetrahedral sites, respectively.

Prototypes of WLEDs were fabricated by coupling GaN-based 432 nm blue LED chips with CSSG:Ce crystal phosphor converters of varying thicknesses (0.8–1.0 mm). These WLED prototypes exhibited an emission spectrum spanning the visible range from 458 to 688 nm (Fig. 27a). As the thickness of the CSSG:Ce phosphor converter increased, a noticeable reduction in the blue LED emission intensity was observed, accompanied by a steady increase in the intensity of the green-yellow emission band. This green-yellow emission reached its maximum at a thickness of approximately 1.0 mm. Beyond this thickness, the emission is expected to approach near-perfect cool white light. Increasing the converter thickness enables an optimal balance between the blue and green-yellow components, ultimately resulting in WLEDs with high color consistency, high CRI values, and favourable CCT, making them suitable for lighting applications.

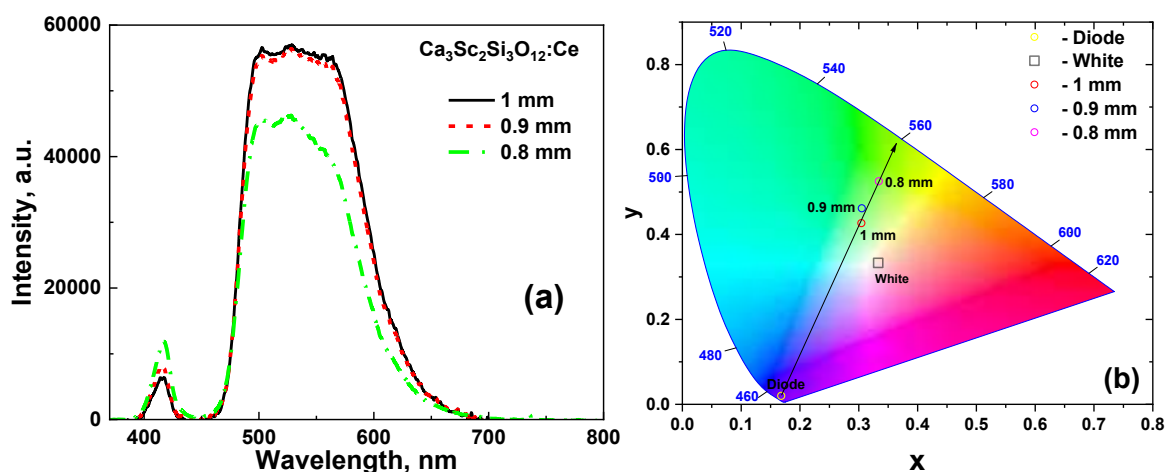


Fig. 27. The emission characteristics of WLED prototype based on the CSSG:Ce crystal converters combined with GaN 432 nm blue LED (a); the color coordinates of WLEDs based on CSSG:Ce crystals with different thickness in the 0.8–1 mm range within the CIE-1931 color space chromaticity diagram (b).

Fig. 27b presents the CIE-1931 chromaticity diagram, illustrating the shift in color coordinates (x, y) of the CSSG:Ce crystal converter as the thickness varies from 0.8 to 1.0 mm. The color coordinates exhibit a non-linear trend, with both x and y values, along with CRI and LE values, increasing as the sample thickness increases. The detailed CIE chromaticity coordinates for the WLED prototypes are provided in Table 9.

Table 9. CIE chromaticity coordinates, CTT and luminous efficiency of a WLED lamp fabricated on the base of 450 nm LED chip and CSSG:Ce crystals with different thicknesses.

Thicknesses of the sample, mm	CIE Coordinates		CCT, K	CRI	LE, lm/W
	x	y			
0.8	0.4567	0.5299	3489	39.7	68
0.9	0.4498	0.5306	3580	46.1	81
1	0.4483	0.5341	3620	42.3	107

Concluding, the main achievements regarding the study CSSG:Ce crystal converter include:

1. The set of CSSG:Ce single crystals was successfully grown for the first time using the Micro-Pulling-Down (MPD) method.
2. The CSSG:Ce crystal converter exhibits high PL efficiency and excellent color stability, making it a strong candidate for the development of energy-efficient solid-state lighting systems.
3. The PL spectra of the CSSG:Ce crystal exhibit a complex emission band, arising from the superposition of bands peaking at 501 and 536 nm, and at 507 and 542 nm, which correspond to emissions from two types of Ce^{3+} centers (Ce1 and Ce2) occupying the dodecahedral sites of the garnet host with asymmetrical local surroundings of Sc^{3+} and Si^{4+} cations and varying crystal field strengths. The PLE spectra reveal broad excitation bands with strong peaks at 440 nm and 310 nm (Ce1), and 457 nm and 331 nm (Ce2), which align with Ce^{3+} 4f–5d transitions. Additionally, a peak at 361 nm indicates the presence of defect centers.
4. The Ce^{3+} luminescence decay the CSSG:Ce crystal exhibits non-exponential behavior, with multiple decay components for both the Ce1 and Ce2 centers, suggesting possible energy-transfer processes between the high-energy and low-energy Ce^{3+} centers.
5. The CIE chromaticity coordinates, CTT and CRI of the WLED prototypes with CSSG:Ce crystal converters change with varying sample thickness, indicating the ability to tune the emission properties and improve the light quality, with potential for nearly perfect cool white light emission.

4.4 Ce^{3+} -Doped $\text{Ca}_3\text{Sc}_2\text{Si}_3\text{O}_{12}$ Single Crystalline Films: Luminescence and Color Conversion Properties for White LED Applications

This part of the thesis presents the main results of the comprehensive investigation into the structural, luminescent, and photoconversion properties of WLED converters based on Ce^{3+} -doped CSSG:Ce SCFs and related film–crystal composite structures.

The CSSG:Ce SCFs, with varying thicknesses, were grown using the LPE method onto three types of SC substrates: (i) undoped $\text{Gd}_3\text{Ga}_{2.5}\text{Al}_{2.5}\text{O}_{12}$, (set A) (ii) Ce^{3+} -doped $\text{Gd}_3\text{Ga}_{2.5}\text{Al}_{2.5}\text{O}_{12}$ (GAGG:Ce (2.5), set B), and (iii) $\text{Gd}_3\text{Ga}_3\text{Al}_2\text{O}_{12}$ (GAGG:Ce (3), set C) (Chapter 4.1.4). The composition and structural properties of these samples were investigated using several analytical techniques (see Chapter 3.2). The luminescence properties of the three sets of SCF samples (A, B, and C) were examined through absorption and CL spectroscopy. Furthermore, the phosphor-conversion properties of these film and film–crystal composite converters were examined under blue LED excitation for the first time. All spectroscopic measurements were conducted at RT.

Fig. 28 presents the absorption spectra of selected epitaxial structures containing CSSG:Ce SCFs grown onto GAGG (2.5), GAGG:Ce (2.5), and GAGG:Ce (3.0) SC substrates (sets A, B, and C, respectively). Representative samples A3, B2, and C3 with average SCF thicknesses of 10, 18, and 19 μm , respectively, were chosen for this investigation. The spectra exhibit several absorption bands within the 200–500 nm range. Broad bands at 341 nm and 440 nm are attributed to Ce^{3+} 4f–5d transitions. Peaks at 275 and 311 nm correspond to Gd^{3+} transitions in the substrates. Additional bands around 256 and 212 nm are linked to transitions of Pb^{2+} flux-related impurity.

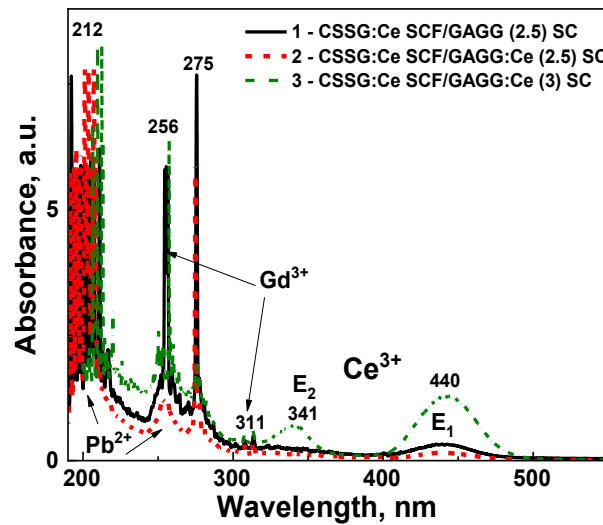


Fig. 28. RT absorption spectra (in log scale) of CSSG:Ce SCFs grown onto GAGG (2.5) (1), GAGG:Ce (2.5) (2) and GAGG:Ce (3.0) (3) SC substrates.

Fig. 29 shows the CL spectra of CSSG:Ce SCFs grown on GAGG-based substrates. All samples exhibit the typical Ce^{3+} double emission bands in the 516–520 nm and 544–550 nm ranges. A significant blue shift of more than 25 nm in the maximum Ce^{3+} emission band compared with YAG:Ce is observed, caused by cation substitution in the garnet lattice (Y^{3+} and Al^{3+} replaced by Ca^{2+} , Sc^{3+} , and Si^{4+}). Minor variations in the emission band positions among different SCF samples are attributed to differences in self-absorption, SCF thickness, and slight deviations in film composition. A sharp peak at 311 nm is associated with Gd^{3+} impurities originating from partial substrate dissolution during film growth.

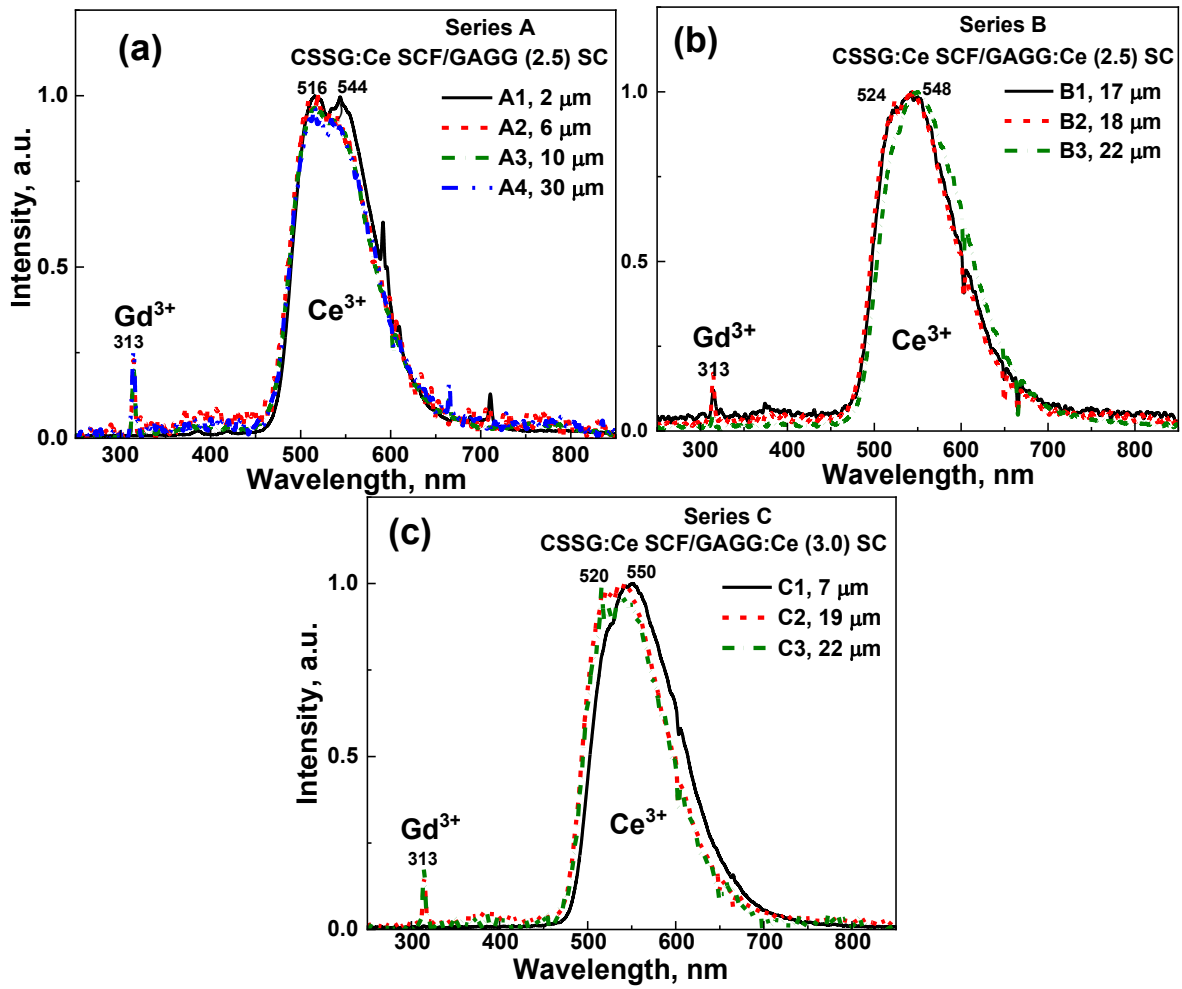


Fig. 29. RT CL spectra of CSSG:Ce SCFs grown onto GAGG (2.5) (a), GAGG:Ce (2.5) (b) and GAGG:Ce (3.0) (c) substrates.

Next goals of this part of work is to investigate the photoconversion efficiency of CSSG:Ce SCFs grown on various GAGG-based substrates for possible use in white LED applications. Fig. 30 presents the emission spectra and chromaticity diagram of blue LED chips combined with CSSG:Ce SCFs grown onto GAGG (2.5), GAGG:Ce (2.5), and GAGG:Ce (3.0) substrates.

These WLED prototypes emit across the full visible range (410–780 nm), featuring blue emission from the LED and yellow emission from Ce^{3+} ions in the garnet film. As the film thickness increases, the yellow component intensifies due to more effective blue light absorption and conversion by Ce^{3+} ions, while the blue component remains nearly unchanged. This demonstrates the potential of these structures for efficient and tunable solid-state lighting.

The photoconversion spectra in Fig. 30b show that the CSSG:Ce SCF/GAGG:Ce (2.5) SC structure, under 450 nm LED excitation, produces the strongest yellow emission, whereas the CSSG:Ce SCF/GAGG:Ce (3.0) SC structure exhibits only moderate intensity in this range. In contrast, films grown on undoped GAGG (2.5) SC substrates generate weak yellow emission due to their smaller thickness (6–30 μm).

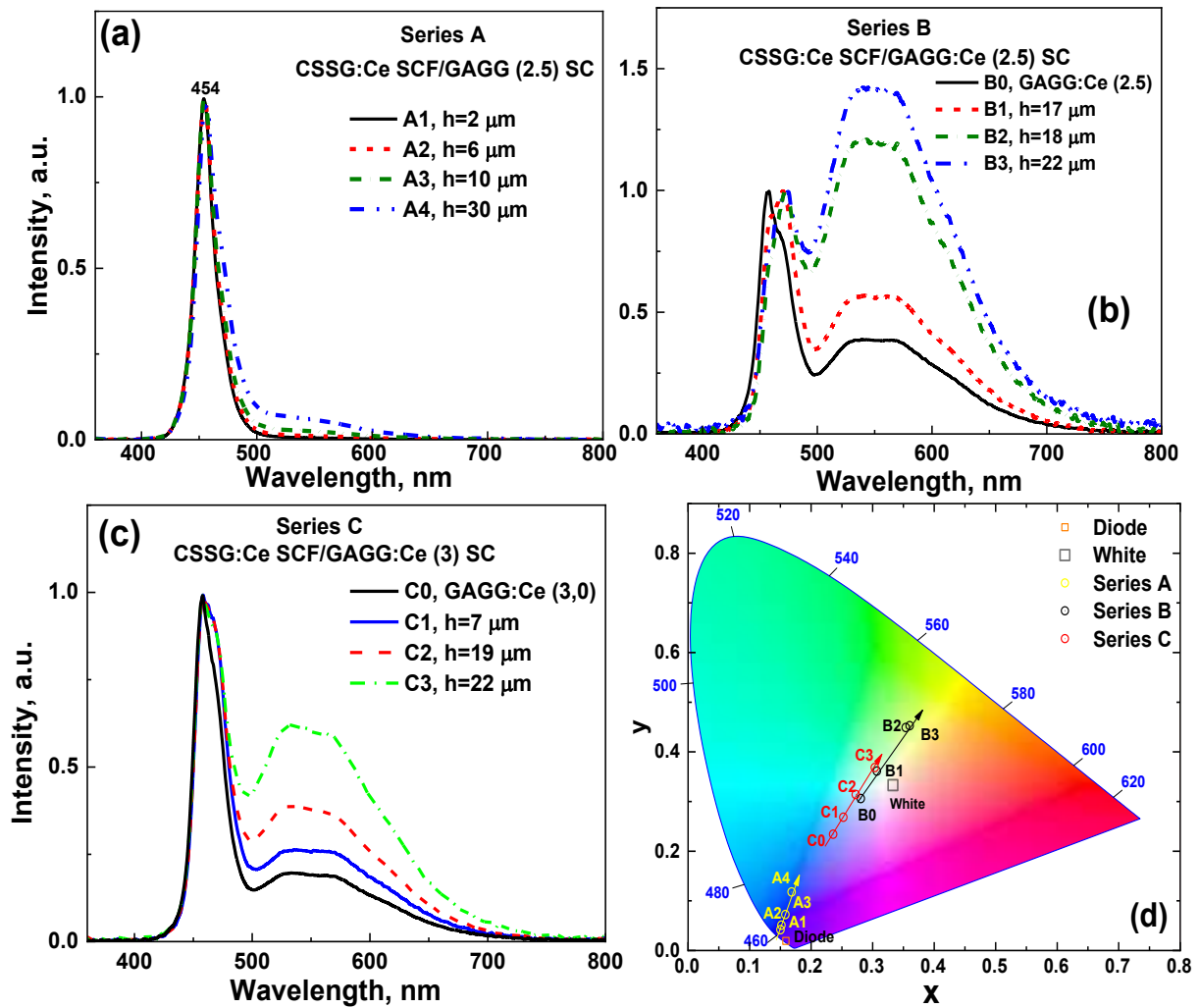


Fig. 30. Emission spectra (a, b, c) and chromaticity diagram (d) of a WLED lamp fabricated on the base of 450 nm LED chip and CSSG:Ce SCFs, grown onto GAGG (2.5) (series A), GAGG:Ce (2.5) (series B) and GAGG (3) (series C) SC substrates. The results for GAGG:Ce (2.5) (B_0) and GAGG:Ce (3) (C_0) SC substrates are presented for comparison.

A systematic variation of SCF thickness enabled the construction of trend lines in the chromaticity diagram, providing insight into color-tuning mechanisms. Specifically, in our experiment, the SCF thicknesses were 2–30 μm for CSSG:Ce SCF/GAGG (2.5), 17–22 μm for CSSG:Ce SCF/GAGG:Ce (2.5), and 7–22 μm for CSSG:Ce SCF/GAGG:Ce (3.0) composite converters. Fig. 30d illustrates the trend lines of chromaticity coordinates for all three structures.

The CSSG:Ce SCF/GAGG (2.5) SC samples shift slightly toward the light-blue region due to low yellow intensity but could reach the green region with thicker films ($>30\ \mu\text{m}$). These findings provide valuable guidance for optimizing the performance of phosphor-converted white LEDs based on epitaxial garnet converters.

Table 10 summarizes the CIE coordinates, CRI, and CCT for all fabricated WLEDs, highlighting their capability to provide high-quality illumination. These parameters serve as essential indicators for evaluating the devices' color rendition, spectral characteristics, and suitability for practical use.

Table 10. Comparison of the CRI, CCT and CIE coordinates of epitaxial structures based on the CSSG:Ce SCFs grown onto GAGG (2.5), GAGG:Ce (2.5) and GAGG:Ce (3.0) substrates.

Samples		SCF thickness, μm	CIE coordinates		CCT, K	CRI
			x	y		
`Set A						
A0	GAGG(2.5) SC	900	0.15	0.04	1620	-
A1	CSSG:Ce SCF/GAGG(2.5) SC	6	0.17	0.12	3243	20
A2	CSSG:Ce SCF/GAGG(2.5) SC	10	0.15	0.05	1625	-
A3	CSSG:Ce SCF/GAGG(2.5) SC	30	0.16	0.07	1726	-
Set B						
B0	GAGG:Ce (2.5) SC	900	0.28	0.31	9146	80
B1	CSSG:Ce SCF/GAGG:Ce(2.5) SC	17	0.31	0.36	6558	74
B2	CSSG:Ce SCF/GAGG:Ce(2.5) SC	18	0.35	0.45	4975	65
B3	CSSG:Ce SCF/GAGG:Ce(2.5) SC	22	0.36	0.45	4839	66
Set C						
C0	GAGG:Ce (3) SC	900	0.24	0.23	-	-
C1	CSSG:Ce SCF/GAGG:Ce(3):SC	7	0.25	0.27	9523	76
C2	CSSG:Ce SCF/GAGG:Ce(3):SC	19	0.27	0.31	9479	75
C3	CSSG:Ce SCF/GAGG:Ce(3):SC	22	0.30	0.37	6672	72

Concluding, the main achievements regarding the CSSG:Ce SCFs and composite CSSG:Ce SCFs/GAGG:Ce epitaxial structures include:

1. CSSG:Ce SCFs were successfully grown on undoped and Ce^{3+} -doped GAGG substrates using the LPE method, demonstrating precise control over film thickness and composition.
2. The photoconversion behavior of the CSSG:Ce SCFs under blue LED excitation was demonstrated, showing efficient conversion of blue light into a broad yellow emission suitable for solid-state lighting applications.
3. The application potential of the developed CSSG:Ce film/GAGG:Ce crystal composite phosphors was demonstrated. In such composite phosphors for WLEDs, the mixing of emissions from the SCF and substrate converters can be used to better tune the CIE coordinates and color temperature of WLEDs compared with conventional YAG:Ce crystal counterparts.
4. Samples of CSSG:Ce SCF(GAGG:Ce (2.5) SC and CSSG:Ce SCF/GAGG:Ce (3) SC composite converters with corresponding film thickness 17 and 22 μm , show the best conversion properties from all samples under study and close to ideal white light with CCT 6558 K and 6672 K, respectively.

4.5. Ce^{3+} -Doped $\text{Ca}_2\text{YMgScSi}_3\text{O}_{12}$ Single Crystalline Films: Luminescence and Color Conversion Properties for White LED Applications

This part of the thesis presents the main results of the study of the structural, luminescent, and photoconversion properties of epitaxial converters based on SCFs of Ce^{3+} -doped mixed $\text{Ca}_{2-x}\text{Y}_{1+x}\text{Mg}_{1+x}\text{Sc}_{1-x}\text{Si}_3\text{O}_{12}:\text{Ce}$ ($x=0\text{--}0.25$) (CYMSSG:Ce) garnet. These SCFs, with varying contents and thicknesses, were LPE-grown onto YAG and YAG:Ce substrates.

The content and structural properties of the SCF samples were investigated using several methods (see part 3.1.4). The luminescent properties of the CSSG:Ce SCF and related composite structures were examined by CL, PL and PLE spectra, PL decay kinetics, and photoconversion analysis. The phosphor-conversion performance of these SCF and SCF–crystal composite converters was investigated under blue LED excitation for the first time.

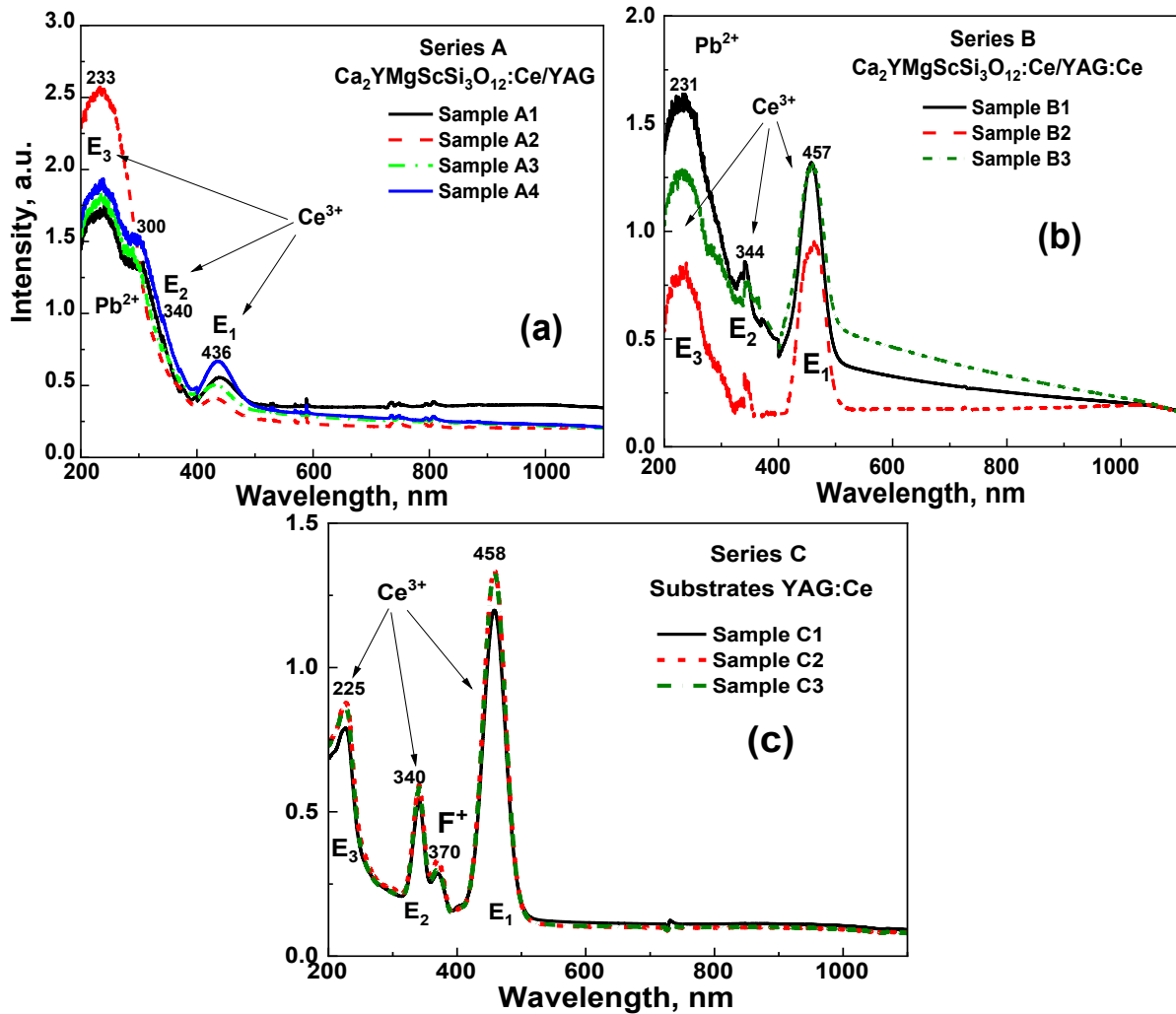


Fig. 31. RT absorption spectra of CYMSSG:Ce SCF/YAG SC (a) and CYMSSG:Ce SCF/ YAG:Ce SC (b) structures in comparison with YAG:Ce substrates (c).

The absorption spectra of the SCFs (Fig. 31a) and composite (Fig. 31b) samples show distinct features in the 200–500 nm range, in agreement with the spectral characteristics of the YAG:Ce substrates. Indeed, broad absorption bands around 341 nm (E_2) and 439–457 nm (E_1), associated

with $\text{Ce}^{3+} 4f \rightarrow 5d^{1,2}$ transitions, appear consistently across all samples. A peak at 230 nm (E_3) also confirms the presence of Ce^{3+} ions in the CYMSSG films. Additionally, an absorption band below 300 nm is observed in the SCFs, attributed to $^1\text{S}_0 \rightarrow ^3\text{P}_1$ and $^1\text{P}_1$ transitions of Pb^{2+} flux dopant introduced in the films during LPE growth. This band overlaps with the E_3 band and reflects interactions between trace Pb^{2+} and Ce^{3+} ions in the films.

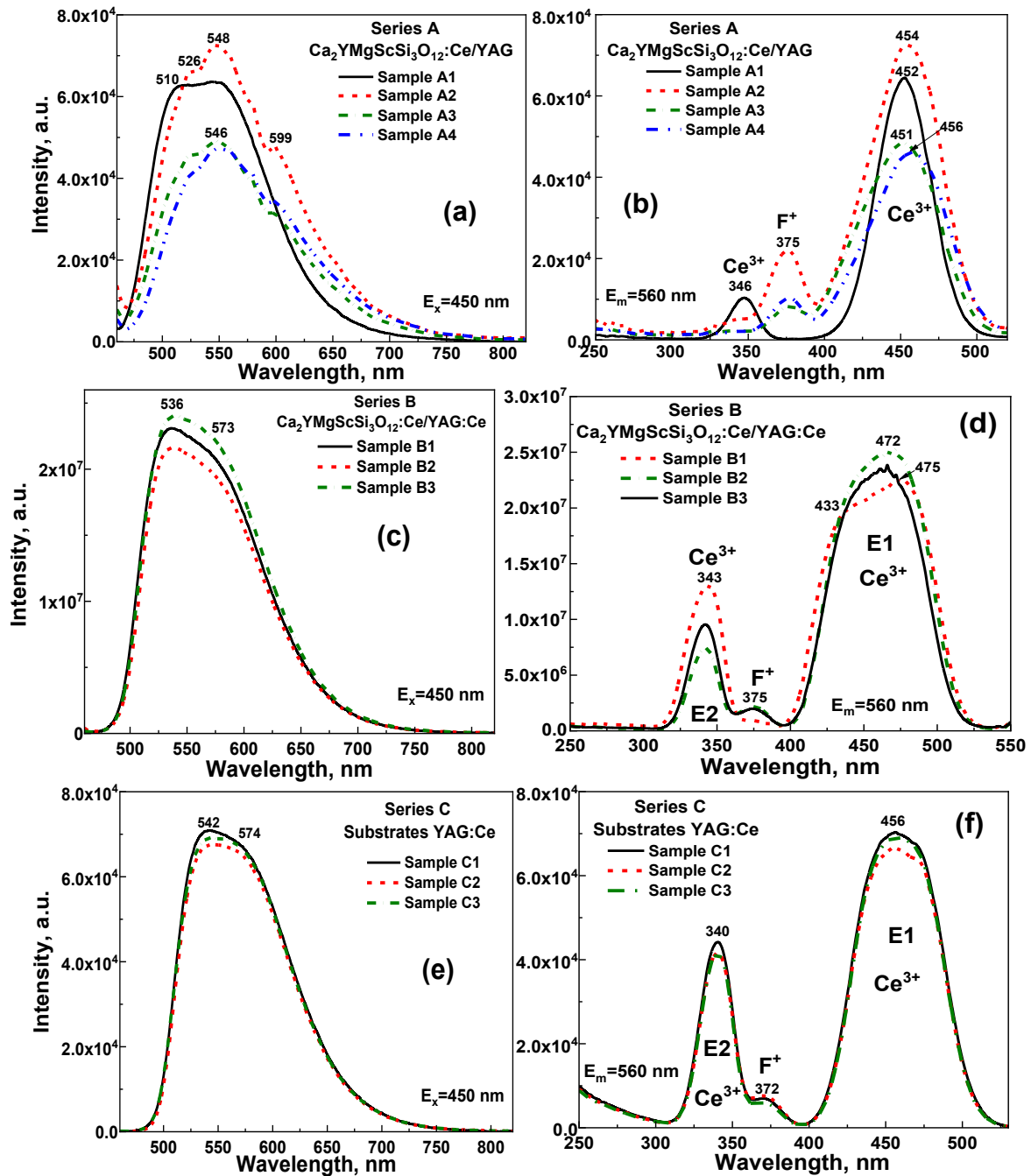


Fig. 32. RT PL (a, c, e) and PLE (b, d, f) spectra of CYMSSG:Ce SCF/YAG SC (a, b- A- series) and CYMSSG:Ce SCF/YAG:Ce SC (c, d – B series) structures in comparison with YAG:Ce SC substrates (c- series C).

Fig. 32 presents the PL and PLE spectra of Series A and B samples, along with Series C substrates. All SCF samples exhibit strong green-yellow luminescence bands resulting from the $5d_1 \rightarrow 4f$ transitions of Ce^{3+} ions. These bands include multiple sub-peaks due to Ce^{3+} occupying

non-equivalent lattice sites within the CYMSSG host. Namely, samples of A set, grown on undoped YAG substrates, show a broader emission with peaks at 510 and 548 nm. A slight blue shift in sample A1 is linked to its lower Ce^{3+} concentration, which reduces energy transfer between different Ce^{3+} centers.

In contrast, samples of B set, grown on YAG:Ce substrates, exhibit a broader, red-shifted emission with peaks at 536 and 573 nm due to spectral overlap and possible energy transfer between the substrate and film. This red shift is also influenced by stronger Ce^{3+} -ligand bond covalency in the CYMSSG host in comparison with YAG:Ce counterpart.

Fig. 32b, Fig. 32d, and Fig. 32f show the PLE spectra of Ce^{3+} ions in YAG:Ce substrates and CYMSSG:Ce SCF/YAG SC and CYMSSG:Ce SCF/YAG:Ce structures. Key excitation peaks near 340 and 456 nm correspond to $4f \rightarrow 5d$ transitions of Ce^{3+} in the dodecahedral sites of the garnet lattice, reflecting the local crystal field and energy splitting. These dual peaks enable efficient Ce^{3+} excitation in both UV and visible ranges, enhancing these phosphors application for lighting and display applications.

Series A samples show peaks at 346 and 454 nm, typical of Ce^{3+} in the CYMSSG host and suitable for UV/blue LED excitation. Series B spectra, combining signals from both film and YAG:Ce substrate, show a peak at 343 nm and a broad blue band centered at 472 nm, composed of multiple sub-peaks from different Ce^{3+} sites in CYMSSG matrix. An additional excitation peak at 375 nm is linked to F^+ centers in YAG substrates (oxygen vacancies with trapped electrons), suggesting that these defects also influence energy transfer and luminescent behaviour of CYMSSG:Ce SCFs.

Phosphor-converted (pc) WLED prototypes were fabricated to evaluate how the content and thickness of CYMSSG:Ce SCFs influence the colorimetric properties of SCF and composite converters. The SCFs were integrated with InGaN blue chips (450 nm peak, 2.6 V, 20 mA). Fig. 33 shows the emission spectra of prototypes using SCFs grown on undoped (set A) and Ce^{3+} -doped (set B) YAG substrates. For comparison, emission from the YAG:Ce substrate (Fig. 33c) is included as well. All spectra are normalized to the peak intensity of the blue (Fig. 33a) or yellow (Fig. 33b, Fig. 33c) emission. The chromaticity diagram (Fig. 33d) shows clear differences between sample series based on substrate composition. Table 11 lists the CIE coordinates, CRI, and CCT of the developed WLEDs, demonstrating their effectiveness in delivering desirable lighting qualities. These metrics are key to assessing the prototypes' color accuracy, spectral balance, and application potential.

WLED prototypes with SCF from set A (CYMSSG:Ce SCFs on undoped YAG substrates), showed chromaticity coordinates in the blue region (Fig. 33 a), indicating that emission is solely due to the SCFs, as the substrates do not contribute to photoconversion. However, only the thickest film (67 μm , sample A4) demonstrated a noticeable shift in color coordinates with increasing thickness, while thinner films showed low conversion efficiency.

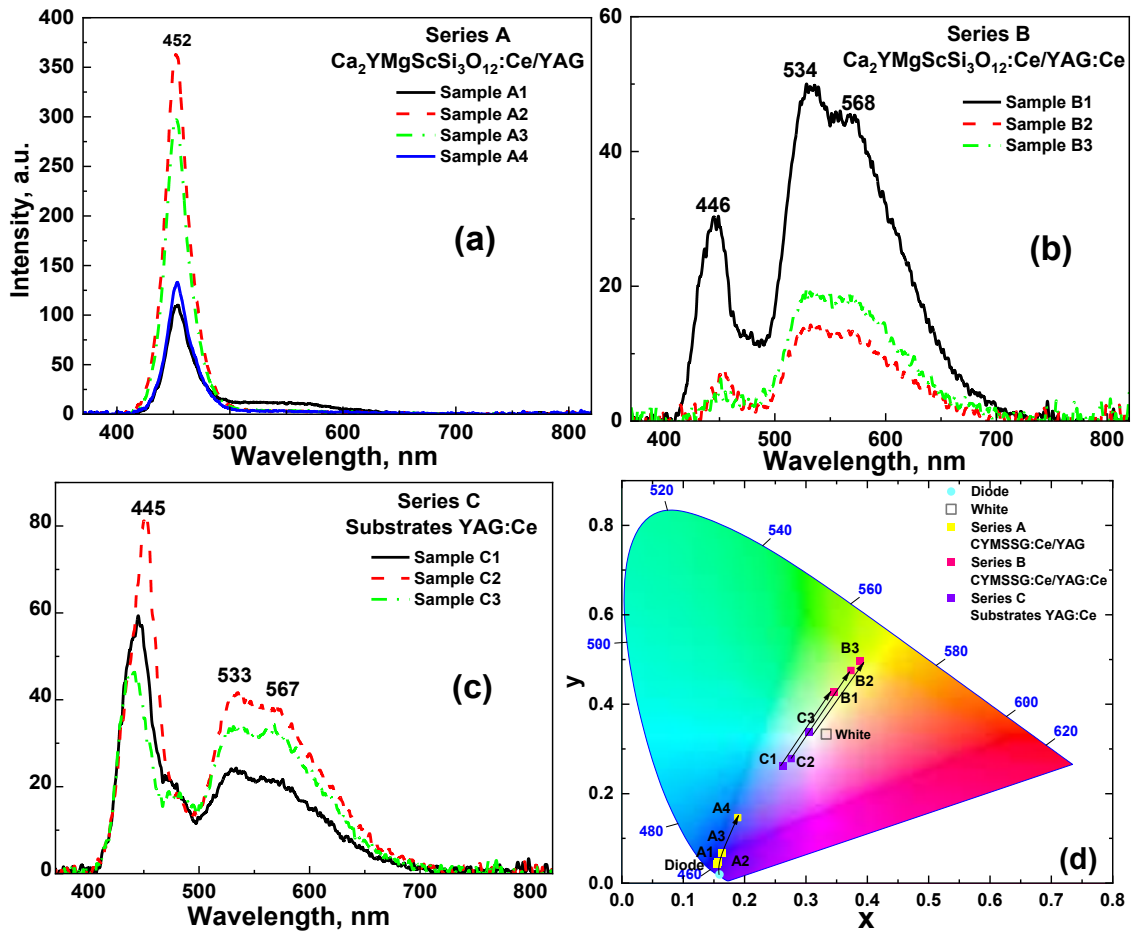


Fig. 33. Emission spectrum (a, b, c) and chromaticity diagram (d) of pc-WLED prototypes fabricated on the base of 450 nm LED chip and CYMSSG:Ce SCF converters grown onto YAG (a) and YAG:Ce (b) SC substrates in comparison with converters based on the YAG:Ce SC substrates (c). The results for YAG:Ce substrates are presented for comparison.

Table 11. Comparison of the CRI, CCT and CIE coordinates of epitaxial structures based on the CYMSSG:Ce SCF samples grown onto YAG (Series A, Series B) and YAG:Ce (Series C) substrates.

Samples	SCF thicknesses, μm	Type and thicknesses of substrate, mm	CIE coordinates		CCT, K	CRI
			x	y		
Series A						
A1	19	1	0.162	0.066	-	-
A2	34	1	0.155	0.043	-	-
A3	49	1	0.156	0.047	-	-
A4	67	1	0.189	0.146	-	-
Series B						
B1	10	C1; 0.5	0.346	0.428	5150	62
B2	11	C2; 0.5	0.374	0.475	4612	59
B3	22	C3; 0.5	0.388	0.496	4406	59
Series C						
C1	-	1	0.263	0.263	-	78
C2	-	1	0.276	0.278	-	75
C3	-	1	0.305	0.338	6838	70

In contrast, WLED prototypes (CYMSSG:Ce onto YAG:Ce substrates) exhibited emission in the green-yellow range. This red shift is primarily driven by the luminescent contribution of the Ce³⁺-doped substrate. Here, the emission is more influenced by substrate composition, though SCF thickness and cation ratios still play a role in tuning photoconversion behavior.

To conclude, the main achievements regarding the CYMSSG:Ce SCFs and composite structures of their base include:

1. CYMSSG:Ce SCFs were successfully grown on undoped and Ce³⁺-doped YAG substrates using the LPE method, with precise control of film composition and thickness.
2. The luminescent properties of the SCFs were characterized, confirming Ce³⁺ incorporation and distinct emission features due to changes in SCF content and thickness, as well as substrate type.
3. The photoconversion behavior of CYMSSG:Ce SCFs under blue LED excitation was demonstrated, showing efficient conversion of blue light to broad green-yellow emission suitable for solid-state lighting applications.
4. The chromaticity and emission characteristics were effectively tuned by adjusting SCF thickness and substrate composition, providing a method for color customization in phosphor-converted white LEDs.

5. MAIN CONCLUSIONS OF THE DOCTORAL DISSERTATION

This PhD thesis is devoted to the development, structural–optical characterization, and application of advanced Ce³⁺-doped garnet-based photoconverters in various material forms - eutectics, micropowders, bulk single crystals, single crystalline films, and composite epitaxial structures - for phosphor-converted white light-emitting diodes (WLEDs). Based on the obtained results, the following general conclusions can be drawn.

1. Demonstration of multiple material platforms for efficient photoconversion. A wide range of Ce³⁺-doped photoconverter architectures was successfully developed, including (Al₂O₃–YAG):Ce eutectics, CSSG:Ce and CYMSSG:Ce micropowders, CSSG:Ce bulk crystals, CSSG:Ce and CYMSSG:Ce single crystalline films (SCFs), and composite SCF/substrate structures. Each platform demonstrates efficient blue-to-visible light conversion, confirming the versatility of garnet-based systems for solid-state lighting applications.

2. Successful implementation of advanced growth and fabrication techniques. The HDC, MPD, solid-state synthesis, and LPE methods were effectively applied to produce high-quality photoconverter materials with controlled composition, microstructure, and thickness. In particular, the first successful growth of CSSG:Ce single crystals by the MPD method and the precise fabrication of SCFs and composite epitaxial structures by LPE growth represent important technological achievements of this work.

3. Identification and understanding of multicenter Ce^{3+} luminescence. A key scientific outcome of the thesis is the detailed investigation of multicenter Ce^{3+} luminescence in complex garnet hosts. The presence of multiple Ce^{3+} centers with different local environments was identified in CSSG:Ce and CYMSSG:Ce materials across different forms (micropowders, crystals, and SCFs). These centers lead to excitation-dependent emission shifts, non-exponential decay kinetics, and broadened emission bands, providing fundamental insight into structure–property relationships in garnet phosphors.

4. Energy transfer processes as a tool for spectral tuning. Efficient energy transfer processes, both between different Ce^{3+} centers and from Ce^{3+} to Mn^{2+} ions, were demonstrated, particularly in CYMSSG-based systems. These processes enable controlled spectral redshifts and emission broadening, offering an effective strategy for tailoring the emission colour and improving colour rendering properties of WLEDs.

5. Optimization of photoconversion performance through thickness and composition control. The emission characteristics of WLED prototypes were shown to be strongly dependent on converter thickness, dopant concentration, and composite design. Optimal thickness ranges were identified for eutectic, micropowder, crystal, and SCF-based converters, enabling efficient white light generation with tuneable chromantical coordinates, correlated colour temperature (CCT) and high colour rendering index (CRI).

6. Advantages of composite and thin-film photoconverter architectures. Composite structures based on SCFs grown on Ce^{3+} -doped garnet substrates demonstrated superior flexibility in tuning chromaticity coordinates and CCT compared to conventional bulk YAG:Ce converters. The mixing of emissions from films and substrates allows precise colour control while maintaining high conversion efficiency and reduced converter thickness.

7. Demonstration of “color-on-demand” WLEDs. By varying garnet composition, dopant content (Ce^{3+} and Mn^{2+}), converter thickness, and architectural design, WLED prototypes with a wide range of emission characteristics—from cool to warm white light—were realized. This confirms the feasibility of designing “color-on-demand” WLEDs based on garnet photoconverters developed in this thesis.

8. Overall scientific and practical impact. The results obtained significantly advance the understanding of Ce^{3+} -activated garnet photoconverters and provide practical guidelines for their implementation in next-generation solid-state lighting. The demonstrated material platforms combine high photoluminescence efficiency, thermal and colour stability, and tuneable emission properties, making them strong candidates for high-performance and customizable WLED applications.

In summary, this dissertation establishes a comprehensive framework for the design, growth, and optimization of garnet-based photoconverters, bridging the fundamental physics of luminescent phosphors with practical WLED device engineering.

REFERENCES

1. P.M. Pattison, S. Bland, N. Bardsley, L. Pattison, Solid-State Lighting Research and Development Multi-Year Program Plan, Unpublished (2014). <https://doi.org/10.13140/2.1.2485.1520>.
2. C.C. Lin, W.-T. Chen, R.S. Liu, Phosphors for White LEDs, Handbook of Advanced Lighting Technology (2017) 181–222. https://doi.org/10.1007/978-3-319-00176-0_15.
3. P. Pust, P.J. Schmidt, W. Schnick, A revolution in lighting, Nature Mater 14 (2015) 454–458. <https://doi.org/10.1038/nmat4270>.
4. E.F. Schubert, J.K. Kim, Solid-State Light Sources Getting Smart, Science 308 (2005) 1274–1278. <https://doi.org/10.1126/science.1108712>.
5. Y.H. Kim, N.S.M. Viswanath, S. Unithrattil, H.J. Kim, W.B. Im, Review—Phosphor Plates for High-Power LED Applications: Challenges and Opportunities toward Perfect Lighting, ECS J. Solid State Sci. Technol. 7 (2017) R3134–R3147. <https://doi.org/10.1149/2.0181801jss>.
6. K. Bando, K. Sakano, Y. Noguchi, Y. Shimizu, Development of High-bright and Pure-white LED Lamps., J. Light & Vis. Env. 22 (1998) 2–5. https://doi.org/10.2150/jlve.22.1_2.
7. S. Pimputkar, J.S. Speck, S.P. DenBaars, S. Nakamura, Prospects for LED lighting, Nature Photon 3 (2009) 180–182. <https://doi.org/10.1038/nphoton.2009.32>.
8. H.-M. Lee, C.-C. Cheng, C.-Y. Huang, The synthesis and optical property of solid-state-prepared YAG:Ce phosphor by a spray-drying method, Materials Research Bulletin 44 (2009) 1081–1085. <https://doi.org/10.1016/j.materresbull.2008.10.006>.
9. S. Fujita, A. Sakamoto, S. Tanabe, Luminescence Characteristics of YAG Glass–Ceramic Phosphor for White LED, IEEE J. Select. Topics Quantum Electron. 14 (2008) 1387–1391. <https://doi.org/10.1109/jstqe.2008.920285>.
10. B. Huang, Y. Ma, S. Qian, D. Zou, G. Zheng, Z. Dai, Luminescent properties of low-temperature-hydrothermally-synthesized and post-treated YAG:Ce (5%) phosphors, Optical Materials 36 (2014) 1561–1565. <https://doi.org/10.1016/j.optmat.2014.04.025>.
11. S. Fujita, S. Tanabe, Thermal Quenching of $\text{Ce}^{3+}:\text{Y}_3\text{Al}_5\text{O}_{12}$ Glass-Ceramic Phosphor, Jpn. J. Appl. Phys. 48 (2009) 120210. <https://doi.org/10.1143/jjap.48.120210>.
12. S. Zhang, W. Zhuang, T. He, Y. Liu, R. Liu, W. Gao, Y. Hu, Z. Long, Study on co-precipitation synthesized $\text{Y}_3\text{Al}_5\text{O}_{12}:\text{Ce}$ yellow phosphor for white LED, Journal of Rare Earths 28 (2010) 713–716. [https://doi.org/10.1016/s1002-0721\(09\)60186-1](https://doi.org/10.1016/s1002-0721(09)60186-1).
13. F. Wang, H. Pan, W. Mao, D. Wang, Optimizations of luminescent materials for white light emitting diodes toward healthy lighting, Heliyon 10 (2024). <https://doi.org/10.1016/j.heliyon.2024.e34795>.
14. Y. Hua, W.-X. Yang, W. Ran, Garnet-structure phosphors with ultra-high color purity red emission for potential warm WLED and flexible-transparent displays, Ceramics International 50 (2024) 50516–50525. <https://doi.org/10.1016/j.ceramint.2024.09.397>.
15. G.H. Liu, Z.Z. Zhou, Y. Shi, Q. Liu, J.Q. Wan, Y.B. Pan, Ce:YAG transparent ceramics for applications of high power LEDs: Thickness effects and high temperature performance, Materials Letters 139 (2015) 480–482. <https://doi.org/10.1016/j.matlet.2014.10.114>.
16. L. Wang, L. Mei, G. He, G. Liu, J. Li, L. Xu, Crystallization and fluorescence properties of Ce:YAG glass-ceramics with low SiO_2 content, Journal of Luminescence 136 (2013) 378–382. <https://doi.org/10.1016/j.jlumin.2012.12.019>.
17. V. Bachmann, C. Ronda, A. Meijerink, Temperature Quenching of Yellow Ce^{3+} Luminescence in YAG:Ce, Chem. Mater. 21 (2009) 2077–2084. <https://doi.org/10.1021/cm8030768>.
18. Y. Tian, Development of phosphors with high thermal stability and efficiency for phosphor-converted LEDs, J Sol State Light 1 (2014). <https://doi.org/10.1186/s40539-014-0011-8>.

19. L. Zhang, Y. Xu, X. Wu, S. Yin, H. You, Strong and pure red-emitting Eu^{3+} -doped phosphor with excellent thermal stability for warm WLEDs, *Mater. Adv.* 3 (2022) 2591–2597. <https://doi.org/10.1039/d1ma01221e>.
20. L. Zhang, Y. Huang, B. Shao, Novel high-efficiency and superior thermal stability red-emitting phosphors for WLEDs, *Dalton Trans.* 54 (2025) 7352–7359. <https://doi.org/10.1039/d5dt00079c>.
21. Q. Sai, Z. Zhao, C. Xia, X. Xu, F. Wu, J. Di, L. Wang, Ce-doped Al_2O_3 –YAG eutectic and its application for white LEDs, *Optical Materials* 35 (2013) 2155–2159. <https://doi.org/10.1016/j.optmat.2013.05.035>.
22. S. Li, Q. Zhu, D. Tang, X. Liu, G. Ouyang, L. Cao, N. Hirotsaki, T. Nishimura, Z. Huang, R.-J. Xie, Al_2O_3 –YAG:Ce composite phosphor ceramic: a thermally robust and efficient color converter for solid state laser lighting, *J. Mater. Chem. C* 4 (2016) 8648–8654. <https://doi.org/10.1039/c6tc03215j>.
23. Y. Zhong, S. Wang, Y. Liu, Q. Gao, K. Wang, X. Wang, Investigation on the leading phase of Al_2O_3 /YAG eutectic crystals prepared by directional solidification, *Int J Ceramic Engine & Sci* 2 (2020) 147–151. <https://doi.org/10.1002/ces2.10055>.
24. X. Wang, Y. Zhong, D. Wang, L. Sun, B. Jiang, J. Wang, Effect of interfacial energy on microstructure of a directionally solidified Al_2O_3 /YAG eutectic ceramic, *J Am Ceram Soc* 101 (2017) 1029–1035. <https://doi.org/10.1111/jace.15317>.
25. L.O. Hryn, Yu.V. Siryk, V.V. Baranov, O.M. Vovk, S.V. Naydenov, S.V. Nizhankovsky, The effect of cerium doping and rate of crystallization on the microstructure of the Al_2O_3 /YAG eutectic composite, *arXiv* (2024). <https://doi.org/10.48550/ARXIV.2412.05316>.
26. O. Vovk, Y. Siryk, S. Nizhankovskyi, A. Fedorov, P. Mateichenko, Morphology and microstructure of crystalline YAG- Al_2O_3 composites grown by the horizontal directional crystallization, *Journal of Alloys and Compounds* 934 (2023) 168004. <https://doi.org/10.1016/j.jallcom.2022.168004>.
27. N.M.C.H.P. Lan, C.X. Thang, D.X. Viet, N.V. Tung, N.D.T. Kien, The synthesis and properties of $\text{Ca}_3\text{Sc}_2\text{Si}_3\text{O}_{12}:\text{Ce}^{3+}$ (CSSG) phosphor are utilized for the development of human-centric lighting light-emitting diodes (HCL-LEDs), *Luminescence* 39 (2024). <https://doi.org/10.1002/bio.4698>.
28. S.K. Sharma, Y.-C. Lin, I. Carrasco, T. Tingberg, M. Bettinelli, M. Karlsson, Weak thermal quenching of the luminescence in the $\text{Ca}_3\text{Sc}_2\text{Si}_3\text{O}_{12}:\text{Ce}^{3+}$ garnet phosphor, *J. Mater. Chem. C* 6 (2018) 8923–8933. <https://doi.org/10.1039/c8tc02907e>.
29. Y. Shimomura, T. Honma, M. Shigeiwa, T. Akai, K. Okamoto, N. Kijima, Photo-luminescence and Crystal Structure of Green-Emitting $\text{Ca}_3\text{Sc}_2\text{Si}_3\text{O}_{12}:\text{Ce}^{3+}$ Phosphor for White Light Emitting Diodes, *J. Electrochem. Soc.* 154 (2007) J35. <https://doi.org/10.1149/1.2388856>.
30. T. Kato, Y. Usui, G. Okada, N. Kawaguchi, T. Yanagida, X-ray induced luminescence properties of Ce-doped $\text{Ca}_3\text{Sc}_2\text{Si}_3\text{O}_{12}$ single crystal, *Nuclear Instruments and Methods in Physics Research Section A: Accelerators, Spectrometers, Detectors and Associated Equipment* 954 (2020) 161301. <https://doi.org/10.1016/j.nima.2018.09.136>.
31. A. Katelnikovas, T. Bareika, P. Vitta, T. Jüstel, H. Winkler, A. Kareiva, A. Žukauskas, G. Tamulaitis, $\text{Y}_{3-x}\text{Mg}_2\text{AlSi}_2\text{O}_{12}$: phosphors – prospective for warm-white light emitting diodes, *Optical Materials* 32 (2010) 1261–1265. <https://doi.org/10.1016/j.optmat.2010.04.031>.
32. M. Shang, J. Fan, H. Lian, Y. Zhang, D. Geng, J. Lin, A Double Substitution of Mg^{2+} – $\text{Si}^{4+}/\text{Ge}^{4+}$ for $\text{Al}_{(1)}^{3+}$ – $\text{Al}_{(2)}^{3+}$ in Ce^{3+} -Doped Garnet Phosphor for White LEDs, *Inorg. Chem.* 53 (2014) 7748–7755. <https://doi.org/10.1021/ic501063j>.
33. A. Katelnikovas, H. Bettentrup, D. Uhlich, S. Sakirzanovas, T. Jüstel, A. Kareiva, Synthesis and optical properties of Ce^{3+} -doped $\text{Y}_3\text{Mg}_2\text{AlSi}_2\text{O}_{12}$ phosphors, *Journal of Luminescence* 129 (2009) 1356–1361. <https://doi.org/10.1016/j.jlumin.2009.07.006>.

34. A. Bindhu, J.I. Naseemabeevi, S. Ganesanpotti, Distortion and energy transfer assisted tunability in garnet phosphors, *Critical Reviews in Solid State and Materials Sciences* 47 (2021) 621–664. <https://doi.org/10.1080/10408436.2021.1935211>.
35. Z. Xia, A. Meijerink, Ce³⁺-Doped garnet phosphors: composition modification, luminescence properties and applications, *Chem. Soc. Rev.* 46 (2017) 275–299. <https://doi.org/10.1039/c6cs00551a>.
36. V. Monteseguro, P. Rodríguez-Hernández, H.M. Ortiz, V. Venkatramu, F.J. Manjón, C.K. Jayasankar, V. Lavín, A. Muñoz, Structural, elastic and vibrational properties of nanocrystalline lutetium gallium garnet under high pressure, *Phys. Chem. Chem. Phys.* 17 (2015) 9454–9464. <https://doi.org/10.1039/c4cp05903d>.
37. W. Gieszczyk, A. Mroziak, P. Bilski, V. Vistovsky, A. Voloshinovskii, K. Paprocki, T. Zorenko, Y. Zorenko, Scintillation and Energy-Storage Properties of Micro-Pulling-Down Grown Crystals of Sc³⁺- and La³⁺-Doped YAlO₃ Perovskite, *Crystals* 10 (2020) 385. <https://doi.org/10.3390/cryst10050385>.
38. W. Gieszczyk, P. Bilski, M. Kłosowski, A. Mroziak, Yu. Zorenko, T. Zorenko, K. Paprocki, Luminescent properties of undoped and Ce³⁺ doped crystals in Y₂O₃ Lu₂O₃ Al₂O₃ triple oxide system grown by micro-pulling-down method, *Optical Materials* 89 (2019) 408–413. <https://doi.org/10.1016/j.optmat.2019.01.023>.
39. Y. Liu, J. Zou, M. Shi, B. Yang, Y. Han, W. Li, Z. Wang, H. Zhou, M. Li, N. Jiang, Effect of gallium ion content on thermal stability and reliability of YAG: Ce phosphor films for white LEDs, *Ceramics International* 44 (2018) 1091–1098. <https://doi.org/10.1016/j.ceramint.2017.10.056>.
40. V. Gorbenko, T. Zorenko, P. Pawlowski, A. Iskalyeva, K. Paprocki, A. Suchocki, Ya. Zhydashchinskii, A. Fedorov, N. Khaidukov, R. Van Deun, F. Schröppel, A. Osvet, M. Batentschuk, Yu. Zorenko, Luminescent and scintillation properties of Ce³⁺ doped Ca₂RMgScSi₃O₁₂ (R = Y, Lu) single crystalline films, *Journal of Luminescence* 195 (2018) 362–370. <https://doi.org/10.1016/j.jlumin.2017.11.052>.
41. V. Gorbenko, T. Zorenko, S. Witkiewicz, K. Paprocki, A. Iskalyeva, A.M. Kaczmarek, R. Van Deun, M.N. Khaidukov, M. Batentschuk, Y. Zorenko, Luminescence of Ce³⁺ multicolors in Ca²⁺-Mg²⁺-Si⁴⁺ based garnet phosphors, *Journal of Luminescence* 199 (2018) 245–250. <https://doi.org/10.1016/j.jlumin.2018.03.058>.
42. Y. Stryk, O. Vovk, L. Gryn, A. Romanenko, V. Baranov, S. Nizhankovskyi, Eutectic Composites in Al₂O₃-Y₂O₃ System Solidified by Horizontal Directed Crystallization Method, *Acta Phys. Pol. A* 141 (2022) 268–272. <https://doi.org/10.12693/aphyspola.141.268>.
43. O. Sidletskiy, K. Lebbou, D. Kofanov, Micro-pulling-down growth of long YAG- and LuAG-based garnet fibres: advances and bottlenecks, *CrystEngComm* 23 (2021) 2633–2643. <https://doi.org/10.1039/d1ce00091h>.
44. Institute of Nuclear Physics Polish Academy of Sciences. Facility for high-temperature crystals growth by micro-pulling down (μ-PD) and Czochralski methods. Available at: <https://web.ifj.edu.pl/dept/no6/nz63/aparatura/microPD/?lang=en> (accessed September 1, 2025)
45. M. Kučera, K. Nitsch, H. Štěpánková, M. Maryško, P. Reiche, Growth and characterization of high purity epitaxial yttrium iron garnet films grown from BaO–B₂O₃–BaF₂ flux, *Phys. Stat. Sol. (a)* 198 (2003) 407–414. <https://doi.org/10.1002/pssa.200306620>.
46. V. Gorbenko, T. Zorenko, S. Witkiewicz, K. Paprocki, O. Sidletskiy, A. Fedorov, P. Bilski, A. Twardak, Y. Zorenko, LPE Growth of Single Crystalline Film Scintillators Based on Ce³⁺ Doped Tb_{3-x}Gd_xAl_{5-y}Ga_yO₁₂ Mixed Garnets, *Crystals* 7 (2017) 262. <https://doi.org/10.3390/cryst7090262>.
47. S. Witkiewicz-Lukaszek, V. Gorbenko, T. Zorenko, Y. Syrotych, J.A. Mares, M. Nikl, O. Sidletskiy, P. Bilski, A. Yoshikawa, Y. Zorenko, Composite Detectors Based on Single-

- Crystalline Films and Single Crystals of Garnet Compounds, *Materials* 15 (2022) 1249. <https://doi.org/10.3390/ma15031249>.
48. Yu. Zorenko, J.A. Mares, P. Prusa, M. Nikl, V. Gorbenko, V. Savchyn, R. Kucerkova, K. Nejezchleb, Luminescence and scintillation characteristics of YAG:Ce single crystalline films and single crystals, *Radiation Measurements* 45 (2010) 389–391. <https://doi.org/10.1016/j.radmeas.2009.09.009>.
 49. V-760 UV-Visible spectrophotometer - JASCO, JASCO Inc. (2017). <https://jascoinc.com/products/spectroscopy/uv-visible-nir-spectrophotometers/models/v-760-uv-vis-spectrophotometer> (accessed September 18, 2025).
 50. Yu. Zorenko, T. Zorenko, V. Gorbenko, V. Savchyn, T. Voznyak, K. Fabisiak, G. Zhusupkalieva, A. Fedorov, Luminescent properties of Al₂O₃:Ce single crystalline films under synchrotron radiation excitation, *Optical Materials* 59 (2016) 141–144. <https://doi.org/10.1016/j.optmat.2016.01.003>.
 51. S.V. Nizhankovskyi, A.V. Tan'ko, Yu.N. Savvin, S.I. Krivonogov, A.T. Budnikov, A.V. Voloshin, Single crystalline YAG:Ce phosphor for powerful solid-state sources of white light. The influence of production conditions on luminescence properties and lighting characteristics, *Optics @ Spectroscopy* 120 (2016) 915–921. <https://doi.org/10.1134/s0030400x16050210>.

Other Scientific Achievements of Author

Publications

1. V. Gorbenko, T. Zorenko, S. Witkiewicz-Łukaszek, **A. Shakhno**, A. Osvet, M. Batentschuk, A. Fedorov, Y. Zorenko, Crystallization and Investigation of the Structural and Optical Properties of Ce³⁺-Doped Y_{3-x}Ca_xAl_{5-y}Si_yO₁₂ Single Crystalline Film Phosphors, *Crystals* 11 (2021) 788. <https://doi.org/10.3390/cryst11070788>.
2. V. Gorbenko, T. Zorenko, **A. Shakhno**, P. Popielarski, A. Osvet, M. Batentschuk, A. Fedorov, S. Mahlik, T. Leśniewski, N. Majewska, Y. Zorenko, Single Crystalline Films of Ce³⁺-Doped Y₃Mg_xSi_yAl_{5-x-y}O₁₂ Garnets: Crystallization, Optical, and Photocurrent Properties, *Materials* 16 (2023) 1869. <https://doi.org/10.3390/ma16051869>.

Conferences

Oral Presentations Given Personally:

1. **A. Shakhno**, V. Gorbenko, T. Zorenko, S. Witkiewicz-Lukaszek, Yu. Zorenko. Composite color converters based on (Ca,Y)₃(Mg,Sc)₂Si₃O₁₂:Ce single crystalline films and Y₃Al₅O₁₂:Ce crystal substrates. *International Conference on Excited States of Transition Elements (ESTE 2023)*, Świeradów Zdrój, Poland.

Oral Presentations Given by Co-Authors:

1. V. Gorbenko, T. Zorenko, **A. Shakhno**, S. Witkiewicz-Lukaszek, N. Majewska, T. Lesniewski, S. Mahlik and Yu. Zorenko. Growth and Optical Properties of Ce³⁺ Doped Y_{3-x}Ca_xAl₂Al_{3-x}Si_xO₁₂ (x=0-0.5) and Gd_{3-x}Ca_xGa₂Al_{3-x}Si_xO₁₂ (x=0-0.3) Single Crystalline Films. *International Conference on Oxide Materials for Electronic Engineering – fabrication, properties and application (OMEE 2021)*, Lviv, Ukraine.

Poster Presentations Given Personally:

1. A. Shakhno, A. Markovskyi, T. Zorenko, Y. Vlasyuk, M. Batentschuk, Yu. Zorenko. Luminescence of Ce³⁺ multicolors in new Ca₂YMgScSi₃O₁₂ micropowder garnet phosphor. *20th International Conference on Defects in Insulating Materials (ICDIM 2020)*, An online conference hosted by the Federal University of Sergipe, Brazil.

2. A. Shakhno, S. Witkiewicz-Lukaszek, V. Gorbenko, K. Paprocki, T. Zorenko, Yu. Zorenko. Micro-powder phosphors based on the Ce^{3+} and Mn^{2+} doped $\text{Ca}_2\text{YMgScSi}_3\text{O}_{12}$ silicate garnet for WLED application. *11th International Conference on Luminescent Detectors and Transformers of Ionizing Radiation (LUMDETR 2021)*, Bydgoszcz, Poland.
3. A. Shakhno, W. Gieszczyk, P. Bilski, T. Zorenko and Yu. Zorenko. Luminescent Properties and Multi-Centres Formation in Ce-Doped $\text{Ca}_3\text{Sc}_2\text{Si}_3\text{O}_{12}$ Single Crystals. *International Conference on Oxide Materials for Electronic Engineering – fabrication, properties and application (OMEE 2021)*, Lviv, Ukraine.
4. A. Shakhno, S. Witkiewicz-Lukaszek, T. Zorenko, J. Elia, A. Osvet, M. Batentschuk, Yu. Zorenko. Luminescence of micropowder phosphors based on the Ce^{3+} and Mn^{2+} doped $\text{Ca}_3\text{Sc}_2\text{Si}_3\text{O}_{12}$ garnets. *The 7th International Workshop on Advanced Spectroscopy and Optical Materials*, Gdańsk, Poland.
5. A. Shakhno, M. Kamiński, S. Mahlik, T. Runka, V. Gorbenko, T. Zorenko, S. Witkiewicz-Lukaszek, Yu. Zorenko. High-pressure luminescence and Raman spectroscopy of the single crystalline films of $\text{Ca}_3\text{Sc}_2\text{Si}_3\text{O}_{12}:\text{Ce}$ and $\text{Ca}_2\text{YMgScSi}_3\text{O}_{12}:\text{Ce}$ garnets. *The 8th International Workshop on Advanced Spectroscopy and Optical Materials*, Gdańsk, Poland.
6. A. Shakhno, O. Vovk, S. Nizhankovskyi, M. Cieszko, Z. Szczepański, T. Zorenko, Yu. Zorenko. Influence of Ce^{3+} doping and crystallization rates on the structural, optical and photoconversion properties of the Al_2O_3 -YAG:Ce eutectic. *12th International Conference on Luminescent Detectors and Transformers of Ionizing Radiation (LUMDETR 2024)*, Riga, Latvia.
7. A. Shakhno, V. Gorbenko, S. Witkiewicz-Lukaszek, T. Zorenko, Yu. Zorenko. Multilayer garnet composites for enhanced photoconversion in high-power white LEDs. *International Conference on Excited States of Transition Elements (ESTE 2025)*, Wrocław, Poland.

Poster Presentations Given by Co-Authors:

1. A. Shakhno, T. Zorenko, A. Markovskyi, O. Vovk, S. Nizhankovskyi, Yu. Siryk, M. Cieszko, Z. Szczepański, Yu. Zorenko. Ce^{3+} doped Al_2O_3 -YAG eutectics as converters for WLED application. *11th International Conference on Luminescent Detectors and Transformers of Ionizing Radiation (LUMDETR 2021)*, Bydgoszcz, Poland.
2. V. Gorbenko, A. Shakhno, S. Witkiewicz-Lukaszek, T. Zorenko, Yu. Zorenko. Photoconversion properties of two- and three-layered epitaxial structures based on Ce^{3+} -doped garnets for advanced phosphor-converted white LEDs. *International Conference on Excited States of Transition Elements (ESTE 2025)*, Wrocław, Poland.

**Author Contributions Statement for the Publication Related to the Doctoral Dissertation
of Ms. Anna Shakhno, entitled:**

*Correlation of structural and optical properties of white light emitting diode converters based
on doped mixed garnets with micro- and nano-ceramic and epitaxial structure*

C1.1. A. Shakhno, T. Zorenko, S. Witkiewicz-Łukaszek, M. Cieszko, Z. Szczepański, O. Vovk, S. Nizhankovskyi, Y. Siryk, Y. Zorenko. Ce ³⁺ Doped Al ₂ O ₃ -YAG Eutectic as an Efficient Light Converter for White LEDs, <i>Materials</i> 16 (2023) 2701	
Authors	Contribution
Anna Shakhno	Collected and analyzed the complete research material; prepared illustrative materials (figures and tables) for publication; fabricated WLED prototypes; performed measurements of the photoconversion properties of these prototypes; and participated in the writing and editing of the manuscript. This contribution constituted approximately [30%] of the total work related to the preparation of the publication.
Tetiana Zorenko	Participated in photoluminescence (PL), photoluminescence excitation (PLE), and decay kinetics measurements of the samples.
Sandra Witkiewicz-Łukaszek	Performed cathodoluminescence (CL) measurements.
Mieczysław Cieszko	Supervised the structural measurements and analyzed the resulting data.
Zbigniew Szczepański	Performed structural measurements and analyzed the resulting data.
Yuriy Zorenko	Contributed conceptually to the design and analysis of the research; participated in manuscript writing and correction.
C2.1. I. Levchuk, A. Osvet , C.J. Brabec, M. Batentschuk, A. Shakhno, T. Zorenko, Y. Zorenko. Micro-powder Ca ₃ Sc ₂ Si ₃ O ₁₂ :Ce silicate garnets as efficient light converters for WLEDs, <i>Optical Materials</i> 107 (2020) 109978.	
Authors	Contribution
Anna Shakhno	Analyzed the complete experimental material; prepared illustrative materials (figures and tables) for publication; and contributed to the writing of the manuscript.

	This contribution constituted approximately [20%] of the total work related to the preparation of the publication.
Ievgen Levchuk	Synthesized micro-powders; collected and analyzed the complete research material; prepared illustrative materials (figures and tables) for publication; participated in optical and structural measurements; fabricated WLED prototypes; performed measurements of the photoconversion properties of these prototypes.
Andres Osvet	Performed key validation experiments; contributed to data verification and quality control.
Miroslaw Batentschuk	Contributed to conceptualization and project management; participated in drafting the original manuscript; involved in critical review and editing.
Tetiana Zorenko	Assisted in experimental investigations; performed validation tasks; created visualizations including figures and graphical abstracts.
Yuriy Zorenko	Contributed to conceptualization and methodology design; carried out validation processes; participated actively in reviewing and editing the manuscript.
C2.2. A. Shakhno , A. Markovskyi, T. Zorenko , S. Witkiewicz-Łukaszek , Y. Vlasyuk, A. Osvet , J. Elia, C.J. Brabec, M. Batentschuk , Y. Zorenko . Micropowder $\text{Ca}_2\text{YMgScSi}_3\text{O}_{12}:\text{Ce}$ Silicate Garnet as an Efficient Light Converter for White LEDs, <i>Materials</i> 15 (2022) 3942.	
Authors	Contribution
Anna Shakhno	<p>Collected and analyzed the complete research material; prepared illustrative materials (figures and tables) for publication; participated in photoluminescence measurements; fabricated WLED prototypes; performed measurements of the photoconversion properties of these prototypes; and contributed to the writing and preparation of the manuscript.</p> <p>This contribution constituted approximately [45%] of the total work related to the preparation of the publication.</p>

Tetiana Zorenko	Participated in photoluminescence (PL) and PL decay kinetics measurements of MP samples.
Sandra Witkiewicz-Łukaszek	Performed the cathodoluminescence (CL) measurements.
Yevheniya Vlasjuk	Synthesized micro-powders; collected and analyzed the complete research material; prepared illustrative materials (figures and tables) for publication; participated in structural measurements.
Andres Osvet	Synthesized MPs and participated in X-ray diffraction (XRD) investigations.
Miroslaw Batentschuk	Supervised MP preparation and XRD investigations.
Yuriy Zorenko	Analyzed all experimental materials and contributed to writing and preparing the manuscript.
C2.3. A. Shakhno, S. Witkiewicz-Łukaszek, V. Gorbenko, T. Zorenko, Y. Zorenko. Luminescence and photoconversion properties of micro-powder phosphors based on the Ce^{3+} and Mn^{2+} doped $\text{Ca}_2\text{YMgScSi}_3\text{O}_{12}$ silicate garnets, <i>Optical Materials: X</i> 16 (2022) 100187	
Authors	Contribution
Anna Shakhno	Synthesized micro-powders; collected and analyzed the complete research material; prepared illustrative materials (figures and tables) for publication; participated in optical and structural measurements; fabricated WLED prototypes; performed measurements of the photoconversion properties of these prototypes; and contributed to the writing and preparation of the manuscript. This contribution constituted approximately [75%] of the total work related to the preparation of the publication.
Sandra Witkiewicz-Łukaszek	Performed the cathodoluminescence (CL) measurements.
Vitalii Gorbenko	Participated in the synthesis of the samples.
Tetiana Zorenko	Participated in photoluminescence (PL) and PL decay kinetics measurements of the sample.
Yuriy Zorenko	Analyzed all experimental materials; participated in writing and preparing the manuscript.

C3.1. **A. Shakhno**, W. Gieszczyk, **P. Bilski**, **S. Witkiewicz-Łukaszek**, **T. Zorenko**, **M. Cieszko**, **Z. Szczepański**, A. Kotlov, **Y. Zorenko**. Luminescence and photoconversion properties of Ce-doped $\text{Ca}_3\text{Sc}_2\text{Si}_3\text{O}_{12}$ crystal, *Journal of Luminescence* 266 (2024) 120311

Authors	Contribution
Anna Shakhno	Collected and analyzed the complete research material; prepared illustrative materials (figures and tables) for publication; fabricated WLED prototypes; participated in structural, optical, and photoconversion measurements; and contributed to the writing and preparation of the manuscript. This contribution constituted approximately [45%] of the total work related to the preparation of the publication.
Paweł Bilski	Managed the crystal preparation process.
Sandra Witkiewicz-Łukaszek	Performed cathodoluminescence (CL) measurements.
Tetiana Zorenko	Participated in photoluminescence (PL), photoluminescence excitation (PLE), and decay kinetics measurements of the samples.
Mieczysław Cieszko	Conducted structural measurements and analyzed the results.
Zbigniew Szczepański	Conducted structural measurements and analyzed the results.
Yuriy Zorenko	Analyzed all experimental data; participated in writing and editing the manuscript.

C4.1. **A. Shakhno**, **S. Witkiewicz-Łukaszek**, **V. Gorbenko**, **T. Zorenko**, **Yu. Zorenko**. Composite color converters based on the $\text{Ca}_3\text{Sc}_2\text{Si}_3\text{O}_{12}:\text{Ce}$ single crystalline films, *Optical Materials: X* 22 (2024) 100328

Authors	Contribution
Anna Shakhno	Collected and analyzed the complete experimental material; fabricated WLED prototypes; prepared illustrative materials (figures and tables) for publication; and contributed to the writing and preparation of the manuscript. This contribution constituted approximately [70%] of the total work related to the preparation of the publication.
Sandra Witkiewicz-Łukaszek	Performed cathodoluminescence (CL) measurements.
Vitalii Gorbenko	Carried out the growth of the SCFs samples.

Tetiana Zorenko	Participated in photoluminescence (PL), photoluminescence excitation (PLE), and decay kinetics measurements of the samples.
Yuriy Zorenko	Analyzed all experimental data; participated in writing and editing the manuscript.
C4.2. A. Shakhno, V. Gorbenko, T. Zorenko, A. Fedorov, Y. Zorenko. Optical and Photoconversion Properties of Ce ³⁺ -Doped (Ca,Y) ₃ (Mg,Sc) ₂ Si ₃ O ₁₂ Films Grown via LPE Method onto YAG and YAG:Ce Substrates, <i>Materials</i> 18 (2025) 3590.	
Authors	Contribution
Anna Shakhno	Collected and analyzed the complete research material; prepared illustrative materials (figures and tables) for publication; fabricated WLED prototypes; participated in structural, optical, and photoconversion measurements; and contributed to the writing and preparation of the manuscript. This contribution constituted approximately [70%] of the total work related to the preparation of the publication.
Yuriy Zorenko	Analyzed all experimental data; participated in writing and editing the manuscript.
Tetiana Zorenko	Participated in photoluminescence (PL), photoluminescence excitation (PLE), and decay kinetics measurements of the samples.
Vitalii Gorbenko	Carried out the growth of the SCFs samples.

Ievgen Levchuk
17.07.2025

Bydgoszcz,

Friedrich-Alexander-Universität Erlangen-Nürnberg (FAU)
Institute of Materials for Electronics and Energy Technology (i-MEET)
Erlangen, Germany

Co-authorship Declaration

I declare that my contribution to the preparation of the publication:

C2.1. I. Levchuk, A. Osvet, C.J. Brabec, M. Batentschuk, A. Shakhno, T. Zorenko, Y. Zorenko, Micro-powder $\text{Ca}_3\text{Sc}_2\text{Si}_3\text{O}_{12}:\text{Ce}$ silicate garnets as efficient light converters for WLEDs, Optical Materials 107 (2020) 109978. <https://doi.org/10.1016/j.optmat.2020.109978>.

which are part of the doctoral dissertation of Ms. Anna Shakhno, involved participation in the synthesis of micro-powders, collection and analysis of the complete research material, preparation of illustrative materials (figures and tables) for the publication, participation in optical and structural measurements, fabrication of WLED prototypes, and performance of measurements of the photoconversion properties of these prototypes.

At the same time, I consent to the submission of the above-mentioned work by Ms. Anna Shakhno as part of her doctoral dissertation in the form of a thematically coherent cycle of works published in scientific journals.



.....
Signature

Friedrich-Alexander-Universität Erlangen-Nürnberg (FAU)
Institute of Materials for Electronics and Energy Technology (i-MEET)
Erlangen, Germany

Co-authorship Declaration

I declare that my contribution to the preparation of the publication:

C2.1. I. Levchuk, A. Osvet, C.J. Brabec, M. Batentschuk, A. Shakhno, T. Zorenko, Y. Zorenko, Micro-powder $\text{Ca}_3\text{Sc}_2\text{Si}_3\text{O}_{12}:\text{Ce}$ silicate garnets as efficient light converters for WLEDs, *Optical Materials* 107 (2020) 109978. <https://doi.org/10.1016/j.optmat.2020.109978>.

C2.2. A. Shakhno, A. Markovskiy, T. Zorenko, S. Witkiewicz-Łukaszek, Y. Vlasjuk, A. Osvet, J. Elia, C.J. Brabec, M. Batentschuk, Y. Zorenko, Micropowder $\text{Ca}_2\text{YMgScSi}_3\text{O}_{12}:\text{Ce}$ Silicate Garnet as an Efficient Light Converter for White LEDs, *Materials* 15 (2022) 3942. <https://doi.org/10.3390/ma15113942>.

which are part of the doctoral dissertation of Ms. Anna Shakhno, involved performing and analyzing X-ray diffraction (XRD) measurements, as well as validation of experimental data.

At the same time, I consent to the submission of the above-mentioned works by Ms. Anna Shakhno as part of her doctoral dissertation in the form of a thematically coherent cycle of works published in scientific journals.



Signature

Mirosław Batentschuk

Nürnberg, 24.07.2025

Friedrich-Alexander-Universität Erlangen-Nürnberg (FAU)
Institute of Materials for Electronics and Energy Technology (i-MEET)
Erlangen, Germany

Co-authorship Declaration

I declare that my contribution to the preparation of the publication:

C2.1. I. Levchuk, A. Osvet, C.J. Brabec, M. Batentschuk, A. Shakhno, T. Zorenko, Y. Zorenko, Micro-powder $\text{Ca}_3\text{Sc}_2\text{Si}_3\text{O}_{12}:\text{Ce}$ silicate garnets as efficient light converters for WLEDs, *Optical Materials* 107 (2020) 109978. <https://doi.org/10.1016/j.optmat.2020.109978>.

C2.2. A. Shakhno, A. Markovskiy, T. Zorenko, S. Witkiewicz-Lukaszek, Y. Vlasjuk, A. Osvet, J. Elia, C.J. Brabec, M. Batentschuk, Y. Zorenko, Micropowder $\text{Ca}_2\text{YMgScSi}_3\text{O}_{12}:\text{Ce}$ Silicate Garnet as an Efficient Light Converter for White LEDs, *Materials* 15 (2022) 3942. <https://doi.org/10.3390/ma15113942>.

which are part of the doctoral dissertation of Ms. Anna Shakhno, involved the conceptual development of the research project, project management, supervision of materials preparation, and participation in the editing and critical review of the manuscript.

At the same time, I consent to the submission of the above-mentioned works by Ms. Anna Shakhno as part of her doctoral dissertation in the form of a thematically coherent cycle of works published in scientific journals



.....
Signature

Co-authorship Declaration

I declare that my contribution to the preparation of the publication:

- C1.1. A. Shakhno, T. Zorenko, S. Witkiewicz-Łukaszek, M. Cieszko, Z. Szczepański, O. Vovk, S. Nizhankovskyi, Y. Siryk, Y. Zorenko, Ce^{3+} Doped Al_2O_3 -YAG Eutectic as an Efficient Light Converter for White LEDs, *Materials* 16 (2023) 2701. <https://doi.org/10.3390/ma16072701>.
- C2.1. I. Levchuk, A. Osvet, C.J. Brabec, M. Batentschuk, A. Shakhno, T. Zorenko, Y. Zorenko, Micro-powder $\text{Ca}_3\text{Sc}_2\text{Si}_3\text{O}_{12}:\text{Ce}$ silicate garnets as efficient light converters for WLEDs, *Optical Materials* 107 (2020) 109978. <https://doi.org/10.1016/j.optmat.2020.109978>.
- C2.2. A. Shakhno, A. Markovskyi, T. Zorenko, S. Witkiewicz-Łukaszek, Y. Vlasyuk, A. Osvet, J. Elia, C.J. Brabec, M. Batentschuk, Y. Zorenko, Micropowder $\text{Ca}_2\text{YMgScSi}_3\text{O}_{12}:\text{Ce}$ Silicate Garnet as an Efficient Light Converter for White LEDs, *Materials* 15 (2022) 3942. <https://doi.org/10.3390/ma15113942>.
- C2.3. A. Shakhno, S. Witkiewicz-Łukaszek, V. Gorbenko, T. Zorenko, Y. Zorenko, Luminescence and photoconversion properties of micro-powder phosphors based on the Ce^{3+} and Mn^{2+} doped $\text{Ca}_2\text{YMgScSi}_3\text{O}_{12}$ silicate garnets, *Optical Materials: X* 16 (2022) 100187. <https://doi.org/10.1016/j.omx.2022.100187>.
- C3.1. A. Shakhno, W. Gieszczyk, P. Bilski, S. Witkiewicz-Łukaszek, T. Zorenko, M. Cieszko, Z. Szczepański, A. Kotlov, Y. Zorenko, Luminescence and photoconversion properties of Ce-doped $\text{Ca}_3\text{Sc}_2\text{Si}_3\text{O}_{12}$ crystal, *Journal of Luminescence* 266 (2024) 120311. <https://doi.org/10.1016/j.jlumin.2023.120311>.
- C4.1. A. Shakhno, S. Witkiewicz-Łukaszek, V. Gorbenko, T. Zorenko, Yu. Zorenko, Composite color converters based on the $\text{Ca}_3\text{Sc}_2\text{Si}_3\text{O}_{12}:\text{Ce}$ single crystalline films, *Optical Materials: X* 22 (2024) 100328. <https://doi.org/10.1016/j.omx.2024.100328>.
- C4.2. A. Shakhno, V. Gorbenko, T. Zorenko, A. Fedorov, Y. Zorenko, Optical and Photoconversion Properties of Ce^{3+} -Doped $(\text{Ca},\text{Y})_3(\text{Mg},\text{Sc})_2\text{Si}_3\text{O}_{12}$ Films Grown via LPE Method onto YAG and YAG:Ce Substrates, *Materials* 18 (2025) 3590. <https://doi.org/10.3390/ma18153590>.

which are part of the doctoral dissertation of Ms. Anna Shakhno, consisted of my participation in photoluminescence (PL), photoluminescence excitation (PLE), and PL decay kinetics measurements of the investigated samples.

At the same time, I consent to the submission of the above-mentioned works by Ms. Anna Shakhno as part of her doctoral dissertation in the form of a thematically coherent cycle of works published in scientific journals.


Signature

Mieczysław Cieszeko

Bydgoszcz, 17.07.2025

Department of Mechatronics
Kazimierz Wielki University in Bydgoszcz
85090, Bydgoszcz, Poland

Co-authorship Declaration

I declare that my contribution to the preparation of the publication:

G.I. A. Shakhno, T. Zorenko, S. Witkiewicz-Lukaszek, M. Cieszeko, Z. Szczepański, O. Vovk, S. Nizhankovskyi, Y. Siryk, Y. Zorenko, Ce^{3+} Doped Al_2O_3 -YAG Eutectic as an Efficient Light Converter for White LEDs, *Materials* 16 (2023) 2701. <https://doi.org/10.3390/ma16072701>.

G.I. A. Shakhno, W. Gieszczyk, P. Bilski, S. Witkiewicz-Lukaszek, T. Zorenko, M. Cieszeko, Z. Szczepański, A. Kotlov, Y. Zorenko, Luminescence and photoconversion properties of Ce-doped $\text{Ca}_3\text{Sc}_2\text{Si}_3\text{O}_{12}$ crystal, *Journal of Luminescence* 266 (2024) 120311. <https://doi.org/10.1016/j.jlumin.2023.120311>.

which are part of the doctoral dissertation of Ms. Anna Shakhno, consisted in supervising of the structural measurements and analyzing the obtained results.

At the same time, I consent to the submission of the above-mentioned works by Ms. Anna Shakhno as part of her doctoral dissertation in the form of a thematically coherent cycle of works published in scientific journals.



.....
Signature

Zbigniew Szczepański

Bydgoszcz, 17.07.2025

Department of Mechatronics
Kazimierz Wielki University in Bydgoszcz
85090, Bydgoszcz, Poland

Co-authorship Declaration

I declare that my contribution to the preparation of the publication:

C1.1. A. Shakhno, T. Zorenko, S. Witkiewicz-Lukaszek, M. Cieszko, Z. Szczepański, O. Voyk, S. Nizhankovskyi, Y. Siryk, Y. Zorenko, Ce³⁺ Doped Al₂O₃-YAG Eutectic as an Efficient Light Converter for White LEDs, Materials 16 (2023) 2701. <https://doi.org/10.3390/ma16072701>.

C3.1. A. Shakhno, W. Gieszczyk, P. Biłski, S. Witkiewicz-Lukaszek, T. Zorenko, M. Cieszko, Z. Szczepański, A. Kotlov, Y. Zorenko, Luminescence and photoconversion properties of Ce-doped Ca₃Sc₂Si₃O₁₂ crystal, Journal of Luminescence 266 (2024) 120311. <https://doi.org/10.1016/j.jlumin.2023.120311>.

which are part of the doctoral dissertation of Ms. Anna Shakhno, consisted in performing structural measurements and analyzing the obtained results.

At the same time, I consent to the submission of the above-mentioned works by Ms. Anna Shakhno as part of her doctoral dissertation in the form of a thematically coherent cycle of works published in scientific journals.



Signature

Department of Physics
Kazimierz Wielki University in Bydgoszcz
85090, Bydgoszcz, Poland

Co-authorship Declaration

I declare that my contribution to the preparation of the publication:

C1.1. A. Shakhno, T. Zorenko, S. Witkiewicz-Lukaszek, M. Cieszko, Z. Szczepański, O. Vovk, S. Nizhankovskyi, Y. Siryk, Y. Zorenko, Ce³⁺ Doped Al₂O₃-YAG Eutectic as an Efficient Light Converter for White LEDs, Materials 16 (2023) 2701. <https://doi.org/10.3390/ma16072701>.

C2.2. A. Shakhno, A. Markovskyi, T. Zorenko, S. Witkiewicz-Lukaszek, Y. Vlasyuk, A. Osvet, J. Elia, C.J. Brabec, M. Batentschuk, Y. Zorenko, Micropowder Ca₂YMgScSi₃O₁₂:Ce Silicate Garnet as an Efficient Light Converter for White LEDs, Materials 15 (2022) 3942. <https://doi.org/10.3390/ma15113942>.

C2.3. A. Shakhno, S. Witkiewicz-Lukaszek, V. Gorbenko, T. Zorenko, Y. Zorenko, Luminescence and photoconversion properties of micro-powder phosphors based on the Ce³⁺ and Mn²⁺ doped Ca₂YMgScSi₃O₁₂ silicate garnets, Optical Materials: X 16 (2022) 100187. <https://doi.org/10.1016/j.omx.2022.100187>.

C3.1. A. Shakhno, W. Gieszczyk, P. Bilski, S. Witkiewicz-Lukaszek, T. Zorenko, M. Cieszko, Z. Szczepański, A. Kotlov, Y. Zorenko, Luminescence and photoconversion properties of Ce-doped Ca₃Sc₂Si₃O₁₂ crystal, Journal of Luminescence 266 (2024) 120311. <https://doi.org/10.1016/j.jlumin.2023.120311>.

C4.1. A. Shakhno, S. Witkiewicz-Lukaszek, V. Gorbenko, T. Zorenko, Yu. Zorenko, Composite color converters based on the Ca₃Sc₂Si₃O₁₂:Ce single crystalline films, Optical Materials: X 22 (2024) 100328. <https://doi.org/10.1016/j.omx.2024.100328>.

which are part of the doctoral dissertation of Ms. Anna Shakhno, consisting in performing cathodoluminescence measurements.

At the same time, I consent to the submission of the above-mentioned works by Ms. Anna Shakhno as part of her doctoral dissertation in the form of a thematically coherent cycle of works published in scientific journals.


Signature

Yuriy Zorenko
Department of Physics
Kazimierz Wielki University in Bydgoszcz
85090, Bydgoszcz, Poland

Bydgoszcz, 10.12.2025

Co-authorship Declaration

I declare that my contribution to the preparation of the publication:

- C1.1. A. Shakhno, T. Zorenko, S. Witkiewicz-Łukaszek, M. Cieszek, Z. Szczepański, O. Vovk, S. Nizhankovskyi, Y. Siryk, Y. Zorenko, Ce^{3+} Doped Al_2O_3 -YAG Eutectic as an Efficient Light Converter for White LEDs, *Materials* 16 (2023) 2701. <https://doi.org/10.3390/ma16072701>.
- C2.1. I. Levchuk, A. Osvet, C.J. Brabec, M. Batentschuk, A. Shakhno, T. Zorenko, Y. Zorenko, Micro-powder $\text{Ca}_3\text{Sc}_2\text{Si}_3\text{O}_{12}:\text{Ce}$ silicate garnets as efficient light converters for WLEDs, *Optical Materials* 107 (2020) 109978. <https://doi.org/10.1016/j.optmat.2020.109978>.
- C2.2. A. Shakhno, A. Markovskyi, T. Zorenko, S. Witkiewicz-Łukaszek, Y. Vlasyuk, A. Osvet, J. Elia, C.J. Brabec, M. Batentschuk, Y. Zorenko, Micropowder $\text{Ca}_2\text{YMgScSi}_3\text{O}_{12}:\text{Ce}$ Silicate Garnet as an Efficient Light Converter for White LEDs, *Materials* 15 (2022) 3942. <https://doi.org/10.3390/ma15113942>.
- C2.3. A. Shakhno, S. Witkiewicz-Łukaszek, V. Gorbenko, T. Zorenko, Y. Zorenko, Luminescence and photoconversion properties of micro-powder phosphors based on the Ce^{3+} and Mn^{2+} doped $\text{Ca}_2\text{YMgScSi}_3\text{O}_{12}$ silicate garnets, *Optical Materials: X* 16 (2022) 100187. <https://doi.org/10.1016/j.omx.2022.100187>.
- C3.1. A. Shakhno, W. Gieszczyk, P. Bilski, S. Witkiewicz-Łukaszek, T. Zorenko, M. Cieszek, Z. Szczepański, A. Kotlov, Y. Zorenko, Luminescence and photoconversion properties of Ce-doped $\text{Ca}_3\text{Sc}_2\text{Si}_3\text{O}_{12}$ crystal, *Journal of Luminescence* 266 (2024) 120311. <https://doi.org/10.1016/j.jlumin.2023.120311>.
- C4.1. A. Shakhno, S. Witkiewicz-Łukaszek, V. Gorbenko, T. Zorenko, Yu. Zorenko, Composite color converters based on the $\text{Ca}_3\text{Sc}_2\text{Si}_3\text{O}_{12}:\text{Ce}$ single crystalline films, *Optical Materials: X* 22 (2024) 100328. <https://doi.org/10.1016/j.omx.2024.100328>.
- C4.2. A. Shakhno, V. Gorbenko, T. Zorenko, A. Fedorov, Y. Zorenko, Optical and Photoconversion Properties of Ce^{3+} -Doped $(\text{Ca},\text{Y})_3(\text{Mg},\text{Sc})_2\text{Si}_3\text{O}_{12}$ Films Grown via LPE Method onto YAG and YAG:Ce Substrates, *Materials* 18 (2025) 3590. <https://doi.org/10.3390/ma18153590>.

which are part of the doctoral dissertation of Ms. Anna Shakhno, consisted of providing substantial intellectual input, including co-developing the research concept, offering methodological guidance, and assisting in the analysis and interpretation of the obtained results. I also participated in data verification and in the substantive and technical editing of the manuscripts prior to their submission for publication.

At the same time, I consent to the submission of the above-mentioned works by Ms. Anna Shakhno as part of her doctoral dissertation in the form of a thematically coherent cycle of works published in scientific journals.



.....
Signature

Vitalii Gorbenko

Bydgoszcz, 27.10.2025

Department of Physics
Kazimierz Wielki University in Bydgoszcz
85090, Bydgoszcz, Poland

Co-authorship Declaration

I declare that my contribution to the preparation of the publication:

C2.3. A. Shakhno, S. Witkiewicz-Lukaszek, V. Gorbenko, T. Zorenko, Y. Zorenko, Luminescence and photoconversion properties of micro-powder phosphors based on the Ce^{3+} and Mn^{2+} doped $\text{Ca}_2\text{YMgScSi}_3\text{O}_{12}$ silicate garnets, Optical Materials: X 16 (2022) 100187. <https://doi.org/10.1016/j.omx.2022.100187>.

C4.1. A. Shakhno, S. Witkiewicz-Lukaszek, V. Gorbenko, T. Zorenko, Yu. Zorenko, Composite color converters based on the $\text{Ca}_3\text{Sc}_2\text{Si}_3\text{O}_{12}:\text{Ce}$ single crystalline films, Optical Materials: X 22 (2024) 100328. <https://doi.org/10.1016/j.omx.2024.100328>.

C4.2. A. Shakhno, V. Gorbenko, T. Zorenko, A. Fedorov, Y. Zorenko, Optical and Photoconversion Properties of Ce^{3+} -Doped $(\text{Ca},\text{Y})_3(\text{Mg},\text{Sc})_2\text{Si}_3\text{O}_{12}$ Films Grown via LPE Method onto YAG and YAG:Ce Substrates, Materials 18 (2025) 3590. <https://doi.org/10.3390/ma18153590>.

which are part of the doctoral dissertation of Ms. Anna Shakhno, consisting of preparation of materials used in the research, including the growth of single crystalline film (SCF) samples by the LPE method.

At the same time, I consent to the submission of the above-mentioned works by Ms. Anna Shakhno as part of her doctoral dissertation in the form of a thematically coherent cycle of works published in scientific journals.



.....

Signature

Article

Ce³⁺ Doped Al₂O₃-YAG Eutectic as an Efficient Light Converter for White LEDs

Anna Shakhno ^{1,2,*} , Tetiana Zorenko ¹ , Sandra Witkiewicz-Łukaszek ¹ , Mieczysław Cieszek ² ,
Zbigniew Szczepański ² , Oleh Vovk ³ , Sergii Nizhankovskyi ³ , Yuriy Siryk ³  and Yuriy Zorenko ^{1,*} 

¹ Department of Physics, Kazimierz Wielki University in Bydgoszcz, 85090 Bydgoszcz, Poland

² Mechantronics Department, Kazimierz Wielki University in Bydgoszcz, 85074 Bydgoszcz, Poland

³ Institute for Single Crystals, National Academy of Sciences of Ukraine, 61178 Kharkiv, Ukraine

* Correspondence: shakhno@ukw.edu.pl (A.S.); zorenko@ukw.edu.pl (Y.Z.); Tel.: +48-693330878 (Y.Z.)

Abstract: Ce³⁺ doped Al₂O₃-YAG eutectics were successfully grown by the horizontal directional crystallization method. The crystallization rate of eutectic growth was changed in the 1–7.5 mm/h range at a growth temperature of 1835 °C. The microstructure of eutectic samples was investigated using scanning electron microscopy and X-ray microtomography. The intrinsic morphology of eutectic represents the stripe-like channel structure with a random distribution of the garnet Y₃Al₅O₁₂ (YAG) and Al₂O₃ (sapphire) phases. The content of these phases in the stripes changes in the 52.9–55.3% and 46.1–47.1% ratios, respectively, depending on the growth rate of the crystallization of the eutectic samples. The luminescent properties of the eutectic demonstrated the dominant Ce³⁺ luminescence in the garnet phase. The luminescence of the Ce³⁺ ions in Al₂O₃ has also been observed and the effective energy transfer processes between Ce³⁺ ions in the Al₂O₃ and YAG garnet phases were revealed under high-energy excitation and excitation in the UV Ce³⁺ absorption bands of sapphire. The phosphor conversion properties and the color characteristics (Al₂O₃-YAG):Ce eutectic with different thicknesses were investigated under excitation by a blue LED. We have also tested the prototypes of white LEDs, prepared using a blue 450 nm LED chip and (Al₂O₃-YAG):Ce eutectic photoconverters with 0.15 to 1 mm thicknesses. The results of the tests are promising and can be used for the creation of photoconverters for high-power white LEDs.

Keywords: Al₂O₃-Y₃Al₅O₁₂ eutectic; Ce³⁺ dopant; luminescence; phosphor converters; white LEDs



Citation: Shakhno, A.; Zorenko, T.; Witkiewicz-Łukaszek, S.; Cieszek, M.; Szczepański, Z.; Vovk, O.; Nizhankovskyi, S.; Siryk, Y.; Zorenko, Y. Ce³⁺ Doped Al₂O₃-YAG Eutectic as an Efficient Light Converter for White LEDs. *Materials* **2023**, *16*, 2701. <https://doi.org/10.3390/ma16072701>

Academic Editor: Dirk Poelman

Received: 23 February 2023

Revised: 23 March 2023

Accepted: 24 March 2023

Published: 28 March 2023



Copyright: © 2023 by the authors. Licensee MDPI, Basel, Switzerland. This article is an open access article distributed under the terms and conditions of the Creative Commons Attribution (CC BY) license (<https://creativecommons.org/licenses/by/4.0/>).

1. Introduction

One of the most promising areas of artificial lighting sources is connected to the production of white light-emitting diodes (WLEDs) due to their remarkable properties, such as a long lifespan, high efficiency, compactness, thermal stability, environmental friendliness, and low voltage operation over conventional light sources. The production of the current WLED lighting system is an established technology that typically combines a blue chip (GaN and InGaN) with a yellow-emitting Y₃Al₅O₁₂:Ce (YAG:Ce) powder phosphor converter (pc) dispersed in silica gel or epoxide resin binder, which are used for fixation powder phosphors onto blue LED chips [1–5]. However, the mentioned organic binders with limited thermal conductivity and poor thermal stability are not suitable for high-power WLEDs. This brings up some problems in the actual use of WLED, such as deterioration of the light efficiency, chromaticity shift, and, eventually, the loss of long-term reliability.

Novel durable phosphors without resin binders have been studied by researchers to address the issue [6–8]. Completely inorganic phosphors, such as transparent ceramic phosphor and glass ceramic phosphor [9,10], are on track to displace the “phosphor powder” and “organic matrix” combination as workable solutions to the degradation of the organic resin matrix. Researchers have explored innovative durable phosphors without resins [6,11] and found the need to increase the phosphor scattering [12] to solve these problems. In this

frame, the composites of the (Al₂O₃-YAG):Ce eutectic attract large interest as an excellent matrix of the phosphor converters due to their higher thermal conductivity in comparison with the YAG:Ce converter [13].

In addition to the above, one of the primary criteria that characterizes low light converter efficiency is the impact of total inner reflection, which transforms a light converter with a regular shape into a waveguide that traps a significant amount of light rays inside itself. This effect can be reduced using a variety of techniques, including adding scattering metal-oxide particles of micron sizes to the converter material [14,15], profiling the light converter's emitting surface [16,17], and using a eutectic compound made up of multiple phase components [10,18–21]. It has been shown in these works that their lighting properties (Al₂O₃-YAG):Ce eutectic were significantly improved compared to traditional materials. In addition, due to the thermal stability of the Ce³⁺ emission, heavy Ce³⁺ doped YAG-Al₂O₃ eutectic has been considered as one of the prospective inorganic materials for pc for high-power warm WLEDs [10,14].

In this work, we have investigated the properties of highly doped Ce³⁺ doped Al₂O₃-YAG eutectic samples, which were crystallized by the horizontal directional crystallization (HDC) method [22] with different crystallization rates. Namely, the current work presents the new systematic results of studying the morphology, structural, and luminescent properties of these materials. Furthermore, the color characteristics and phosphor conversion capabilities of WLED prototypes with pc based on the (Al₂O₃-YAG):Ce eutectic samples with various thicknesses (from 0.15 to 1 mm) were investigated.

2. Sample Preparation and Experimental Techniques

Crystallization of Ce-doped Al₂O₃-YAG eutectic samples was carried out using the HDC method on the “Horizont-3M” set up in a Mo crucible under an Ar, CO, and H₂ environmental atmosphere at a total pressure of 1.3×10^5 Pa at evaluated temperature and rate of solidification.

For the preparation of the initial eutectic charge, an equimolar mixture of Y₂O₃ + CeO₂ (5N purity) and Al₂O₃ (4N purity) oxides was used. These powders were thoroughly mixed in a drum for several hours and the resulting mixture was tableted. The tablets were annealed at 1200 °C for several hours and the annealed tablets served as a “green body” for crystallization. Crystallization was performed by the HDC method on standard installations for Mo crucibles with a size of 240 × 75 × 35 mm³, according to the modes for the YAG crystals' growing method [22]. During crystallization, different parts of the crystal were grown with different crystallization rates (Figure 1 and Table 1).

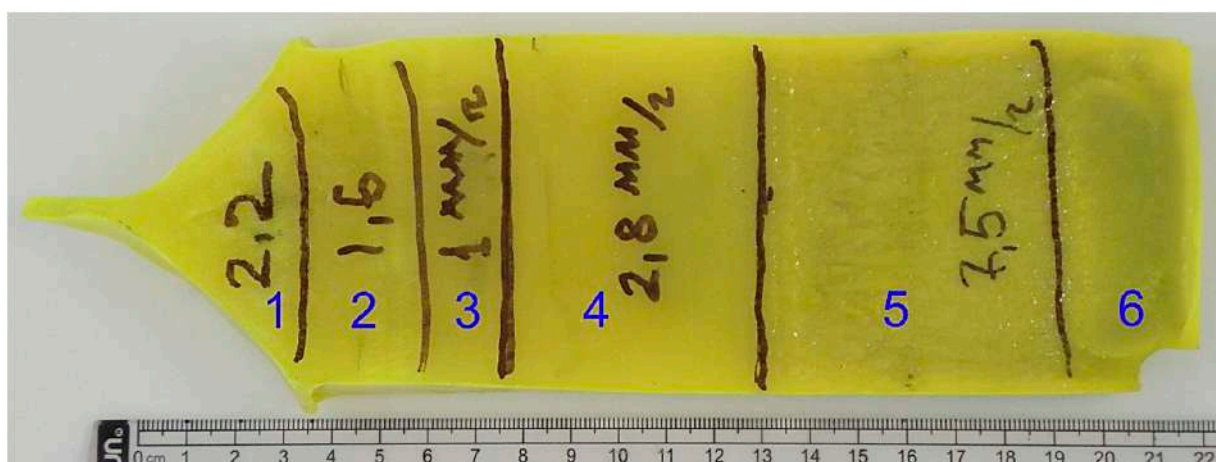


Figure 1. The (Al₂O₃-YAG):Ce eutectic ingot, different parts of the ingot grown at different crystallization rates (Table 1).

Table 1. Modes of crystallization of eutectic samples.

Sample	Rate of Crystallization, mm/h	Melt Temperature, °C	Gradient, K/cm	Al ₂ O ₃ , Surf. %	YAG, Surf. %
2	1.6	1835	30	47.1 ± 2.4	52.9 ± 2.4
3	1	1835	30	46.1 ± 1.3	54.0 ± 1.3
4	2.8	1835	30	44.7 ± 1.3	55.3 ± 0.7
5	7.5	1835	30	45.2 ± 0.7	54.8 ± 0.7

The nominal CeO₂ content in the melt was 1 molar %. Moreover, due to the low segregation coefficient of Ce³⁺ ions, the actual Ce content in the Al₂O₃ and YAG phases can be notably less. For instance, the cerium segregation coefficient at the growth of YAG:Ce crystals is 0.2–0.25 [23]. However, we cannot measure the actual Ce³⁺ content in the garnet and sapphire phases separately. Carbon dopant may also be present in small amounts in the eutectic samples due to the carbon lining of the growth chamber being used.

The crystallized (Al₂O₃-YAG):Ce eutectic ingot and parts of the different crystallization rates are demonstrated in Figure 1. The surface of the eutectic crystal is marked in Sections 1–6 which was crystallized at different growth rates (Table 1). Samples from Sections 2–5 were investigated in this work. Samples were sliced forward perpendicular in the direction of crystal growth. There were no inclusions or cracks visibly seen in the eutectic slices, which had the bright yellow hue typical of Ce-doped YAG crystals.

The cooled crystal was cut into pieces that were grown at the same rate. Samples for research were then cut out of each part. Cutting was performed with diamond circular saws using water for cooling. The surfaces of the samples were polished with a diamond abrasive, and the samples were glued to the polishing table with paraffin wax. This wax was then wiped with a solvent.

The structural properties of these samples were characterized by electronic scanning microscopy (SEM, JSM-6390LV, JEOL Ltd., Tokyo, Japan), X-ray diffractions (modified DRON 4 spectrometer), and X-ray microtomography with a 0.5 µm resolution (SkyScan 1272 spectrometer). Namely, Table 1 shows the data obtained on the basis of analyses of the SEM surface images. In this instance, image analysis with the use of special software, installed in our SEM, allowed us to examine SEM images and determine the area fractions of various phases, which were distinguished by their contrast or color. The software can be calibrated to the specific magnification and pixel resolution of the images to ensure respective accuracy.

For characterization of the properties of the Ce³⁺ doped Al₂O₃-YAG eutectic samples under study, scanning electron microscopy (SEM), X-ray diffractions (XRD), X-ray microtomography (µCT), cathodoluminescence (CL), photoluminescence (PL), PL excitation spectra (PLE), PL decay kinetics, and photoconversion spectra (PC) were used. Furthermore, the photoconversion properties of the (Al₂O₃-YAG):Ce eutectic samples (color chromaticity coordinates (CIE), color correlated temperature (CTT), and color rendering index (CRI)) and luminous efficacy (LE) under blue LED excitation were investigated as well.

CL spectra were obtained by using an electron gun of a SEM JEOL JSM-820 microscope (JEOL Ltd., Tokyo, Japan), additionally equipped with a Stellar Net spectrometer with a cooled TE-detector CCD operating in the 200–1200 nm range. PL emission and excitation spectra, as well as PL decay kinetics, were measured using an FS-5 spectrometer (Edinburg Instruments Ltd., Livingston, UK). The photoconversion spectra (PC) measurements were performed using a fiber-optic spectrophotometer, AvaSpec-ULS 2048-LTEC, and an integrating sphere, AvaSphere-50-IRRAD. The photoconverters prepared from (Al₂O₃-YAG):Ce eutectics were excited by the blue LED (30 mA, 2.9V) with a wavelength of 454 nm. All measurements were performed at room temperature (RT).

3. Structural Properties of Eutectics

SEM images of the morphology of (Al₂O₃-YAG):Ce eutectic samples of the different parts are demonstrated in Figure 2. The Al₂O₃ phase is visible as the dark stripes, and the

YAG phase is visible as the light stripes of the images in Figure 2 (see also [24,25]). The obtained eutectic was grown under conditions close to equilibrium solidification. Still, its morphology looks like the “chines script”. As for similar eutectics produced at higher crystallization rates, which also applies to the $(\text{Al}_2\text{O}_3\text{-YAG})\text{:Ce}$ eutectic system, they are far from stable [26]. Due to their closer physical properties (the refractive index and density of the sapphire Al_2O_3 ($n = 1.77$ and $\rho = 3.99 \text{ g/cm}^3$, respectively), they are a little smaller than the ones of YAG ($n = 1.83$ and $\rho = 4.56 \text{ g/cm}^3$) and the two phases may have less backscatter and total reflection loss at the edges. This leads to what is possible to create homogeneous light propagation without significant scattering losses at small refraction. Even for a thin sample, extending the optical path length results in more efficient Ce^{3+} excitation. As a result, the eutectic structures can produce light more effectively than conventional particle-dispersed LEDs [27].

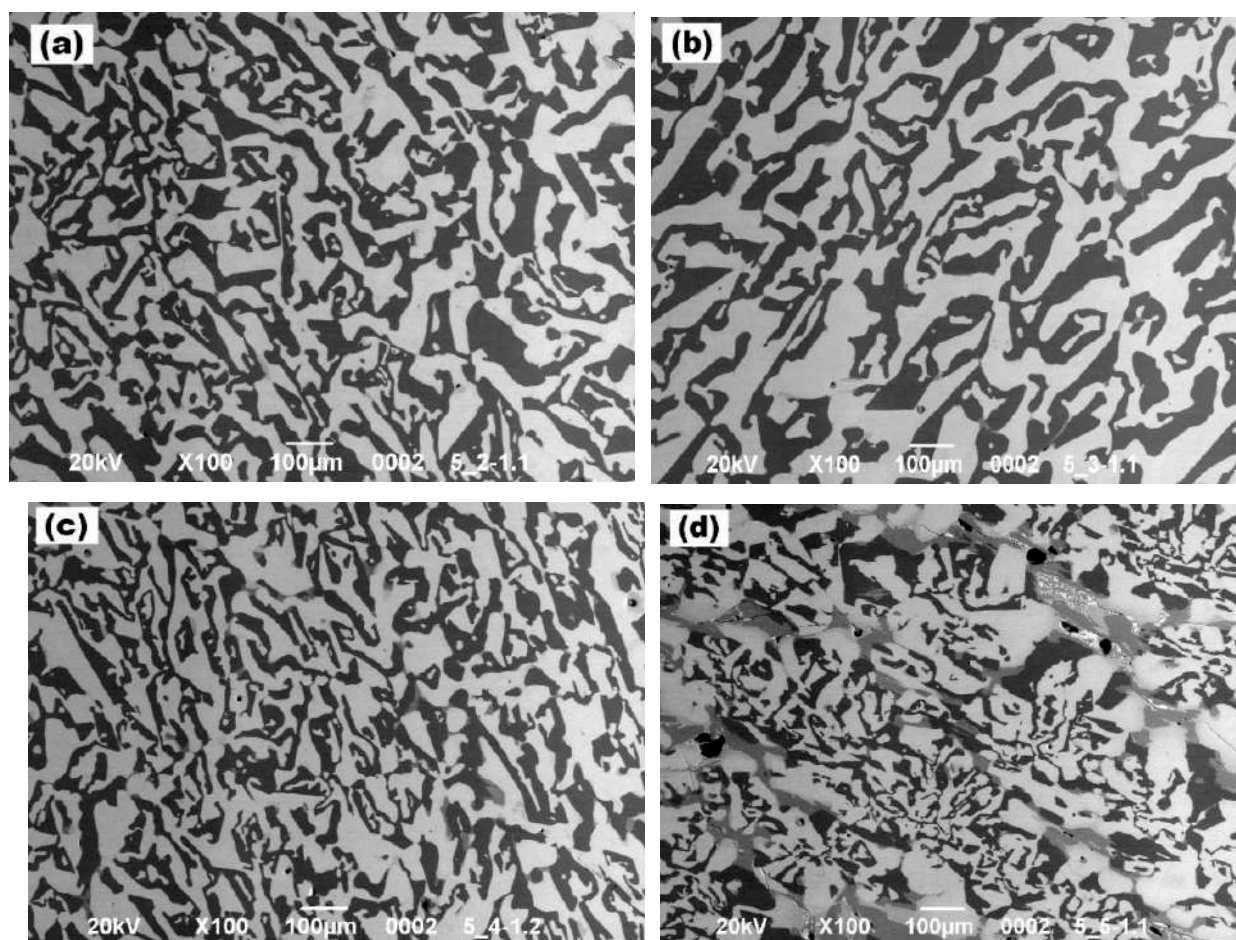


Figure 2. SEM images of the $(\text{Al}_2\text{O}_3\text{-YAG})\text{:Ce}$ eutectic: (a) sample 2, (b) sample 3, (c) sample 4, and (d) sample 5.

For samples 2–5, the phase composition of eutectic crystals was identified. Figure 3 displays the XRD patterns of these two eutectic samples in comparison with the standard ICSD diffraction patterns for YAG (#23,848) and $\alpha\text{-Al}_2\text{O}_3$ (corundum) (#63,647). The samples consist of pure YAG and corundum phase. The rate of melt solidification and the distance from the ingot seeding point determine the form and concentration of phases. The XRD patterns did not show (with an accuracy of the method of 0.1%) evidence of any other crystalline phases, particularly the yttrium aluminum perovskite YAlO_3 (YAP) phase. Thus, the YAP phase does not dominantly appear under the solidification conditions utilized in this work. However, a small amount of YAP:Ce phase (below 0.1%) was detected in all the eutectic samples under study using the more sensitive PL investigation.

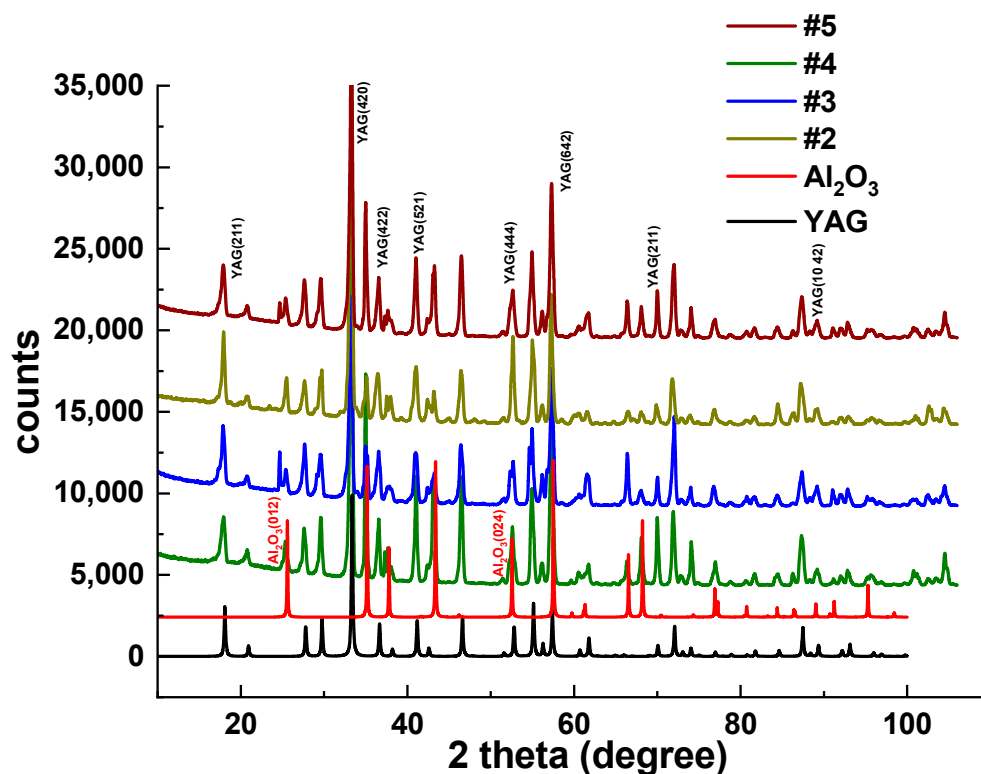


Figure 3. XRD patterns of 2–5 eutectic samples in comparison with Al_2O_3 (ICSD #63,647) and YAG (ICSD #23,848) phases.

The X-ray microtomography (SkyScan 1272 spectrometer) investigations (Figure 4) of the samples under study show that the $(\text{Al}_2\text{O}_3\text{--YAG})\text{:Ce}$ eutectic structure containing a random spatial distribution of the stripes of main garnet (white) and sapphire (gray) phases. The reconstructed 3D image of the eutectic structure is demonstrated in [28]. Table 2 shows the data obtained on the basis of the internal analysis of the images obtained by the microtomography (Figure 4). A detailed description of this method is described in the reference [29]. Namely, the analysis of the sample histogram, based on the mixture model, ref. [29] showed the volume fractions of both phases in the eutectic samples under study (Table 2).

Figure 5 shows the determined graphs of gray level distributions of both phases in the image of sample two, proportional to its content (Table 2). However, it should be emphasized here that the difference in the position of both observed peaks is also related to the difference in the X-ray absorption ability of the YAG and sapphire phases $\mu \sim \rho \cdot Z_{\text{eff}}^4$, where ρ is the density and Z_{eff} is the effective atomic number, being equal to 35 for YAG and 11.2 for a sapphire.

Table 2. The sapphire and garnet phase proportions of the eutectic samples.

Sample	Al_2O_3 Phase Content, %	YAG Phase Content, %
2	54.39	46.61
3	50.02	49.98
4	45.58	54.42
5	46.60	53.4

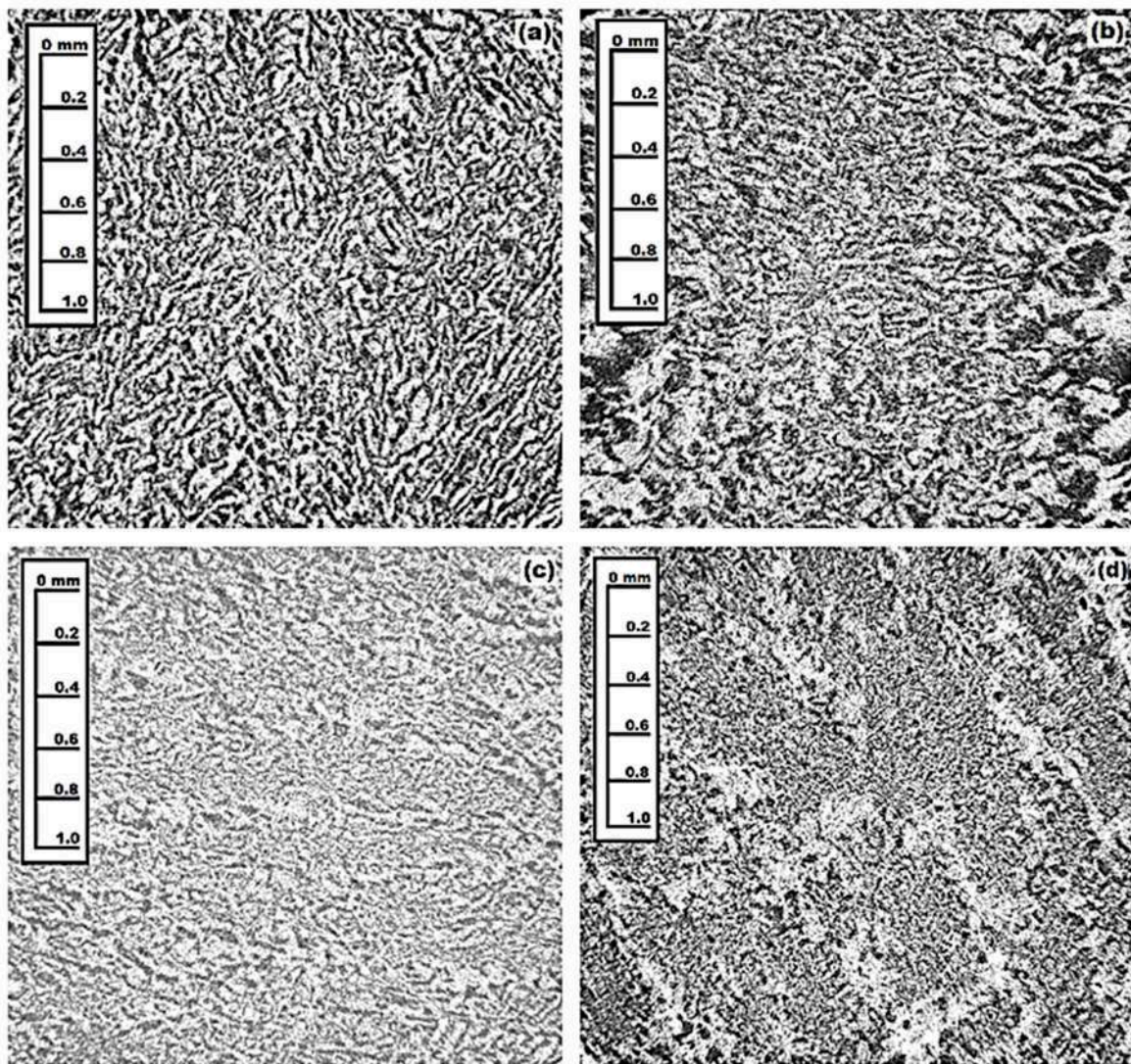


Figure 4. X-ray microtomography of the $(\text{Al}_2\text{O}_3\text{-YAG})\text{:Ce}$ eutectic: garnet (white) and sapphire (gray) phases distribution for samples 2 (a), 3 (b), 4 (c), and 5 (d).

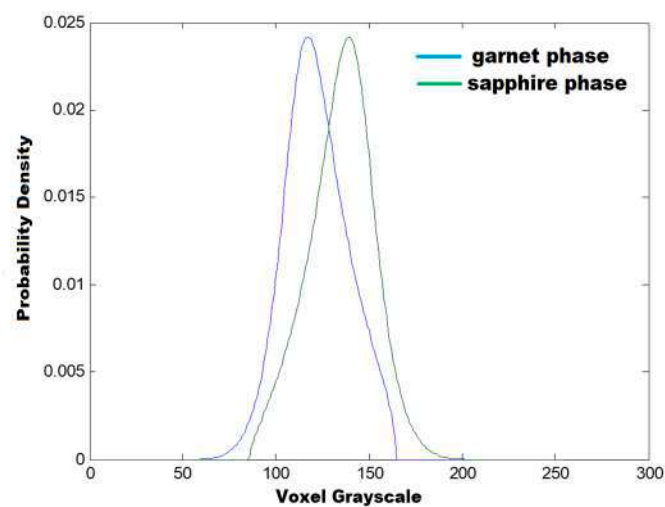


Figure 5. Graphs of the calculated density function in two subsets of voxels, corresponding to YAG (white) and sapphire (gray) phases in the microtomography image presented in Figure 4a for sample 2.

4. Luminescent Properties

4.1. Cathodoluminescence Spectra

The CL spectra of the samples under study (Figure 6) show only the intensive Ce^{3+} emission band peaked at the 547–553 nm range, caused by the presence of the YAG:Ce garnet phase. This result indicates also the existence of an effective energy transfer from the Al_2O_3 :Ce sapphire phase to the YAG:Ce garnet phase in these eutectics under high-energy excitation. Interestingly, the maximum of the Ce^{3+} emission band in CL spectra is notably shifted in the red range with an increase in the crystallization rate and distance from the seed of eutectic (Table 1). This effect can be connected with a deviation of the Ce content in the respective eutectic samples and changing the crystal field strength in the dodecahedral positions of the garnet host [30] due to the incorporation of relatively large Ce^{3+} ions (ionic radius of 1.143 Å in CN = 8) instead of Y^{3+} cations (1.019 Å; CN = 8). Finally, that resulted in the observed long-wavelength shift of the Ce^{3+} emission spectra.

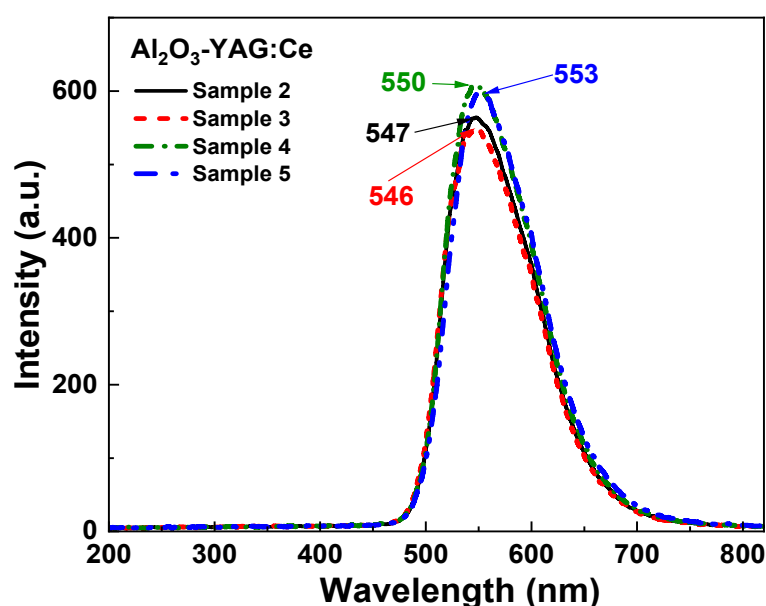


Figure 6. CL spectra of the $(\text{Al}_2\text{O}_3\text{-YAG})\text{:Ce}$ eutectic samples under study.

4.2. PL and PLE Spectra

Figure 7 shows the PL and PLE spectra of the selected sample four of Ce^{3+} doped Al_2O_3 -YAG eutectic. The radiation transitions of the Ce^{3+} ions in this sample were stimulated at 265, 340, and 450 nm light (Figure 7a). Such excitation results in a yellow-green PL emission band peaking at about the 547–556 nm range, corresponding to the 4f-5d transitions of Ce^{3+} ions in the YAG:Ce garnet phase. Namely, the spin-orbit splitting of the ground state allows for the decomposition of the PL emission band under 450 nm excitation into two components with centers at about 539 nm ($5d^1 \rightarrow {}^2F_{5/2}$) and 584 nm ($5d^1 \rightarrow {}^2F_{7/2}$) [31,32]. It can be assumed that the observed shift of the Ce^{3+} emission band is connected with the different probabilities of $5d^1 \rightarrow {}^2F_{5/2,7/2}$ transitions under different excitation wavelengths and peculiarities of the energy transfer between the sapphire and garnet phases.

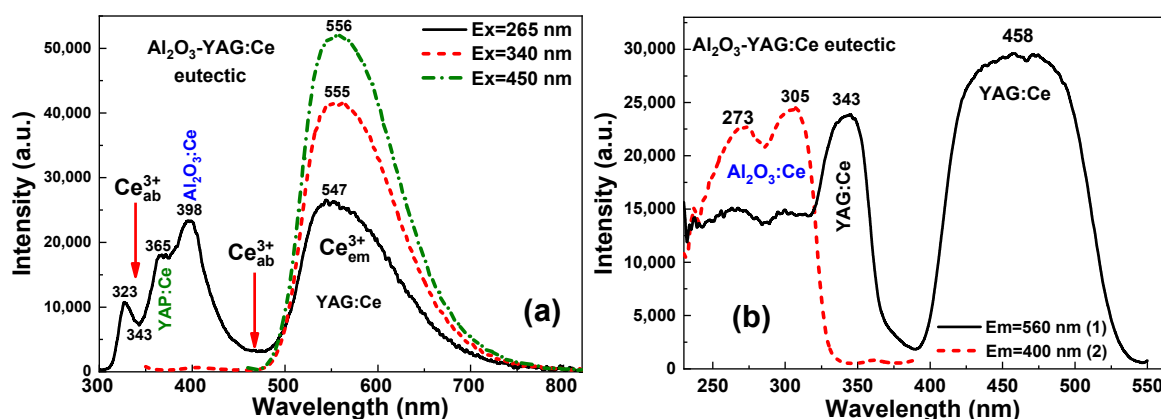


Figure 7. PL emission spectra (a) and PLE spectra (b) of (Al₂O₃-YAG):Ce eutectic (sample 4) under excitation at different wavelengths (a) and registration of Ce³⁺ luminescence in the garnet ((b), curve 1) and sapphire phase ((b), curve 2).

The PLE spectra of the Ce³⁺ emission in the garnet phase in the (Al₂O₃-YAG):Ce eutectic sample four are displayed in Figure 7b, curve one. The two main bands in these spectra that peaked at 343 and 458 nm are related to the 4f-5d transitions of Ce³⁺ ions in the YAG:Ce garnet. The full width at a half maximum (FWHM) of the 458 nm excitation peak is about 100 nm, which suits well with blue LED chips of various emission wavelengths [33].

The decay kinetics of the Ce³⁺ luminescence of (Al₂O₃-YAG):Ce eutectic, recorded in the vicinity of the Ce³⁺ emission band at 560 nm under excitation in the Ce³⁺ absorption band in the garnet phase at 460 nm, is shown in Figure 8, curve one. The decay kinetics of the Ce³⁺ luminescence in the garnet phase are strongly exponential and the decay constant is equal to 66 ns, which is characteristic of Ce³⁺ luminescence in other garnet compounds [34].

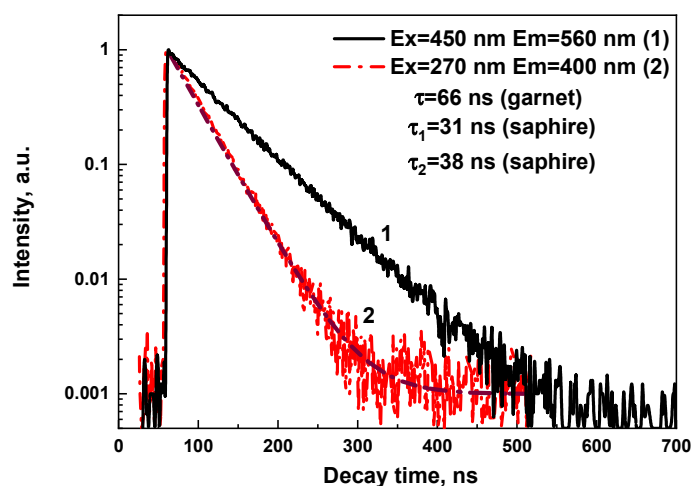


Figure 8. Decay kinetics of (Al₂O₃-YAG):Ce eutectic (sample 4) corresponding to the Ce³⁺ luminescence in the YAG:Ce (1) and Al₂O₃:Ce (2) phases under excitation in the respective PLE bands at 450 nm (1) and 270 nm (2).

The PL emission spectra of this (Al₂O₃-YAG):Ce eutectic sample four also show the complex emission band in the UV range, peaked at 396 nm (Figure 7a, curve one), corresponding to the Ce³⁺ luminescence in the Al₂O₃:Ce phase [34]. The bands peaked at 273 and 305 nm in the PLE spectrum of this luminescence monitored at 400 nm (Figure 7b, curve 2), which are caused by the respective 4f-5d (²E and ³T_{2g}) transitions of Ce³⁺ ions in the Al₂O₃ host [35]. Furthermore, the effective energy transfer processes are observed between Ce³⁺ ions in the Al₂O₃ phase to the garnet phase under high-energy excitation

and excitation in the corresponding UV bands. The confirmation of such transfer is also quite nonexponential decay kinetics of the Ce^{3+} luminescence in the $\text{Al}_2\text{O}_3\text{:Ce}$ phase under excitation at 260 nm in the vicinity of the respective PLE band (Figure 8, curve two). The approximation of the respective decay curve two in Figure 8 shows the presence of the two components with decay times of $t_1 = 31$ ns and $t_2 = 38$ ns, respectively. Furthermore, the 35 ns average decay time was used for the characterization of the decay profiles of this luminescence and its value is noticeably lower, though consistent with the lifetime of the Ce^{3+} luminescence in the $\text{Al}_2\text{O}_3\text{:Ce}$ single crystalline films, being equal to 42 ns [35]. Moreover, such nonexponential decay profiles of the Ce^{3+} luminescence in the sapphire phase in the eutectic samples are strongly temperature dependent. This means that the energy transfer from the sapphire phase to the garnet phase increases with increasing temperatures. These new results will be presented soon in a separate paper.

It is worth noting here that the presence of the small content (less than 1%) YAP:Ce perovskite phase was also tested in the PL emission spectra of the $(\text{Al}_2\text{O}_3\text{-YAG})\text{:Ce}$ eutectic sample under 265 nm excitation (Figure 6, curve 1). Most probably, the observed bump peaked at 365 nm in this spectrum in Figure 7a corresponds to the Ce^{3+} luminescence in the YAP host. However, the shape of the Ce^{3+} emission band in the YAP:Ce phase is strongly affected by the presence of the Ce^{3+} absorption band in the garnet phase, which peaked at 343 nm.

5. WLED Prototype Creation

We have also tested the photoconversion (PC) prototypes of WLEDs, prepared using a blue 450 nm LED chip and Ce-doped $\text{Al}_2\text{O}_3\text{-YAG}$ eutectic photoconverters (pc) with thicknesses in the 0.15–1 mm range (Figure 9). The results of the tests are quite encouraging. The emission spectrum for these WLEDs covers the visible range from 460 to 820 nm with warmer light, in comparison with the standard YAG:Ce photoconverter [36]. Figure 9 shows also the dependence of the PC properties of the $(\text{Al}_2\text{O}_3\text{-YAG})\text{:Ce}$ eutectic on the thickness of the samples. Namely, when the eutectic thickness grows, the blue LED's intensity declines while the intensity of the yellow emission band rises. The blue light is almost entirely absorbed, and the yellow emission achieves its peak intensity at a thickness of around 1.0 mm.

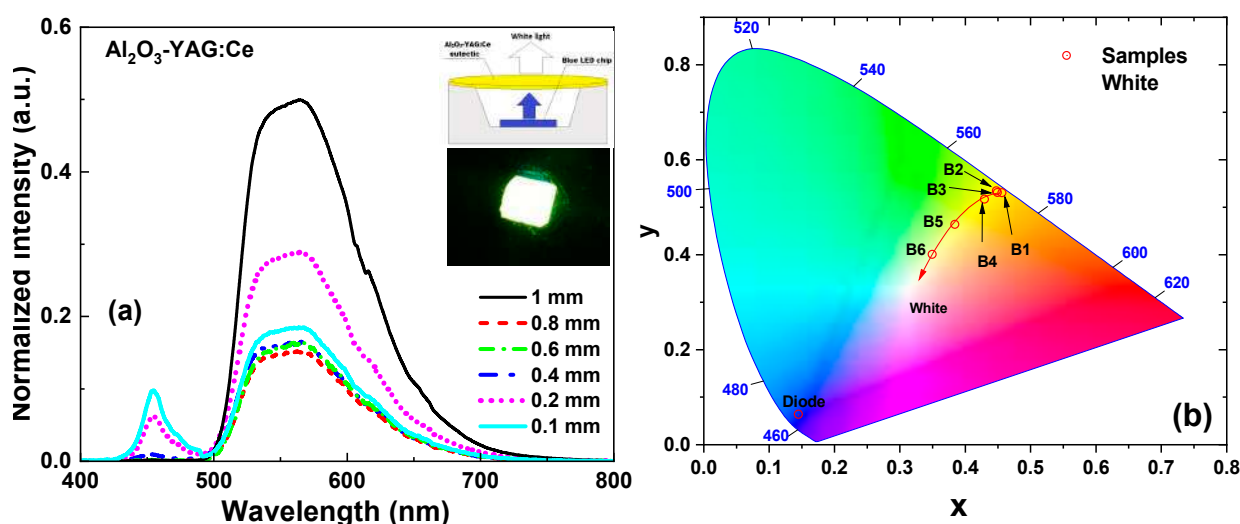


Figure 9. The spectral performance of $(\text{Al}_2\text{O}_3\text{-YAG})\text{:Ce}$ eutectic samples under 450 nm blue LED excitation (a); color coordinates of $(\text{Al}_2\text{O}_3\text{-YAG})\text{:Ce}$ eutectic based LEDs in CIE-1931 color space chromaticity diagram (b).

The CIE-1931 chromaticity diagram in Figure 8b also displays the changes in color coordinates (x , y) of the $(\text{Al}_2\text{O}_3\text{-YAG})\text{:Ce}$ eutectic with different thicknesses in the 0.15–1 mm range. The coordinates have a nonlinear distribution, and the x and y values rise with the

eutectic thickness. We assumed that decreasing the thicknesses from 0.4 mm to 0.1 mm can be used to create white colors with various color temperatures. The CIE chromaticity coordinates of WLED prototypes are shown in Table 3. Namely, the combination of the (Al₂O₃-YAG):Ce eutectic sample with different thicknesses in the 0.4–0.15 mm range enables tuning of the white light shades from warm white (CCT = 3810 K) to warm/daylight white (CCT ~5120 K) [37,38]. Based on the obtained results, presented in Figure 9 and Table 3, we can expect that the ideal white color can be achieved for a eutectic converter thickness of about 0.1–0.15 mm under 450 nm LED excitation. Due to significantly smaller lightguide losses and the small intrinsic reflection losses, the thickness of the eutectic converter is significantly smaller than the optimal thickness of the YAG:Ce (0.25%) crystal counterpart (0.5–0.55 mm), grown from the melt with nominal cerium content of 1 molar % [39].

Table 3. CIE chromaticity coordinates, CCT and luminous efficiency of a WLED lamp fabricated on the base of 450 nm LED chip and (Al₂O₃-YAG):Ce eutectic (sample 4) with different thicknesses.

Thicknesses of Sample 4 h, mm	CIE Coordinates		CCT, K	CRI	LE (lm/W)
	x	y			
1 (B1)	0.4567	0.5299	3489	39.7	68
0.8 (B2)	0.4498	0.5306	3580	46.1	81
0.6 (B3)	0.4483	0.5341	3620	42.3	107
0.4 (B4)	0.4300	0.5165	3810	55.9	120.4
0.2 (B5)	0.4047	0.4633	4530	67.4	132
0.15 (B6)	0.35	0.40	5120	72.5	142.5

We have provided the results of measurements of the luminous efficiency (Lm/W) of the WLED prototypes with a gradual reduction of the eutectic thicknesses from 1 to 0.15 mm (the last column in Table 3). As can be seen from this table, the LE value steadily increases when the thickness of the eutectic converter decreases up to 0.15 mm. Finally, the WLED prototype eutectic converter with a thickness of 0.15 mm shows a luminous efficiency of above 140 Lm/W.

6. Conclusions

In this study, Ce³⁺ doped Al₂O₃-YAG eutectic samples were crystallized using the horizontal directional crystallization method at a growth temperature of 1835 °C, with varying crystallization rates in the 1–7.5 mm/h range. The microstructure of the eutectic samples was analyzed using scanning electron microscopy, X-ray diffraction, and X-ray microtomography. The samples consisted primarily of the YAG and Al₂O₃ phases, with a small amount (below 1%) of the YAP:Ce perovskite phase also observed in Al₂O₃-YAG via a photoluminescence spectra. The eutectic morphology exhibited a stripe-like channel structure with the random distribution of the garnet and sapphire phases. The content of these phases in the stripes varied depending on the growth rate of the eutectic samples, with ranges of 52–54% and 48–46% for the garnet and sapphire, respectively.

The luminescent properties of the eutectic samples demonstrated the dominant Ce³⁺ emission band in the garnet phase and the weak Ce³⁺ luminescence in the sapphire phase. Furthermore, the effective energy-transfer processes between Ce³⁺ ions in the Al₂O₃ and YAG garnet phases were observed under high-energy excitation, as well as excitation in the UV Ce³⁺ absorption bands of sapphire.

We have investigated the photoconversion properties of (Al₂O₃-YAG):Ce eutectic samples with different thicknesses, under excitation by a blue LED. We also tested prototypes of white LEDs prepared using (Al₂O₃-YAG):Ce eutectic photoconverters, with thicknesses ranging from 0.15 to 1 mm, and a blue 450 nm emitting LED chip. We have found that the combination of (Al₂O₃-YAG):Ce eutectic with thicknesses in the 0.4–0.15 mm range and 450 nm LED excitation enables tuning of the white light tones from warm white (CCT ~ 3800 K) to white daylight (CCT ~ 5100 K). Furthermore, the ideal white color can be achieved for a eutectic converter thickness in the 0.1–0.15 mm range, and the respective WLED prototype exhibits a luminous efficiency above 140 Lm/W.

Author Contributions: A.S. collected and analyzed the structural and optical properties of samples, and participated in the writing and preparation of the paper; S.W.-Ł. performed and analyzed cathodoluminescence measurements; T.Z. participated in measurements of PL, PLE, and decay kinetics of the samples; M.C. and Z.S. performed and analyzed structural measurements; O.V., S.N. and Y.S. fulfilled growth of the eutectic samples, performed SEM and XRD measurements and analyzed their results; Y.Z. conceptually contributed to the research and analysis of the whole experimental material and participated in the writing and correction of the paper. All authors have read and agreed to the published version of the manuscript.

Funding: The work was performed in the framework of the Polish NCN 2022/45/B/ST8/01757 project and the frame of the NAS of Ukraine project #0120U101754.

Institutional Review Board Statement: Not applicable.

Informed Consent Statement: Not applicable.

Data Availability Statement: Not applicable.

Conflicts of Interest: The authors declare no conflict of interest.

References

1. Nakamura, S.; Senoh, M.; Iwasa, N.; Nagahama, S.-I.; Yamada, T.; Mukai, T. Superbright Green InGaN Single-Quantum-Well-Structure Light-Emitting Diodes. *Jpn. J. Appl. Phys.* **1995**, *34*, L1332–L1335. [\[CrossRef\]](#)
2. Nakamura, S.; Mukai, T.; Senoh, M. Candela-class high-brightness InGaN/AlGaN double-heterostructure blue-light-emitting diodes. *Appl. Phys. Lett.* **1994**, *64*, 1687–1689. [\[CrossRef\]](#)
3. Schlotter, P.; Schmidt, R.; Schneider, J. Luminescence conversion of blue light emitting diodes. *Appl. Phys. A* **1997**, *64*, 417–418. [\[CrossRef\]](#)
4. Zhong, Y.; Sun, P.; Gao, X.; Liu, Q.; Huang, S.; Liu, B.; Deng, B.; Yu, R. Synthesis and optical properties of new red-emitting SrBi₂Ta₂O₉:Eu³⁺ phosphor application for w-LEDs commercially based on InGaN. *J. Lumin.* **2019**, *212*, 45–51. [\[CrossRef\]](#)
5. Xia, Z.; Meijerink, A. Ce³⁺-Doped garnet phosphors: Composition modification, luminescence properties and applications. *Chem. Soc. Rev.* **2016**, *46*, 275–299. [\[CrossRef\]](#)
6. Nishiura, S.; Tanabe, S.; Fujioka, K.; Fujimoto, Y. Properties of transparent Ce:YAG ceramic phosphors for white LED. *Opt. Mater.* **2011**, *33*, 688–691. [\[CrossRef\]](#)
7. Fujita, S.; Sakamoto, A.; Tanabe, S. Luminescence Characteristics of YAG Glass–Ceramic Phosphor for White LED. *IEEE J. Sel. Top. Quantum Electron.* **2008**, *14*, 1387–1391. [\[CrossRef\]](#)
8. Nishiura, S.; Tanabe, S. Preparation and optical properties of Eu²⁺ and Sm³⁺ co-doped glass ceramic phosphors emitting white color by violet laser excitation. *J. Ceram. Soc. Jpn.* **2008**, *116*, 1096–1099. [\[CrossRef\]](#)
9. Fujita, S.; Tanabe, S. Thermal Quenching of Ce³⁺:Y₃Al₅O₁₂ Glass–Ceramic Phosphor. *Jpn. J. Appl. Phys.* **2009**, *48*, 120210. [\[CrossRef\]](#)
10. Sai, Q.; Zhao, Z.; Xia, C.; Xu, X.; Wu, F.; Di, J.; Wang, L. Ce-doped Al₂O₃–YAG eutectic and its application for white LEDs. *Opt. Mater.* **2013**, *35*, 2155–2159. [\[CrossRef\]](#)
11. He, H.; Oetting, W.; Brott, M.; Basu, S. Pair-Wise Multifactor Dimensionality Reduction Method to Detect Gene–Gene Interactions in A Case-Control Study. *Hum. Hered.* **2009**, *69*, 60–70. [\[CrossRef\]](#)
12. Li, S.; Wang, L.; Hirosaki, N.; Xie, R. Color Conversion Materials for High-Brightness Laser-Driven Solid-State Lighting. *Laser Photon. Rev.* **2018**, *12*, 1800173. [\[CrossRef\]](#)
13. Li, S.; Zhu, Q.; Tang, D.; Liu, X.; Ouyang, G.; Cao, L.; Hirosaki, N.; Nishimura, T.; Huang, Z.; Xie, R.-J. Al₂O₃–YAG:Ce composite phosphor ceramic: A thermally robust and efficient color converter for solid state laser lighting. *J. Mater. Chem. C* **2016**, *4*, 8648–8654. [\[CrossRef\]](#)
14. Shen, X.; Chen, H.; Lin, J.; Li, Y.; Lin, H.; Chen, J.; Chen, C. Analysis and Modeling of Optical and Thermal Properties of Phosphor Converted White Light Emitting Diode. *IEEE Access* **2019**, *7*, 118679–118689. [\[CrossRef\]](#)
15. Tang, Y.; Zhou, S.; Chen, C.; Yi, X.; Feng, Y.; Lin, H.; Zhang, S. Composite phase ceramic phosphor of Al₂O₃–Ce:YAG for high efficiency light emitting. *Opt. Express* **2015**, *23*, 17923. [\[CrossRef\]](#) [\[PubMed\]](#)
16. Huh, D.; Kim, W.; Kim, K.; Son, S.; Park, J.; Ju, S.; Chae, D.; Baek, S.; Lee, H. Enhancing light conversion efficiency of YAG:Ce phosphor substrate using nanoimprinted functional structures. *Nanotechnology* **2020**, *31*, 144003. [\[CrossRef\]](#)
17. Singh, G.; Mehta, D.S. White-light generation using a remote-phosphor-coated diffusing surface excited by the high-brightness blue light-emitting diode. *J. Inf. Disp.* **2014**, *15*, 91–98. [\[CrossRef\]](#)
18. Yamada, S.; Yoshimura, M.; Sakata, S.-I.; Taishi, T.; Hoshikawa, K. Colony structure in Ce-doped Al₂O₃/YAG eutectic systems grown by vertical Bridgman technique. *J. Cryst. Growth* **2016**, *448*, 1–5. [\[CrossRef\]](#)
19. Liu, Y.; Zhang, M.; Nie, Y.; Zhang, J.; Wang, J. Growth of YAG:Ce³⁺–Al₂O₃ eutectic ceramic by HDS method and its application for white LEDs. *J. Eur. Ceram. Soc.* **2017**, *37*, 4931–4937. [\[CrossRef\]](#)
20. Nie, Y.; Han, J.; Liu, Y.; Zhang, M.; Zhang, J. Isotropy in large-size Al₂O₃/Y₃Al₅O₁₂ eutectic ceramic grown by Horizontal Directional Solidification method. *Mater. Sci. Eng. A* **2017**, *704*, 207–211. [\[CrossRef\]](#)

21. Naydenov, S.V.; Vovk, O.M.; Siryk, Y.V.; Nizhankovskyi, S.V.; Pritula, I.M. Efficiency of planar light converters based on Al_2O_3 -YAG:Ce eutectic crystals. *Funct. Mater.* **2021**, *28*, 533–541. [\[CrossRef\]](#)
22. Vovk, O.; Siryk, Y.; Nizhankovskyi, S.; Fedorov, A.; Mateichenko, P. Morphology and Microstructure of Crystalline YAG- Al_2O_3 Composites Grown by the Horizontal Directional Crystallization. *SSRN J.* **2022**. [\[CrossRef\]](#)
23. Arjoca, S.; Villora, E.G.; Inomata, D.; Aoki, K.; Sugahara, Y.; Shimamura, K. Temperature dependence of Ce:YAG single-crystal phosphors for high-brightness white LEDs/LDs. *Mater. Res. Express* **2015**, *2*, 055503. [\[CrossRef\]](#)
24. Mizutani, Y.; Yasuda, H.; Ohnaka, I.; Maeda, N.; Waku, Y. Coupled growth of unidirectionally solidified Al_2O_3 -YAG eutectic ceramics. *J. Cryst. Growth* **2002**, *244*, 384–392. [\[CrossRef\]](#)
25. Frazer, C.S.; Dickey, E.C.; Sayir, A. Crystallographic texture and orientation variants in Al_2O_3 -Y $3\text{Al}_5\text{O}_{12}$ directionally solidified eutectic crystals. *J. Cryst. Growth* **2001**, *233*, 187–195. [\[CrossRef\]](#)
26. Yasuda, H.; Ohnaka, I.; Mizutani, Y.; Morikawa, T.; Takeshima, S.; Sugiyama, A.; Waku, Y.; Tsuchiyama, A.; Nakano, T.; Uesugi, K. Three-dimensional observation of the entangled eutectic structure in the Al_2O_3 -YAG system. *J. Eur. Ceram. Soc.* **2005**, *25*, 1397–1403. [\[CrossRef\]](#)
27. Naydenov, S.V.; Vovk, O.M.; Siryk, Y.V.; Nizhankovskyi, S.V.; Pritula, I.M. Improved efficiency of planar light converters based on Al_2O_3 -YAG: Ce eutectic crystals: Physical Trends and Limits. *arXiv* **2021**, arXiv:2105.08259. [\[CrossRef\]](#)
28. Szczepański, Z. Wrocław2 Cube01 ir Rec0000 [Video]. Youtube. 2 December 2022. Available online: <https://www.youtube.com/watch?v=dkpfvFGdjco> (accessed on 2 December 2020).
29. Cieszko, M.; Szczepański, Z.; Gadzała, P. Determination of bone porosity based on histograms of 3D μCT images. *J. Mater. Sci.* **2014**, *50*, 948–959. [\[CrossRef\]](#)
30. Cantarano, A.; Testemale, D.; Homeyer, E.; Okuno, H.; Potdevin, A.; Dujardin, C.; Ibanez, A.; Dantelle, G. Drastic Ce $^{3+}$ Insertion Enhancement in YAG Garnet Nanocrystals Through a Solvothermal Route. *Front. Mater.* **2021**, *8*, 768087. [\[CrossRef\]](#)
31. Zorenko, Y.; Zych, E.; Voloshinovskii, A. Intrinsic and Ce $^{3+}$ -related luminescence of YAG and YAG:Ce single crystals, single crystalline films and nanopowders. *Opt. Mater.* **2009**, *31*, 1845–1848. [\[CrossRef\]](#)
32. Zorenko, Y.; Gorbenko, V.; Voznyak, T.; Savchyn, V.; Bilski, P.; Twardak, A. Peculiarities of luminescent and scintillation properties of YAG:Ce phosphor prepared in different crystalline forms. *Opt. Mater.* **2012**, *34*, 1314–1319. [\[CrossRef\]](#)
33. Wang, X.; Zhou, G.; Zhang, H.; Li, H.; Zhang, Z.; Sun, Z. Luminescent properties of yellowish orange Y 3Al_5 -xSi $_{10}$ O $_{12}$ -xNx:Ce phosphors and their applications in warm white light-emitting diodes. *J. Alloys Compd.* **2012**, *519*, 149–155. [\[CrossRef\]](#)
34. Barzowska, J.; Kubicki, A.; Grinberg, M.; Kaczmarek, S.; Łuczyński, Z.; Wojtowicz, A.J.; Koepke, C. Photoluminescence kinetics of YAG crystals activated with Ce, and Ce and Mg. *Acta Phys. Pol. A* **1999**, *95*, 395–402. [\[CrossRef\]](#)
35. Zorenko, Y.; Zorenko, T.; Gorbenko, V.; Savchyn, V.; Voznyak, T.; Fabisiak, K.; Zhusupkalieva, G.; Fedorov, A. Luminescent properties of Al_2O_3 :Ce single crystalline films under synchrotron radiation excitation. *Opt. Mater.* **2016**, *59*, 141–144. [\[CrossRef\]](#)
36. Wei, N.; Lu, T.; Li, F.; Zhang, W.; Ma, B.; Lu, Z.; Qi, J. Transparent Ce:Y 3Al_5 O $_{12}$ ceramic phosphors for white light-emitting diodes. *Appl. Phys. Lett.* **2012**, *101*, 061902. [\[CrossRef\]](#)
37. Shakhno, A.; Markovskiy, A.; Zorenko, T.; Witkiewicz-Łukaszek, S.; Vlasjuk, Y.; Osvet, A.; Elia, J.; Brabec, C.J.; Batentschuk, M.; Zorenko, Y. Micropowder Ca $_2\text{YMgScSi}_3\text{O}_{12}$:Ce Silicate Garnet as an Efficient Light Converter for White LEDs. *Materials* **2022**, *15*, 3942. [\[CrossRef\]](#)
38. Shakhno, A.; Witkiewicz-Łukaszek, S.; Gorbenko, V.; Zorenko, T.; Zorenko, Y. Luminescence and photoconversion properties of micro-powder phosphors based on the Ce $^{3+}$ and Mn $^{2+}$ doped Ca $_2\text{YMgScSi}_3\text{O}_{12}$ silicate garnets. *Opt. Mater. X* **2022**, *16*, 100187. [\[CrossRef\]](#)
39. Nizhankovskyi, S.V.; Tan'Ko, A.V.; Savvin, Y.N.; Krivonogov, S.I.; Budnikov, A.T.; Voloshin, A.V. Single crystalline YAG:Ce phosphor for powerful solid-state sources of white light. The influence of production conditions on luminescence properties and lighting characteristics. *Opt. Spectrosc.* **2016**, *120*, 915–921. [\[CrossRef\]](#)

Disclaimer/Publisher's Note: The statements, opinions and data contained in all publications are solely those of the individual author(s) and contributor(s) and not of MDPI and/or the editor(s). MDPI and/or the editor(s) disclaim responsibility for any injury to people or property resulting from any ideas, methods, instructions or products referred to in the content.



Micro-powder $\text{Ca}_3\text{Sc}_2\text{Si}_3\text{O}_{12}:\text{Ce}$ silicate garnets as efficient light converters for WLEDs

Ievgen Levchuk^a, Andres Osvet^a, Christoph J. Brabec^a, Mirosław Batentschuk^a, Anna Shakhno^b, Tetiana Zorenko^b, Yuriy Zorenko^{b,*}

^a Universität Erlangen-Nürnberg, Institute i-MEET, Martensstraße 7, 91058, Erlangen, Germany

^b Institute of Physics, Kazimierz Wielki University in Bydgoszcz, 85090, Bydgoszcz, Poland

ARTICLE INFO

Keywords:

WLED
Converters
Ca–Si based Garnets
Micropowder
Luminescence

ABSTRACT

A novel synthesis method of $\text{Ca}_3\text{Sc}_2\text{Si}_3\text{O}_{12}:\text{Ce}$ micropowder with very bright photo-luminescence (PL) has been developed. The conventional solid-state reaction has been modified for $\text{Ca}_3\text{Sc}_2\text{Si}_3\text{O}_{12}:\text{Ce}$ microparticle crystallization. Pre-synthesis of metal and silicon oxide blends with subsequent high-temperature treatment in reducing (H_2/N_2) atmosphere enables obtaining $\text{Ca}_3\text{Sc}_2\text{Si}_3\text{O}_{12}:\text{Ce}$ micropowder with a high PL quantum yield of about 60–70% at Ce^{3+} content in the 2.5–5 at.% range, which is highly attractive for LED technology. Additionally, the $\text{Ca}_3\text{Sc}_2\text{Si}_3\text{O}_{12}:\text{Ce}$ phosphors with Ce concentration in the 0.5–2.5% range display higher thermal stability of photoluminescence in comparison with a commercial YAG:Ce phosphor.

1. Introduction

Development of solid-state lighting devices based on a combination of blue light-emitting diodes (LEDs) and phosphor converters is of extremely high commercial interest due to their potentially higher efficiencies, long lifetimes, and environmental friendliness in comparison with conventional light sources. Nowadays, the white LEDs (WLEDs) replace step-by-step the traditional light sources because their efficiency is higher than that of fluorescent tubes. The WLEDs do not contain mercury and other harmful elements. At present, the combination of a blue LED chip and yellow-emitting $\text{Y}_3\text{Al}_5\text{O}_{12}:\text{Ce}$ (YAG:Ce) garnet phosphor is a conventional WLED device [1]. Meanwhile, the development of phosphors is actively continuing in order to optimize their parameters like the color correlated temperature and color rendering index of WLEDs.

One of the most interesting alternative phosphors to YAG:Ce is $\text{Ca}_3\text{Sc}_2\text{Si}_3\text{O}_{12}:\text{Ce}$ (CSSG:Ce) silicate garnet. In general, the silicate garnet phosphors are very promising, because they show high quantum yield with broadband emission spectra and, furthermore, a high thermal stability of luminescence.

The synthesis and optical properties of Ce^{3+} doped $\text{Ca}_3\text{Sc}_2\text{Si}_3\text{O}_{12}$ silicate garnet for an application in white LEDs have been firstly reported by Shimomura et al. [2]. This phosphor can be synthesized by a conventional solid-state high-temperature reaction. It shows the

broadband Ce^{3+} photoluminescence (PL) with a maximum at 505 nm in the green spectral range and the PL excitation band at 455 nm in the blue spectral range. The CIE color coordinates of this phosphor are equal to $x = 0.30$ and $y = 0.59$, and also shows a high thermal stability. These properties of the GSSG:Ce phosphor are very important for high-power WLEDs due to their large heat generation, leading to a drop of the luminescence intensity because of thermal quenching under normal operation conditions. Namely, in comparison with $(\text{Y,Gd,Ce})_3\text{Al}_5\text{O}_{12}:\text{Ce}$ garnet phosphor, the CSSG:Ce garnet shows remarkably high thermal stability of the luminescence up to 200 °C. For example, at a temperature of 150 °C it still shows a relative intensity of over 90% compared to around 55% in YAG diluted with Gd.

The effect of different fluxes on the luminescent properties of the green CSSG:Ce phosphor has been studied by using solid state synthesis in a reducing atmosphere at 1250 °C [3–7]. It has been found that without flux the CSSG phase cannot be synthesized. On the other hand, by using H_3BO_3 , LiF, CaF_2 and NH_4Cl the garnet phase can be obtained. Most probably, the CaF_2 is the best flux for synthesizing the CSSG:Ce phosphor from the viewpoint of the luminescence intensity. Based on CSSG:Ce phosphor, a WLED prototype has been fabricated and correlated color temperature of this light source is lower than that of the commercial WLED with YAG:Ce.

The CSSG:Ce phosphor has been obtained at a lower temperature using the gel-combustion method as compared to the conventional solid-

* Corresponding author.

E-mail address: zorenko@ukw.edu.pl (Y. Zorenko).

<https://doi.org/10.1016/j.optmat.2020.109978>

Received 22 March 2020; Received in revised form 28 April 2020; Accepted 1 May 2020

Available online 30 May 2020

0925-3467/© 2020 Elsevier B.V. All rights reserved.

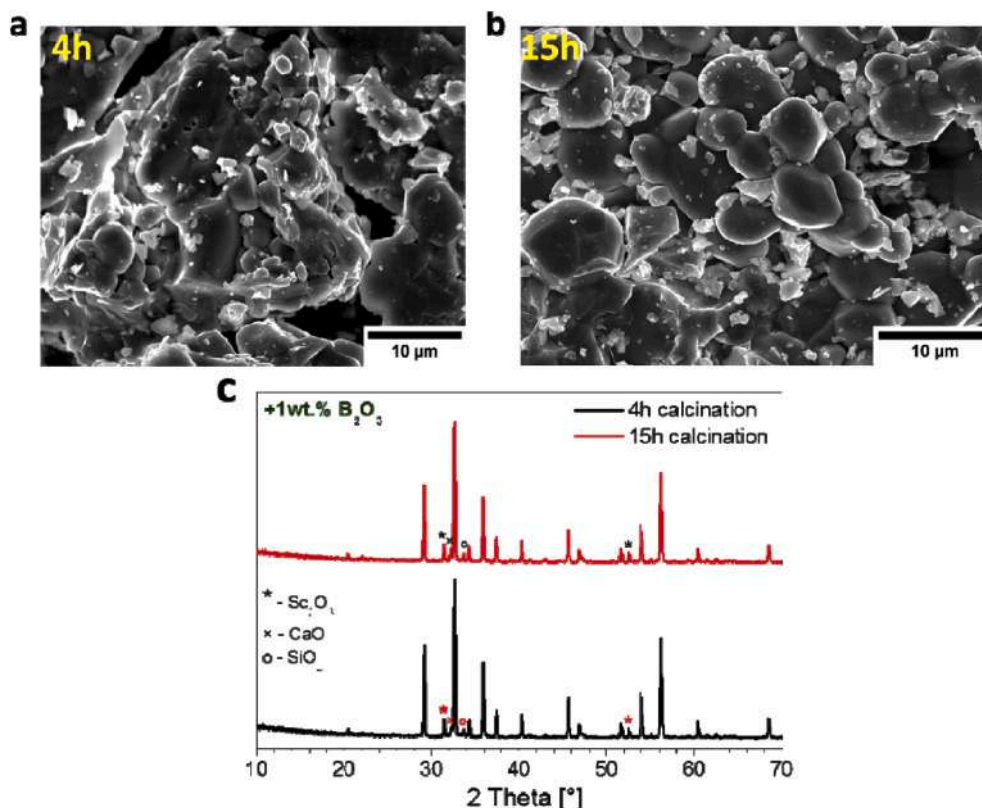


Fig. 1. Influence of calcination time on morphological and structural properties of CSSG:0.5%Ce MPs, prepared using 1 wt% B_2O_3 as flux. (a) - SEM images of calcinated samples for 4 h (a) and 15 h (b). (c) - XRD patterns of these samples.

state reaction method [4]. Such a phosphor has particle size of about 1 μm , which is much less than the size of particles obtained by the solid-state reaction. Smaller particle size can reduce internal scattering when particles are mixed with silicon and coated onto a blue LED chip. CSSG:Ce phosphors additionally containing Al^{3+} cations have been synthesized as well. It has been shown that Al^{3+} alloying enhances the photoluminescence performance as well as the quantum efficiency of phosphor to 46.8% [7].

In this work, we present a novel synthesis method of CSSG:Ce micropowder with outstandingly bright PL and a record high PL quantum yield (PLQY) of about 70%. The samples of this garnet display also higher thermal stability of the PL photoluminescence in comparison with a commercial YAG:Ce phosphor.

2. Synthesis of CSSG:Ce micropowder samples and experimental techniques

CSSG:Ce microcrystalline powders (MP) have been synthesized by

modified solid-state phase synthesis technique. In comparison with the previous reports [2–7], additional 900 °C pre-heating treatment for the pressed pellets of starting oxides has been used. This allows obtaining more homogenous MP blends by taking into account the fact that homogeneity of samples strongly enhances the luminescent properties of the phosphors. Calcination process has been performed at 1400 °C in reducing atmosphere (N_2/H_2). First of all, we have investigated the influence of annealing time on morphology, structure, and optical properties of CSSG:Ce MP samples with a nominal Ce^{3+} concentration of 0.5 at % (Fig. 1).

In the most popular method of solid-state preparation of phosphors, using a flux can improve the morphology of grains and enhance the PL intensity of the material. In our preliminary experiments on CSSG:Ce solid-state synthesis without flux, garnet compounds have not been obtained and only gehlenite compositions have been detected by XRD method. In opposite, by using B_2O_3 flux for improvement of the condition of solid-state reaction, garnet phase has been successfully obtained. Fig. 1a and b demonstrate the scanning electron microscopy (SEM)

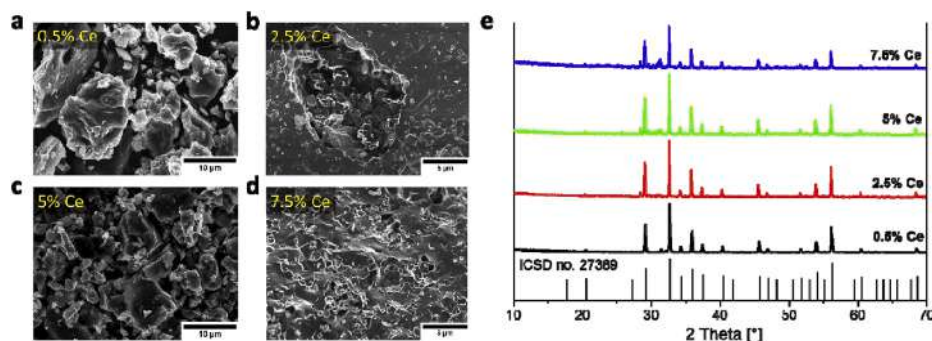


Fig. 2. SEM images of CSSG:Ce MPs samples with different Ce content, prepared using CaF_2 as flux. (b) XRD patterns. (c) PLE and PL spectra. (d) PL decay curves.

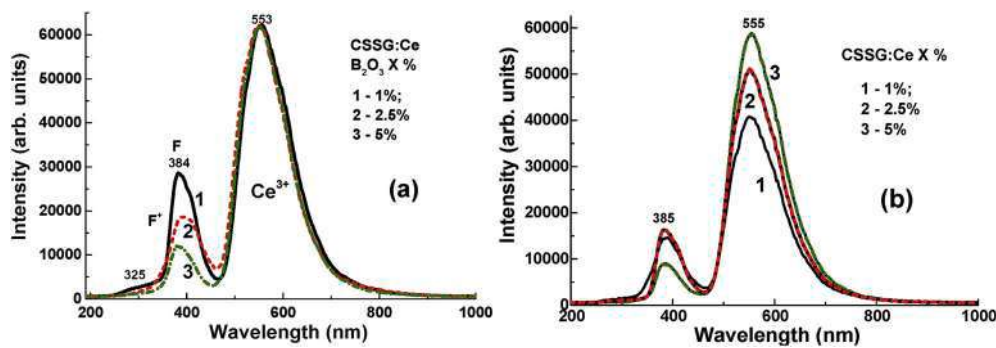


Fig. 3. RT CL spectra of CSSG:Ce MP samples, sintered with different content of B_2O_3 flux (a) and different concentration of Ce^{3+} ions (b).

images of CSSG:0.5% Ce MPs, calcinated for 4 h and 15 h at 1400 °C. Obviously, average size of obtained sphere-like MPs is larger for the sample annealed for 15 h than for the case of the 4 h annealed sample due to MP growth during the reaction. The X-ray diffraction (XRD) study shows almost pure phases of CSSG in both cases and excellent correspondence with the respective ICSD-27389 pattern. However, some minor amounts of impurity phases of unreacted starting materials, namely CaO , Sc_2O_3 and SiO_2 , also exist (Fig. 1c). On the other hand, there are no diffraction peaks from the flux phase. Prolonged annealing time has no significant influence on phase purity, nevertheless, the optical properties of the annealed samples are improved (see Fig. 1).

To increase the PLQY, an alternative flux such as CaF_2 has been tested to avoid possible boron incorporation into the CSS structure, which may prevent increasing the PLQY. Following the same sample preparation methodology, CaF_2 flux has been used instead of B_2O_3 flux (Fig. 2). The series of the CSSG:Ce MP samples containing a nominal Ce^{3+} concentration of 0.5, 2.5, 5 and 7.5 at. % have been synthesized by taking into account the optimal synthesis conditions under using CaF_2 flux. The obtained samples display non-uniform morphology in SEM (Fig. 2) and larger grainsize in comparison with the material synthesized with B_2O_3 as flux (Fig. 1). The XRD shows an almost pure garnet phase with a minor amount of Sc_2O_3 and CaO as an impurity phase (Fig. 2e, black line) as well as a complete absence of diffraction peaks from the flux phase.

For characterization of the properties of the CSSG:Ce MPs under study, the cathodoluminescence (CL), PL, PL excitation spectra (PLE), PL decay kinetics, PLQY as well as photoconversion spectra (PC) were used. The CL spectra were investigated at room temperature (RT) using a scanning electron microscope SEM JEOL JSM-820, additionally equipped with a spectrometer Stellar Net's with a TE-cooled CCD detector working in the 200–1200 nm range. PL emission and excitation spectra, as well as PL decay kinetics, were measured using a FS-5 spectrometer (Edinburg Instruments). The PC spectra and PLQY measurements were performed by using a fiber-optic spectrophotometer AvaSpec-ULS 2048-LTEC and the integrating sphere AvaSphere-50-IRRAD. The photoconverter prepared from CSSG:Ce MPs was excited by the blue LED with a wavelength of $\lambda = 464$ nm.

3. Luminescent properties of CSSG:Ce MP samples

The electronic configuration of Ce^{3+} is $[Xe]4f^15d^0$. Generally in CSSG:Ce garnet the Ce^{3+} ion occupies the D_2 symmetry Ca^{2+} site, so that the 5d level is initially split into a lower doublet (E_g) and a higher triplet (T_{2g}) by the cubic component of the crystal field and then further split by the distortion from cubic symmetry. A first-principles study [8] has calculated the energies of the $4f^1$ and $5d^1$ levels of Ce^{3+} in CSSG host with different types of charge compensation mechanisms. Therefore, the wide absorption/PLE bands and the PL emission peaks in the MP samples under study originate from the $4f$ – $5d$ transitions of Ce^{3+} ions. The splitting of the Ce^{3+} energy level is induced by both the covalence effect

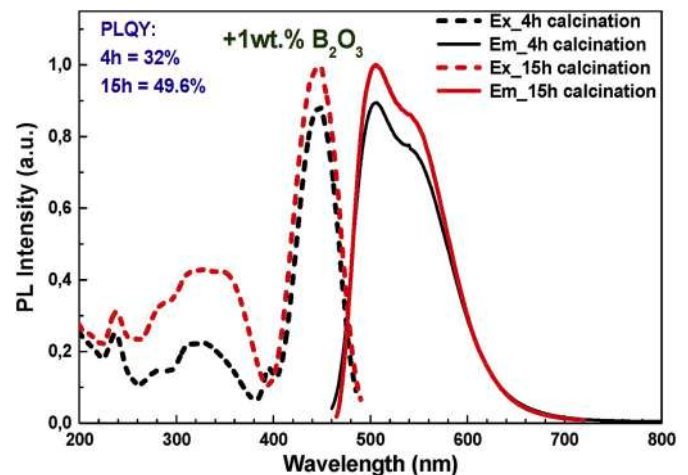


Fig. 4. Influence of calcination time on RT PL and PLE spectra of CSS:0.5%Ce MPs, prepared using 1 wt% B_2O_3 as a flux.

(nephelauxetic effect) and the crystal field effect.

CL spectra. The CL spectra of CSSG:Ce MPs samples, sintered with different content of B_2O_3 flux and different concentration of Ce^{3+} ions at RT are shown in Fig. 3a and b, respectively. The dominant luminescence band peaked at 553–555 nm range in these MP samples corresponds to the $5d^1 \rightarrow 4f(2F_{5/2}, 7/2)$ transitions of Ce^{3+} ion in these garnet hosts. The position of this band is slightly red-shifted from 553 to 555 nm in CSSG:Ce MPs with increasing the Ce content from 1 to 5% (Fig. 3, curves 1–3).

Apart from the luminescence of Ce^{3+} ions, other emission bands in the UV range are also present in the CL spectra of CSSG:Ce MPs. The main UV band peaks at 384–385 nm. The other low-intensity UV band peaked at 325 nm is also present in the CL spectra of these MP samples. Similar low-intensity bands in the UV range in the Ca^{2+} - Mg^{2+} and Si^{4+} based garnets were attributed in works [9,10] to the luminescence of the defects centers. In our opinion, the presence of large oxygen vacancies is expected in the Ca^{2+} - Mg^{2+} - Si^{4+} based garnets due to the possible deviation in the content of these ions and the necessity of the local charge compensation, as well as due to MP sintering in the reducing (H_2/N_2) atmosphere. For this reason, the bands in the 325 nm and 384–385 nm range can correspond to the luminescence of F^+ and F centers, respectively (singly and doubly charged oxygen vacancies) in the CSSG host [10,11].

PL and PLE spectra. The PL spectra of CSSG:Ce MP samples, sintered by using B_2O_3 and CaF_2 fluxes (Figs. 4–6, respectively) have typical double Ce^{3+} 5d-4f emission bands peaked at 506 and 547 nm corresponding to the transitions to two spin-orbit components $2F_{5/2,7/2}$ (separated by ~ 2000 cm^{-1}) of the ground state. The PLE spectra show a series of bands in 200–500 nm range, which are attributed to the absorption of the allowed transitions from the 4f ground state to the 5d

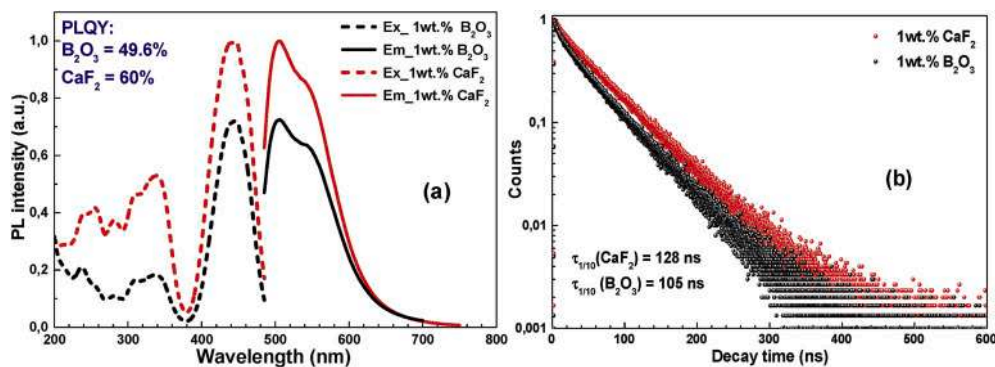


Fig. 5. Effect of flux (B₂O₃ and CaF₂) on the luminescent properties of CSSG:0.5%Ce MPs. (a) - PLE and PL spectra; (b) - PL decay kinetics.

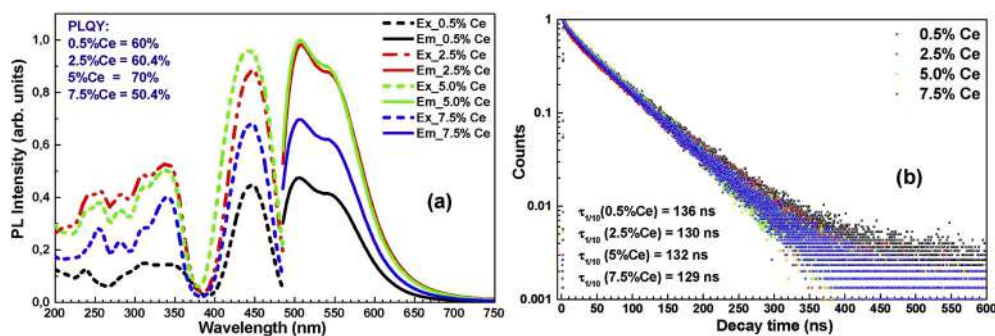


Fig. 6. Investigations of PL and PLE (a) spectra and PL decay kinetics (b) of CSSG:Ce MP samples with different Ce³⁺ concentration.

levels of Ce³⁺.

It is important to note here that the prolongation of the annealing time from 4 to 15 h leads to enhancement of the PLQY of CSSG:Ce MP samples, sintered from B₂O₃ flux, from 32% to 49.6% (Fig. 4). This effect may be a consequence of improvement of the garnet crystal structure during the sintering.

The PL and PLE spectra of CSSG:0.5% Ce MPs synthesized in the presence of CaF₂ flux are identical to the ones of the sample synthesized using B₂O₃ (Fig. 5a), but the PLQY significantly increased from 49.6% to 60%. PL-decay measurements support this observation (Fig. 5b), showing that the sample synthesized with B₂O₃ has a faster decay time (105 ns) than that of the sample synthesized with CaF₂ (128 ns). In the case of CaF₂, the decay curve is closer to a single-exponential behaviour, indicating less quenching and a higher PLQY in comparison with the samples fabricated with B₂O₃ flux. The value of a PL-decay time of 128 ns for Ce³⁺ in the CSSG sample is of the same order as that of other Ce³⁺ doped phosphors [12].

The influence of the Ce³⁺ concentration in 0.5–7.7 at.% range on PLQY of in CSSG:Ce MPs has been studied as well (Fig. 6). Under excitation in the blue spectral range, all the obtained MP samples show characteristic luminescence broad bands with maximums at 506 and 547 nm due to the Ce³⁺ 5d–4f transitions. Furthermore, the samples have high PLQY of 50–70% depending on the Ce³⁺ content in the mentioned range (Fig. 6a). It has been found that for CSSG:Ce5% MP, PLQY is 70%, which is the highest value of the reported ones so far, to the best of our knowledge. For higher Ce³⁺ concentration of 7.5 at. %, the PLQY drops to 50.4% due to self-quenching of excited Ce³⁺ ions.

The measured PL decay times fit very well to the PLQY values of the samples (Fig. 6b). For the CSSG:0.5% Ce MP sample the PL decay time is a bit longer than that for the CSSG:5% Ce sample, although PLQY of CSSG:0.5% Ce is lower in the case of CSSG:5% Ce. It should be noted that the decay time of CSSG:0.5% Ce MP deviates more from a single-exponential curve than that of CSSG: 5% Ce MPs. Most probably, the faster decay component in the 0–50 ns range is a result of some energy

transfer from the excited states to other Ce³⁺ emission centers, which may explain the lower PLQY in the sample with lower activator concentration.

4. Ce³⁺ multicenter formation in CSSG:Ce phosphor

The RT PL emission spectra of CSSG:Ce 5% MPs are shown in Fig. 7a under excitation in the maxima of the characteristic PLE bands (Fig. 7b). The PL spectra of these samples show the intensive luminescence in the form of wide bands peaked in the green range, which are related to the 5d¹→4f(²F_{5/2,7/2}) transitions of Ce³⁺ ions. Meanwhile, with increasing the excitation wavelength from 233 to 433 nm, the PL spectra of CSSG:Ce MPs show the blue shift from 501.5 to 495 nm firstly and then the red shift from 495 to 505 nm (Fig. 7a, curves 1–5 and 6, respectively). Therefore, the shift of the main maxima of the PL spectra of CSSG:Ce MPs occurs non-monotonically with increasing the excitation wavelength. Such a behavior of the PL emission spectra clearly indicates the Ce³⁺ multicenter formation in CSSG:Ce garnet (see Fig. 8).

The detailed analyses of the normalized PL spectra of CSSG:Ce MPs (Fig. 7a) confirms the above-mentioned conclusion. Namely, the PL spectra of CSSG:Ce MPs under excitation in the long-wavelength and high-wavelength wings of the Ce³⁺ related band at 344 nm and 443 nm, demonstrate two pairs of the Ce³⁺ emission bands peaked at 495 and 541 nm and 505 and 547 nm (Fig. 7a), related mainly to the different Ce1 and Ce2 centers, respectively.

The PLE spectra of CSSG:Ce MPs at RT are shown in Fig. 5b. Several sets of excitation bands are distinguished in the 200–500 nm spectral range. The strongest bands E₁ (437 nm), E₂ (339 nm) and E₃ (256 nm) can be attributed to the 4f–5d (²E and T_{2g}) transitions of the **first Ce1 center**, in accordance with previous studies [11,13]. The other sets of excitation bands E₁'' (449 nm), E₂'' (311 nm), and E₃'' (256 nm) can be attributed to the 4f¹→5d¹ transitions of the **second Ce2 centers** with a different local environment in comparison with the Ce1 center [13]. The excitation band peaked at 280 nm can be related to a defect center, most

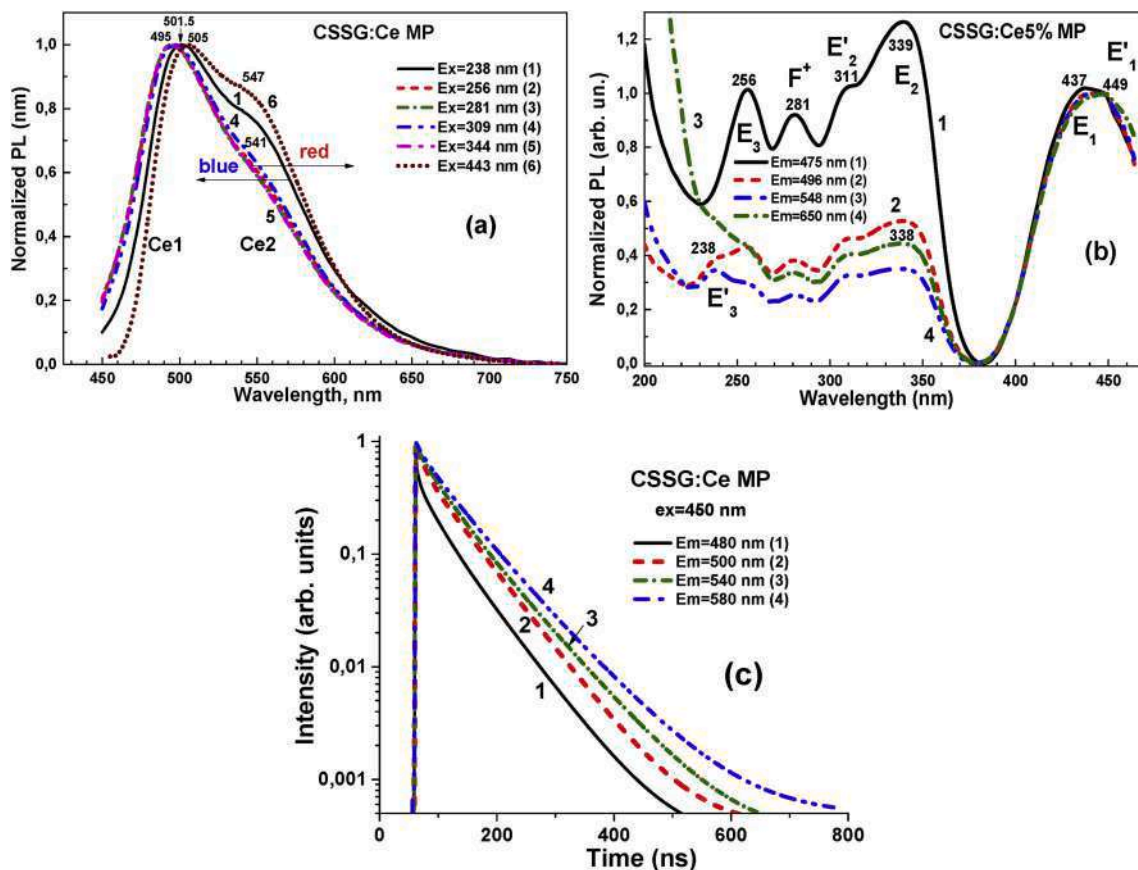


Fig. 7. Detailed luminescent properties of CSSG:Ce:5% Ce MPs at RT. Emission (a) and excitation (b) recorded in different parts of the respective spectra. PL decay kinetics (c) at RT recorded under blue light (450 nm) excitation in different parts of Ce³⁺ emission band. (For interpretation of the references to color in this figure legend, the reader is referred to the Web version of this article.)

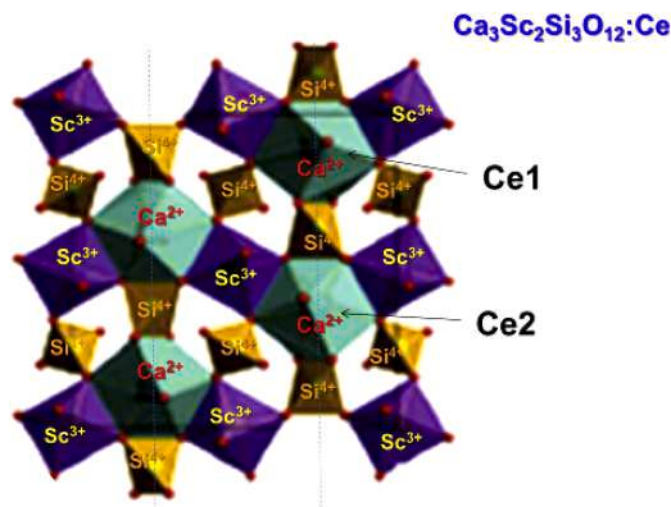


Fig. 8. Visualization of possible Ce1 and Ce2 centers in structure of Ca₃Sc₂Si₃O₁₂:Ce garnet.

probably to the F center [11]. The emission of these centers in CSSG:Ce host can excite the luminescence of Ce³⁺ ions as well [11].

The decay kinetics of the Ce³⁺ luminescence, recorded in the different parts of Ce³⁺ emission spectrum is shown in Fig. 7a. Similarly to other Ca²⁺-Si⁴⁺ based garnets [9,10,13,14], the decay kinetics of the Ce³⁺ emission in CSSG:Ce MPs is strongly non-exponential, and a three-component fit of the decay curves $I = \sum A_i \exp(-t/\tau_i)$ was used for

Table 1

Parameters of three exponent approximation of the decay curves presented in Fig. 7c.

Emission wavelength	t_1 , ns	A_1	t_2 , ns	A_2	t_3 , ns	A_3
480 nm	4.7	0.13	27.2	0.17	63.5	0.26
500 nm	12.45	0.33	37.6	0.31	67.3	0.31
540 nm	14.0	0.07	51.1	0.37	74.9	0.44
580 nm	14.6	0.08	59.1	0.42	83.6	0.39

the qualitative description of the luminescence timing properties (see also [15]). Although such a three-exponential approximation does not describe correctly the luminescence decay behavior in the case of quenching due to the energy transfer, the decay time values can be considered as an estimation of the luminescence decay times of the respective Ce³⁺ multicenters (Table 1). Namely, the decay luminescence in CSSG:Ce MPs can be presented by the three components τ_i , $i = 3$ with different decay times, related to the different Ce³⁺ centers. The decay kinetics of the luminescence in the CSSG:Ce 5% MP sample at registration in the different parts of the Ce³⁺ emission bands (Fig. 5c) confirms this conclusion. Namely, the values of τ_1 , τ_2 and τ_3 decay times of the Ce³⁺ luminescence in CSSG:Ce MPs, registered at 480 and 580 nm under excitation at 450 nm, increase from 4.7 ns; 27.2 ns and 63.5 ns–14.6 ns; 59.1 ns and 83.6 ns, respectively (Table 1).

Such a behavior of the decay curves in CSSG:Ce MPs can also indicate the possible energy transfer from high-energy to low-energy Ce³⁺ emitting centers in this garnet [11,13–16]. The different decay times in CSSG:Ce MPs can correspond to the different Ce³⁺ centers in the dodecahedral positions of the garnet lattice with various local surroundings by oxygen and cations (Sc³⁺ and Si⁴⁺ ions in the octahedral

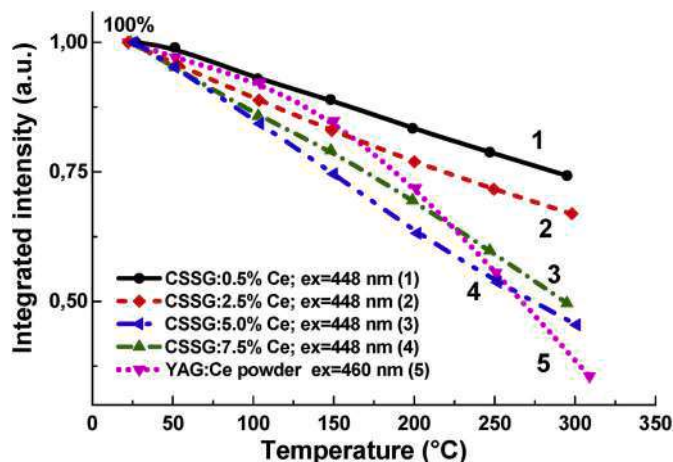


Fig. 9. Temperature dependence of integral emission in 450–700 nm spectral range for CSSG:Ce MP samples with different Ce^{3+} concentrations in comparison with commercial YAG:Ce powder.

and tetrahedral positions, respectively, Fig. 6).

5. Temperature-quenching characteristics of CSSG:Ce phosphor

It is well known that the temperature of LED package rises because of heat generation by the LED itself. The phosphors used for color conversion material in WLED must have low thermal quenching behavior at least up to 150 °C. For this reason, we have performed the measurements of temperature-quenching characteristics of the developed phosphors [2], e. g. the measurements of the temperature dependence for the luminescence intensity of CSSG:Ce MP samples (Fig. 9). The data of commercial OSRAM YAG:Ce phosphor are also shown in Fig. 9 as a reference. As can be seen from Fig. 9, the PL of CSSG:Ce phosphors is less quenched at lower Ce doping concentration (0.5–2.5%) than that of a commercially available YAG:Ce phosphor, even at higher temperature

(>200 °C). Therefore, this phosphor is a very suitable color-conversion material for the LEDs. However, at higher doping levels (5–7.5%), the thermal quenching of PL is more enhanced.

6. WLED prototype creation

To demonstrate application possibility of the developed of CSSG:Ce phosphor, a WLED has been fabricated by coating the CSSG:Ce phosphor in epoxy resin on the GaN 432 nm blue LED chip driven by 130 mA and 3.5 V (Fig. 10a). The emission spectrum of this WLED is quite broad and covers the entire visible range (from 400 to 780 nm). Fig. 10a shows the emission spectrum of such white LED having the CIE chromaticity coordinates equal to $x = 0.29$ and $y = 0.38$.

The fabricated device with bright light characteristics demonstrates that the WLEDs based on CSSG:Ce MPs are very promising and can be applicable for indoor and outdoor lighting systems. Meanwhile, the application potential of CSSG:Ce phosphor can be realized mainly in the high power WLEDs due to better temperature dependence of the emission (see Fig. 9).

7. Conclusions

A novel synthesis method of $\text{Ca}_3\text{Sc}_2\text{Si}_3\text{O}_{12}:\text{Ce}$ (CSSG:Ce) microparticle powder is developed by modified solid-state phase synthesis technique using B_2O_3 and CaF_2 fluxes. This method allows one to synthesize CSSG:Ce phosphors having very bright photoluminescence with a high PLQY of about 60–70% at a Ce concentration of 2.5–5 at %. We have confirmed that CSSG:Ce phosphors with Ce^{3+} content in the 0.5–2.5% at. % range display also higher thermal stability of photoluminescence in comparison to a commercial YAG:Ce phosphor.

We have also observed the formation at least two Ce^{3+} centers in the $\text{Ca}_3\text{Sc}_2\text{Si}_3\text{O}_{12}:\text{Ce}$ garnet in the emission and excitation spectra of the MPs under study, as well as in the decay kinetics of the Ce^{3+} luminescence. Such Ce^{3+} centers possess different spectral behaviours (the positions of the emission and excitation bands as well as the PL decay kinetics) due to the different local surroundings and crystal field strength environments

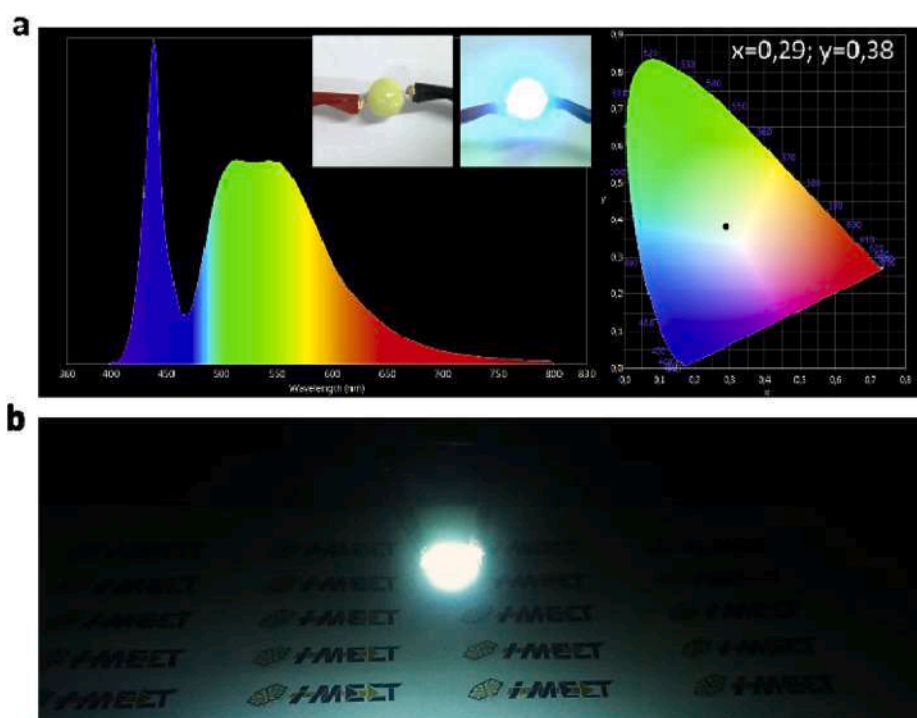


Fig. 10. (a) - CIE chromaticity coordinates and emission spectrum of a WLED lamp fabricated on the base of 432 nm LED chip and CSSG:5%Ce phosphor. Inset shows appearance of a well-packaged LED lamp in operation. (b) - demonstration of the white LED in dark room.

of the respective dodecahedral positions of the garnet host. Such an inhomogeneity of the local environments of the dodecahedral positions of the garnet host arises at substitution of the octahedral positions by heterovalence Mg^{2+} and Sc^{3+} ions and the tetrahedral positions by Si^{4+} ions.

The efficient prototype of WLED lamp has been fabricated using CSSG:Ce phosphor and GaN 432 nm blue LED chip for demonstration of the application possibility of the developed of CSSG:Ce phosphor. Such a lamp emits the white light with the CIE chromaticity coordinates $x = 0.29$ and $y = 0.38$.

Declaration of competing interest

The authors declare that they have no known competing financial interests or personal relationships that could have appeared to influence the work reported in this paper.

CRediT authorship contribution statement

Ievgen Levchuk: Investigation, Methodology, Writing - original draft, Writing - review & editing. **Andres Osvet:** Investigation, Validation. **Christoph J. Brabec:** Conceptualization, Project administration. **Mirosław Batentschuk:** Conceptualization, Project administration, Writing - original draft, Writing - review & editing. **Anna Shakhno:** Data curation, Formal analysis. **Tetiana Zorenko:** Investigation, Validation, Visualization. **Yuriy Zorenko:** Conceptualization, Methodology, Validation, Writing - review & editing.

Acknowledgements

The work was performed in the framework of Polish NCN 2017/25/


B/ST8/02932 project.

References

- [1] C.-C. Sun, Y.-Y. Chang, T.-H. Yang, T.-Y. Chung, C.-C. Chen, T.-X. Lee, D.-R. Li, C.-Y. Lu, Z.-Y. Ting, B. Glorieux, Y.-C. Chen, K.-Y. Lai, C.-Y. Liu, *J. Solid State Light.* 1 (2014) 19.
- [2] Y. Shimomura, T. Honma, M. Shigeiwa, T. Akai, K. Okamoto, N. Kijima, *J. Electrochem. Soc.* 154 (2007) J35.
- [3] Y. Chen, M. Gong, K.W. Cheah, *Mater. Sci. Eng., B* 166 (2010) 24.
- [4] Y. Liu, J. Hao, W. Zhuang, Y. Hu, *J. Phys. Appl. Phys.* 42 (2009) 245102.
- [5] Y. Liu, W. Zhuang, Y. Hu, W. Gao, J. Hao, *J. Alloys Compd.* 504 (2010) 488.
- [6] R. Fernández-González, J. Velázquez, V. Rodríguez, F. Rivera-López, A. Lukowiak, A. Chiasera, M. Ferrari, R. Gonçalves, J. Marrero-Jerez, F. Lahoz, *RSC Adv.* 6 (2016) 15054.
- [7] Y.F. Wu, Y.H. Chan, Y.T. Nien, I.G. Chen, *J. Am. Ceram. Soc.* 96 (2013) 234.
- [8] W. Ding, J. Wen, J. Cheng, L.-x. Ning, Y.-c. Huang, C.-k. Duan, M. Yin, *Chin. J. Chem. Phys.* 28 (2015) 150.
- [9] Tyagi, F. Meng, M. Koschan, S.B. Donnal, H. Rothfuss, C.L. Melcher, *J. Phys. D Appl. Phys.* 46 (2013) 475302.
- [10] Y. Wu, F. Meng, Q. Li, M. Koschan, C.L. Melcher, *Phys. Rev. Appl.* 2 (2014), 044009.
- [11] V. Gorbenco, T. Zorenko, I. Levchuk, A. Osvet, M. Batentschuk, Y. Zorenko, et al., *CrystEngComm* 19 (2017) 3689.
- [12] T. Kano, S. Shionoya, W. Yen, S. Shionoya, W.M. Yen, CRC Press Inc., Boca Raton, FL, USA, 1999, pp. 499–508.
- [13] V. Gorbenco, T. Zorenko, S. Witkiewicz, K. Paprocki, A. Iskalyeva, A. M. Kaczmarek, R. Van Deun, M.N. Khaidukov, M. Batentschuk, Yu Zorenko, *J. Lumin.* 199 (2018) 245.
- [14] A.P. Jadhav, A. Pawar, C.W. Kim, H.G. Cha, U. Pal, Y.S. Kang, *J. Phys. Chem. C* 113 (2009) 16652.
- [15] A. Lukowiak, A. Chiasera, A. Chiappini, G.G. Righini, M. Ferrari, *Active sol-gel materials, fluorescence spectra, and lifetimes*, in: L. Klein, M. Aparicio, A. Jitianu (Eds.), *Handbook of Sol-Gel Science and Technology*, Springer, 2016, pp. 1–43, 2016.
- [16] L. Zhou, W. Zhou, F. Pan, R. Shi, L. Huang, H. Liang, P.A. Tanner, X. Du, Y. Huang, Y. Tao, L. Zheng, *Chem. Mater.* 28 (2016) 2834.

Article

Micropowder $\text{Ca}_2\text{YMgScSi}_3\text{O}_{12}:\text{Ce}$ Silicate Garnet as an Efficient Light Converter for White LEDs

Anna Shakhno ^{1,*}, Anton Markovskiy ¹, Tetiana Zorenko ¹, Sandra Witkiewicz-Lukaszek ¹, Yevheniya Vlasyuk ², Andres Osvet ², Jack Elia ², Christoph J. Brabec ², Mirosław Batentschuk ^{2,*} and Yuriy Zorenko ^{1,*} 

¹ Institute of Physics, Kazimierz Wielki University in Bydgoszcz, 85090 Bydgoszcz, Poland; gorbenco@ukw.edu.pl (A.M.); tetiana.zorenko@ukw.edu.pl (T.Z.); sanwit@ukw.edu.pl (S.W.-L.)

² Institute of Materials for Electronics and Energy Technology (i-MEET), Department of Materials Science and Engineering VI, University of Erlangen-Nürnberg, 91058 Erlangen, Germany; yevgeniya.vlasyuk@fau.de (Y.V.); andres.osvet@fau.de (A.O.); jack.elia@fau.de (J.E.); christoph.brabec@fau.de (C.J.B.)

* Correspondence: shakhno@ukw.edu.pl (A.S.); mirosław.batentschuk@fau.de (M.B.); zorenko@ukw.edu.pl (Y.Z.); Tel.: +48-693330878 (Y.Z.)

Abstract: This work is dedicated to the crystallization and luminescent properties of a prospective $\text{Ca}_2\text{YMgScSi}_3\text{O}_{12}:\text{Ce}$ (CYMSSG:Ce) micropowder (MP) phosphor converter (pc) for a white light-emitting LED (WLED). The set of MP samples was obtained by conventional solid-phase synthesis using different amounts of B_2O_3 flux in the 1–5 mole percentage range. The luminescent properties of the CYMSSG:Ce MPs were investigated at different Ce^{3+} concentrations in the 1–5 atomic percentage range. The formation of several Ce^{3+} multicenters in the CYMSSG:Ce MPs was detected in the emission and excitation spectra as well as the decay kinetics of the Ce^{3+} luminescence. The creation of the Ce^{3+} multicenters in CYMSSG:Ce garnet results from: (i) the substitution by the Ce^{3+} ions of the heterovalent Ca^{2+} and Y^{3+} cations in the dodecahedral position of the garnet host; (ii) the inhomogeneous local environment of the Ce^{3+} ions when the octahedral positions of the garnet are replaced by heterovalent Mg^{2+} and Sc^{3+} cations and the tetrahedral positions are replaced by Si^{4+} cations. The presence of Ce^{3+} multicenters significantly enhances the Ce^{3+} emission band in the red range in comparison with conventional YAG:Ce phosphor. Prototypes of the WLEDs were also created in this work by using CYMSSG:Ce MP films as phosphor converters. Furthermore, the dependence of the photoconversion properties on the layer thickness of the CYMSSG:Ce MP was studied as well. The changes in the MP layer thickness enable the tuning of the white light thons from cold white/daylight to neutral white. The obtained results are encouraging and can be useful for the development of a novel generation of pcs for WLEDs.

Keywords: WLED; phosphor converters; Ca^{2+} - Mg^{2+} - Si^{4+} -based garnets; micropowder; luminescence; Ce^{3+} multicenters



Citation: Shakhno, A.; Markovskiy, A.; Zorenko, T.; Witkiewicz-Lukaszek, S.; Vlasyuk, Y.; Osvet, A.; Elia, J.; Brabec, C.J.; Batentschuk, M.; Zorenko, Y. Micropowder $\text{Ca}_2\text{YMgScSi}_3\text{O}_{12}:\text{Ce}$ Silicate Garnet as an Efficient Light Converter for White LEDs. *Materials* **2022**, *15*, 3942. <https://doi.org/10.3390/ma15113942>

Academic Editor: Ingo Dierking

Received: 10 April 2022

Accepted: 24 May 2022

Published: 1 June 2022

Publisher's Note: MDPI stays neutral with regard to jurisdictional claims in published maps and institutional affiliations.



Copyright: © 2022 by the authors. Licensee MDPI, Basel, Switzerland. This article is an open access article distributed under the terms and conditions of the Creative Commons Attribution (CC BY) license (<https://creativecommons.org/licenses/by/4.0/>).

1. Introduction

With development of blue-emitting light-emitting diodes (LEDs) based on AlInGaN semiconductor chips, the lighting industry is in a technical breakthrough. In the past few years, these LEDs, in combination with blue-to-yellow light converters emitting white light (WLEDs), have caused quite a stir in the lighting industry. With their long service life, low production costs, and high efficiency, WLEDs are a suitable environmentally friendly alternative to conventional light bulbs and fluorescent lamps. They are also competitive thanks to their low energy consumption and resource-saving production. As a result, these diodes are significantly more ecological in terms of production and application than conventional light sources. They also have a useful color rendering index (CRI) and an easily adjustable correlated color temperature (CCT) [1–5]. LED technology can be found in

the industry in many application areas, for example, in the automotive industry, in medical technology, and in lighting and sensor technology [6–10].

Development and spectroscopic investigation of Ca^{2+} - Si^{4+} -based garnets are very conducive for designing novel generations of phosphor converters (pc) in so-called *planar-type technology* for high-power WLED [11,12] and new materials for luminescent thermometry as well [13]. Nowadays, the development of such types of phosphors is a prospective direction in semiconductor lighting technology [12–19]. Currently, for the production of high-power WLEDs, YAG:Ce garnets in crystal or ceramic form are mainly used in combination with blue LED [11,20–23].

Of all the Ca-Si-based garnet phosphors, the most well-known is $\text{Ca}_3\text{Sc}_2\text{Si}_3\text{O}_{12}$ (CSSG) garnet, doped with different types of rare-earth or/and transition metal ions [11,20,24]. The simultaneous localization of Ce^{3+} ions and other rare-earth and transition metal ions in the different valence states in the dodecahedral sites enables the creation of a wide class of novel silicate-based garnet phosphors. Furthermore, additional Y^{3+} - Mg^{2+} pair-alloying into the $\text{Ca}_3\text{Sc}_2\text{Si}_3\text{O}_{12}$:Ce garnet host opens additional possibilities for the modification of luminescent properties and the development of more efficient types of pc for WLED [13,25]. Namely, such an approach allows achieving the more suitable redshift of the emission spectra and better color properties of pc-WLEDs in comparison with conventional YAG:Ce pc [13,25].

The current work aims to study the characteristics of the luminescent properties of Ce^{3+} -doped $\text{Ca}_2\text{YMgScSi}_3\text{O}_{12}$ (CYMSSG:Ce) microcrystalline powder (MP) phosphors prepared using conventional solid-state synthesis, which can be used as an efficient pc for the creation of high-power WLEDs. Prototypes of pc-WLEDs based on CYMSSG:Ce MP planar layers of different thicknesses were fabricated in this work and their pc properties were investigated as well. The development of this type of phosphor is nowadays a hot topic in lighting technology, especially given that currently only phosphors based on YAG:Ce crystal or ceramic garnet are available for the production of power WLEDs with the excitation of blue LEDs.

2. Synthesis of CYMSSG:Ce Micropowder Samples and Their Structural Qualities

CYMSSG:Ce MP were synthesized by conventional solid synthesis as an effective production method based on a solid–solid reactions, and in this case, between the microcrystalline grains of the raw components. During the synthesis of MPs from CaO , Y_2O_3 , MgO , Sc_2O_3 , and SiO_2 raw oxides with 4N purity, they were first weighed and then ground in agate solution for 20 min to obtain the greatest homogeneity of the powder. It is necessary to note here that the homogeneity of the samples significantly enhances the luminescent properties of the phosphors. The final phosphor mass was baked in an Al_2O_3 crucible at a heating rate of $20\text{ }^\circ\text{C}/\text{min}$ to $1300\text{ }^\circ\text{C}$ for 10 h in a reducing atmosphere (95% N_2 + 5% H_2).

In the solid-state method, the preparation of phosphors using flux can substantially support the formation of the garnet phase and enables the obtaining of microparticles with high quantum yield. The application of flux can also significantly improve the morphology of the grains and, in this way, additionally enhance the material PL intensity. For this reason, the synthesis of CYMSSG:Ce MP samples was performed using B_2O_3 flux with concentration in the 1–5 wt.% range with respect to the total weight of the garnet charge. By using B_2O_3 flux to improve the condition of the solid-state reaction, the $\text{Ca}_2\text{YMgScSi}_3\text{O}_{12}$ garnet phase in the MP samples under study was successfully obtained (Figures 1 and 2).

Figure 1 demonstrates the SEM images of the CYMSSG:Ce MP samples synthesized from the charge containing 1 wt.%, 2.5 wt.%, and 5 wt.% B_2O_3 flux agent. Overall, the structure of the garnet is visible in all MP samples under study. From Figure 1, the influence of the flux and its concentration on the formation of the cubic particles with a garnet structure can also be observed. Cubic grains corresponding to the garnet structure are present in small amounts in the MP sample synthesized at a concentration of 1 wt.% B_2O_3 (Figure 1a). Furthermore, strong grain agglomeration is visible for this MP sample. On the contrary, the MP samples synthesized from compounds with a higher B_2O_3 content

(Figure 1b,c) have a more homogeneous garnet structures, especially for the sample with the highest (5 wt.%) flux concentration (Figure 1c). That means that increasing the flux content leads to a uniformity of the grain distribution and some increase in the average grain size, up to 5–8 μm for a Ba_2O_3 concentration of 5 wt.%.

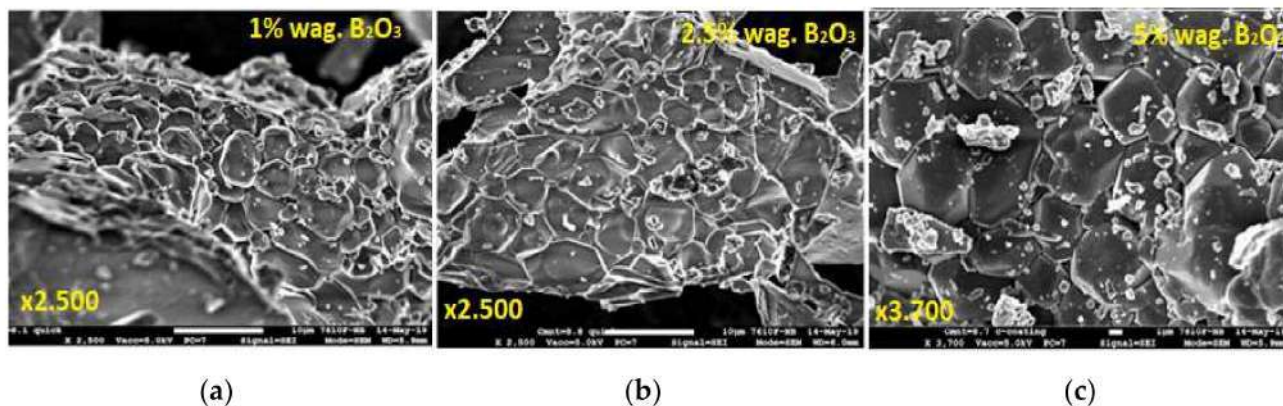


Figure 1. SEM images of CYMSSG: 2.5%Ce MPs, prepared using different amounts of B_2O_3 flux agent: (a) 1 wt.%, (b) 2.5 wt.%, and (c) 5 wt.%.

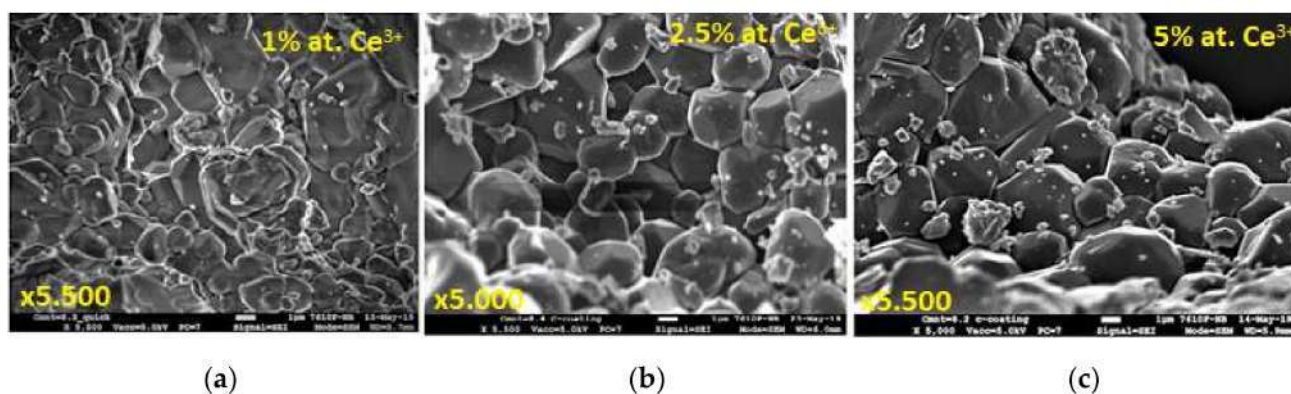


Figure 2. SEM images of CYMSSG:Ce MPs samples with different Ce^{3+} concentrations, prepared using 2.5 wt.% B_2O_3 flux agent: (a) 1 at.%, (b) 2.5 at.%, and (c) 5 at.%.

SEM images of CYMSSG:Ce MPs synthesized with an activator concentration in the 1–5% range are shown in Figure 2. Generally, garnet grains are visible in all samples. However, the strong grain agglomeration is observed for samples with the lowest Ce^{3+} content of 1%. Furthermore, the quantity of agglomerates is significantly lower in the samples with Ce^{3+} contents of 2.5 and 5 at.%, especially in the last one (Figure 2c). For the last sample, the most uniform distributions of the grain are observed, with their average size in the 3–5 μm range.

The X-ray diffraction (XRD) of MP samples sintered with different B_2O_3 flux amounts (Figure 3a) and different Ce^{3+} concentrations shows almost pure phases of $\text{Ca}_3\text{Sc}_2\text{Si}_3\text{O}_{12}$ garnet (CSSG) in both cases and excellent correspondence with the respective ICSD-27389 pattern. However, some minor amounts of unreacted starting materials, (SiO_2) as well as the secondary phases ($\text{Ca}_2\text{Ce}_8\text{O}_{26}\text{Si}_6$, YBO_3), are also observed in the XRD patterns (Figure 3).

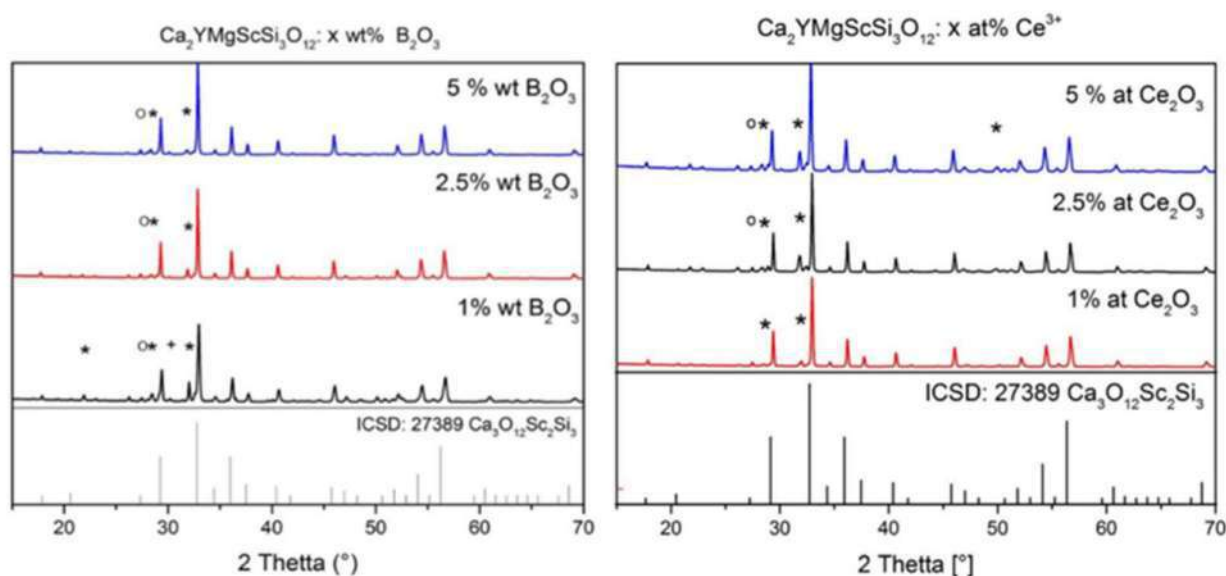


Figure 3. XRD patterns of CYMSSG:Ce MPs with different flux and activator amounts: (a) x wt.% B_2O_3 and (b) x at.% Ce_2O_3 , where * is $Ca_2Ce_8O_{26}Si_6$, + is SiO_2 , and o is YBO_3 .

From the XRD data, a garnet phase with maxima corresponding mostly to $Ca_3Sc_2Si_3O_{12}$ was detected. The main peak of the garnet at about 32.7° (2θ), which belongs to the {024} family of lattice planes, is very well defined in these compositions. However, additional peaks, which cannot be precisely identified, can be seen in Figure 3.

It is noticeable here that the peaks are shifted by several 2θ . The incorporation of Mg^{2+} ions into the crystal lattice is a probable reason for the discernible shift to the right. The Mg^{2+} ions take the lattice sites of the Sc^{3+} ions. Due to the smaller ionic radius, the lattice spacing increases, which means that 2θ increases accordingly. As a result of the substitution with Y^{3+} and Mg^{2+} , a newly modified silicate garnet structure that is not yet known in the database has probably emerged.

Furthermore, the increase in B_2O_3 achieves better single-phase character. This is illustrated by the peaks at around 32° (2θ) and between 51 and 52° (2θ) (Figure 3a). The proportion of the $Ca_2Ce_8O_{26}Si_6$ foreign phase and the intensity of the corresponding peak decreases with the increasing B_2O_3 concentration.

As expected, a garnet phase similar to that of $Ca_3Sc_2Si_3O_{12}$ could also be detected in a series of measurements with different concentrations of Ce ions using XRD analysis (Figure 3b). The main peaks of the silicate garnet phase are consistent with those of synthesized samples. However, as already mentioned, these are shifted. By increasing the CeO_2 concentration, the intensity of the peak at 33° increases, and the proportion of the $Ca_2Ce_8O_{26}Si_6$ foreign phase increases as well.

3. Photoluminescence Quantum Yield of CYMSSG:Ce MPs

The photoluminescence quantum yield (PLQY) of the CYMSSG:Ce MPs depending on the synthesis conditions is given in Table 1. The PLOY values ranges lie between 42.1 and 63.6%, depending mainly on the content of the garnet phase in the MP samples under study. The highest quantum efficiency has the MP sample with an activator concentration of 2.5 at.% and a B_2O_3 flux agent content of 2.5 wt.%. Correspondingly, the garnet content in these MP samples is highest as well and equal to 82% (Table 1). It is necessary to note that second phases do not influence the emission properties in the Ce^{3+} emission spectral region and serve as light scattering centers and, probably, as emission centers in the UV region in the samples investigated in this work (see results below).

Table 1. The garnet/secondary phase proportions and PLQY of the CYMSSG:Ce MPs sintered with different flux and activator contents.

Nominal Chemical Composition $\text{Ca}_2\text{MgYScSi}_3\text{O}_{12}:\text{Ce}$	Garnet Content, %	Secondary Phases Content, (%)	PLQY, %
1 at.% Ce^{3+} + 1 wt.% B_2O_3	49.5	CaO (10.9); SiO_2 (21.8) YBO_3 (5); Ce_2O_3 (12.9)	42.1
1 at.% Ce^{3+} + 2.5 wt.% B_2O_3	80	$\text{Ca}_2\text{Ce}_8\text{O}_{26}\text{Si}_6$ (11); SiO_2 (7); CaO_2 (2)	54.5
1 at.% Ce^{3+} + 5 wt.% B_2O_3	80	$\text{Ca}_2\text{Ce}_8\text{O}_{26}\text{Si}_6$ (9) SiO_2 (4); Ce_2O_3 (5); YBO_3 (2)	47.9
1 at.% Ce^{3+} + 2.5 wt.% B_2O_3	81	$\text{Ca}_2\text{Ce}_8\text{O}_{26}\text{Si}_6$ (9); SiO_2 (1); Ce_2O_3 (2); MgO (2); Ca (5)	48.5
2.5 at.% Ce^{3+} + 2.5 wt.% B_2O_3	82	$\text{Ca}_2\text{Ce}_8\text{Si}_6\text{O}_{26}$ (14); Ce_2O_3 (2); SiO_2 (2);	63.6
5 at.% Ce^{3+} + 2.5 wt.% B_2O_3	62	$\text{Ca}_2\text{Ce}_8\text{O}_{26}\text{Si}_6$ (13); SiO_2 (17) CaO_2 (2); MgO (6)	44.3

The largest garnet phase content, in the 80–82% range, is observed for the MP samples sintered with a Ba_2O_3 flux content in the 2.5–5 at.% range and the activator concentration in the 1–2.5% range. The most optimal condition is the sintering with a flux content of 2.5 wt.% B_2O_3 and a Ce^{3+} concentration of 2.5 at.%, enabling 82% garnet content in the MP sample (Table 1).

Some ways of improving the PLQY were investigated. For instance, an efficiency of more than 71% was achieved by the synthesis of CYMSSG:Ce in pellets by a two-step synthesis process. This was a case in which only 68% of the main phase was detected by XRD analysis.

4. Luminescent and Photoconversion Properties of CYMSSG:Ce MP Samples

For characterization of the optical properties of the CYMSSG:Ce MPs under study, the cathodoluminescence (CL), photoluminescence emission (PE) and excitation spectra (PLE), PL decay kinetics, and PLQY and photoconversion spectra (PC) measurements were used. The CL spectra were investigated using the e-beam from a scanning electron microscope SEM JEOL JSM-820 (JEOL, Warsaw, Poland) additionally equipped with a Stellar Net spectrometer with a TE-cooled CCD detector working in the 200–1200 nm range. PL and PLE spectra and PL decay kinetics were measured using an FS-5 spectrometer (Edinburgh Instruments, Livingston, UK). An EPL-450 picosecond pulsed diode laser was used to measure of the decay kinetics, and the typical average power of this laser is 0.15 mW (Edinburgh Instruments). The PC spectra and PLQY measurements were performed using a fiber-optic spectrophotometer AvaSpec-ULS 2048-LTEC (Avantes, Apeldoorn, The Netherlands), and an integrating sphere AvaSphere-50-IRRAD. The photoconverter (pc) prepared from CYMSSG:Ce MP films of different thicknesses was excited by the blue LED at a wavelength of $\lambda = 450$ nm. All luminescence measurements were performed at room temperature (RT).

4.1. Cathodoluminescence Spectra

The normalized CL spectra of the CYMSSG:Ce MPs samples sintered with different amounts of B_2O_3 flux and different concentrations of Ce^{3+} ions are shown in Figure 4a,b, respectively. The dominant luminescence band with a peak in the 550–555 nm range in all MP CYMSSG:Ce samples corresponds to the $5d^1 \rightarrow 4f$ ($^2F_{5/2,7/2}$) transitions of Ce^{3+} in these garnet compounds. The position of the Ce^{3+} band is slightly red-shifted from 551 to 555 nm in the MP samples with an increase of the flux contents from 1 wt.% to 5 wt.% (Figure 4a) and Ce^{3+} content from 1 to 5% (Figure 4b).

Apart from the luminescence of the Ce^{3+} ions in the garnet structure in the visible range, the other emission bands in the UV range peaked in the 380–392 nm range are also observed in the CL spectra for the CYMSSG:Ce MPs. Furthermore, the lowest UV luminescence efficiency is observed in the CL spectra of the CYMSSG:Ce MP sample sintered with flux and activator contents of 2.5 wt.% and 5 at.%, respectively (Figure 4b).

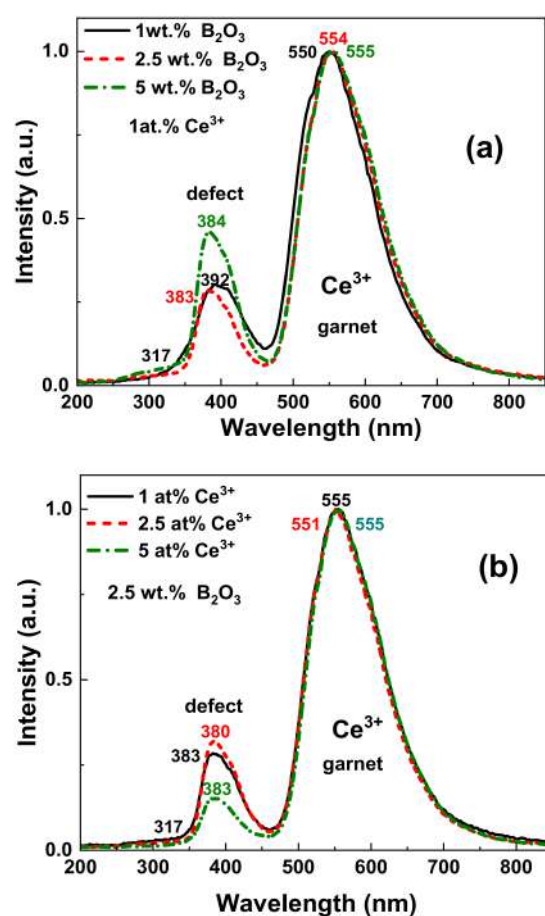


Figure 4. Normalized CL spectra of CYMSSG:Ce MPs sintered with different amounts of B_2O_3 flux (a) and different concentrations of Ce^{3+} ions (b).

It is important to note here that the low intensity bands in the UV range of Ca^{2+} - Mg^{2+} - Si^{4+} -based garnets usually are assigned to defect luminescence [26,27]. According to the authors [26,27], the presence of a high concentration of oxygen vacancies in these garnets is expected due to possible deviations in the concentration of heterovalent Ca^{2+} , Mg^{2+} , and Si^{4+} cations and the demands for local charge compensation. For this reason, the bands peaked at 317 nm and the 380–392 nm range may correspond to the luminescence of the F^+ and F centers (single- and double-charged oxygen vacancies, respectively) in the CYMSSG host [27,28]. However, it is also worth mentioning here that, due to the relatively large contents of the secondary phases in the tested MP samples, the luminescence spectra in the UV range may also partly correspond to the Ce^{3+} luminescence in these compounds. However, a visible correlation between the contents of the secondary phases and the intensity of the UV luminescence was not observed for the tested CYMSSG:Ce MP samples.

4.2. PL and PLE Spectra

The PL spectra of the CYMSSG:Ce (1 at.%) MPs (Figure 5a) sintered with different B_2O_3 flux amounts show wide bands peaked in the 565–575 nm range, which corresponds to the Ce^{3+} radiation transitions from the lowest $5d^1$ level of the excited state to the $4f(^2F_{5/2,7/2})$ levels of the ground state. Increasing the concentration of B_2O_3 leads to a shift in the emission spectra of the Ce^{3+} ions to the long-wavelength spectral range (Figure 5a) [11,27–29].

The PLE spectra of these MP samples (Figure 5b) show several bands in the 250–550 nm region. The main band E_1 peaked in the 460–465 nm range is explained by the absorption of the allowed transitions from the $4f$ ground state to the lowest $5d^1$ levels of the Ce^{3+} ions. Moreover, two MP samples, synthesized with a higher concentration of boron oxide, have a E_2 band peaked at 356 nm, which also corresponds to the $4f(5d^2)$ excitation band of the Ce^{3+}

ions. The low intensity of the E_2 band in comparison with conventional YAG:Ce garnets (Figure 4b) is characteristic of Ca^{2+} (or Mg^{2+})- Si^{4+} -based garnets (see also [27,30,31]).

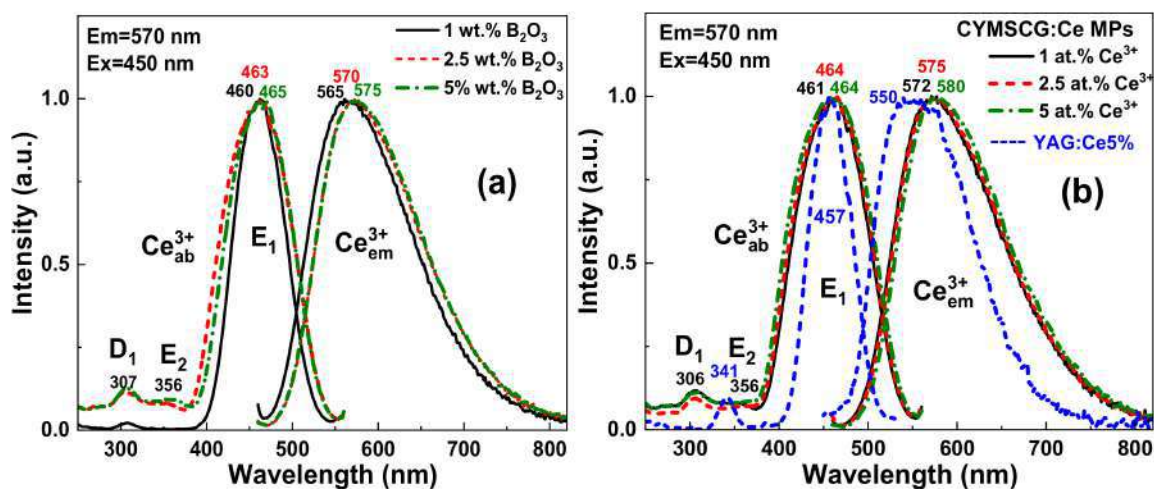


Figure 5. PL spectra and PLE spectra of CYMSSG:Ce (1 at.%) MPs sintered with different amounts of B_2O_3 flux (a) and PL spectra and PLE spectra of CYMSSG:Ce MP samples with different concentrations of Ce^{3+} ions sintered with a B_2O_3 flux content of 2.5 wt.% (b).

Figure 5b demonstrates the PL and PLE spectra of the CYMSSG:Ce MPs with variable Ce^{3+} ion concentrations in the range 1–5 at.% synthesized with a flux B_2O_3 concentration of 2.5 wt.%. Increasing the Ce^{3+} concentration in these MP samples leads to the increases of the crystal field strength in the dodecahedron position of the garnet compounds, which results in a long-wavelength shift in the Ce^{3+} emission spectrum (Figure 5b). Moreover, the PL emission and excitation spectra of all CYMSSG:Ce MP samples is considerably broadened in comparison with the conventional CSSG:Ce and YAG:Ce phosphors (Figure 5b). Namely, the PL emission spectrum in CYMSSG:Ce MPs shifted with respect to YAG:Ce spectrum by more than 40 nm into the red range, extending up to even 800 nm. The respective FWHM of the Ce^{3+} emission bands increases from 124.5 nm in the YAG:Ce 5% to 139.5 nm in the CYMSSG:Ce5% MPs. The FWHM of the main Ce^{3+} excitation band in the PLE excitation spectrum of the CYMSSG:Ce MPs is also significantly larger in the CYMSSG:Ce5% MPs (104 nm) in comparison with the YAG:Ce5% sample (56 nm) (Figure 5b). Such results, without any doubt, indicate the existence of different Ce^{3+} centers in the CYMSSG garnets (see also [27,30–33] for details).

It is also worth noting that the PLE spectra of these MP samples (Figure 5a) also contain a band in the UV range peaked at 308 nm, which can correspond to the excitation of the defect luminescence in the CYMSSG host in the bands peaked in the 380–393 nm range (Figure 2). Such emission bands are overlapped with the E_1 and E_2 excitation bands of the Ce^{3+} luminescence in the garnets. That results in the excitation of the Ce^{3+} luminescence via the luminescence of the defects centers. Thus, energy transfer between the defect and Ce^{3+} centers is observed in all CYMSSG:Ce MP samples under study.

Figure 6 shows the PL decay kinetics of the MP CSSG:Ce samples with different concentrations of B_2O_3 flux (a) and Ce^{3+} activator (b). The approximation parameters of the respective decay curves are given in Tables 2 and 3, respectively.

Similarly to other Ca^{2+} - Si^{4+} -based garnets [26,32,33], the decay kinetics of the Ce^{3+} emission in $\text{Ca}_2\text{YMgScSi}_3\text{O}_{12}:\text{Ce}$ MPs is non-exponential. For this reason, the three-exponential fit of the decay curves was used for the quantitative description of the luminescence timing properties (Tables 1 and 2). Although such a three-exponential approximation does not describe the luminescence decay behavior correctly at quenching due to the energy transfer, the decay time values can be considered as estimations of the luminescence decay times of the respective Ce^{3+} multicenters.

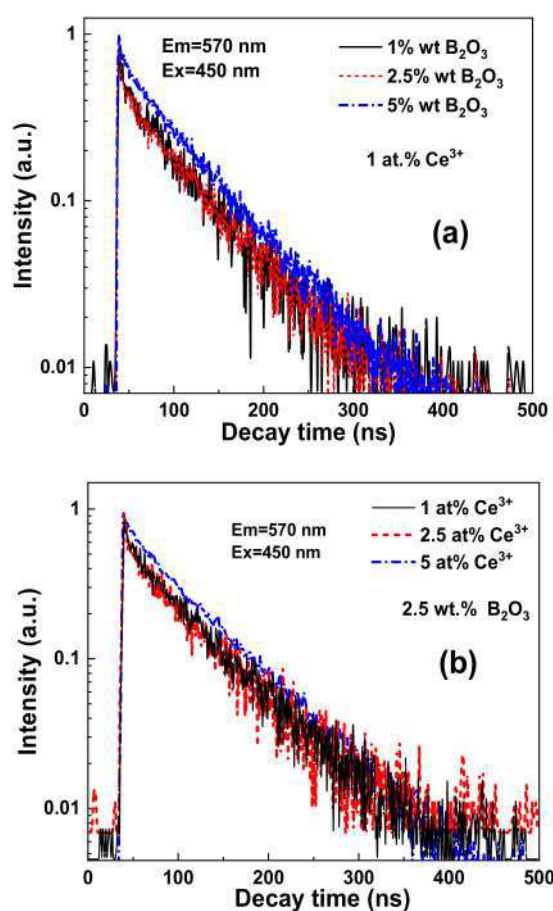


Figure 6. PL decay kinetics at RT recorded at 570 nm under blue light excitation (450 nm) in MPs sintered with different amounts of B₂O₃ flux (a) and different concentrations of Ce³⁺ ions (b).

Table 2. Parameters of three exponential approximations of the decay curves presented in Figure 6a (Em = 570 nm, Ex = 450 nm).

x% wag. B ₂ O ₃	t ₁ , ns	A ₁	t ₂ , ns	A ₂	t ₃ , ns	A ₃
1	4.44	21.59	42.1	21.58	66.88	21.78
2.5	5.31	8.12	54.5	29.46	68.17	29.75
5	3.93	53.17	47.9	48.64	58.62	55.74

Table 3. Parameters of three exponential approximations of the decay curves presented in Figure 6b (Em = 570 nm, Ex = 450 nm).

x% at. Ce ³⁺	t ₁ , ns	A ₁	t ₂ , ns	A ₂	t ₃ , ns	A ₃
1	8.49	26.79	51.65	65.93	80.18	57.11
2.5	6.90	26.87	72.03	34.59	73.13	32.18
5	11.54	29.05	72.79	33.99	79.74	42.03

5. Ce³⁺ Multicenter Formation in CYMSSG:Ce Phosphor

The RT PL emission spectra of the CYMSSG:5%Ce MPs are shown in Figure 7a under excitation in the characteristic PLE bands (Figure 7b). The PL spectra of these samples show the intensive luminescence in the form of wide bands peaked in the green range related to the 5d¹ → 4f(²F_{5/2,7/2}) transitions of the Ce³⁺ ions. Moreover, by increasing the excitation wavelength from 420 to 480 nm, the PL spectra of the CYMSSG:Ce MPs are significantly red-shifted from 564 to 587 nm and slightly narrowed (Figure 7a). (Figure 7a, curves 1–9, respectively). Furthermore, the shift in the main maxima of the PL spectra of the

CYMSSG:Ce MPs and the intensity in the peak positions occurs non-monotonically with the increasing excitation wavelength (Figure 8a,b) in comparison with the similar dependencies for the YAG:Ce SCF sample (not shown in Figure 8). Behavior such as that shown in the PL emission spectra indicates the Ce^{3+} multicenter formation in the CYMSSG:Ce garnet.

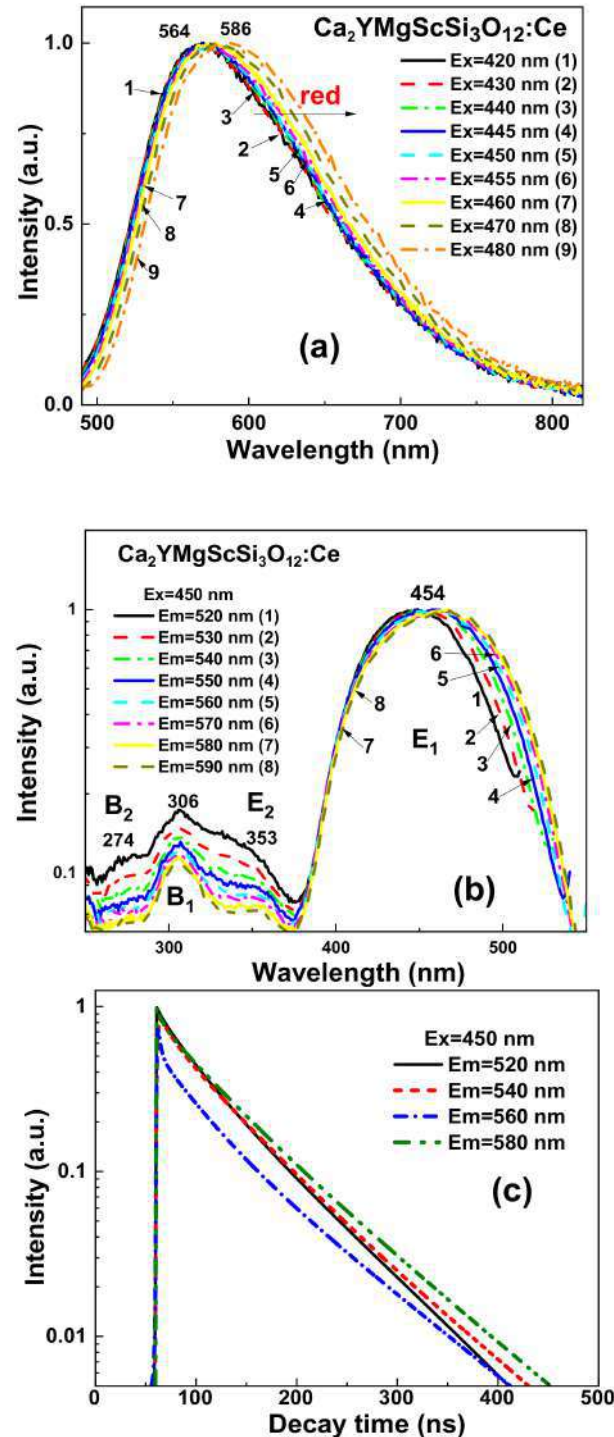


Figure 7. Detailed luminescent properties of $\text{Ca}_2\text{YMgScSi}_3\text{O}_{12}:\text{Ce}5\%$ MPs at RT. Emission (a) and excitation (b) recorded in different parts of the respective spectra. PL decay kinetics (c) at RT recorded under blue light (450 nm) excitation in different parts of the Ce^{3+} emission band.

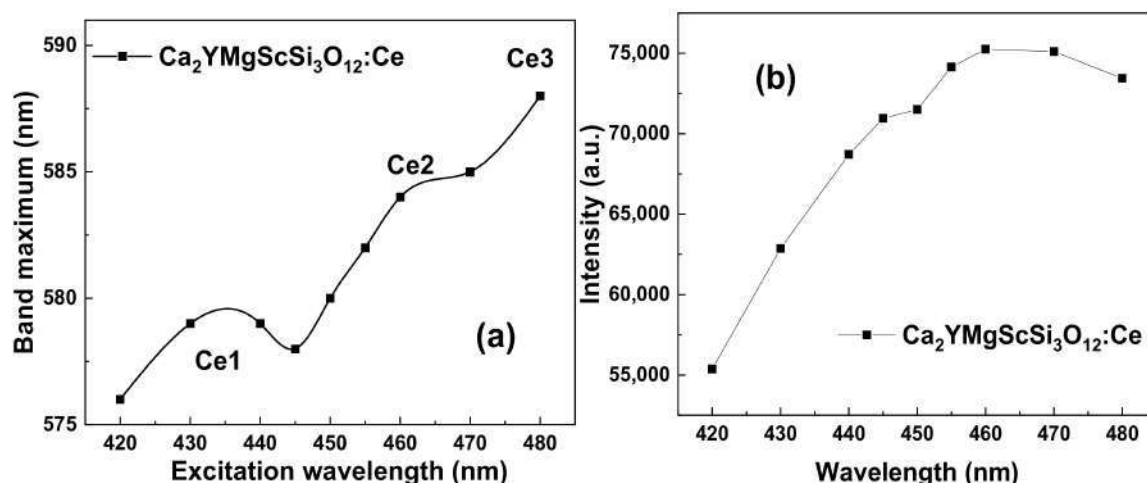


Figure 8. Dependencies of the maxima (a) and intensities (b) in the peak positions of Ce^{3+} emission bands on excitation wavelength in $\text{Ca}_2\text{YMgScSi}_3\text{O}_{12}:\text{Ce}$ MPs (see Figure 7a,b).

The normalized excitation spectra of the Ce^{3+} luminescence in the $\text{Ca}_2\text{YMgScSi}_3\text{O}_{12}:\text{Ce}$ MP samples are shown in Figure 7b. In these spectra, the most intensive excitation bands, E_1 and E_2 , peaked in the 454 nm (E_1) and 353 nm (E_2) ranges, are attributed to the intrinsic transitions from the $4f^2(F_{5/2})$ level of the ground state to the $5d$ (E_2) excited level of the Ce^{3+} ions (Table 4). The excitation bands peaked at 306 nm (B_1 band) and 274 nm (B_2 band) are also observed in the excitation spectra of the $\text{Ca}_2\text{YMgScSi}_3\text{O}_{12}:\text{Ce}$ MPs (Figure 7a,b). These excitation bands are not related to the intrinsic transitions of the Ce^{3+} ions and probably correspond to the Ce^{3+} luminescence excitation by the emission of the defect centers or the emission of flux-related impurities [30,31].

Table 4. Spectral characteristics of the different Ce^{3+} multcenters in $\text{Ca}_2\text{YMgScSi}_3\text{O}_{12}:\text{Ce}$ garnet.

Type of Centers	Maximum of Dominant Emission Band, nm	Position of E_2 and E_1 Excitation Bands, nm	$\Delta E = E_2 - E_1$, eV	Stokes Shift, eV
Ce1	569	349;446	0.773	0.601
Ce2	573	358;458	0.756	0.542
Ce3	586	354;461	0.813	0.574

The decay kinetics of the Ce^{3+} luminescence in the $\text{Ca}_2\text{YMgScSi}_3\text{O}_{12}:\text{Ce}$ MPs registered at 520–580 nm under excitation at 450 nm are shown in Figure 7c. Due to the strong non-exponentiality of the decay kinetics, the three-exponential fit of the decay curves was used for the quantitative description of the luminescence timing properties (Table 5).

Table 5. Parameters of three exponential approximations of the decay curves presented in Figure 7c.

Emission Wavelength	t_1 , ns	A_1	t_2 , ns	A_2	t_3 , ns	A_3
520 nm	6.38	0.05	36.32	0.39	77.64	0.48
540 nm	15.47	0.12	66.76	0.61	79.04	0.51
560 nm	2.54	0.85	37.34	0.29	90.71	0.25
580 nm	5.31	0.14	44.72	0.34	85.19	0.49

Behavior such as that shown in the decay curves of the $\text{Ca}_2\text{YMgScSi}_3\text{O}_{12}:\text{Ce}$ MPs can also indicate possible energy transfer from high-energy to low-energy Ce^{3+} emitting centers in these garnets [32,33]. The different decay times in the $\text{Ca}_3\text{Sc}_2\text{Si}_3\text{O}_{12}:\text{Ce}$ SCF can correspond to the different Ce^{3+} centers in the dodecahedral positions of the garnet lattice with various local surroundings by oxygen and cations (Sc^{3+} and Si^{4+} ions in the octahedral

and tetrahedral positions, respectively, and Ca^{2+} and Y^{3+} cations in the dodecahedral positions of the garnet host; Figure 9).

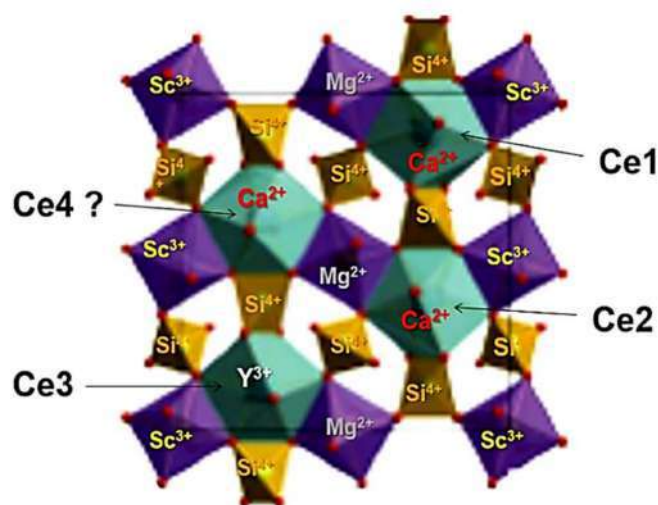


Figure 9. Visualization of possible Ce^{3+} multicenter formation in the structure of $\text{Ca}_2\text{YMgScSi}_3\text{O}_{12}:\text{Ce}$ garnet.

6. WLED Prototype Creation

To demonstrate the application possibility of the development of CYMSSG:Ce phosphor, WLED prototypes were fabricated by coating a blue LED with an emission wavelength of 450 nm with several films containing CYMSSG:Ce phosphor embedded in epoxy resin (Figure 10a). PC measurements of the WLED prototypes were performed after each successive PC layer of a thickness of approximately 100–120 μm . The emission spectra of these WLEDs are quite broad and cover the entire visible range from 400 to 780 nm. The emission spectra of the WLED prototypes also show a significant decrease in the intensity of the blue component and a respective continuous increase in the intensity of the yellow emission by increasing the total film thickness (Figure 10a). As can be seen from Figure 10b, the color coordinates move to the diagram's center by increasing the total thickness of the PC film. Finally, the WLED prototypes, based on six films of CYMSSG:Ce MP PC, give quite cold white emissions with the correlated color coordinates (CCC) $x = 0.315$; $y = 0.31$ and a correlated color temperature (CCT) of 6930 K. Furthermore, as the thickness of the photoconverter film increases, the color coordinates move to the center of the diagram, including the warm white color pattern. However, these trends of the photoconverting properties of the developed WLED prototypes are quite limited by the conversion efficiency of the CYMSSG:Ce MP phosphor with a Ce^{3+} concentration of 1 at.%. To obtain a precise tuning of the photoconversion properties (CCC and CCT), the CYMSSG:Ce MP phosphor with Ce^{3+} concentration above 1% can be used as well.

The fabricated device with bright-light characteristics demonstrates that the WLEDs based on the CYMSSG:Ce MPs are very promising and can be applied to lighting systems (Figure 10a, insert). The CIE chromaticity coordinates of the prototype WLEDs are shown in Table 6.

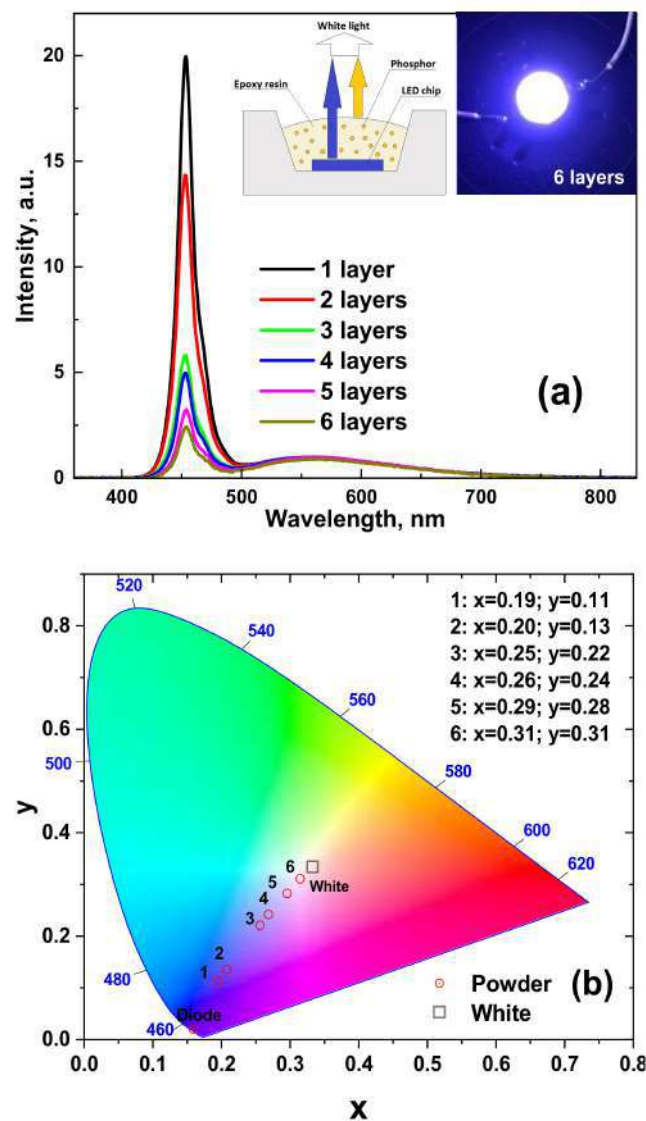


Figure 10. Emission spectrum (a) and chromaticity diagram (b) of a WLED lamp fabricated on the base of 450 nm LED chip and CYMSSG:1%Ce phosphor.

Table 6. CIE chromaticity coordinates of a WLED lamp fabricated on the base of 450 nm LED chip and CYMSSG:1%Ce phosphor.

Samples	Unpolished Samples (h = 1 mm)	
	CIE Coordinates	
	x	y
1 layer	0.195	0.112
2 layers	0.208	0.134
3 layers	0.257	0.220
4 layers	0.279	0.241
5 layers	0.296	0.282
6 layers	0.315	0.31

7. Conclusions

Microcrystalline powder (MP) samples of $\text{Ca}_2\text{YMgScSi}_3\text{O}_{12}:\text{Ce}$ garnet with Ce^{3+} concentrations in the range of 1–5 at.% were obtained using solid-state synthesis by adding B_2O_3 flux in the 1–5 wt. % concentration of the total charge content. To determine the

luminescent properties of the CYMSSG:Ce MPs, the cathodoluminescence (CL) spectra, photoluminescence (PL) emission and excitation spectra, PL decay kinetics, and the PL quantum yields (PL QY) were measured.

The obtained results confirm the Ce^{3+} multicenter formation in the MP of the CYMSSG:Ce garnet. It is mainly caused by the location of the Ce^{3+} ions in the dodecahedral positions of the Ca^{2+} and Y^{3+} cations, and the different local surroundings of these centers. Namely, Ce^{3+} multicenters such as those in the mentioned dodecahedral positions of the garnet host possess additional local asymmetry and crystal field strength due to inhomogeneity in the local environment of these positions during the substitutions at the octahedral sites by heterovalent Mg^{2+} and Sc^{3+} ions and the at the tetrahedral sites by Si^{4+} ions. Based on the results of the optical investigations, the luminescent characteristics of different Ce^{3+} -based multicenters were estimated.

The application potential of the developed CYMSSG:Ce MP phosphor was demonstrated. Planar WLED prototypes were fabricated by coating GaN 450 nm blue LED chips with several 100–120 μm thick layers of CYMSSG:Ce MP phosphor mixed with epoxy resin. Furthermore, the WLED prototypes, based on five CYMSSG:Ce MP photoconverters, give emissions close to white light with the coordinates $x = 0.315$; $y = 0.31$ and a color temperature of 6930 K.

Author Contributions: A.S. collected and analyzed the structural and optical properties of MPs and participated in writing and preparation of the paper; A.M. participated in preparation of the prototypes of WLED and measured their photoconversion properties; S.W.-L. performed and analyzed the cathodoluminescence measurements; Y.V. and A.O. performed the synthesis of MPs and taking part in XRD investigations; T.Z. participated in measurements of PL of PL decay kinetics of MP samples and analyzed them; J.E. performed and analyzed the XRD measurements; C.J.B. and M.B. managed the MP preparation and XRD investigations; Y.Z. analyzed the whole experimental materials and participated in writing and preparation of the paper. All authors have read and agreed to the published version of the manuscript.

Funding: The work was performed in the framework of the Polish NCN 2017/25/B/ST8/02932 project and partly in the frame of NCN 2019/33/B/ST3/00406 project.

Institutional Review Board Statement: Not applicable.

Informed Consent Statement: Not applicable.

Data Availability Statement: Not applicable.

Conflicts of Interest: The authors declare no conflict of interest.

References

- Schubert, E.F. *Light-Emitting Diodes*, 2nd ed.; Cambridge University Press: New York, NY, USA, 2006.
- Withnall, R.; Silver, J. Luminescence of phosphors. In *Handbook of Visual Display Technology*; Chen, J., Cranton, W., Fihn, M., Eds.; Springer: Berlin/Heidelberg, Germany, 2012.
- CIE. *Commission Internationale de l'Eclairage Proceedings*; Cambridge University Press: Cambridge, UK, 1995.
- Bass, M. *Handbook of Optics*; R.R. Donnelly & Sons Company: Chicago, IL, USA, 1995.
- Jargus, J.; Vitasek, J.; Nedoma, J.; Vasinek, V.; Martinek, R. Effect of Selected Luminescent Layers on CCT, CRI, and Response Times. *Materials* **2019**, *12*, 2095. [[CrossRef](#)] [[PubMed](#)]
- Li, X.; Jiang, Y.; Li, J.; Shi, Z.; Zhu, G.; Wang, Y. Integrated photonics chip with InGaN/GaN light-emitting diode and bended waveguide for visible-light communications. *Opt. Laser Technol.* **2019**, *114*, 103–109. [[CrossRef](#)]
- Xu, Y.; Chen, Z.; Gong, Z.; Xia, Z.; Yuan, T.; Gu, Z.; Zhao, W.; Chen, J. Hybrid modulation scheme for Visible Light Communication using CMOS camera. *Opt. Commun.* **2019**, *440*, 89–94. [[CrossRef](#)]
- Yan, D.; Mao, X.; Xie, S.; Cong, J.; Chen, H. Design Fully Integrated Driver Circuit for Phosphorescent White Light-Emitting-Diode High Speed Real-Time Wireless Communication. *IEEE Photonics J.* **2019**, *11*, 1–10. [[CrossRef](#)]
- Song, Y.H.; Ji, E.K.; Jeong, B.W.; Jung, M.K.; Kim, E.Y.; Yoon, D.H. High power laser-driven ceramic phosphor plate for outstanding efficient white light conversion in application of automotive lighting. *Sci. Rep.* **2016**, *6*, 31206. [[CrossRef](#)]
- Steigerwald, D.A.; Bhat, J.C.; Collins, D.; Fletcher, R.M.; Holcomb, M.O.; Ludowise, M.J.; Martin, P.S.; Rudaz, S.L. Illumination with solid state lighting technology. *IEEE J. Sel. Top. Quantum Electron.* **2002**, *8*, 310–320. [[CrossRef](#)]
- Levchuk, I.; Osvet, A.; Brabec, C.J.; Batentschuk, M.; Shakhno, A.; Zorenko, T.; Zorenko, Y. Micro-powder $\text{Ca}_3\text{Sc}_2\text{Si}_3\text{O}_{12}:\text{Ce}$ silicate garnets as efficient light converters for WLEDs. *Opt. Mater.* **2020**, *107*, 109978. [[CrossRef](#)]

12. Shimomura, Y.; Honma, T.; Shigeiwa, M.; Akai, T.; Okamoto, K.; Kijima, N. Photoluminescence and Crystal Structure of Green-Emitting $\text{Ca}_3\text{Sc}_2\text{Si}_3\text{O}_{12}:\text{Ce}^{3+}$ Phosphor for White Light Emitting Diodes. *J. Electrochem. Soc.* **2007**, *154*, J35. [\[CrossRef\]](#)
13. Katelnikovas, A.; Bareika, T.; Vitta, P.; Jüstel, T.; Winkler, H.; Kareiva, A.; Žukauskas, A.; Tamulaitis, G. $\text{Y}_{3-x}\text{Mg}_2\text{AlSi}_2\text{O}_{12}$: Phosphors—Prospective for warm-white light emitting diodes. *Opt. Mater.* **2010**, *32*, 1261–1265. [\[CrossRef\]](#)
14. Zhong, J.; Zhuang, W.; Xing, X.; Liu, R.; Li, Y.; Liu, Y.; Hu, Y. Synthesis, Crystal Structures, and Photoluminescence Properties of Ce^{3+} -Doped $\text{Ca}_2\text{LaZr}_2\text{Ga}_3\text{O}_{12}$: New Garnet Green-Emitting Phosphors for White LEDs. *J. Phys. Chem. C* **2015**, *119*, 5562–5569. [\[CrossRef\]](#)
15. Li, G.; Tian, Y.; Zhao, Y.; Lin, J. Recent progress in luminescence tuning of Ce^{3+} and Eu^{3+} -activated phosphors for pc-WLEDs. *Chem. Soc. Rev.* **2015**, *44*, 8688–8713. [\[CrossRef\]](#) [\[PubMed\]](#)
16. Shang, M.; Fan, J.; Lian, H.; Zhang, Y.; Geng, D.; Lin, J. A Double Substitution of Mg^{2+} – Si^{4+} / Ge^{4+} for $\text{Al}(1)3+$ – $\text{Al}(2)3+$ in Ce^{3+} -Doped Garnet Phosphor for White LEDs. *Inorg. Chem.* **2014**, *53*, 7748–7755. [\[CrossRef\]](#)
17. Katelnikovas, A.; Bettentrup, H.; Uhlich, D.; Sakirzanovas, S.; Jüstel, T.; Kareiva, A. Synthesis and optical properties of Ce^{3+} -doped $\text{Y}_3\text{Mg}_2\text{AlSi}_2\text{O}_{12}$ phosphors. *J. Lumin.* **2009**, *129*, 1356–1361. [\[CrossRef\]](#)
18. Kishore, M.S.; Kumar, N.P.; Chandran, R.G.; Setlur, A.A. Solid Solution Formation and Ce^{3+} Luminescence in Silicate Garnets. *Electrochem. Solid-State Lett.* **2010**, *13*, J77. [\[CrossRef\]](#)
19. Feng, G.; Jiang, W.; Liu, J.; Li, C.; Zhang, Q.; Miao, L.; Wu, Q. Synthesis and luminescence properties of Al_2O_3 @YAG: Ce core-shell yellow phosphor for white LED application. *Ceram. Int.* **2018**, *44*, 8435–8439. [\[CrossRef\]](#)
20. Chen, L.-C.; Tseng, Z.-L.; Chang, W.-W.; Lin, Y.W. Warm white light-emitting diodes using organic–inorganic halide perovskite materials coated YAG: Ce^{3+} phosphors. *Ceram. Int.* **2018**, *44*, 3868–3872. [\[CrossRef\]](#)
21. Gu, G.; Xiang, W.; Yang, C.; Fan, W.; Lv, Y.; Zhang, Z.; Liang, X. A Novel Single-Component White-Emitting Tb and Mn Co-Doped Large-Sized $\text{Y}_3\text{Al}_5\text{O}_{12}:\text{Ce}^{3+}$ Single Crystal for White LED. *Sci. Adv. Mater.* **2016**, *8*, 1354–1360. [\[CrossRef\]](#)
22. Du, Y.; Shao, C.; Dong, Y.; Yang, Q. Electroluminescent properties of WLEDs with the structures of Ce:YAG single crystal/blue chip and $\text{Sr}_2\text{Si}_5\text{N}_8:\text{Eu}^{2+}$ /Ce:YAG single crystal/blue chip. *J. Disp. Technol.* **2016**, *12*, 323–327. [\[CrossRef\]](#)
23. Zhao, B.Y.; Liang, X.; Chen, Z.; Xie, C.; Luo, L.; Zhang, Z.; Xiang, W. Studies on optical properties and Ce concentration of Ce:YAG single crystal for WLEDs. *Chem. J. Chin. Univ.* **2014**, *25*, 230–236. [\[CrossRef\]](#)
24. Pan, Z.; Xu, Y.; Hu, Q.; Li, W.; Zhou, H.; Zheng, Y. Combination cation substitution tuning of yellow-orange emitting phosphor $\text{Mg}_2\text{Y}_2\text{Al}_2\text{Si}_2\text{O}_{12}:\text{Ce}^{3+}$. *RSC Adv.* **2015**, *5*, 9489–9496. [\[CrossRef\]](#)
25. Tyagi, M.; Meng, F.; Koschan, M.; Donald, S.B.; Rothfuss, H.; Melcher, C.L. Effect of codoping on scintillation and optical properties of a Ce-doped $\text{Gd}_3\text{Ga}_3\text{Al}_2\text{O}_{12}$ scintillator. *J. Phys. D Appl. Phys.* **2013**, *46*, 475302. [\[CrossRef\]](#)
26. Melcher, C.L.; Koschan, M.; Zhuravleva, M.; Wu, Y.; Rothfuss, H.; Meng, F.; Tyagi, M.; Donald, S.; Yang, K.; Hayward, J.P.; et al. Scintillator Design via Codoping. In Proceedings of International Symposium on Radiation Detectors and Their Uses (ISR2016). *J. Phys. Soc. Jpn.* **2016**, *11*, 020001. [\[CrossRef\]](#)
27. Gorbenko, V.; Zorenko, T.; Paprocki, K.; Iskalyeva, A.; Fedorov, A.; Schröppel, F.; Levchuk, I.; Osvet, A.; Batentschuk, M.; Zorenko, Y. Epitaxial growth of single crystalline film phosphors based on the Ce^{3+} -doped $\text{Ca}_2\text{YMgScSi}_3\text{O}_{12}$ garnet. *CrystEngComm* **2017**, *19*, 3689–3697. [\[CrossRef\]](#)
28. Gorbenko, V.; Zorenko, T.; Witkiewicz, S.; Paprocki, K.; Iskalyeva, A.; Kaczmarek, A.M.; Van Deun, R.; Khaidukov, M.N.; Batentschuk, M.; Zorenko, Y. Luminescence of Ce^{3+} multicenters in Ca^{2+} - Mg^{2+} - Si^{4+} based garnet phosphors. *J. Lumin.* **2018**, *199*, 245–250. [\[CrossRef\]](#)
29. Gorbenko, V.; Zorenko, T.; Pawlowski, P.; Iskalyeva, A.; Paprocki, K.; Suchocki, A.; Zhydashchuk, Ya.; Fedorov, A.; Khaidukov, N.; Van Deun, R.; Schröppel, F.; et al. Luminescent and scintillation properties of Ce^{3+} doped $\text{Ca}_2\text{RMgScSi}_3\text{O}_{12}$ (R = Y, Lu) single crystalline films. *J. Lumin.* **2018**, *195*, 362–370. [\[CrossRef\]](#)
30. Gorbenko, V.; Zorenko, T.; Witkiewicz-Lukaszek, S.; Shakhno, A.; Osvet, A.; Batentschuk, M.; Fedorov, A.; Zorenko, Y. Crystalization and Investigation of the Structural and Optical Properties of Ce^{3+} -Doped $\text{Y}_{3-x}\text{Ca}_x\text{Al}_{5-y}\text{Si}_y\text{O}_{12}$ Single Crystalline Film Phosphors. *Crystals* **2021**, *11*, 788. [\[CrossRef\]](#)
31. Khaidukov, N.M.; Makhov, V.N.; Zhang, Q.; Shi, R.; Liang, H. Extended broadband luminescence of dodecahedral multisite Ce^{3+} ions in garnets $\{\text{Y}_3\}[\text{MgA}](\text{BAlSi})\text{O}_{12}$ (A = Sc, Ga, Al; B = Ga, Al). *Dye Pigment.* **2017**, *142*, 524–529. [\[CrossRef\]](#)
32. Khaidukov, N.M.; Zhidkova, I.A.; Kirikova, N.Y.; Makhov, V.N.; Zhang, Q.; Shi, R.; Liang, H. Mechanism for bifurcation of broadband luminescence spectra from Ce^{3+} ions at dodecahedral sites in garnets $\{\text{CaY}_2\}[\text{M}_2](\text{Al}_2\text{Si})\text{O}_{12}$ (M = Al, Ga, Sc). *Dye Pigment.* **2018**, *148*, 189–195. [\[CrossRef\]](#)
33. Setlur, A.A.; Heward, W.J.; Gao, Y.; Srivastava, A.M.; Chandran, R.G.; Shankar, M.V. Crystal Chemistry and Luminescence of Ce^{3+} -Doped $\text{Lu}_2\text{CaMg}_2(\text{Si,Ge})_3\text{O}_{12}$ and Its Use in LED Based Lighting. *Chem. Mater.* **2006**, *18*, 3314–3322. [\[CrossRef\]](#)



Luminescence and photoconversion properties of micro-powder phosphors based on the Ce^{3+} and Mn^{2+} doped $\text{Ca}_2\text{YMgScSi}_3\text{O}_{12}$ silicate garnets

A. Shakhno^{*}, S. Witkiewicz-Łukaszek, V. Gorbenko, T. Zorenko, Yu Zorenko^{**}

Institute of Physics, Kazimierz Wielki University in Bydgoszcz, 85090, Bydgoszcz, Poland

ARTICLE INFO

Keywords:

WLED
Phosphor converters
 Ca^{2+} , Mg^{2+} , Si^{4+} -based garnets
Micropowders
Solid-state synthesis
Luminescence

ABSTRACT

This work is dedicated to study the synthesis processes and luminescence properties of micro-crystalline powder phosphors of Ce^{3+} and Mn^{2+} doped $\text{Ca}_2\text{YMgScSi}_3\text{O}_{12}$ garnets (CYMSSG:Ce and CYMSSG:Ce,Mn). The photoluminescence emission spectra and decay kinetics confirm the formation of Ce^{3+} multicenters in the CYMSSG:Ce powder phosphor due to local inhomogeneity of the different dodecahedral positions and presence of the energy transfer between high-energy and low energy Ce^{3+} emission centers in this garnet. The effective Ce^{3+} to Mn^{2+} energy transfer process is observed in CYMSSG:Ce, Mn phosphors resulting in the redshift of the emission spectra in comparison with CYMSSG:Ce counterpart. We have shown that CYMSSG:Ce and CYMSSG:Ce, Mn powder phosphors can be used as an efficient photoconverter (PC) for creation of the high-power white LEDs (WLEDs). The prototypes of PC-WLEDs, based on 450 nm emitting blue LED and planar layers of CYMSSG:Ce and CYMSSG:Ce, Mn microcrystalline powder phosphors, embedded in the epoxy resin, were prepared and their photoconversion properties were investigated as well.

1. Introduction

The research of WLEDs is today one of the most promising fields in artificial lighting technology due to their exceptional qualities such as extended life, high efficiency, and environmental friendliness when compared to incandescent bulbs. Moreover, they have a good color rendering index (CRI) and an effortlessly movable correlated color temperature (CCT). These WLEDs are widely used in the car industry, lighting, sensor innovation and therapeutic technique. Currently, the conventional WLED structure is a blue LED chip combined with a yellow light-emitting YAG:Ce photoconverter (PC) [1]. Although YAG:Ce garnet has thermal stability of the luminescence at high temperatures, an alternative is still being sought today due to the lack of red-light emission, especially for headlights.

Among all the Ca-Si based garnet phosphors, the $\text{Ca}_3\text{Sc}_2\text{Si}_3\text{O}_{12}$ (CSSG) garnet is the well-known analog that can be doped with different types of rare earth and/or transition metals ions [2–4]. The simultaneous localization of Ce^{3+} ions and other rare-earth and transition metal ions in different valence states in the dodecahedral sites allows for the

generation of a large new class of silicate-based phosphors garnets. Furthermore, the additional alloying of Y^{3+} - Mg^{2+} pairs in the $\text{Ca}_3\text{Sc}_2\text{Si}_3\text{O}_{12}$:Ce garnet host opens additional possibilities for modifying the luminescence properties and developing the more efficient PC species for WLEDs [3,4]. In particular, such an approach gives rise to the proper redshift of the emission spectrum and better color characteristics of PC-WLEDs as compared with the conventional YAG:Ce PCs [3–5].

However, since the white light obtained in this way has a low proportion of red light, the CRI is low and the CCT is high (cold white light). To eliminate these drawbacks, the yellow phosphorescent components (YAG:Ce, etc.) are mixed with the red phosphorescent components such as $\text{CaAlSiN}_3\text{:Eu}^{2+}$, $(\text{Sr,Ca})\text{Si:Eu}^{2+}$, and $(\text{Ba,Sr,Ca})_2\text{Si}_5\text{N}_8\text{:Eu}^{2+}$ [6–8]. However, this method can cause some variation during WLED manufacturing. As a rule, using a single orange or green/red phosphorescent component instead of a mixture of phosphorescent components may help to partially reduce this variation.

Mn^{2+} ions are known to emit the 500–800 nm light depending on the host [9–11,25–29]. In a tetrahedral environment, the luminescence is usually green. In an octahedral structure with a stronger crystal field, the

Given his role as Guest Editor of this journal, Yu Zorenko had no involvement in the peer-review of articles for which he was an author and had no access to information regarding their peer-review. Full responsibility for the peer-review process for this article was delegated to another Editor.

^{*} Corresponding author.

^{**} Corresponding author.

E-mail addresses: annshakhno@gmail.com (A. Shakhno), zorenko@ukw.edu.pl (Y. Zorenko).

<https://doi.org/10.1016/j.omx.2022.100187>

Received 27 February 2022; Received in revised form 3 September 2022; Accepted 4 September 2022

Available online 3 October 2022

2590-1478/© 2022 The Authors. Published by Elsevier B.V. This is an open access article under the CC BY-NC-ND license (<http://creativecommons.org/licenses/by-nc-nd/4.0/>).

luminescence shifts from orange to red. The main drawback of the Mn^{2+} activator is difficulty in blue LED pumping because its d-d absorption transition prohibits parity. For this reason, to use Mn^{2+} as an emitting ion, its emission must be sensitized by the energy transfer (ET) from another ion whose absorption transition is allowed by the selection rule. Ce^{3+} ions have already been proven to be highly effective sensitizing ions for the Mn^{2+} luminescence [12–14]. Keeping in mind that both Ce^{3+} ions produce their luminescence, co-doping one of them with Mn^{2+} and the matrix will probably allow the formation of phosphors whose luminescence covers the spectral range from blue to red.

The paper presents new systematic results of comparative studies of the luminescence properties of silicate garnets microcrystalline powder phosphors $\text{Ca}_2\text{YMgScSi}_3\text{O}_{12}$ (CYMSSG) doped with Ce^{3+} and Mn^{2+} ions, synthesized by conventional solid-state synthesis, which can be used to create efficient WLED converters. Currently, the development of this type of phosphor is an auspicious direction in semiconductor lighting technology, especially given that currently only phosphors based on YAG:Ce crystal or ceramic garnet are available for the production of power WLEDs with excitation of blue LEDs.

2. Synthesis of CYMSSG:Ce micropowder samples and experimental techniques

The microcrystalline powders of Ce^{3+} and Mn^{2+} doped CYMSSG garnets were obtained by the conventional solid-state synthesis with the use of Ba_2O_3 flux in a concentration of 5 wt % of the total charge content. The series of the CYMSSG micropowder samples containing a nominal Ce^{3+} and Mn^{2+} concentration of 1 at. % have been synthesized by taking into account the optimal synthesis conditions under using B_2O_3 flux [24]. The purity of raw materials was 99.9% (CaCO_3 and MnO_2) and 99., 99% (MgO , Y_2O_3 , CeO_2 , Ba_2O_3). The suppliers of raw materials were Sigma-Aldrich (CaCO_3 , MgO), Merk (B_2O_3 , Y_2O_3) and Alfa Aesar (CeO_2 , MnO_2). The thermal treatment of powders was performed in the air atmosphere firstly at 900 °C for 8 h and then at 1350 °C for 24 h. By using the flux in this method of solid-state preparation of phosphors, the morphology of grains can be improved what increases the PL intensity of the material.

The structural properties and cathodoluminescence (CL) spectra of micropowders were measured using a scanning electron microscope SEM JEOL JSM-820, additionally equipped with a spectrometer Stellar Net with a TE-cooled CCD detector working in the 200–1200 nm range. The photoluminescence (PL) emission and excitation spectra as well as the PL decay kinetics were measured using a FS-5 spectrometer (Edinburg Instruments). The luminescence properties of Ce^{3+} - Mn^{2+} doped CYMSSG micropowders were compared with the reference CSSG:Ce micropowder sample as well as with the properties of Ce^{3+} and Mn^{2+} doped single crystalline film counterparts [2,5].

3. Structural properties

The garnets crystallize in a body-centered system with eight formula units per unit cell. The space group is Ia3d. In this structure, the

dodecahedron has A atoms, each surrounded by eight oxygen atoms, forming a polyhedron with a D_2 symmetry point. Each atom in site B is surrounded by six oxygen atoms in octahedral space with a C_{3i} point of symmetry. In the classic garnet structure $\text{A}_3\text{X}_5\text{O}_{12}$, the position of D_2 site A is occupied only by rare-earth ions.

In this work, the CYMSSG host was doped with Ce^{3+} and co-doped with Mn^{2+} . It has already been demonstrated that Ce^{3+} ions replace only A atoms in the decahedral A positions in the $\text{A}_3\text{B}_2\text{X}_3\text{O}_{12}$ garnet structure when Mn^{2+} ions can exchange both cations A and B in the decahedral and octahedral sites, respectively [12,13]. No impurity phases associated with Ce^{3+} and Mn^{2+} doping were detected [12,13]. This indicates that the mentioned dopants fully dissolve in the garnet host material to form a solid solution.

The SEM images of the synthesized microcrystalline powder phosphors with an activator concentration of 1 at. % Ce^{3+} and 1 at.% Mn^{2+} are shown in Fig. 1. Generally, the formation of.

Garnet grains are found in all samples. In all cases, agglomeration of crystal grains can also be observed. This can be caused by the high temperature of the sintering process or the use of flux. The obtained samples display non-uniform morphology in SEM (Fig. 1).

4. Luminescence properties

The electron configuration of Ce^{3+} ions is $[\text{Xe}]4f^15d^0$. Generally, in CSSG:Ce garnets, Ce^{3+} ions occupy the D_2 symmetric Ca^{2+} site, so the 5 d level is first split into a low doublet (E_g) and a high triplet (T_{2g}), and then further split into the well-known five-fold levels due to the distortion of cubic symmetry. First-principles studies [15] calculated the $4f^1$ and $5d^1$ level energies of Ce^{3+} in CSSG host cells with different charge compensation mechanisms. Therefore, the broad absorption/PLE band and PL emission peaks of the micropowder samples under study are derived from the $4f$ – $5d$ transitions of Ce^{3+} ions. The splitting of the Ce^{3+} energy levels is caused by both the covalent bond effect (nephelauxetic effect) and the crystal field effect.

CL spectra. The CL spectra of CYMSSG:Ce micropowders show the broad Ce^{3+} luminescence band peaked at 554 nm, originated from the radiative transitions from $5d$ to $^2F_{5/2}$ and $^2F_{7/2}$ levels, respectively. In addition to the emission of Ce^{3+} and Mn^{2+} ions, other emission bands in the UV range peaking at 384 nm are also present in the CL spectra of the CYMSSG:Ce micropowders. Similar low-intensity bands in the UV range of Ca^{2+} , Mg^{2+} , and Si^{4+} based garnets have been assigned to the defect center emission [16,17]. In our opinion, it is expected that a large concentration of the oxygen vacancies will be present in these garnets due to possible deviations in the content of two and four charged ions and the need for local charge compensation [17,18]. Therefore, the band in the UV range may correspond to the emission of the F^+ center (one-charged oxygen vacancies) of the CYMSSG host [17,18].

The CL spectrum of Mn doped CYMSSG micropowders shows two emission bands: the yellow emission band around 567 nm (Mn^{2+} (I) center) and the red emission band peaked around 676 nm (Mn^{2+} (II) center). In general, the Mn^{2+} emission is caused by the spin-forbidden $^4T_1(^4G) \rightarrow ^6A_1(^6S)$ transitions of 3 d^5 levels [4,19]. By the analogy with

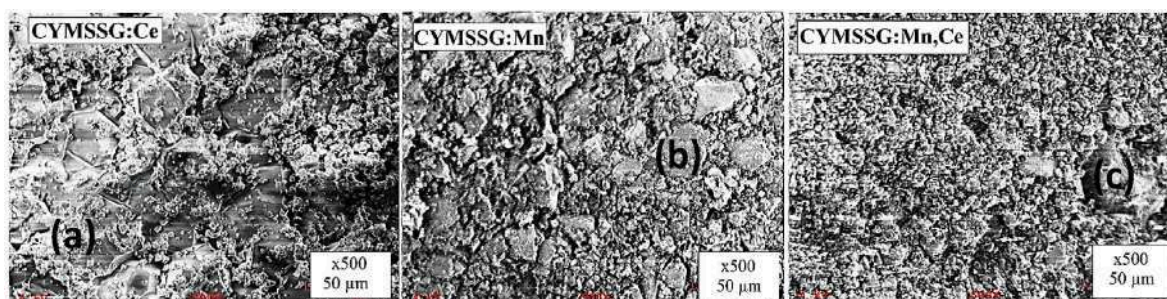


Fig. 1. SEM images, at the magnification (x500) of micropowder samples of CYMSSG garnets, doped with Ce^{3+} (a), Mn^{2+} (b) and Ce^{3+} - Mn^{2+} (c) ions.

the results of [4,19] on the luminescence of $\text{Ca}_3\text{Sc}_2\text{Si}_3\text{O}_{12}:\text{Mn}$ garnet, the presence of two emission bands in CYMSSG:Mn micropowder is caused by two types of Mn^{2+} centers. Namely, the presence of the emission bands of Mn^{2+} ($\text{Mn}^{2+}(\text{I})$ and $\text{Mn}^{2+}(\text{II})$) centers presuppose that Mn ions CYMSSG also can occupy both Ca^{2+} and Sc^{3+} sites. Meanwhile, another reason for the presence of the red emission band with a peak of 676 nm also corresponds to the luminescence of Mn^{4+} centers. Such a valence state of manganese ions typically is formed in garnets for the local compensation of $\text{Mn}^{2+}:\text{Mn}^{4+}$ pairs [21,22]. The bumps at 734–753 nm range in the CL spectra of CYMSSG:Mn and CYMSSG:Ce, Mn micropowders most probably correspond to the luminescence of Mn^{3+} ions [28,29] or/and to the emission centers based on the aggregates of charged oxygen vacancies [17,18].

The CL spectrum of Ce, Mn doubly doped CYMSSG micropowder shows the notable shift of the main emission band up to 590 nm in comparison with the respective band in the CYMSSG:Mn micropowder sample (Fig. 2) presumably due to $\text{Ce}^{3+} \rightarrow \text{Mn}^{2+}$ energy transfer and the large contribution of $\text{Mn}^{2+}(\text{I})$ and $\text{Mn}^{2+}(\text{II})$ centers.

PL and PLE spectra. The RT PL emission spectra of the CYMSSG:Ce micropowders under excitation in the 400–500 nm range in the vicinity of the characteristic absorption band of Ce^{3+} ions are shown in Fig. 3a. Fig. 3b demonstrates the respective excitation spectra of the Ce^{3+} luminescence, recorded in the different parts of the broad Ce^{3+} emission band. The PL spectra of CYMSSG:Ce micropowders show a strong wide emission band peaked in the yellow range, related to the radiative $5d^1 \rightarrow 4f$ ($^2F_{5/2,7/2}$) transitions of Ce^{3+} ions. When the excitation wavelength is increased from 410 nm to 490 nm, the PL spectrum of CYMSSG:Ce micropowder shows a redshift from 540 nm to 595 nm (Fig. 3a). Furthermore, the shift of the main maximum of the PL spectrum of CYMSSG:Ce sample does not occur nonlinearly with the increase of the excitation wavelength (Fig. 4, curve 1). Such behavior of the PL emission spectrum confirms the formation of Ce^{3+} multicenters in the CYMSSG:Ce garnet [2,17,18].

The excitation spectra of the Mn^{2+} luminescence in CYMSSG:Mn powder (Fig. 5, curve 1) in the UV (<300 nm) range correspond to the charge transfer transitions (CTT) from Mn^{2+} ions to conductive bands of host (see Refs. [22,26] for details). This excitation spectra in the visible range consist also the characteristic the sharp-line bands peaked at 414 and 419 nm related to the $^6A_1 \rightarrow ^4A_1$, 4E transitions of Mn^{2+} ions and two other bands with the maxima approximately at 451 and 470 nm which can be related correspondingly to $^6A_1 \rightarrow ^4T_1$, 4T_2 transitions of Mn^{2+} ions [25–27]. It should be noted that all the mentioned Mn^{2+} related

excitation bands have very week intensity due to the spin-forbidden origin of transitions which are slightly allowed by spin-orbit interaction [25–27]. Apart from the Mn^{2+} excitation bands, other wide band peaked at 457 nm is present in the excitation spectra of CYMSSG:Mn micropowder (Fig. 5, curve 1), which can be related to the $^5E \rightarrow ^3T_2$ transitions of Mn^{3+} ions [28,29] and partly to the $4f$ ($^2F_{5/2}$) $\rightarrow 5d^1$ transitions of Ce^{3+} ions as the trace impurity in CYMSSG:Mn powder located just in this spectral range (Fig. 3b). It is very interesting that the long-wavelength absorption band of Ce^{3+} ions is located just in the same position as the $^6A_1 \rightarrow ^4T_1$, 4T_2 excitation bands of Mn^{2+} and Mn^{3+} ions. This can be an important condition for the simultaneous energy transfer both to Mn^{2+} and Ce^{3+} ions in the CYMSSG:Mn host/or for the mutual energy transfer between the Ce^{3+} and Mn^{2+} and Mn^{3+} ions.

Indeed, under excitation at 410 nm in the vicinity of characteristic Mn^{2+} excitation band (Fig. 5, curve 1), the PL spectra of CYMSSG:Mn micropowder show the emission band peaked at 590 nm, and the bump at 680 nm, corresponding to the $\text{Mn}^{2+}(\text{I})$ and $\text{Mn}^{2+}(\text{II})$ centers luminescence ($^4T_1 \rightarrow ^6A_1$ transitions [22,27]), and wide emission band peaked at 790 nm, corresponding to the Mn^{3+} luminescence ($^5T_2 \rightarrow ^5E$ and $^1T_2 \rightarrow ^5E$ transitions, respectively [28,29]) (Fig. 5, curve 2).

The decay kinetics of the $\text{Mn}^{2+}(\text{I})$ and $\text{Mn}(\text{II})$ centers luminescence in CYMSSG:Mn samples, registered at 575 nm and 680 nm, respectively, under excitation in the vicinity of the Mn^{2+} CTT excitation band at 275 nm band, shows one exponential course with the decay constant of 3.76 and 5.67 ms, respectively. These are typical decay time values for the Mn^{2+} luminescence in other garnet compounds [22,27,29].

Based on the two emission bands identified in the PL spectra, we suggested that Mn^{2+} ions can occupy both Ca^{2+} and Sc^{3+} sites in the $\text{Ca}_2\text{YMgScSi}_3\text{O}_{12}$ garnet. On the Ca^{2+} site, the covalency and crystal field effects are weaker than on the Sc^{3+} site. As a result, higher-energy Mn^{2+} emissions may be occupying the Ca^{2+} site, which has a weaker crystal field, whereas lower-energy Mn^{2+} emissions can occupy the Sc^{3+} site [20].

We can observe the significant differences in the PL emission and PLE spectra for CYMSSG:Ce, Mn micropowder (Fig. 6) in comparison with CYMSSG:Ce micropowder (Fig. 3). Indeed, in the PL spectra, a redshift of the main emission band is observed with increasing excitation wavelength from 556 nm to 597 nm. Such region is notably red-shifted in comparison with the observed shift of CYMSSG:Ce micropowders due to the contribution of the Ce^{3+} and Mn^{2+} luminescence (Fig. 6a). Namely, as compared with the luminescence spectra of CYMSSG:Ce micropowder, the luminescence spectra of the CYMSSG:Ce, Mn sample have a large redshift of about 10 nm, which indicates the energy transfer from Ce^{3+} to Mn^{2+} ions. Furthermore, we have observed also differences in the large shift dependences of the maximum of the PL spectrum of CYMSSG:Ce and CYMSSG:Ce, Mn micropowders with increasing the excitation wavelength (Fig. 4, curves 1 and 2, respectively).

The PLE spectra in the 250–550 nm range, recorded in the CYMSSG:Ce, CYMSSG:Ce,Mn, and CYMSSG:Mn micropowder samples in the different parts of the emission bands (Figs. 3b, 5b and 6b) consist of the three bands corresponding to the transitions from the $4f$ ground state to the $5d$ levels of Ce^{3+} ions in the dodecahedral positions of the garnet host. The lowest energy bands peaked in the 450–460 nm range for CYMSSG:Ce and 465–469 nm, which are much stronger, than the PLE bands peaked in the UV range at 320 and 308 nm, respectively. Such behavior of the PLE spectra for both samples suggests that.

Higher-energy excited levels can be located near the conduction band and the Ce^{3+} luminescence under excitation in the UV bands can be quenched by photoionization. Interestingly, the shift of the maxima of the lowest excitation band in the 450–470 nm ranges shows the same tendency as their respective luminescence bands in the CYMSSG:Ce and CYMSSG:Ce, Mn micropowder samples. In general, the stronger crystal field in the dodecahedral positions of the garnet host, affecting Ce^{3+} ions, shifts the lowest excitation level to lower energy and the higher excitation level to higher energy.

The decay kinetics of the Ce^{3+} luminescence in the Ce^{3+} and Mn^{2+}

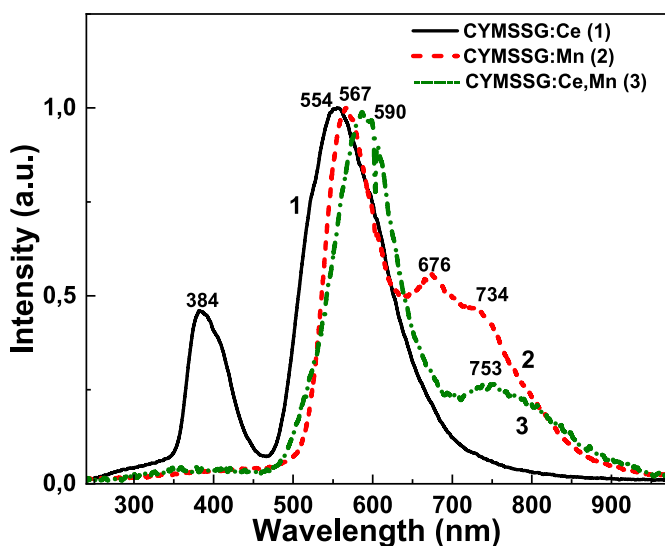


Fig. 2. Normalized CL spectra of CYMSSG:Ce (1), CYMSSG:Mn (2) and CYMSSG:Ce, Mn (3) micropowders.

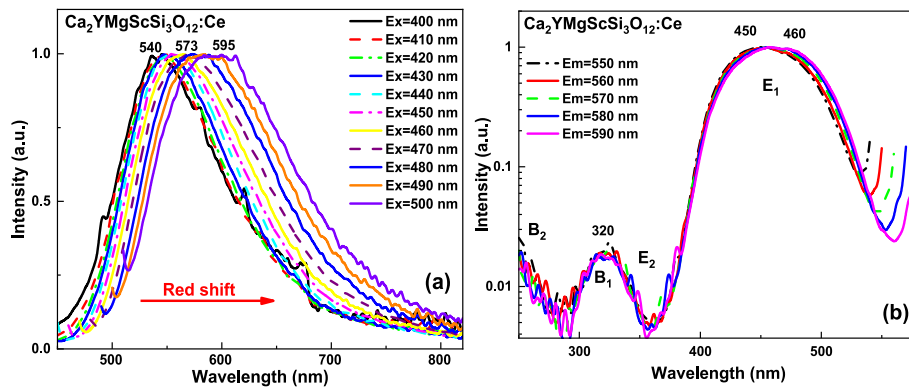


Fig. 3. (a) - normalized PL emission spectra of CYMSSG:Ce micropowder under excitation in the 400–500 nm range, corresponding to the different parts of Ce^{3+} related absorption band; (b) - PL excitation spectra of CYMSSG:Ce micropowder, recorded in 550–600 nm in different parts of the Ce^{3+} emission band.

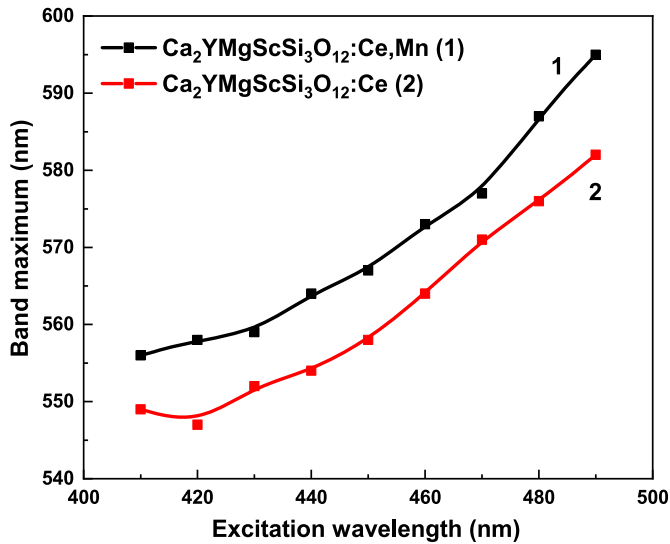


Fig. 4. Dependences of the maxima in the peak positions of Ce^{3+} emission bands on the excitation wavelength in CYMSSG:Ce (1) and CYMSSG:Ce,Mn (2) micropowders.

doped $\text{Ca}_2\text{YMgScSi}_3\text{O}_{12}$ micropowders, recorded in the 540–590 nm range under excitation at 450 nm, is shown in Fig. 7a and b, respectively. The decay profiles of the Ce^{3+} emission in these micropowders are strongly non-exponential due to the energy transfer processes from high-energy (HE) to low energy (LE) emitting Ce^{3+} centers (see Refs. [2,3,17,

18] for details) as well as due to $\text{Ce}^{3+} \rightarrow \text{Mn}^{2+}$ energy transfer [4,19]. For this reason, a three-component fit of the decay curves $I = \sum A_i \exp(-t/\tau_i)$ was used for the qualitative description of the luminescence timing properties (Table 1, Table 2) [23]. The dependences of the decay time values measured in the different parts of the Ce^{3+} emission bands of CYMSSG:Ce and CYMSSG:Ce, Mn micropowders, are shown in Fig. 8. The

Main differences in the observed trends in these figures are relate to the different contributions of the $\text{Ce}_{\text{HE}}^{3+} \rightarrow \text{Ce}_{\text{LE}}^{3+}$ and $\text{Ce}_{\text{HE,LE}}^{3+} \rightarrow \text{Mn}^{2+}$ processes in the luminescence decay kinetics of respective micro-powder samples under study.

Generally all Ce^{3+} multicenters can be excited simultaneously using different conditions of excitation. However, the contribution of each centers in the main emission bands is very different due to the various light efficiency of these centers and energy transfer from higher energetic Ce^{3+} center should cause energy transfer to the lowest energetic Ce center.

We would like to mention also here that the Ce^{3+} multicenters are also very effectively excited in the Ce, Mn doped CMSSG micropowders. However, the Mn^{2+} ions excited efficiently only in the Ce^{3+} related absorption bands, e.g. mainly due to $\text{Ce}^{3+} \rightarrow \text{Mn}^{2+}$ energy transfer. As a result, the PL spectra of CMSSG:Ce, Mn powder sample represents a mix of emission Ce^{3+} multicenters and Mn^{2+} ions (Fig. 6a).

5. Color characteristics of LED

To demonstrate the application possibility of the development of CYMSSG:Mn, Ce phosphor, two WLED prototypes were prepared by the covering a blue 450 nm LED with the several PC layers with a thickness approximately of 100–120 μm of each layer, containing the mixture of

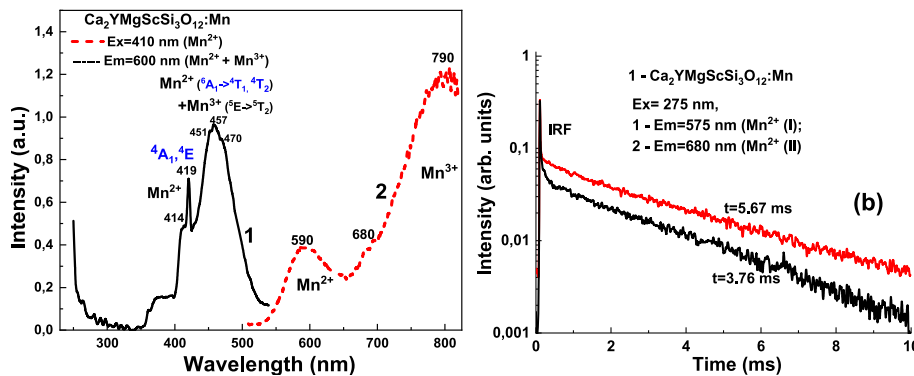


Fig. 5. (a) - PL excitation spectra of CYMSSG:Mn micropowder, recorded at 590 nm in the vicinity of Mn^{2+} emission band (1) and PL emission spectra of this sample under excitation in the at 410 range, corresponding to the of Mn^{2+} related absorption band (2). (b) - decay kinetics of PL at 575 nm in CYMSSG:Mn powders under excitation at 275 nm in the vicinity of Mn^{2+} CTT excitation band. IRF- instrumental response function of the excitation pulse.

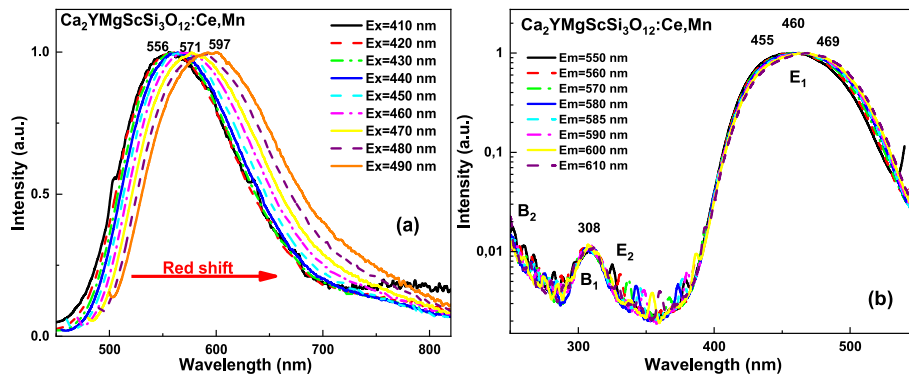


Fig. 6. (a) – Normalized PL emission spectra of CYMSSG:Ce, Mn micro-powder under excitation in the 410–490 nm range, corresponding to the different parts of Ce^{3+} related absorption band; (b) - PL excitation spectra of CYMSSG:Ce, Mn micropowder, recorded in 550–610 nm in different parts of the Ce^{3+} and Mn^{2+} emission bands.

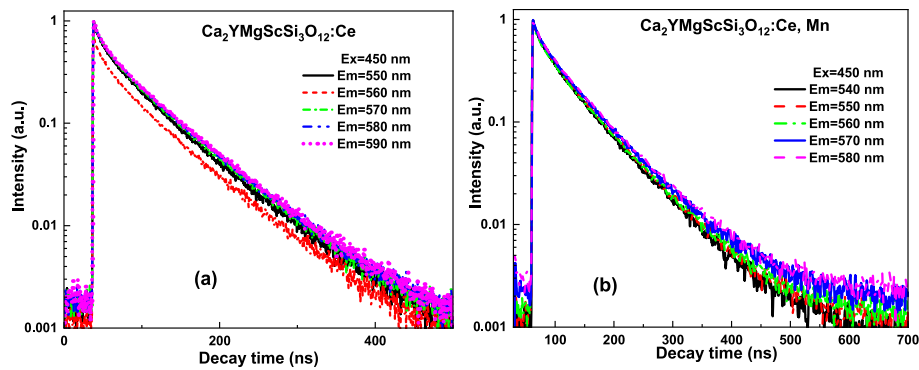


Fig. 7. (a) - PL decay kinetics of CYMSSG:Ce micro-powder, recorded in the different parts of the Ce^{3+} emission band in the 550–590 nm range under excitation at 450 nm; (b) - PL decay kinetics of CYMSSG:Ce, Mn micro-powder, recorded in the different parts of the Mn^{2+} , Ce^{3+} emission band in the 540–580 nm range under excitation at 450 nm.

Table 1

Parameters of three exponential approximation of the decay curves are presented in Fig. 6a.

Emission wavelength, nm	t_1 , ns	A_1	t_2 , ns	A_2	t_3 , ns	A_3
540	1.71	970.54	24.79	2687.37	68.65	4436.44
550	3.02	955.64	25.03	2481.03	69.52	4456.59
560	2.72	762.85	22.36	2092.09	68.81	4607.21
570	4.41	444.28	22.58	1815.38	69.21	3367.53
580	3.21	1146.89	24.41	2578.12	70.75	4610.28

Table 2

Parameters of three exponential approximations of the decay curves are presented in Fig. 6b.

Emission wavelength, nm	t_1 , ns	A_1	t_2 , ns	A_2	t_3 , ns	A_3
550	7.48	1908.49	28.06	2574.85	68.39	4001.29
560	8.91	1087.79	32.85	1680.3	71.40	2704.25
570	7.45	1709.09	31.47	2774.8	73.49	4697.83
580	7.12	1346.12	31.83	2744.55	74.36	4738.18
590	7.69	1117.95	30.58	2189.61	72.87	4069.65

epoxy resin and CYMSSG:Ce and CYMSSG:Ce, Mn micropowders. The photoconversion properties of these WLEDs were also investigated and presented in Fig. 9. The emission spectra of both WLED prototypes show a significant decrease in the intensity of the blue component and a respective increase in the intensity of the yellow emission with the increasing quantity of layers and a total thickness of PC. For this reason,

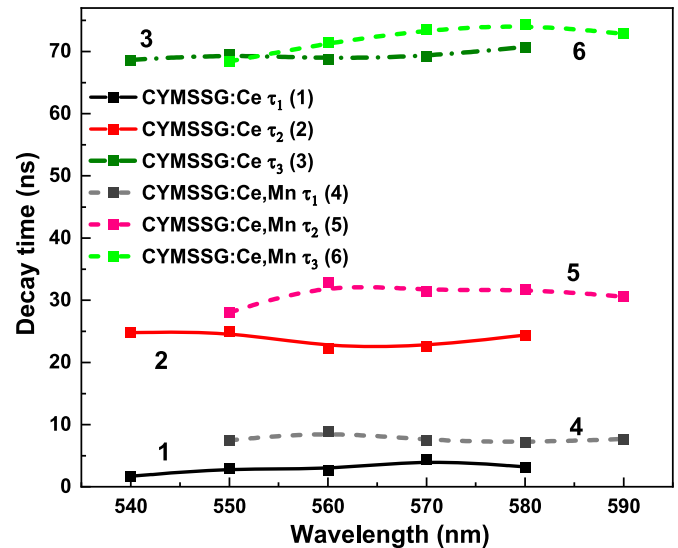


Fig. 8. The dependences of the decay time values measured in the different parts of the main emission bands of CYMSSG:Ce and CYMSSG:Ce, Mn micropowders.

the color coordinates of the device move to the diagram's center with an increase in PC layer thickness for both WLED samples. Finally, the WLED prototype, based on the five-layered CYMSSG:Ce micro-powder PC, gives quite cold white emission with CRI of 86, CCT of 8699 K, and

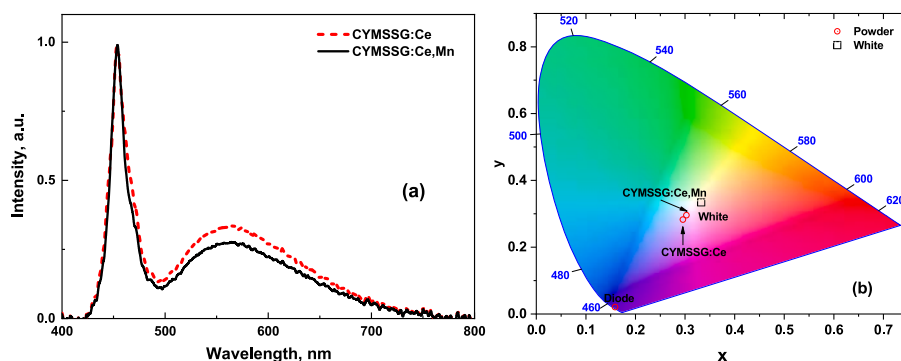


Fig. 9. Emission spectrum (a) and chromaticity diagram (b) of a WLED lamp fabricated on the base of 450 nm LED chip, CYMSSG:Ce and CYMSSG:Ce, Mn phosphor.

coordinates $x = 0.29$; $y = 0.28$. Furthermore, for the WLED prototype, based on the five-layered CYMSSG:Ce, Mn micropowder PC, quite warmer white emission was obtained with CRI of 87, CCT of 7607 K, and color coordinates $x = 0.30$; $y = 0.29$. Such results confirm that the Ce, Mn doubly doping of CYMSSG garnet host can result in the creation of effective photo-converters for WLEDs with tuning color of white emission.

6. Conclusions

The microcrystalline powders of CYMSSG:Ce, CYMSSG:Mn and CYMSSG:Ce, Mn garnets were obtained using the solid-state synthesis with adding of B_2O_3 flux in the 5 wt % concentration of the total charge content. To determine the luminescence properties of these micropowder samples, the cathodoluminescence (CL) spectra, photoluminescence (PL) emission, excitation spectra, and PL decay kinetics were measured.

The CL and PL spectra of CYMSSG:Ce micropowders show the dominant Ce^{3+} emission band in the yellow range peaked at 540 nm. Furthermore, the PL spectra of CYMSSG:Ce micropowders show a non-monotonical redshift from 540 nm to 595 nm with increasing the excitation wavelength from 410 nm to 490 nm in the vicinity of the Ce^{3+} absorption band. The non-monotonic dependences of Ce^{3+} decay time are observed also with an increase of monitoring wavelengths in the 540–580 nm range in the vicinity of the Ce^{3+} emission band. Such behavior of the PL emission spectra and decay kinetics confirms the formation of Ce^{3+} multicenters in the CYMSSG:Ce garnet due to local inhomogeneity of the different dodecahedral positions in Ca^{2+} , Si^{4+} based garnet hosts and the presence of the effective energy transfer processes between high-energy end low energy Ce^{3+} emission centers.

We have found that Mn^{2+} ions may either substitute for Ca^{2+} cations of CYMSSG host and generate the yellow emission band peaked at 565 nm and/or substitute for Sc^{3+} cations to generate the red emission band peaked at 676 nm. The effective Ce^{3+} to Mn^{2+} energy transfer process is observed in CYMSSG:Ce, Mn micropowder samples resulting in the redshift of the emission spectra to 590 nm in comparison with CYMSSG:Ce counterpart.

The application possibility of the developed CYMSSG:Ce and CYMSSG:Ce, Mn micro-crystalline powder phosphors was demonstrated. The planar WLED prototypes were fabricated by the coating of GaN 450 nm blue LED chip with several ~ 100 – 120 μm thick layers, containing CYMSSG:Ce and CYMSSG:Ce, Mn powder phosphors mixed with epoxy resin. The WLED prototype, which is based on the five CYMSSG:Ce PC layers, emits the cold white light with a CRI of 86 and a CCT of 8699 K, with coordinates $x = 0.29$; $y = 0.28$. Meanwhile, the photoconversion properties of the WLED prototype with CYMSSG:Ce, Mn PC show quite warmer white light with a CRI of 87, CCT of 7607 K, and color coordinates $x = 0.30$; $y = 0.29$. For this reason, tuning of the Ce and Mn content in the CYMSSG:Ce, Mn micro-crystalline powder phosphor, gives the possibility to fabricate WLED with “color-on

demand” photoconversion properties related to the color temperature of white light.

CRediT authorship contribution statement

A. Shakhno: collected and analyzed the structural and optical properties of samples and participated in writing and preparation of paper. **S. Witkiewicz-Lukaszek:** performed and analyzed cathodoluminescence measurements. **V. Gorbenko:** participated in measurements of PL of PL decay kinetic of SC sample. **T. Zorenko:** participated in the synthesis of the samples. **Yu Zorenko:** analyzed whole experimental materials and participated in writing and preparation of paper.

Declaration of competing interest

The authors declare that they have no known competing financial interests or personal relationships that could have appeared to influence the work reported in this paper.

Acknowledgments

The work was performed in the frames of the Polish National Science Centre (NCN) 2017/25/B/ST8/02932 project and partly supported by NCN 2019/33/B/ST3/00406 project.

References

- [1] Y. Shimomura, T. Kurushima, M. Shigeiwa, N. Kijima, J. Electrochem. Soc. 155 (2008) J45.
- [2] I. Levchuk, A. Osvet, C.J. Brabec, M. Batentschuk, A. Shakhno, T. Zorenko, Yu Zorenko, Opt. Mater. 107 (2020), 109978.
- [3] N. Khaidukov, Yu Zorenko, T. Zorenko, M. Batentschuk, e. a. pss RRL 11 (2017), 170001.
- [4] Y. Liu, X. Zhang, Z. Hao, Y. Luo, X.J. Wang, J. Zhang, J. Mater. Chem. 21 (2011), 16379.
- [5] V. Gorbenko, T. Zorenko, S. Witkiewicz, K. Paprocki, A. Iskalyeva, A. M. Kaczmarek, R. Van Deun, M.N. Khaidukov, M. Batentschuk, Y. Zorenko, J. Lumin. 199 (2018) 245.
- [6] R. Mueller-Mach, G. Mueller, M.R. Krames, T. Trottier, J. Sel. Top. Quantum Electron. 8 (2002) 339.
- [7] K. Uheda, N. Hiroaki, Y. Yamamoto, A. Naito, T. Nakajima, H. Yamamoto, J. Electrochem. Solid-State Lett. 9 (2006) H22.
- [8] Y.Q. Li, J.E.J. van Steen, J.W.H. van Krevel, G. Botty, A.C.A. Delsing, F.J. DiSalvo, G. de With, H.T. Hintzen, J. Alloys Compd. 417 (2006) 273.
- [9] C.K. Chang, T.M. Chen, J. Appl. Phys. Lett. 90 (2007), 161901.
- [10] W.J. Yang, T.M. Chen, J. Appl. Phys. Lett. 88 (2006), 101903.
- [11] W.J. Yang, L. Luo, T.M. Chen, N.S. Wang, J. Chem. Mater. 17 (2005) 3883.
- [12] U. Caldino, J.L. Hernandez-Pozos, C. Flores, A. Speghini, M. Bettinelli, J. Phys. Condens. Matter (2005) 7297.
- [13] C. Guo, L. Luan, Y. Xu, F. Gao, L. Liang, J. Electrochem. Soc. 155 (2008) J310.
- [14] S. Ye, J. Zhang, X. Zhang, S. Lu, X. Ren, X. Wang, J. Appl. Phys. 101 (2007), 033513.
- [15] A.A. Setlur, W.J. Heward, Y. Gao, A.M. Srivastava, R.G. Chandran, M.V. Shankar, J. Chem. Mater. 18 (2006) 3314.
- [16] Y. Wu, F. Meng, Q. Li, M. Koschan, C.L. Melcher, Phys. Rev. Applied. 2 (2014), 044009.

- [17] V. Gorbenko, T. Zorenko, K. Paprocki, A. Iskaliyeva, A. Fedorov, F. Schröppel, I. Levchuk, A. Osvet, M. Batentschuk, Yu Zorenko, *CrystEngComm* 19 (2017) 3689.
- [18] V. Gorbenko, T. Zorenko, P. Pawlowski, A. Iskaliyeva, K. Paprocki, A. Suchocki, Ya Zhydashchikov, A. Fedorov, N. Khaidukov, R. Van Deun, F. Schröppel, A. Osvet, M. Batentschuk, Yu. Zorenko. *Journal of Luminescence*. 195 (2018) 362.
- [19] D. Pasiński, E. Zych, J. Sokolnicki, *J. Lumin.* 169 (2016) 862.
- [20] K.V. Ivanovskikh, A. Meijerink, F. Piccinelli, A. Speghini, E.I. Zinin, C. Ronda, M. Bettinelli, *J. Lumin.* 130 (2010) 893–901.
- [21] Yu Zorenko, V. Gorbenko, T. Voznyak, M. Batentschuk, A. Osvet, A. Winnacker, *J. Lumin.* 130 (2010) 380.
- [22] Yu Zorenko, V. Gorbenko, T. Zorenko, B. Kuklinski, M. Grinberg, K. Wiśniewski, P. Bilski, *Opt. Mater.* 36 (2014) 1680.
- [23] L. Zhou, W. Zhou, F. Pan, R. Shi, L. Huang, H. Liang, P.A. Tanner, X. Du, Y. Huang, Y. Tao, L. Zheng, *Chem. Mater.* 28 (2016) 2834.
- [24] A. Shakhno, A. Markovskiy, T. Zorenko, S. Witkiewicz-Lukaszek, Y. Vlasjuk, A. Osvet, J. Elia, C.J. Brabec, M. Batentschuk, Yu Zorenko, *Materials* 15 (11) (2022) 3942.
- [25] J.W. Stout, *J. Chem. Phys.* 31 (1959) 709.
- [26] M.A. Noginov, G.B. Loutts, M. Warren, *J. Opt. Soc. Am.* B 16 (1999) 475.
- [27] Yu Zorenko, V. Gorbenko, T. Voznyak, M. Batentschuk, A. Osvet, A. Winnacker, *J. Lumin.* 130 (2010) 380.
- [28] S. Kuck, S. Hartung, S. Hurling, K. Peterman, G. Huber, *Phys. Rev. B* 57 (1998) 2203.
- [29] K. Wisniewski, Yu Zorenko, V. Gorbenko, T. Zorenko, B. Kuklinski, M. Grinberg, *J. Phys. Conf. Serie* 249 (2010), 012015, 1-8.



Full Length Article

Luminescence and photoconversion properties of Ce-doped $\text{Ca}_3\text{Sc}_2\text{Si}_3\text{O}_{12}$ crystal[☆]

A. Shakhno^{a,b,*}, W. Gieszczyk^c, P. Bilski^c, S. Witkiewicz-Łukaszek^a, Tetiana Zorenko^a, M. Cieszko^b, Z. Szczepański^b, A. Kotlov^d, Yu Zorenko^{a,**}

^a Department of Physics, Kazimierz Wielki University in Bydgoszcz, 85090, Bydgoszcz, Poland

^b Mechantronics Department, Kazimierz Wielki University in Bydgoszcz, 85-074, Bydgoszcz, Poland

^c Institute of Nuclear Physics Polish Academy of Sciences in Krakow, 31345, Krakow, Poland

^d Deutsches Elektronen-Synchrotron (DESY), 22607, Hamburg, Germany

ARTICLE INFO

Keywords:

Ca-Si based garnets
Ce³⁺ dopant
Micro-pulling-down method
Multicenter formation
Luminescence
Synchrotron radiation
Phosphor-converter
WLED

ABSTRACT

This work is dedicated to investigation of the luminescent properties of the prospective photoconversion material based on the crystal of Ce³⁺ doped $\text{Ca}_3\text{Sc}_2\text{Si}_3\text{O}_{12}$ (CSSG) garnet. The GSSG:Ce crystal was grown using the micro-pulling-down (μPD) method. The CSSG:Ce crystal exhibited an intensive photoluminescence (PL) emission band with two sub-bands peaked at 504 and 545 nm, corresponding to 5d-4f (²F_{5/2;7/2}) transitions. Furthermore, we have investigated also the formation of cerium multicenters in the GSSG:Ce crystal using analyses of the structure of Ce³⁺ photoluminescence emission and excitation spectra under excitation of the luminescence of this crystal by synchrotron radiation. The formation of Ce³⁺-multicenters in CSSG:Ce garnet is caused by the local inhomogeneity of the dodecahedral sites of garnet lattice due to localization of the hetero-valent Sc³⁺ and Si⁴⁺ cations in the octahedral and tetrahedral positions of the garnet host. The existence of Ce³⁺ multicenters resulted in a significant enhancement of the Ce³⁺ emission band in the red range and improving the performance of conventional YAG:Ce phosphor. The next task of our work was to evaluate the possibility of application of the GSSG:Ce crystal as a light phosphor-converter (pc) for white light-emitting diodes (WLEDs). In the frame of this task, we have successfully developed a prototype of WLED by employing the CSSG:Ce crystal as a phosphor-converter (pc) with blue 450 emitting LED as well as investigated the color characteristics of this pc-WLED.

1. Introduction

White light-emitting diodes are widely adopted for lighting applications due to their remarkable attributes, including high efficiency, extended operational lifetime, and environmental sustainability compared to conventional light sources. The prevalent configuration of WLEDs involves combining blue LED chips with yellow-emitting Ce³⁺ doped $\text{Y}_3\text{Al}_5\text{O}_{12}$:Ce (YAG:Ce) garnet phosphor converters (pc). However, despite the good thermal stability of the Ce³⁺ luminescence in YAG:Ce at high temperatures, the absence of a red-emitting component in YAG:Ce phosphor converters requires the exploration of alternative

phosphors [1]. Therefore, there is a growing interest in identifying and developing alternative phosphor materials to address the above limitation in order to enhance the color rendering capabilities of pc-WLEDs.

The $\text{Ca}_3\text{Sc}_2\text{Si}_3\text{O}_{12}$:Ce (CSSG:Ce) silicate garnet emerges as an interesting alternative phosphor to YAG:Ce [2–6]. These phosphors demonstrate a high quantum yield what allows efficient conversion of excitation energy into emitted light. Additionally, they possess broad-band emission spectra, allowing for a wide range of visible light emission [7]. Moreover, silicate garnet phosphors, including CSSG:Ce, exhibit excellent thermal stability of luminescence, making them well-suited for applications requiring elevated temperatures. Their

[☆] We understand that the Corresponding Author is the contact for the Editorial process (including Editorial Manager and direct communications with the office). He/she is responsible for communicating with the other authors about progress, submissions of revisions and final approval of proofs. We confirm that we have provided a current, correct email address which is accessible by the Corresponding Author and which has been configured to accept email from: annshakhno@gmail.com; zorenko@ukw.edu.pl

^{*} Corresponding author. Department of Physics, Kazimierz Wielki University in Bydgoszcz, 85090, Bydgoszcz, Poland.

^{**} Corresponding author.

E-mail addresses: annshakhno@gmail.com (A. Shakhno), zorenko@ukw.edu.pl (Y. Zorenko).

<https://doi.org/10.1016/j.jlumin.2023.120311>

Received 6 September 2023; Received in revised form 19 October 2023; Accepted 7 November 2023

Available online 22 November 2023

0022-2313/© 2023 The Authors. Published by Elsevier B.V. This is an open access article under the CC BY license (<http://creativecommons.org/licenses/by/4.0/>).

application as alternative phosphors offer promising prospects for enhancing the performance and versatility of lighting technologies.

Practical application of the CSSG:Ce garnet holds vast potential in various forms such as crystal, single-crystalline film (SCF), micro-powder (MP) and nanopowder (NP). These forms enable the creation and development also cathodoluminescent materials, scintillators, lasers, and pc-WLEDs. The ongoing advancements in this phosphor type present promising opportunities within the field of semiconductor lighting technology. Consequently, a comprehensive investigation of the optical and structural properties of CSSG:Ce garnet is being strongly required [2,6,8–10].

This study focuses on the growth of Ce^{3+} -doped CSSG:Ce crystal by the micro-pulling-down method and investigation of their structural and luminescent properties using conventional optical methods and advanced luminescent spectroscopy under synchrotron radiation (SR) excitation. Furthermore, we have also investigated the color characteristics and phosphor conversion capabilities of WLED prototypes based on the CSSG:Ce crystal converters with varying thickness ranging from 0.8 to 1 mm. Our objective is to gain insights into the performance and potential of CSSG:Ce crystal as a phosphor converter for high-power WLED applications.

2. The growing technique and experimental techniques

The Ce^{3+} -doped CSSG crystal was grown through a micro-pulling-down method at the Institute of Nuclear Physics of Polish Academy of Sciences in Krakow, Poland. This method allowed the growth of the crystal from a molten state, resulting in the formation of a high-quality garnet crystal doped with Ce^{3+} ions. The CaO (Merck), Sc_2O_3 (Sigma-Aldrich), SiO_2 (Merck) and CeO_2 (Sigma-Aldrich) raw powders with a purity of 99.99 % were used. Stoichiometric amounts of CaO , Sc_2O_3 , and SiO_2 were thoroughly mixed in the agate mortar to prepare a batch material for crystal growth experiments. To achieve Ce-doped CSSG crystal samples, CO_2 oxide in a concentration of 1 mol %, was employed as an admixture.

The prepared batch material, weighing 1.5 g, was loaded into a molybdenum crucible positioned directly on the graphite substrate following the heating process. To establish a suitable temperature gradient within the crystal growth area, three layers of ceramic thermal insulations composed of alumina and magnesium-stabilized zirconium dioxide were implemented. The closed chamber of the micro-pulling-down (μPD) furnace underwent an initial evacuation process, reducing the pressure to approximately 3.1 μbar . Then the chamber was filled with an inert gas (argon) to achieve the normal pressure. The crystal growth process occurred at a consistent pulling rate of 1.5 mm/min, utilizing an Al_2O_3 crystal as a seed. Throughout the entire growth experiment, the volumetric flow rate of argon remained at approximately 20 l/min.

To characterize the properties of the CSSG:Ce crystal under study, various structural and spectroscopic techniques were employed. The structural properties of these CSSG:Ce crystal samples were investigated using X-ray microtomography with a resolution of 0.5 μm (SkyScan 1272 spectrometer). The real composition of SCF samples was determined using a KEYENCE's Digital Microscope VHX-7000 (Mechelen, Belgium). Cathodoluminescence (CL), photoluminescence (PL), emission and PL excitation spectra (PLE), as well as PL decay kinetics were used for the characterization of the luminescent properties of the CSSG:Ce crystal. The CL spectra were obtained at room temperature (RT) using a scanning electron microscope (SEM, JSM-6390LV, JEOL Ltd., Tokyo, Japan), which was equipped with a Stellar Net spectrometer featuring a cooled TE-detector CCD that operated within the 200–1200 nm range. PL emission and excitation spectra, along with PL decay kinetics, were measured using an FS-5 spectrometer (Edinburg Instruments Ltd., Livingston, United Kingdom). Additionally, the luminescence of CSSG:Ce crystal sample was investigated at 12 K under synchrotron radiation excitation with energy in the 3.6–15 eV range at the Superlumi station at

HASYLAB (DESY, Hamburg). Photoconversion spectra measurements CSSG:Ce crystals with thickness in the 0.8–1 mm range were performed using an AvaSpec-ULS 2048-LTEC fiber-optic spectrophotometer and an AvaSphere-50-IRRAD integrating sphere.

3. Structural properties

The radial deviation of the CSSG:Ce crystal content was established using a KEYENCE Digital Microscope VHX-7000. This device was equipped with a Laser-based Elemental Analyzer to enable instantaneous analysis of the material. The results of this analysis are shown in Table 1. The analysis of encompassed measurements was taken at five different points on the crystal sample, with ensuing averaging of the results to enhance accuracy of the content determination. The obtained results show some advance of Ca^{2+} and Si^{4+} cations and deficit of Sc^{3+} ions in comparison with stoichiometric content of the $\text{Ca}_3\text{Sc}_2\text{Si}_3\text{O}_{12}$ garnet. For compensation of the charge excess, the cation vacancies V_{Sc} and Ca_{Sc} antisite defects can be created. However, such an assumption needs the detailed confirmation using EPR or other sensitive methods.

Furthermore, X-ray microtomography was used to investigate the internal structure of the $\text{Ca}_3\text{Sc}_2\text{Si}_3\text{O}_{12}$:Ce crystal, specifically to detect the existence of microdefects and phases different from the primary garnet phase. Visualization of these studies is presented in Fig. 1. It can be seen that the central part of the crystal consists of one dominant CSSG garnet phase. However, a secondary phase can be also observed at the edges of the crystal. The presence of the second phase at the crystal edges can be explained by the specific conditions of the crystal growth using the MPD method. The presence of other phases along the edges is a typical phenomenon and can be attributed to the specific growth conditions and solidification process, especially at the walls of crucible. During the MPD process, a crystal is grown by slowly pulling a seed crystal through a melt of the desired material. This controlled solidification allows the crystal to be formed from the molten material as it cools and crystallizes. However, certain factors can contribute to the formation of secondary phases, especially along the edges of the crystal. These factors can include thermal gradients, impurity concentration, solidification dynamics, segregation effects and crystallographic mismatch. In our case, we assume that the secondary phase at the edges of the crystal is formed due to overheating the melt at crucible walls and some segregation effects. To be more precise, differences in the density and composition of the material lead to segregation during solidification. Therefore, we can observe formation of the perovskite or other phase at the edges of the crystal with higher temperature of melting than that of the garnet. As a result of this circumstance, specifically, the existence of a secondary phase along the crystal's edges, *optical investigations of the crystal were exclusively conducted on its central part.*

4. Luminescent properties

4.1. Cathodoluminescence spectra

Fig. 2 shows the CL spectrum of the Ce^{3+} -doped $\text{Ca}_3\text{Sc}_2\text{Si}_3\text{O}_{12}$ crystal sample. This spectrum exhibits the characteristic double emission bands centered at 508 nm and 539 nm, corresponding to the $5d^1 \rightarrow 4f(^2F_{5/2}; 7/2)$ transitions of Ce^{3+} ions in dodecahedral positions of the garnet host

Table 1

The nominal composition (in oxide powders) and the actual composition (in the crystal) of CSSG:Ce crystal grown via the MPD method.

	Nominal crystal content	Actual crystal content
1	$\text{Ca}_3\text{Sc}_2\text{Si}_3\text{O}_{12}:\text{Ce}$	$\text{Ca}_{3.45}\text{Sc}_{1.37}\text{Si}_{3.18}\text{O}_{12}:\text{Ce}$
2	$\text{Ca}_3\text{Sc}_2\text{Si}_3\text{O}_{12}:\text{Ce}$	$\text{Ca}_{3.37}\text{Sc}_{1.43}\text{Si}_{3.2}\text{O}_{12}:\text{Ce}$
3	$\text{Ca}_3\text{Sc}_2\text{Si}_3\text{O}_{12}:\text{Ce}$	$\text{Ca}_{2.97}\text{Sc}_{1.21}\text{Si}_{3.82}\text{O}_{12}:\text{Ce}$
4	$\text{Ca}_3\text{Sc}_2\text{Si}_3\text{O}_{12}:\text{Ce}$	$\text{Ca}_{2.92}\text{Sc}_{1.12}\text{Si}_{3.96}\text{O}_{12}:\text{Ce}$
5	$\text{Ca}_3\text{Sc}_2\text{Si}_3\text{O}_{12}:\text{Ce}$	$\text{Ca}_{2.49}\text{Sc}_{1.25}\text{Si}_{4.26}\text{O}_{12}:\text{Ce}$
Average	$\text{Ca}_3\text{Sc}_2\text{Si}_3\text{O}_{12}:\text{Ce}$	$\text{Ca}_{3.04}\text{Sc}_{1.28}\text{Si}_{3.68}\text{O}_{12}:\text{Ce}$

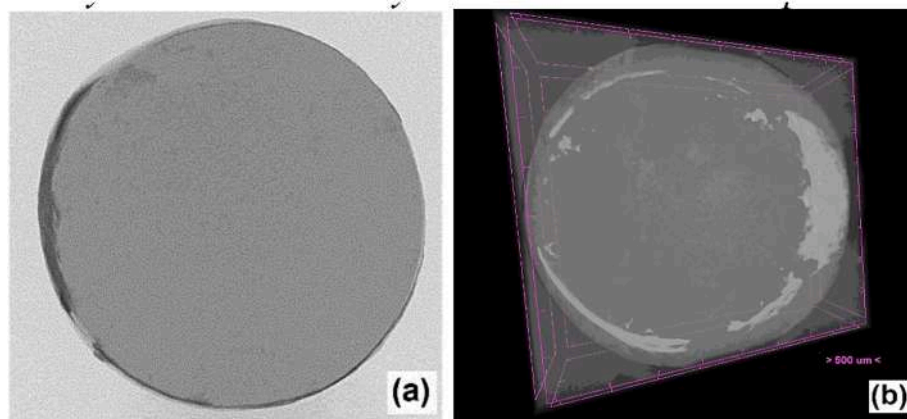


Fig. 1. The radiograph of the sample acquired through X-ray tomography is depicted in (a), while the reconstructed three-dimensional image of the CSSG:Ce crystal structure is presented in (b).

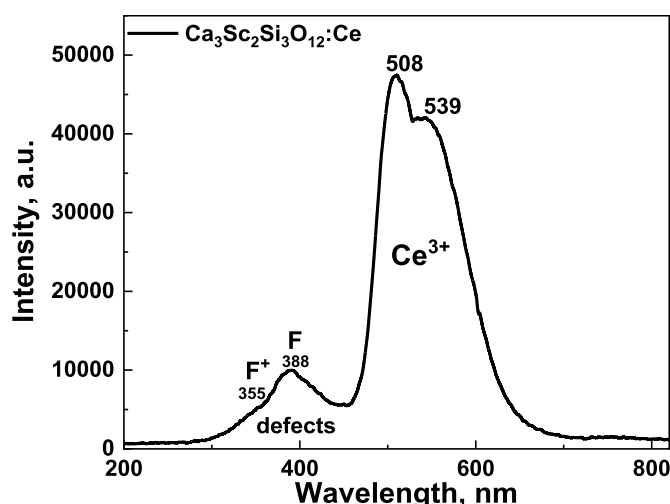


Fig. 2. RT CL spectrum of the CSSG:Ce crystal sample.

[4,7]. Generally, Fig. 2 illustrates the impact of substitution of Y^{3+} and Al^{3+} cations with Ca^{2+} , Sc^{3+} , and Si^{4+} cations in the dodecahedral, octahedral, and tetrahedral positions of the $Y_3Al_5O_{12}$ garnet host. This causes a significant shift of the maximum of the Ce^{3+} emission band towards the blue range from 540 to 508 nm compared to the YAG:Ce single crystal [11]. is observed due to substitution of Y^{3+} cations with Ca^{2+} ions in the dodecahedral positions, Al^{3+} cations with Sc^{3+} cations in the octahedral sites and Al^{3+} cations on Si^{4+} ions in the tetrahedral positions of the garnet host. The overall influence of such type substitution results in the presence of smaller crystal field strengths in the different dodecahedral sites of the CSSG garnet lattice, where the Ce^{3+} ions are located.

In addition to the luminescence emitted by Ce^{3+} ions, there are other high-energy emission bands are present in the CL spectrum of CSSG:Ce crystal. Particularly, the wide bands are observed in the ultraviolet (UV) range with maxima at 355 and 388 nm. Similar broad low-intensity bands in the UV range are observed in Ca^{2+} - Si^{4+} and Mg^{2+} - Si^{4+} -based garnets and these bands typically have been associated with the luminescence of defect centers [12–16]. Namely, the nature these two UV bands can be attributed to the luminescence of F- and F^+ centers, respectively, due to high concentration of oxygen vacancies in the Ca^{2+} - Mg^{2+} - Si^{4+} based garnets [12–16]. The presence of these charged vacancies may be caused by variations in the Ca^{2+} and Si^{4+} content, as well as by need for local charge compensation of the excess of one cations during the crystal growth in an oxygen-free atmosphere [17,18].

4.2. Photoluminescence spectra and Ce^{3+} multicenter formation

Under excitation with 400 nm light, the PL spectrum of the CSSG:Ce crystal (Fig. 3a) consists of the typical double Ce^{3+} 5d-4f emission bands, peaked at 501 and 536 nm, corresponding to the transitions from the lowest 5d₁ level to the two spin-orbit components $^2F_{5/2,7/2}$ (separated by $\sim 2000\text{ cm}^{-1}$) of the ground state (Fig. 3a). However, under excitation with different wavelengths in the 400–450 nm range, these bands are notably shifted to the red range and maxima of the double bands are located at 507 and 542 nm for 460 nm excitation, primarily associated with distinct Ce1 and Ce2 centers, respectively. The red shift in the primary maxima of the PL spectra and variations in intensity at the peak positions of CSSG:Ce crystal occur in a non-monotonic way with increasing excitation wavelength (Fig. 3c), as opposed to the absence of the mentioned changes for the YAG:Ce reference crystal (not presented in Fig. 3c) [4,7].

The PLE spectra of CSSG:Ce crystal are illustrated in Fig. 3b. The PLE spectra of luminescence show a set of broad bands located in the blue-green range. Within the wavelength range of 250–550 nm, multiple sets of excitation bands are observed. Notably, the strongest E1 (440 nm) and E2 (310 nm) bands, can be attributed to the 4f–5d (E_g and T_{2g}) transitions of the primary Ce1 center, agreeing with the results of prior research [4,19,20]. Similarly, additional sets of excitation bands, E1' (457 nm) and E2' (331 nm), can be associated with the 4f₁→5d₁ transitions of the secondary Ce2 centers. These centers exhibit distinct local environments when compared to the Ce1 center. Additionally, the excitation band peaking at 361 nm possibly corresponds to a defect center, most probably the F^+ center [4].

The decay kinetic profiles of the Ce^{3+} luminescence in the CSSG:Ce crystal, registered at the range 490–570 nm under excitation at 450 nm, are shown in Fig. 3d. Similar to other Ca^{2+} - Si^{4+} garnets based [21–23], the decay kinetics of Ce^{3+} emission in CSSG:Ce crystals exhibit a strong non-exponential behavior. Due to this, a three-exponential fit of the decay curves, given by equation $I = \sum A_i \cdot \exp(-t/\tau_i)$, was used to qualitatively deservations of the luminescence timing profiles. In spite of the fact that a three-exponential approximation does not fully describe the luminescence decay in cases of quenching via energy transfer, the decay time values can be considered as estimations for the luminescence decay times of respective Ce^{3+} multicenters (Table 2). Specifically, the luminescence decay kinetics of the CSSG:Ce crystal, measured at the appropriate wavelengths (namely, at 490 nm and 570 nm), are manifested by three components τ_i , where $i = 3$, each with a unique decay time associated with distinct Ce1 and Ce2 centers. In particular, the decay times (τ_1 , τ_2 and τ_3) of the Ce1 center emission in the CSSG:Ce crystal, recorded at 490 nm under excitation at 450 nm, are equal to 3.7 ns, 21.7 ns and 64.0 ns when the luminescence decay times of Ce2

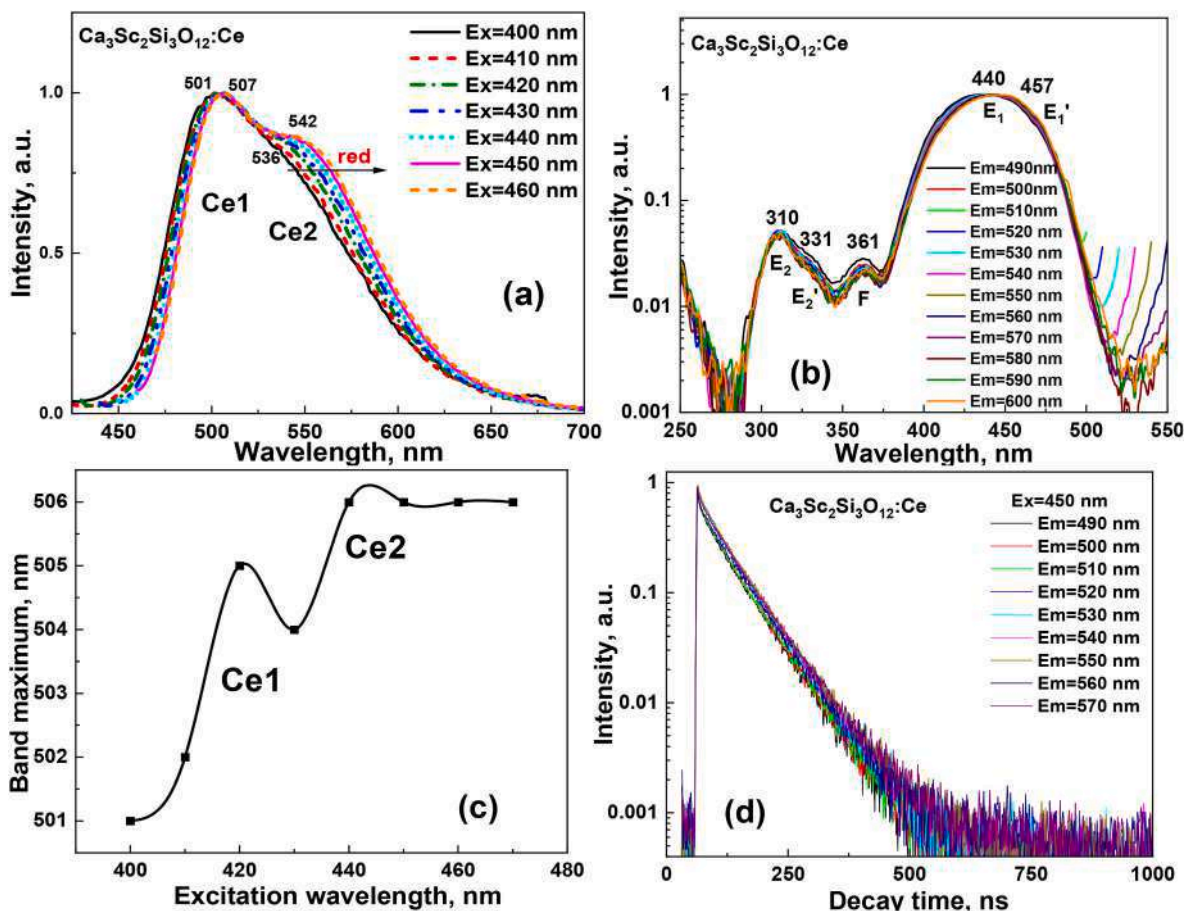


Fig. 3. Details of the luminescent properties of CSSG:Ce crystal at RT. Emission (a) and excitation (b) spectra were recorded in different parts of the respective Ce^{3+} emission/excitation bands. (c) - dependences of the maxima in the peak positions of Ce^{3+} emission bands on the excitation wavelength in CSSG:Ce crystal. (d) PL decay kinetics at RT were recorded under blue light (450 nm) excitation in different parts of the Ce^{3+} emission band.

Table 2

Parameters of three exponential approximation of the decay curves presented in Fig. 3d.

Emission wavelength, nm	t_1 , ns	A_1	t_2 , ns	A_2	t_3 , ns	A_3
490	3.7	148.7	21.7	426.4	64.0	1762.4
500	3.7	144.2	21.7	423.3	64.0	1760.8
510	4.9	1125.7	37.0	1212.1	69.9	2130.8
520	4.8	828.8	27.4	862.8	65.9	2759.4
530	5.8	662.2	31.5	854.6	67.0	2866.9
540	4.4	1005.8	31.8	1169.4	69.1	2828.5
550	3.5	596.4	26.3	820.6	67.4	2865.8
560	2.3	543.9	20.9	382.1	66.9	1569.4
570	5.0	754.7	44.8	1757.8	76.5	1942.3

center, recorded at 570 nm under the same excitation, is significantly large and amounts to 5.0 ns, 44.8 ns and 76.5 ns (see Table 2).

This behavior of the decay curves in CSSG:Ce crystal may also indicate a possible energy transfer from high-energy to low-energy Ce^{3+} centers in this garnet [19,20,24]. Different decay times can correspond to different Ce^{3+} centers in the dodecahedral sites of $\text{Ca}_3\text{Sc}_2\text{Si}_3\text{O}_{12}$ garnet host with various local environments with oxygen ions cations due to the local inhomogeneity at localization of Sc^{3+} and Si^{4+} ions in octahedral and tetrahedral sites, respectively [7].

Spectral characteristics of the different Ce^{3+} multicenters in CSSG:Ce crystal are summarized in Table 3.

Table 3

Spectral characteristics of the different Ce^{3+} multicenters in $\text{Ca}_3\text{Sc}_2\text{Si}_3\text{O}_{12}$:Ce garnet.

Type of centers	Maximum of dominant emission bands, nm	Position of E2 and E1 excitation bands, nm	$\Delta E = E_2 - E_1$, eV	Stokes shift, eV
Ce1	501; 536	312; 434	1.117	0.382
Ce2	506; 542	309; 446	1.233	0.330

5. Low-temperature luminescence under synchrotron radiation

The luminescent properties of the $\text{Ca}_3\text{Sc}_2\text{Si}_3\text{O}_{12}$:Ce crystal were investigated also at 12 K under excitation by SR with an energy in the 3.7–20.6 eV range at the new Superlumi station located at P66 beamline at PETRA storage ring at DESY (Hamburg, Germany) [25]. The PL emission and excitation spectra as well as the PL decay kinetics were measured in time gate between SR pulses with a repetition time of 16 ns and a duration of 0.127 ns.

The emission spectra of $\text{Ca}_3\text{Sc}_2\text{Si}_3\text{O}_{12}$:Ce crystal are shown in Fig. 4. The dominant double luminescence bands peaked in the green-yellow range are related to the $5d^1 \rightarrow 4f$ ($^2F_{5/2,7/2}$) transitions of Ce^{3+} ion in this garnet host. Meanwhile, with increasing the excitation wavelength from 20.64 eV (60 nm) to 4.13 eV (300 nm), the position of emission band of the CSSG:Ce crystal shows the red shift from 493 to 502 nm firstly and then the blue shift from 502 nm to 498 nm (Fig. 4, Table 4). Therefore, the shift of the main maxima of the PL spectra of the CSSG:Ce crystal occurs non-monotonically with increasing the excitation

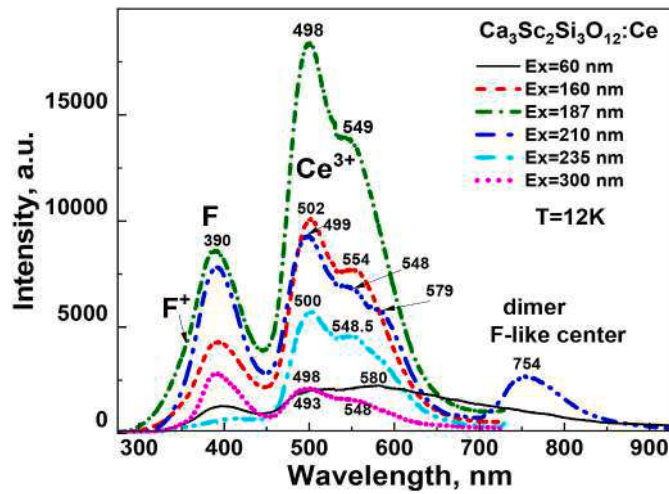


Fig. 4. Luminescence spectra of CSSG:Ce crystal at 12 K under excitation by SR in the interband transition range at 20.63 eV (60 nm) (1), exciton range at 7.74 eV (2) and 6.62 eV (187 nm) (3) as well as in the range of defect band at 5.895 eV (210 nm) (4) and Ce^{3+} absorption band at 5.27 eV (235 nm) (5) and 4.13 eV (300 nm) (6).

Table 4

Spectral characteristics of the different Ce^{3+} multicenters in CSSG:Ce crystal.

Excitation energy, eV	Position of emission bands, nm		Additional bands, nm
20.63	493	580	580
7.74	502	554	
6.62	498	549	
5.89	499	548	579
5.27	500	548.5	
4.13	498	548	

wavelength. Furthermore, the additional peaks at 579–580 nm are well resolved under excitation at 20.64 eV (60 nm) in the range of interband transitions and defect-related band at 5.895 eV (210 nm). Such a behavior of the PL emission spectra clearly indicates the Ce^{3+} multicenter formation in CSSG:Ce garnet. Therefore, the emission spectra of the CSSG:Ce crystal under excitation at the different wavelengths, demonstrate overlapped two pairs of the Ce^{3+} emission bands peaked mainly at 493–502 nm and 548–554 nm ranges (Fig. 4), related to the different Ce1 and Ce2 centers [4,7,26].

Apart from the luminescence of Ce^{3+} ions, other emission bands in the UV range are also present in the emission spectra of CSSG:Ce crystal. The main UV band are peaked at 390 nm in CSSG:Ce crystal. However, the high-energy wing of this band is notably elongated due to the presence of another high-energy emission band of F^+ centers peaked at 355 nm. Taking into account published data on the luminescence of charged oxygen vacancies in the different oxide compounds [4,7,27], the complex UV emission bands with sub-bands peaked in the 388–390 nm and 355–360 nm ranges can correspond to the luminescence of F^+ and F centers (one and two charged oxygen vacancies, respectively) in the garnet hosts. Another low intensity luminescence band peaking at 590 nm on the low-energy wing of Ce^{3+} emission band and well resolved band peaked at 754 nm can be related to the different dimmer or more complicated centers, based on the couples of F^+ and F centers in CSSG host (Fig. 4) [28].

The excitation spectra of Ce^{3+} and defect luminescence in CSSG:Ce crystal in the 60–334 nm (20.7–3.7 eV) range at 12 K, are shown in Fig. 5. Several sets of excitation bands are distinguished in the 3.5–10 eV range. The broad absorption band centered at 5.22 eV (238 nm) is due to $4f \rightarrow 5d_3$ absorption transition of Ce^{3+} ions. The strong bands in the exciton range correspond to creation of excitons bound with different Ce^{3+} centers. Furthermore, some difference in the positions of these

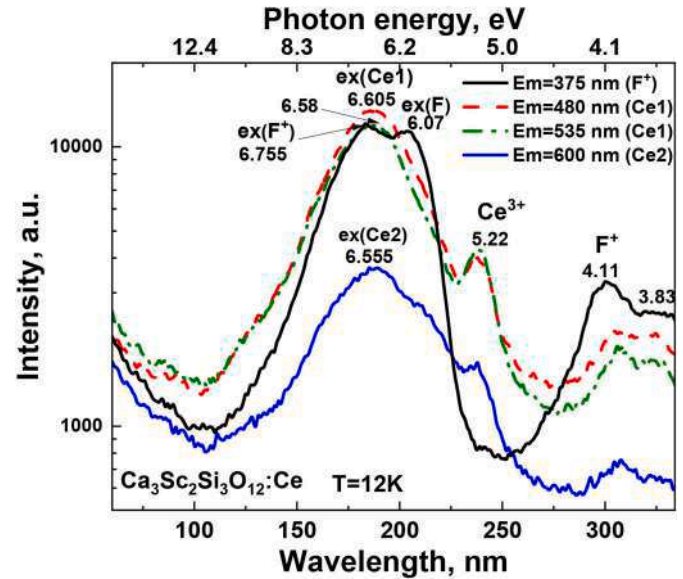


Fig. 5. Excitation spectra of Ce^{3+} -centers in CSSG:Ce crystal at 12 K in the 334–60 nm range (20.66–3.71 eV), monitored at 375 nm (1), 480 nm (2), 535 nm (3) and 600 nm (4).

excitation bands at registration of the Ce^{3+} luminescence at 480–530 nm range and at 600 nm enables the correct determination of the energy creation of excitons bound with Ce1 and Ce2 centers which is equal to 6.605 eV and 6.555 eV, respectively. The notable increase of the intensity of Ce^{3+} luminescence and other emission centers as well in 12–20.6 eV range (Fig. 5b) is caused by the multiplication of the electronic excitations in this energy range [27–31].

The excitation band for luminescence of defect centers, recorded at 375 nm in CSSG:Ce crystal, is mostly associated with intrinsic transitions of F^+ centers in the bands peaked at 323 nm (3.83 eV) and 256 nm (4.83 eV), respectively. Additionally, the prominent band peaked at 183 nm (6.755 eV) in the exciton range aligns with the energy of creation of an excitons bound to this center followed by the electron-hole recombination on these defects [32–34]. However, the strong band peaked at 205.5 nm (6.02 eV) in this excitation spectrum is rather correspond to the F center luminescence and most probably is related to the creation of an exciton bound with F centers. The support of this conclusion is connected with substantial differences in the decay kinetics of the luminescence at 375 nm under excitation in 205.5 nm (6.02 eV) band in comparison with the decay kinetics under excitation in the 323 nm (3.83 eV) and 256 nm (4.83 eV) bands of F^+ centers.

The decay kinetic profiles corresponding to the F and F^+ center luminescence in the CSSG:Ce crystal, recorded at 375 nm, are shown in Fig. 6. Similarly to other Ca^{2+} - Si^{4+} based garnets, the non-exponential decay kinetics of the F^+ center emission most probably is caused by the energy transfer to Ce^{3+} ions. Namely, the values of decay times of the F^+ luminescence in CSSG:Ce crystal, registered at 375 nm under excitation in the 301 nm (4.11 eV) and 323 nm (3.83 eV) bands, are equal to $\tau_2 = 7.2$ ns and $\tau_3 = 4.9$ ns, respectively. Such a behavior of the decay curves of the F^+ center luminescence in the CSSG:Ce crystal can also indicate the possible energy transfer both to high-energy or low-energy Ce^{3+} emitting centers in this garnet. The different decay times of the F^+ center luminescence in the CSSG:Ce crystal can correspond to the excitation of different Ce^{3+} centers in the dodecahedral positions of the garnet lattice with various local surroundings by oxygen and cations (Sc^{3+} and Si^{4+} ions in the octahedral and tetrahedral positions, respectively) [7]. However, the decay profiles of the dominant F center luminescence (Fig. 6) present the fast component with a decay time of $\tau_1 = 2.21$ ns, related to the allowed transitions from singlet excited level and the second slow component corresponding to the partly allowed

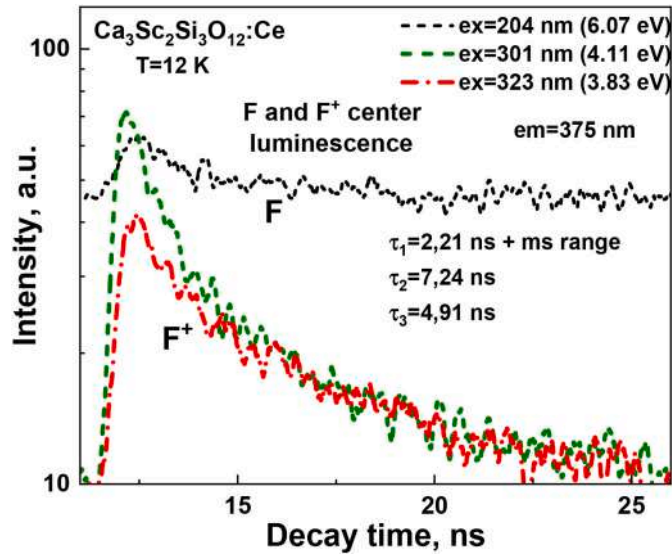


Fig. 6. Decay kinetics of F^+ and F centers luminescence in CSSG:Ce crystal at 12 K under excitation by SR with different wavelengths in the characteristic points of excitation spectra in Fig. 5.

transition in this center from the triplet relaxed level [7,12–16].

6. Photoconversion properties

In order to show the potential applications of the CSSG:Ce crystal phosphor, prototypes of cool white light-emitting diodes (WLEDs) were developed. These WLED prototypes utilized CSSG:Ce crystal phosphor-converters (pc) with varying thickness ranging from 1 to 0.8 mm. These phosphor-converters were coupled with GaN 432 nm blue emitting LED chips. The emission spectrum of these WLEDs covers the visible range, producing cool white light spanning from 458 to 688 nm. Additionally, Fig. 7 illustrates the connection between the photoconverter properties of the CSSG:Ce crystal and the sample's thickness. Notably, as the pc-thickness increases, there is a reduction in the intensity of the blue LED emission, accompanied by a raising in the intensity of the green-yellow emission band. This green-yellow emission reaches its maximum intensity at an approximate thickness of 1.0 mm. We assume that at further increasing the sample thickness beyond 1 mm, it becomes possible to obtain emissions much closer to white light. This has the potential to lead to the achievement of a nearly perfect cool white light

emission with large CCC and CRI values.

In Fig. 7b, the CIE-1931 chromaticity diagram shows the shift in color coordinates (x , y) of the CSSG:Ce crystal across various thicknesses ranging from 0.8 to 1.0 mm. Notably, these coordinates follow a non-linear pattern, with both x and y values as well as CRI and LE values increasing as the thickness of the sample grows. The CIE chromaticity coordinates of the WLED prototypes are detailed in Table 5.

7. Conclusions

The $\text{Ca}_3\text{Sc}_2\text{Si}_3\text{O}_{12}:\text{Ce}$ crystal doped with Ce^{3+} was grown using the μPD method. The actual content of the grown crystal was probed through EDS analysis. Additionally, X-ray microtomography was employed to examine the internal structure of the crystal, specifically targeting the identification of secondary phases distinct from the primary garnet phase.

The luminescence characteristics of the $\text{Ca}_3\text{Sc}_2\text{Si}_3\text{O}_{12}:\text{Ce}$ crystal were explored using conventional cathodoluminescence and photoluminescence as well as luminescent spectroscopy under excitation by synchrotron radiation with energy in the 3.7–20 eV range. The 5d - 4f transitions of Ce^{3+} ions were identified in the form of the dominant emission band both in cathodoluminescence and photoluminescence spectra. The luminescence of F^+ and F center is also observed in the CL and PL spectra in the UV range.

We have also observed the formation of at least two Ce^{3+} centers (Ce1 and Ce2) in the emission and excitation spectra as well as in the decay kinetics of the Ce^{3+} luminescence of $\text{Ca}_3\text{Sc}_2\text{Si}_3\text{O}_{12}:\text{Ce}$ crystal. Such Ce^{3+} centers possess different spectral behaviors (the positions of the emission and excitation bands as well as the PL decay kinetics) due to the different local surroundings and crystal field strength of the respective dodecahedral positions of the garnet host. Such an inhomogeneity of local environment of the dodecahedral positions of the garnet host is caused by the substitution of the octahedral positions by

Table 5

CIE chromaticity coordinates, CTT and luminous efficiency of a WLED lamp fabricated on the base of 450 nm LED chip and CSSG:Ce crystals with different thicknesses.

Thicknesses of the sample, mm	CIE Coordinates		CCT, K	CRI	LE, lm/W
	x	y			
0.8	0.4567	0.5299	3489	39.7	68
0.9	0.4498	0.5306	3580	46.1	81
1	0.4483	0.5341	3620	42.3	107

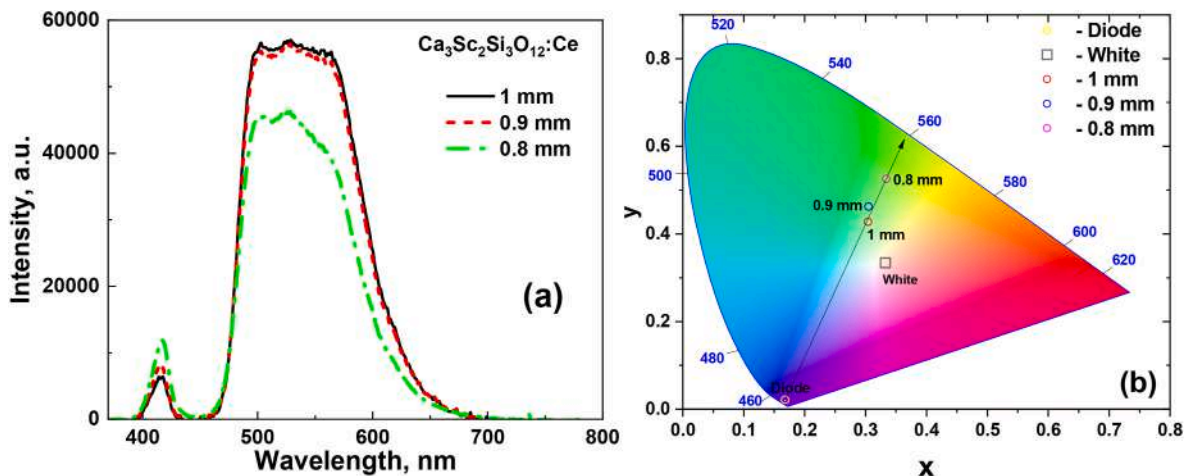


Fig. 7. The spectral characteristics of CSSG:Ce crystals combined with GaN 432 nm blue LED (a); the color coordinates of LEDs based on CSSG:Ce crystals with different thickness in the 0.8–1 mm range within the CIE-1931 color space chromaticity diagram (b).

heterovalent Sc^{3+} ions and the tetrahedral positions by Si^{4+} ions.

Based on the results of optical luminescence investigations, the characteristics of Ce1 and Ce2 center were estimated: the positions of dominant emission bands (501; 536 nm and 506; 542 nm at RT) and excitation bands (312; 434 nm and 309; 446 nm at RT), the Stokes shift (0.382 and 0.330 eV at RT), as well as the energy of creation of an excitons bound with Ce1 and Ce2 centers (6.605 eV and 6.555 eV at 12K), respectively. We have also determined the luminescent characteristics and energetic structure of F^+ and F centers in the CSSG host, including the energy of creation of excitons bound with F and F^+ centers being equal to 6.07 eV and 6.755 eV at 12K, respectively.

Finally, we have investigated the photoconversion properties of $\text{Ca}_3\text{Sc}_2\text{Si}_3\text{O}_{12}:\text{Ce}$ crystals with different thicknesses ranging from 1.0 to 0.8 mm, combined with GaN 432 nm blue LED chip. We suggest that extending the sample thickness above 1 mm may result in emission that exhibits greater proximity to white light characteristics. This can ensure effective matching of different shades of white light devices.

Author contributions

Anna Shakhno performed the measurements and analyzation of the structural, optical and photoconversion properties of CSSG:Ce crystals and participated in the writing and preparation of paper; Mieczysław Cieszek and Zbigniew Szczepański performed structural measurements and analyzed their results; Wojciech Gieszczyk performed growth of the CSSG:Ce crystal; Paweł Bilski managed the crystal preparation; Sandra Witkiewicz-Łukaszek performed cathodoluminescence measurements; Tetiana Zorenko participated in measurements of PL, PLE, and decay kinetics of the samples; Alexei Kotlov supervised the measurements with synchrotron radiation; Yuriy Zorenko analyzed all experimental data and participated in writing and editing of the paper.

Institutional review board statement

Not applicable.

Informed consent statement

Not applicable.

Authors' agreement

We wish to confirm that there are no known conflicts of interest associated with this publication and there has been no significant financial support for this work that could have influenced its outcome.

We confirm that the manuscript has been read and approved by all named authors and that there are no other persons who satisfied the criteria for authorship but are not listed. We further confirm that the order of authors listed in the manuscript has been approved by all of us.

We confirm that we have given due consideration to the protection of intellectual property associated with this work and that there are no impediments to publication, including the timing of publication, with respect to intellectual property. In so doing we confirm that we have followed the regulations of our institutions concerning intellectual property.

2010.2023.

Anna Shakhno.

Declaration of competing interest

We wish to confirm that there are no known conflicts of interest associated with this publication and there has been no significant financial support for this work that could have influenced its outcome.

We confirm that the manuscript has been read and approved by all named authors and that there are no other persons who satisfied the criteria for authorship but are not listed. We further confirm that the

order of authors listed in the manuscript has been approved by all of us.

We confirm that we have given due consideration to the protection of intellectual property associated with this work and that there are no impediments to publication, including the timing of publication, with respect to intellectual property. In so doing we confirm that we have followed the regulations of our institutions concerning intellectual property.

We understand that the Corresponding Author is the contact for the Editorial process (including Editorial Manager and direct communications with the office). He/she is responsible for communicating with the other authors about progress, submissions of revisions and final approval of proofs. We confirm that we have provided a current, correct email address which is accessible by the Corresponding Author and which has been configured to accept email from annshakhno@gmail.com; zorenko@ukw.edu.pl.

Signed by all authors as follows: A. Shakhno, W. Gieszczyk, P. Bilski, S. Witkiewicz-Łukaszek, Tetiana Zorenko, M. Cieszek, Z. Szczepański, A. Kotlov, Yu. Zorenko.

Data availability

Data will be made available on request.

Acknowledgments

The work was performed in the framework of the Polish NCN 2022/45/B/ST8/01757 project and partly supported by the NCN 2018/31/B/ST8/03390 project.

References

- [1] M. Xu, J. Chang, J. Wang, C. Wu, F. Hu, $\text{Al}_2\text{O}_3\text{-YAG:Ce}$ composite ceramics for high-brightness lighting, *Opt Express* 27 (2019) 872, <https://doi.org/10.1364/oe.27.000872>.
- [2] T. Kato, Y. Usui, G. Okada, N. Kawaguchi, T. Yanagida, X-ray induced luminescence properties of Ce-doped single crystal, *Nucl. Instrum. Methods Phys. Res. Sect. A Accel. Spectrom. Detect. Assoc. Equip.* 954 (2020), 161301, <https://doi.org/10.1016/j.nima.2018.09.136>.
- [3] Y. Shimomura, T. Honma, M. Shigeiwa, T. Akai, K. Okamoto, N. Kijima, Photoluminescence and crystal structure of green-emitting $\text{Ca}_3\text{Sc}_2\text{Si}_3\text{O}_{12}:\text{Ce}^{3+}$ phosphor for white light emitting diodes, *J. Electrochem. Soc.* 154 (2007) J35, <https://doi.org/10.1149/1.2388856>.
- [4] V. Gorbunov, T. Zorenko, S. Witkiewicz, K. Paprocki, A. Iskalyeva, A. M. Kaczmarek, R. Van Deun, M.N. Khaidukov, M. Batentschuk, Y. Zorenko, Luminescence of Ce^{3+} multivalent centers in $\text{Ca}^{2+}\text{-Mg}^{2+}\text{-Si}^{4+}$ based garnet phosphors, *J. Lumin.* 199 (2018) 245–250, <https://doi.org/10.1016/j.jlumin.2018.03.058>.
- [5] Y. Liu, X. Zhang, Z. Hao, Y. Luo, X. Wang, L. Ma, J. Zhang, Luminescence and energy transfer in $\text{Ca}_3\text{Sc}_2\text{Si}_3\text{O}_{12}:\text{Ce}^{3+},\text{Mn}^{2+}$ white LED phosphors, *J. Lumin.* 133 (2013) 21–24, <https://doi.org/10.1016/j.jlumin.2011.12.052>.
- [6] K.V. Ivanovskikh, A. Meijerink, F. Piccinelli, A. Speghini, E.I. Zinin, C. Ronda, M. Bettinelli, Optical spectroscopy of $\text{Ca}_3\text{Sc}_2\text{Si}_3\text{O}_{12}$, $\text{Ca}_3\text{Y}_2\text{Si}_3\text{O}_{12}$ and $\text{Ca}_3\text{Lu}_2\text{Si}_3\text{O}_{12}$ doped with Pr^{3+} , *J. Lumin.* 130 (2010) 893–901, <https://doi.org/10.1016/j.jlumin.2009.12.031>.
- [7] I. Levchuk, A. Osvet, C.J. Brabec, M. Batentschuk, A. Shakhno, T. Zorenko, Y. Zorenko, Micro-powder $\text{Ca}_3\text{Sc}_2\text{Si}_3\text{O}_{12}:\text{Ce}$ silicate garnets as efficient light converters for WLEDs, *Opt. Mater.* 107 (2020), 109978, <https://doi.org/10.1016/j.optmat.2020.109978>.
- [8] Y. Chen, M. Gong, K.W. Cheah, Effects of fluxes on the synthesis of $\text{Ca}_3\text{Sc}_2\text{Si}_3\text{O}_{12}:\text{Ce}^{3+}$ green phosphors for white light-emitting diodes, *Mater. Sci. Eng., B* 166 (2010) 24–27, <https://doi.org/10.1016/j.mseb.2009.09.024>.
- [9] Y.-F. Wu, Y.-H. Chan, Y.-T. Nien, I.-G. Chen, Crystal structure and optical performance of Al^{3+} and Ce^{3+} codoped $\text{Ca}_3\text{Sc}_2\text{Si}_3\text{O}_{12}$ green phosphors for white LEDs, *J. Am. Ceram. Soc.* 96 (2012) 234–240, <https://doi.org/10.1111/jace.12034>.
- [10] F. Piccinelli, A. Speghini, G. Mariotto, L. Bovo, M. Bettinelli, Visible luminescence of lanthanide ions in $\text{Ca}_3\text{Sc}_2\text{Si}_3\text{O}_{12}$ and $\text{Ca}_3\text{Y}_2\text{Si}_3\text{O}_{12}$, *J. Rare Earths* 27 (2009) 555–559, [https://doi.org/10.1016/s1002-0721\(08\)60287-2](https://doi.org/10.1016/s1002-0721(08)60287-2).
- [11] S.V. Nizhankovsky, A.Ya Dan'ko, O.V. Zelenskaya, V.A. Tarasov, YuV. Zorenko, V. M. Puzikov, L.A. Grin', A.G. Trushkovskii, V.P. Savchin, Cathodoluminescence and scintillation characteristics of YAG:Ce crystals grown by horizontal directional crystallization in a protective atmosphere, *Tech. Phys. Lett.* 35 (2009) 964–966, <https://doi.org/10.1134/s1063785009100265>.
- [12] Z. Pan, Y. Xu, Q. Hu, W. Li, H. Zhou, Y. Zheng, Combination cation substitution tuning of yellow-orange emitting phosphor $\text{Mg}_2\text{Y}_2\text{Al}_2\text{Si}_2\text{O}_{12}:\text{Ce}^{3+}$, *RSC Adv.* 5 (2015) 9489–9496, <https://doi.org/10.1039/c4ra14425b>.

- [13] M. Raukas, J. Kelso, Y. Zheng, K. Bergenek, D. Eisert, A. Linkov, F. Jermann, Ceramic phosphors for light conversion in LEDs, *ECS J. Solid State Sci. Technol.* 2 (2012) R3168–R3176, <https://doi.org/10.1149/2.023302jss>.
- [14] L.M. Chepyga, A. Osvet, I. Levchuk, A. Ali, Y. Zorenko, V. Gorbenko, T. Zorenko, A. Fedorov, C.J. Brabec, M. Batentschuk, New silicate based thermographic phosphors $\text{Ca}_3\text{Sc}_2\text{Si}_3\text{O}_{12}:\text{Dy}$, $\text{Ca}_3\text{Sc}_2\text{Si}_3\text{O}_{12}:\text{Dy,Ce}$ and their photoluminescence properties, *J. Lumin.* 202 (2018) 13–19, <https://doi.org/10.1016/j.jlumin.2018.05.039>.
- [15] V. Gorbenko, T. Zorenko, A.M. Kaczmarek, R. Van Deun, A. Fedorov, Y. Zorenko, Eu^{3+} multicenter formation and luminescent properties of $\text{Ca}_3\text{Sc}_2\text{Si}_3\text{O}_{12}:\text{Eu}$ and $\text{Ca}_2\text{YScMgSiO}_{12}:\text{Eu}$ single crystalline films, *Opt. Mater.* 90 (2019) 70–75, <https://doi.org/10.1016/j.optmat.2019.02.030>.
- [16] L. Zhou, W. Zhou, F. Pan, R. Shi, L. Huang, H. Liang, P.A. Tanner, X. Du, Y. Huang, Y. Tao, L. Zheng, Spectral properties and energy transfer of a potential solar energy converter, *Chem. Mater.* 28 (2016) 2834–2843, <https://doi.org/10.1021/acs.chemmater.6b00763>.
- [17] Yu.V. Zorenko, A.S. Voloshinovskii, G.M. Stryganyuk, I.V. Konstankevych, Ultraviolet luminescence of single crystals and single-crystal films of YAlO_3 , *Opt. Spectrosc.* 96 (2004) 70–76, <https://doi.org/10.1134/1.1643988>.
- [18] A. Shakhno, A. Markovskiy, T. Zorenko, S. Witkiewicz-Lukaszek, Y. Vlasjuk, A. Osvet, J. Elia, C.J. Brabec, M. Batentschuk, Y. Zorenko, Micropowder $\text{Ca}_2\text{YMgScSi}_3\text{O}_{12}:\text{Ce}$ silicate garnet as an efficient light converter for white LEDs, *Materials* 15 (2022) 3942, <https://doi.org/10.3390/ma15113942>.
- [19] J. Ueda, S. Tanabe, (INVITED) Review of luminescent properties of Ce^{3+} -doped garnet phosphors: new insight into the effect of crystal and electronic structure, *Opt. Mater. X* 1 (2019), 100018, <https://doi.org/10.1016/j.omx.2019.100018>.
- [20] V. Gorbenko, T. Zorenko, P. Pawlowski, A. Iskaliyeva, K. Paprocki, A. Suchocki, Ya Zhydashchevskii, A. Fedorov, N. Khaidukov, R. Van Deun, F. Schröppel, A. Osvet, M. Batentschuk, Yu Zorenko, Luminescent and scintillation properties of Ce^{3+} -doped $\text{Ca}_2\text{RMgScSi}_3\text{O}_{12}$ ($\text{R} = \text{Y, Lu}$) single crystalline films, *J. Lumin.* 195 (2018) 362–370, <https://doi.org/10.1016/j.jlumin.2017.11.052>.
- [21] A.A. Setlur, W.J. Heward, Y. Gao, A.M. Srivastava, R.G. Chandran, M.V. Shankar, Crystal chemistry and luminescence of Ce^{3+} -doped $\text{Lu}_2\text{CaMg}_2(\text{Si,Ge})_3\text{O}_{12}$ and its use in LED based lighting, *Chem. Mater.* 18 (2006) 3314–3322, <https://doi.org/10.1021/cm060898c>.
- [22] M. Tyagi, F. Meng, M. Koschan, S.B. Donnal, H. Rothfuss, C.L. Melcher, Effect of codoping on scintillation and optical properties of a Ce-doped $\text{Gd}_3\text{Ga}_3\text{Al}_2\text{O}_{12}$ scintillator, *J. Phys. D Appl. Phys.* 46 (2013), 475302, <https://doi.org/10.1088/0022-3727/46/47/475302>.
- [23] Y. Wu, F. Meng, Q. Li, M. Koschan, C.L. Melcher, Role of Ce^{4+} in the scintillation mechanism of codoped $\text{Gd}_3\text{Ga}_3\text{Al}_2\text{O}_{12}:\text{Ce}$, *Phys. Rev. Appl.* 2 (2014), <https://doi.org/10.1103/physrevapplied.2.044009>.
- [24] N.M. Khaidukov, I.A. Zhidkova, N.Y. Kirikova, V.N. Makhov, Q. Zhang, R. Shi, H. Liang, Mechanism for bifurcation of broadband luminescence spectra from Ce^{3+} ions at dodecahedral sites in garnets $\{\text{CaY}_2\}[\text{M}_2](\text{Al}_2\text{Si})\text{O}_{12}$ ($\text{M} = \text{Al, Ga, Sc}$), *Dyes Pigments* 148 (2018) 189–195, <https://doi.org/10.1016/j.dyepig.2017.09.012>.
- [25] V. Pankratov, A. Kotlov, Luminescence spectroscopy under synchrotron radiation: from SUPERLUMI to FINESTLUMI, *Nucl. Instrum. Methods Phys. Res. Sect. B Beam Interact. Mater. Atoms* 474 (2020) 35–40, <https://doi.org/10.1016/j.nimb.2020.04.015>.
- [26] A. Yoshikawa, V. Chani, Growth of optical crystals by the micro-pulling-down method, *MRS Bull.* 34 (2009) 266–270, <https://doi.org/10.1557/mrs2009.77>.
- [27] Yu.V. Zorenko, A.S. Voloshinovskii, I.V. Konstankevych, Luminescence of F^+ and F^- centers in YAlO_3 , *Opt. Spectrosc.* 96 (2004) 532–537, <https://doi.org/10.1134/1.1719141>.
- [28] Yu Zorenko, K. Fabisiak, T. Zorenko, A. Mandowski, Q. Xia, M. Batentschuk, J. Friedrich, G. Zhusupkalieva, Comparative study of the luminescence of $\text{Al}_2\text{O}_3:\text{Ce}$ and Al_2O_3 crystals under synchrotron radiation excitation, *J. Lumin.* 144 (2013) 41–44, <https://doi.org/10.1016/j.jlumin.2013.06.043>.
- [29] T. Zorenko, V. Gorbenko, A. Petrosyan, W. Gieszczyk, P. Bilski, Yu Zorenko, Intrinsic and defect-related luminescence of YAlO_3 and LuAlO_3 single crystals and films, *Opt. Mater.* 86 (2018) 376–381, <https://doi.org/10.1016/j.optmat.2018.10.029>.
- [30] P.A. Tanner, L. Fu, L. Ning, B.-M. Cheng, M.G. Brik, Soft synthesis and vacuum ultraviolet spectra of $\text{YAG}:\text{Ce}^{3+}$ nanocrystals: reassignment of Ce^{3+} energy levels, *J. Phys. Condens. Matter* 19 (2007), 216213, <https://doi.org/10.1088/0953-8984/19/21/216213>.
- [31] V. Gorbenko, T. Zorenko, K. Paprocki, A. Iskaliyeva, A. Fedorov, F. Schröppel, I. Levchuk, A. Osvet, M. Batentschuk, Yu Zorenko, Epitaxial growth of single crystalline film phosphors based on the Ce^{3+} -doped $\text{Ca}_2\text{YMgScSi}_3\text{O}_{12}$ garnet, *CrystEngComm* 19 (2017) 3689–3697, <https://doi.org/10.1039/c7ce00630f>.
- [32] V. Gorbenko, T. Zorenko, S. Witkiewicz-Lukaszek, A. Shakhno, A. Osvet, M. Batentschuk, A. Fedorov, Y. Zorenko, Crystallization and investigation of the structural and optical properties of Ce^{3+} -doped $\text{Y}_3-\text{xCaAl}_5-\text{ySi}_2\text{O}_{12}$ single crystalline film phosphors, *Crystals* 11 (2021) 788, <https://doi.org/10.3390/cryst11070788>.
- [33] Y. Zorenko, T. Zorenko, T. Voznyak, A. Mandowski, Q. Xia, M. Batentschuk, J. Friedrich, Luminescence of F^+ and F^- centers in $\text{Al}_2\text{O}_3-\text{Y}_2\text{O}_3$ oxide compounds, *IOP Conf. Ser. Mater. Sci. Eng.* 15 (2010), 012060, <https://doi.org/10.1088/1757-899x/15/1/012060>.
- [34] A. Pujats, M. Springis, The F^- type centres in YAG crystals, *Radiat. Eff. Defect Solid* 155 (2001) 65–69, <https://doi.org/10.1080/10420150108214094>.



Composite color converters based on the $\text{Ca}_3\text{Sc}_2\text{Si}_3\text{O}_{12}:\text{Ce}$ single crystalline films

A. Shakhno^{a,b,*}, S. Witkiewicz-Łukaszek^a, V. Gorbenko^a, T. Zorenko^a, Yu. Zorenko^{a,**}

^a Department of Physics, Kazimierz Wielki University in Bydgoszcz, 85090, Bydgoszcz, Poland

^b Department of Mechatronics, Kazimierz Wielki University in Bydgoszcz, 85090, Bydgoszcz, Poland

ARTICLE INFO

Keywords:

Ca-Si based garnets
 Ce^{3+} dopant
 Liquid phase epitaxy
 Luminescence
 Phosphor-converters
 WLED

ABSTRACT

The study is dedicated to investigation of the structural, luminescent and photoconversion properties of epitaxial converters based on the single crystalline films of Ce^{3+} doped $\text{Ca}_3\text{Sc}_2\text{Si}_3\text{O}_{12}$ (CSSG:Ce) garnet. These SCFs with different thicknesses were grown using the liquid phase epitaxy method onto: (i) undoped $\text{Gd}_3\text{Ga}_{2.5}\text{Al}_{2.5}\text{O}_{12}$ (GAGG (2.5)) substrates; (ii) Ce^{3+} doped $\text{Gd}_3\text{Ga}_{2.5}\text{Al}_{2.5}\text{O}_{12}$ (GAGG:Ce (2.5)) and $\text{Gd}_3\text{Ga}_3\text{Al}_2\text{O}_{12}$ (GAGG:Ce (3)) substrates. For the first time, we have examined the phosphor conversion properties of the mentioned film and film-crystal converters under the excitation of a blue LED. We have established a trend line in the color coordinate diagram by systematically varying the film thickness in the 2–30 μm , 17–22 μm and 7–22 μm ranges for CSSG:Ce film/GAGG (2.5) crystal, CSSG:Ce film/GAGG:Ce (2.5) crystal and CSSG:Ce film/GAGG:Ce (3) crystal composite converters, respectively.

1. Introduction

Currently, white light-emitting diodes (WLEDs) are progressively displacing traditional light sources due to their heightened efficiency relative to the fluorescent tubes or light bulbs. WLEDs are superior to conventional light sources owing to their energy-saving attributes, extended operational longevity, elevated luminous efficacy, and environmentally sustainable characteristics. Furthermore, it is worth noting the absence of mercury and other hazardous components in WLEDs [1, 2].

The manufacture of contemporary WLED lighting systems represents a well-established technology. Typically, this process entails the integration of a blue chip (constructed with GaN and InGaN) with a yellow-emitting $\text{Y}_3\text{Al}_5\text{O}_{12}:\text{Ce}$ (YAG:Ce) powder phosphor converter (pc). These phosphor particles are dispersed within a silica gel or epoxy resin binder, serving to affix the powder phosphors onto the blue LED chips [3–6]. Nonetheless, the limited thermal stability of silicone and epoxy resins leads to alterations in emission color and a decrease in operational lifespan, posing critical challenges in maintaining the long-term performance of the LEDs [7].

In response to this challenge, researchers have undertaken investigations into innovative, robust phosphors which eliminate the need

for resin binders [8,9]. Promising developments include entirely inorganic phosphors, such as transparent ceramics, glass ceramics, single crystalline film and single crystal phosphors [10,11], which can substitute the traditional combination of "phosphor powder" and "organic matrix". These advancements hold significant potential for mitigating the issues associated with the degradation of organic resin matrices. This approach offers a solution to the challenges related to the heat resistance and color stability within LED technology, holding the potential to advance the field significantly.

In addition to thermal stability, the parameters of correlated color temperature (CCT) and color rendering index (CRI) are of paramount significance in the design and development of WLED systems. For this reason, the development of new phosphor materials is an urgent undertaking. This urgency stems from the limitations found with using YAG:Ce as a phosphor converter. These limitations are demonstrated as high CCT and low CRI [12].

The adaptability of the garnet structure, which permits ion substitution within its dodecahedral, octahedral, and tetrahedral sites, offers the potential to alter the YAG garnet to fulfill the demands of WLEDs' applications. In contemporary research, a novel category of garnet phosphors, incorporating Ce^{3+} doping in $\text{A}_3\text{B}_2\text{C}_3\text{O}_{12}$ silicate garnets, where [A] includes Ca, Y, and rare earth ions, [B] consists of Mg, Sc, Al,

* Corresponding author. Department of Physics, Kazimierz Wielki University in Bydgoszcz, 85090, Bydgoszcz, Poland.

** Corresponding author.

E-mail addresses: annshakhno@gmail.com (A. Shakhno), zorenko@ukw.edu.pl (Yu. Zorenko).

<https://doi.org/10.1016/j.omx.2024.100328>

Received 3 January 2024; Received in revised form 20 May 2024; Accepted 27 May 2024

Available online 29 May 2024

2590-1478/© 2024 The Authors. Published by Elsevier B.V. This is an open access article under the CC BY license (<http://creativecommons.org/licenses/by/4.0/>).

Ga, and {C} comprises Ga, Al, Si, is being considered for the development of high-intensity WLEDs [13,14].

Between garnet phosphors based on calcium and silicon, the $\text{Ca}_3\text{Sc}_2\text{Si}_3\text{O}_{12}$ (CSSG) mixed garnet is a famous material, recognized for its compatibility with various rare earth and transition metal ions for doping [15–18]. Indeed, the Ce^{3+} doped CSSG:Ce garnet represents a noteworthy substitute for YAG:Ce garnet, owing to its higher emission intensity and exceptional thermal stability, surpassing those of YAG:Ce [16–22]. According to our previous research, this type of phosphor exhibits a high quantum yield, enabling the effective conversion of excitation energy into emitted light [23]. The utilization of these Ca–Si-based phosphors has the potential to significantly enhance the effectiveness and flexibility of lighting technologies.

This research focuses on the growth of CSSG:Ce single-crystalline films (SCFs) using the liquid phase epitaxy (LPE) technique onto undoped and Ce^{3+} doped $\text{Gd}_3\text{Al}_{5-x}\text{Ga}_x\text{O}_{12}$ ($x = 2.5$ and 3) substrates and application of these epitaxial structures as effective solid-state WLED converters. Structural and luminescent properties of CSSG:Ce SCFs were investigated with using X-ray diffraction, absorption and cathodoluminescence. Furthermore, the photoconversion characteristics of the mentioned epitaxial structures based on the CSSG:Ce SCFs with various thicknesses and GAGG:Ce ($x = 2.5$ and 3) substrates with different gallium contents were investigated for the first time.

2. SCF growth and experimental techniques

Three different sets of SCFs with nominal compositions of CSSG:Ce, with thicknesses ranging from 6 to 30 μm , were prepared using the LPE method. The films were crystallized within a temperature range of 975–990 $^{\circ}\text{C}$ from a supercooling melt-solution based on $\text{PbO-B}_2\text{O}_3$ (12:1 mole/mole) flux. The growth of CSSG:Ce SCFs were performed onto undoped GAGG (2.5) substrate (serie A) and two Ce^{3+} doped GAGG:Ce (2.5) substrates (serie B) and GAGG:Ce (3) substrates (serie C) with orientation close to (100). The thickness of GAGG and GAGG:Ce substrates was equal to 0.9 mm. The Ce content both in $\text{Ca}_3\text{Sc}_2\text{Si}_3\text{O}_{12}$:Ce SCFs and GAGG:Ce substrates was about of 0.09–1 at. %. The details of the growth process for the Ca–Si-based films and the selection of respective mole ratios for this growth can be found in the references [22, 24,25].

The SCF thickness h (μm) was measured using weighing method on the high-precision scales. This method involved weighing the substrate both before and after the SCF growth cycle. The thickness of the SCF was calculated using the formula: $h = (\mathbf{m} - \mathbf{m}_s) / 2 \cdot \mathbf{S} \cdot \rho$, where \mathbf{m} is the mass of the substrate with the grown single crystalline film in (g), \mathbf{m}_s is the mass of the substrate (g), \mathbf{S} is the area of the substrate (cm^2), and ρ is the density of the film (g/cm^3) ($\rho = 3.52 \text{ g}/\text{cm}^3$ for CSSG [26]).

The real composition of SCF samples was determined using a KEYENCE VHX-7000 Digital Microscope (Mechelen, Belgium) equipped a Laser-based Elemental Analyzer. This device facilitates quick analysis of the material, ensuring the accuracy and efficiency of the evaluation process. Namely, this microscope enabled control and precise assessment of deviations in the cation content in samples up to $\pm 5\%$ accuracy. Indeed, the obtained results indicate some deviation in the content of Ca, Sc and Si cations in the tested SCF samples with respect to the stoichiometric formula $\text{Ca}_3\text{Sc}_2\text{Si}_3\text{O}_{12}$ with accuracy less than ± 0.15 formula untint (Table 1). For this reason, throughout the whole paper, we will use the indication of the nominal composition of the SCFs.

The structural quality of CSSG:Ce SCFs on the different GAGG substrates was assessed using XRD measurements conducted with a DRON 4 spectrometer and a $\text{CuK}\alpha$ X-ray source. For these measurements we selected a particular $\text{Ca}_3\text{Sc}_2\text{Si}_3\text{O}_{12}$ SCF C1 sample with a Ce^{3+} content of 0.095 at.% and thickness equal to 6 μm (Fig. 1). Typically, the test sample, with a thickness less than 10 μm , is used to confirm the single crystallinity of the films of the specified compound onto GAGG substrate. The limitation of thickness of the test sample, within the range of a few micrometres, follows from the considerable X-ray absorption in

Table 1

The nominal composition (in melt-solution) and the real composition of LPE grown CSSG:Ce SCFs of A, B and C series.

Sample	Nominal content	Real SCF content
A1	$\text{Ca}_3\text{Sc}_2\text{Si}_3\text{O}_{12}$:Ce	$\text{Ca}_{3.12}\text{Sc}_{1.8}\text{Si}_{3.08}\text{O}_{12}$:Ce
A2	$\text{Ca}_3\text{Sc}_2\text{Si}_3\text{O}_{12}$:Ce	$\text{Ca}_{3.1}\text{Sc}_{1.87}\text{Si}_{3.07}\text{O}_{12}$:Ce
A3	$\text{Ca}_3\text{Sc}_2\text{Si}_3\text{O}_{12}$:Ce	$\text{Ca}_{3.05}\text{Sc}_{1.94}\text{Si}_{3.01}\text{O}_{12}$:Ce
B1	$\text{Ca}_3\text{Sc}_2\text{Si}_3\text{O}_{12}$:Ce	$\text{Ca}_{2.95}\text{Sc}_{2.13}\text{Si}_{2.92}\text{O}_{12}$:Ce
B2	$\text{Ca}_3\text{Sc}_2\text{Si}_3\text{O}_{12}$:Ce	$\text{Ca}_{2.97}\text{Sc}_{2.08}\text{Si}_{2.95}\text{O}_{12}$:Ce
B3	$\text{Ca}_3\text{Sc}_2\text{Si}_3\text{O}_{12}$:Ce	$\text{Ca}_{2.98}\text{Sc}_{2.06}\text{Si}_{2.96}\text{O}_{12}$:Ce
C1	$\text{Ca}_3\text{Sc}_2\text{Si}_3\text{O}_{12}$:Ce	$\text{Ca}_{3.01}\text{Sc}_{1.99}\text{Si}_{2.98}\text{O}_{12}$:Ce
C2	$\text{Ca}_3\text{Sc}_2\text{Si}_3\text{O}_{12}$:Ce	$\text{Ca}_{3.03}\text{Sc}_{1.95}\text{Si}_{3.02}\text{O}_{12}$:Ce
C3	$\text{Ca}_3\text{Sc}_2\text{Si}_3\text{O}_{12}$:Ce	$\text{Ca}_{3.05}\text{Sc}_{1.93}\text{Si}_{3.02}\text{O}_{12}$:Ce

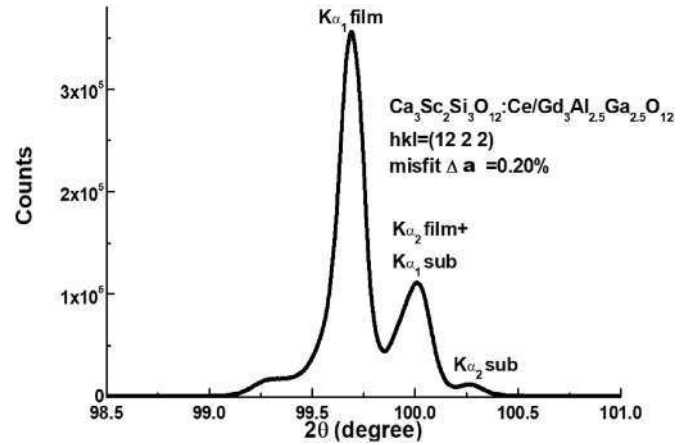


Fig. 1. XRD patterns of (12 2 2) plane of $\text{Ca}_3\text{Sc}_2\text{Si}_3\text{O}_{12}$:Ce A3 SCF grown onto GAGG (2.5) substrate.

the investigated garnet matrices. Therefore, the intensity of reflections from the GAGG substrate diminishes as the film thickness increases. This verification occurs before growing the main set of samples, which have higher thicknesses and can reach up to even 100 μm .

Based on the XRD pattern for (1222) plane of sample, we have calculated the misfit between the lattice constants of SCFs and the GAGG substrate. The misfit, represented as $\Delta a = (a_{\text{SCF}} - a_{\text{sub}}) / a_{\text{sub}} \cdot 100\%$, was determined to be 0.2 %, as illustrated in Fig. 1. This result serves as a confirmation of the high crystalline quality exhibited by the chosen SCF sample.

To analyze the characteristics of the three sets of SCF samples (A, B, and C), the following spectroscopic techniques were used. Absorption spectra and cathodoluminescence (CL) spectra were employed to characterize the luminescent properties of the CSSG:Ce SCFs. These spectra were measured at room temperature (RT). The SCFs' absorption spectra were obtained using a Jasco V730 spectrophotometer. The CL spectra were measured with using a JEOL JSM-6390LV scanning electron microscope (SEM) as e-beam source. This SEM was equipped also with a Stellar Net spectrometer, completed with a cooled TE-detector CCD, functioning within the 200–1200 nm range.

Measurements of photoconversion spectra of epitaxial structures based on the CSSG:Ce SCFs with thickness in the 2–30 μm range, grown using LPE method onto GAGG (2.5), GAGG:Ce (2.5) and GAGG:Ce (3) substrates, were conducted using an AvaSpec-ULS 2048-LTEC fiber-optic spectrophotometer along with an AvaSphere-50-IRRAD integrating sphere (Avantes, Netherlands).

3. Absorption and luminescent properties

3.1. Absorption spectra

The absorption spectra of the chosen samples of composite epitaxial

structures, containing the CSSG:Ce SCFs grown onto GAGG (2.5) (series A), GAGG:Ce (2.5) (series B), and GAGG:Ce (3.0) (series C) substrates, are illustrated in Fig. 2. To present these spectra, we chose representative SCF samples from each series based on their average thickness. Specifically, for series A, B and C, we selected A3, B2 and C3 SCF samples with a thickness of 10 μm , 18 μm , and of 19 μm , respectively (Table 1). The absorption spectra of these SCFs display several bands within the 200–500 nm range. The broad absorption bands at 341 nm and 440 nm (marked as E_2 and E_1 bands, respectively) observed in all composite structures are attributed to the transitions from $4f$ ($^2F_{5/2}$) to $5d_1$ (2E) levels of Ce^{3+} ions [27]. The distinct peaks at 275 and 311 nm in the absorption spectra correspond to the $^8S_{7/2} \rightarrow ^6I_{3/2}$, and $^8S_{7/2} \rightarrow ^6P_{7/2}$ transitions of Gd^{3+} ions in GAGG based substrates [28–30]. The first absorption band of Gd^{3+} ions overlaps with the absorption band around 256 nm, attributed to the intrinsic $^1S_0 \rightarrow ^3P_1$ transitions of Pb^{2+} flux-related impurity in the SCF samples [31–33]. Other absorption band of Pb^{2+} impurity at 212 nm corresponds to the $^1S_0 \rightarrow ^1P_1$ transitions

3.2. CL spectra

The RT CL spectra CSSG:Ce SCF/GAGG (2.5) SC, CSSG:Ce SCF/GAGG:Ce (2.5) SC, and CSSG:Ce/GAGG:Ce (3) SC are depicted in Fig. 3a, b, c in comparison with CL spectra GAGG:Ce (2.5) substrates as reference samples (Fig. 3c).

Fig. 3c shows the emission spectra of GAGG:Ce crystals with different Ga concentrations (2.5 and 3), which were used as substrates for the growing films. The dominant luminescent bands in these crystal samples, correspond to the $5d_1 \rightarrow 4f$ ($^2F_{5/2,7/2}$) transitions of Ce^{3+} ions. As the gallium content decreases from 3 to 2.5, a minor red shift in the position of the Ce^{3+} luminescence band from 551 to 547 nm is observed. This shift is due to the increase of the crystal field strength in the dodecahedral positions of garnet host, where the Ce^{3+} ions are localized, as a result of the change in the centroid shift. Namely, this centroid shift increases with an increase in the polarizability of the anion and a decrease in the average electronegativity of the matrix cations, e. g. as a result of decrease in the contribution Ga– O^{2-} bonds with large covalency compared to Al^{3+} – O^{2-} bonds [34].

Fig. 3a, b and 3c display the CL spectra of the film parts of CSSG:Ce SCFs/GAGG (2.5) SC, CSSG:Ce SCFs/GAGG:Ce (2.5) SC and CSSG:Ce SCFs/GAGG:Ce SC epitaxial structures, respectively. These figures consist of the Ce^{3+} emission spectra in the form of typical double emission bands centered at 516–520 nm and 544–550 nm ranges, corresponding to the $5d_1 \rightarrow 4f$ ($^2F_{5/2,7/2}$) transitions of Ce^{3+} ions positioned

in the dodecahedral sites of the garnet host [17,23]. The spectra demonstrate the effects of replacing Y^{3+} and Al^{3+} cations with Ca^{2+} , Sc^{3+} , and Si^{4+} in the dodecahedral, octahedral, and tetrahedral positions of the $\text{Y}_3\text{Al}_5\text{O}_{12}$ garnet lattice. This cation substitution causes a significant shift of over 25 nm in the maximum Ce^{3+} emission band towards the blue spectrum, altering it from 540 nm to between 513 and 519 nm, in contrast to the YAG:Ce single crystal [35]. A small differences in the positions of Ce^{3+} emission bands in the CL spectra (Fig. 3) probably is mainly connected with various rate of the self-absorption of the Ce^{3+} luminescence by respective absorption bands in SCF samples with different thickness and some very small deviation in the Ca^{2+} , Sc^{3+} and Si^{4+} content at growth of CSSG:Ce SCF samples onto the different GAGG substrates (Table 1). The sharp peak at 311 nm, observed in Fig. 3, b-d, corresponds to the $^8S_{7/2} \rightarrow ^6P_{7/2}$ transitions of Gd^{3+} trace impurity in SCF samples due to the dissolving part of GAGG substrates in the initial stage of LPE growth.

4. Photoconversion properties

To confirm the conversion properties of CSSG:Ce SCFs and composite converters on their base in white solid-state lighting applications, Fig. 4a, b, and 4c illustrate the emission spectra of a blue LED chip combined with CSSG:Ce SCFs grown onto GAGG (2.5), GAGG:Ce (2.5) and GAGG:Ce (3) substrates, correspondingly. The emission spectra of these prototypes of WLEDs are quite broad, covering the entire visible range from 410 to 780 nm [23]. To simplify the description of the emission spectrum, the spectra are typically segmented into blue and yellow components. The blue component corresponds to the emission of the blue LED, while the yellow component is attributed to the Ce^{3+} luminescence within the garnet matrix. With an increase in CSSG:Ce film thickness, there is a noticeable increase in the intensity of the yellow component, while the intensity of the blue component remains largely unchanged. It can be attributed to the maximum light yield of this component at a specific concentration of Ce^{3+} ions in the films when excited by a blue LED with a defined spectral characteristic.

The photoconversion spectra presented in Fig. 4 reveal that the CSSG:Ce SCF/GAGG:Ce SC (2.5) composite structure exhibits the most intense yellow component. The emission spectra of the CSSG:Ce SCFs/GAGG:Ce (3) SC structures display an average intensity of the yellow component.

CSSG:Ce SCFs/GAGG:Ce (3) SC structures display an average intensity of the yellow component. However, for the CSSG:Ce SCFs grown on GAGG (2.5) substrates without cerium dopant, the intensity of yellow component is weak (Fig. 4a) due to the very low thickness of SCF samples in the 6–30 range.

For comparative analysis, three trend lines for CSSG SCFs grown with different substrates (GAGG (2.5), GAGG:Ce (2.5) and GAGG (3.0)) are shown on the chromaticity color diagram (Fig. 5). The chromaticity color coordinates of the combination of excitation and emission light from CSSG:Ce SCF/GAGG (2.5) SCs have a tendency to shift towards the green region of radiation. However, due to the low intensity of the yellow component at film thicknesses ranging from 6 to 30 μm , they shifted only to the light blue region of emission. This shift can be significantly improved by using CSSG:Ce films thicker than 30 μm .

The measured photoconversion properties strongly indicate the potential of CSSG:Ce SCFs and composite structure on their base for the creation of WLED lighting systems. Table 2 provides details on the CIE chromaticity coordinates, CRI, and CCT of the WLED prototypes, underscoring their capability to provide useful lighting characteristics.

The chromaticity diagram for CSSG:Ce SCF/GAGG:Ce (2.5) SC and CSSG:Ce SCF/GAGG:Ce (3) SC structures show the tendency to shift towards the yellow-green range of radiation with increasing SCF thicknesses. However, the CSSG:Ce SCF; $h = 17 \mu\text{m}$ /GAGG:Ce (2.5) SC and CSSG:Ce SCF, $h = 22 \mu\text{m}$ /GAGG:Ce (3) SC structures show the best conversion properties. Such epitaxial structures give practically ideal white light with CCT 6558 K and 6672 K at enough useful values of CRI

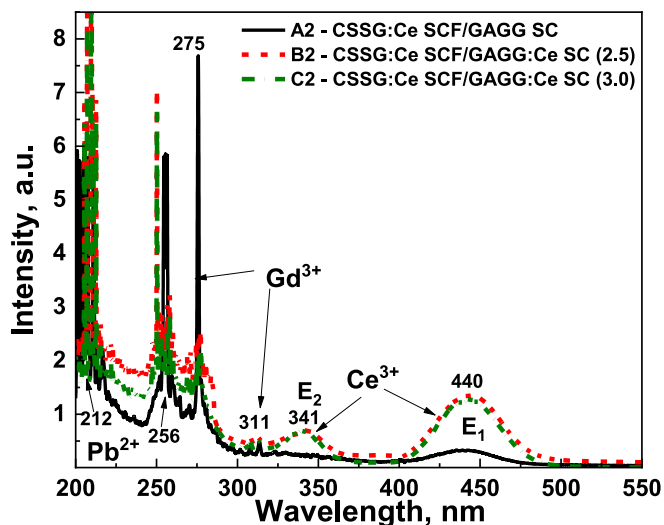


Fig. 2. RT absorption spectra (in log scale) of CSSG:Ce films grown onto GAGG (2.5) (1 curve), GAGG:Ce (2.5) (2 curve) and GAGG:Ce (3.0) (3 curve).

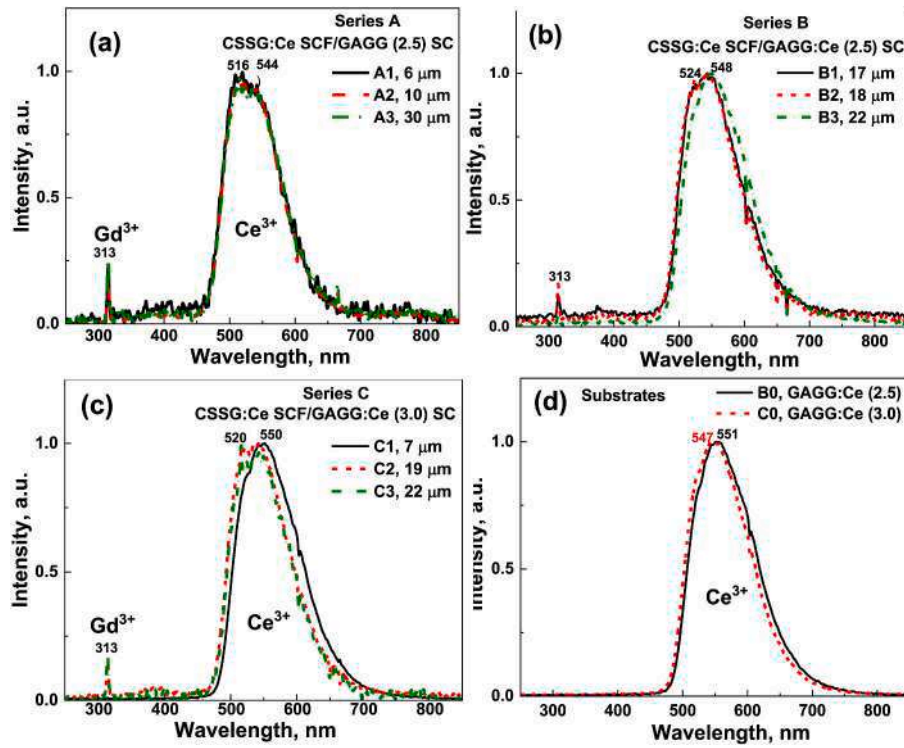


Fig. 3. RT CL spectra of CSSG:Ce films grown onto GAGG (2.5) (a), GAGG:Ce (2.5) (b) and GAGG:Ce (3.0) (c) substrates in comparison with CL spectra of GAGG:Ce crystals with different gallium content (d).

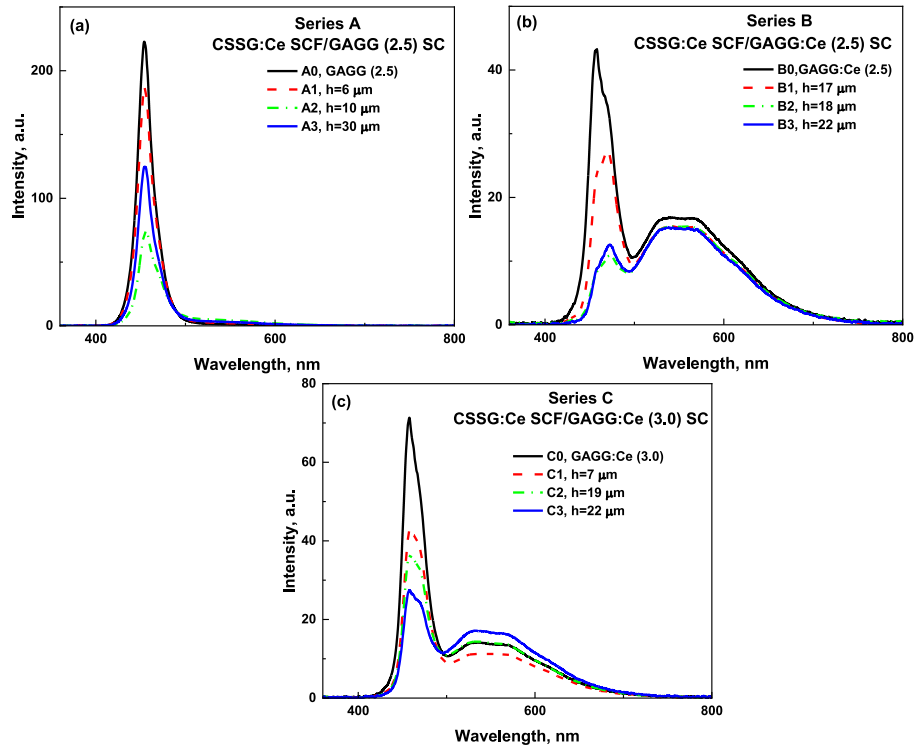


Fig. 4. Emission spectrum (a, b, c) and chromaticity diagram (d) of a WLED lamp fabricated on the base of 450 nm LED chip and $Ce_3Sc_2Si_3O_{12}:Ce$ thin films on GAGG substrates.

being equal to 74 and 72, respectively (see Table 2).

5. Conclusions

Three sets of CSSG:Ce single crystalline films with different thicknesses in the 6–30 μm range were grown using the liquid phase epitaxy

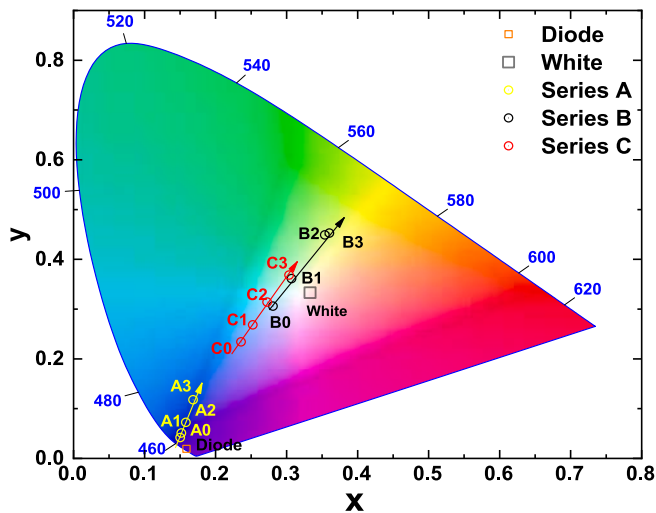


Fig. 5. Chromaticity diagram of a WLED prototype fabricated on the base of 450 nm LED chip and CSSG:Ce SCFs grown onto GAGG 2.5 (series A), GAGG:Ce 2.5 (series B) and GAGG 3 (series C) substrates. The results for GAGG:Ce (2.5) and GAGG:Ce (3) substrates are presented for comparison.

Table 2

Comparison of the CRI, CCT and CIE coordinates of epitaxial structures based on the CSSG:Ce SCF samples grown onto GAGG (2.5), GAGG:Ce (2.5) and GAGG:Ce (3.0) substrates.

Samples		SCF thickness	CIE coordinates		CCT, K	CRI
			x	y		
Series A						
A0	GAGG (2.5) SC	900 μm	0.15	0.04	1620	–
A1	CSSG:Ce SCF/GAGG (2.5) SC	6 μm	0.17	0.12	3243	20
A2	CSSG:Ce SCF/GAGG (2.5) SC	10 μm	0.15	0.05	1625	–
A3	CSSG:Ce SCF/GAGG (2.5) SC	30 μm	0.16	0.07	1726	–
Series B						
B0	GAGG:Ce (2.5) SC	900 μm	0.28	0.31	9146	80
B1	CSSG:Ce SCF/(GAGG:Ce (2.5) SC	17 μm	0.307	0.36	6558	74
B2	CSSG:Ce SCF/(GAGG:Ce (2.5) SC	18 μm	0.35	0.45	4975	65
B3	CSSG:Ce SCF/(GAGG:Ce (2.5) SC	22 μm	0.36	0.45	4839	66
Series C						
C0	GAGG:Ce (3) SC	900 μm	0.24	0.23	–	–
C1	CSSG:Ce SCF/GAGG:Ce (3) SC	7 μm	0.25	0.27	9523	76
C2	CSSG:Ce SCF/GAGG:Ce (3) SC	19 μm	0.27	0.31	9479	75
C3	CSSG:Ce SCF/GAGG:Ce (3) SC	22 μm	0.30	0.37	6672	72

method from melt-solutions based on the $\text{PbO-B}_2\text{O}_3$ flux onto undoped $\text{Gd}_3\text{Ga}_{2.5}\text{Al}_{2.5}\text{O}_{12}$ (GAGG (2.5)) crystal substrates as well as Ce^{3+} doped $\text{Gd}_3\text{Ga}_{2.5}\text{Al}_{2.5}\text{O}_{12}$ (GAGG:Ce (2.5)) and $\text{Gd}_3\text{Ga}_3\text{Al}_2\text{O}_{12}$ (GAGG:Ce (3)) crystal substrates. The single crystallinity of the films was confirmed by the respective XRD pattern of the selected CSSG:Ce film/GAGG crystal sample.

The optical behavior of film and composite converters was investigated using absorption and cathodoluminescence spectra. Furthermore, the phosphor conversion properties of the mentioned film and film-crystal converters were examined for first time under the excitation of

a blue 454 nm LED. We have established also a trend line in the color coordinate diagram by systematically varying the film thickness in the 6–30 μm , 17–22 μm and 7–22 μm ranges for CSSG:Ce film/GAGG (2.5) crystal, CSSG:Ce film/GAGG:Ce (2.5) crystal and CSSG:Ce film/GAGG:Ce (3) crystal composite converters, respectively.

The application potential of the developed CSSG:Ce film/GAGG:Ce crystal composite phosphors was demonstrated. Such composite phosphors for WLEDs, containing the Ce-doped GAGG:Ce crystal converter, and additionally CSSG:Ce film converter, the mixing of emissions from the film and substrate converters can be used for better tuning of CRI coordinates and color temperature of WLEDs in comparison to conventional YAG:Ce crystals counterpart. Indeed, samples of CSSG:Ce film/(GAGG:Ce (2.5) crystal and CSSG:Ce film/GAGG:Ce (3) crystal composite converters with film thickness 17 and 22 μm show the best conversion properties from all samples under study and close to ideal white light with CCT 6558 K and 6672 K, respectively.

CRediT authorship contribution statement

A. Shakhno: Writing – original draft, Investigation, Data curation. **S. Witkiewicz-Lukaszek:** Investigation. **V. Gorbenko:** Methodology. **T. Zorenko:** Investigation. **Yu. Zorenko:** Writing – review & editing, Supervision.

Declaration of competing interest

We wish to confirm that there are no known conflicts of interest associated with this publication and there has been no significant financial support for this work that could have influenced its outcome.

We confirm that the manuscript has been read and approved by all named authors and that there are no other persons who satisfied the criteria for authorship but are not listed. We further confirm that the order of authors listed in the manuscript has been approved by all of us.

We confirm that we have given due consideration to the protection of intellectual property associated with this work and that there are no impediments to publication, including the timing of publication, with respect to intellectual property. In so doing we confirm that we have followed the regulations of our institutions concerning intellectual property.

We understand that the Corresponding Author is the contact for the Editorial process (including Editorial Manager and direct communications with the office). He/she is responsible for communicating with the other authors about progress, submissions of revisions and final approval of proofs. We confirm that we have provided a current, correct email address which is accessible by the Corresponding Author and which has been configured to accept email from annshakhno@gmail.com; zorenko@ukw.edu.pl.

Data availability

Data will be made available on request.

Acknowledgments

The work was performed in the frames of Polish NCN 2022/45/B/ST8/01757 project and partly supported by Ministry of Science and Education of Poland in frame RID/SP/0048/2024/01 project.

References

- [1] P.M. Pattison, S. Bland, N. Bardsley, L. Pattison, Solid-state lighting research and development multi-year program plan, Unpublished, <https://doi.org/10.13140/2.1.2485.1520>, 2014.
- [2] C.C. Lin, W.-T. Chen, R.S. Liu, Phosphors for white LEDs, handbook of advanced lighting technology, 181–222, https://doi.org/10.1007/978-3-319-00176-0_15, 2017.

- [3] C.-C. Sun, Y.-Y. Chang, T.-H. Yang, T.-Y. Chung, C.-C. Chen, T.-X. Lee, D.-R. Li, C.-Y. Lu, Z.-Y. Ting, B. Glorieux, Y.-C. Chen, K.-Y. Lai, C.-Y. Liu, Packaging efficiency in phosphor-converted white LEDs and its impact to the limit of luminous efficacy, *J Sol State Light* 1 (2014), <https://doi.org/10.1186/s40539-014-0019-0>.
- [4] S. Nakamura, M. Senoh, N. Iwasa, S. Nagahama, T. Yamada, T. Mukai, Superbright green InGaN single-quantum-well-structure light-emitting diodes, *Jpn. J. Appl. Phys.* 34 (1995) L1332, <https://doi.org/10.1143/jjap.34.L1332>.
- [5] P. Schlöter, R. Schmidt, J. Schneider, Luminescence conversion of blue light emitting diodes, *Appl. Phys. Mater. Sci. Process* 64 (1997) 417–418, <https://doi.org/10.1007/s003390050498>.
- [6] Y. Zhong, P. Sun, X. Gao, Q. Liu, S. Huang, B. Liu, B. Deng, R. Yu, Synthesis and optical properties of new red-emitting $\text{SrBi}_2\text{Ta}_2\text{O}_9:\text{Eu}^{3+}$ phosphor application for w-LEDs commercially based on InGaN, *J. Lumin.* 212 (2019) 45–51, <https://doi.org/10.1016/j.jlumin.2019.03.057>.
- [7] K. Bando, K. Sakano, Y. Noguchi, Y. Shimizu, Development of high-bright and pure-white LED lamps, *J. Light Vis. Environ.* 22 (1998) 2–5, https://doi.org/10.2150/jlve.22.1_2.
- [8] S. Nishiura, S. Tanabe, K. Fujioka, Y. Fujimoto, Properties of transparent Ce:YAG ceramic phosphors for white LED, *Opt. Mater.* 33 (2011) 688–691, <https://doi.org/10.1016/j.optmat.2010.06.005>.
- [9] S. Fujita, A. Sakamoto, S. Tanabe, Luminescence characteristics of YAG glass-ceramic phosphor for white LED, *IEEE J. Sel. Top. Quant. Electron.* 14 (2008) 1387–1391, <https://doi.org/10.1109/jstqe.2008.920285>.
- [10] S. Fujita, S. Tanabe, Thermal quenching of $\text{Ce}^{3+}:\text{Y}_3\text{Al}_5\text{O}_{12}$ Glass-ceramic phosphor, *Jpn. J. Appl. Phys.* 48 (2009) 120210, <https://doi.org/10.1143/jjap.48.120210>.
- [11] Q. Sai, Z. Zhao, C. Xia, X. Xu, F. Wu, J. Di, L. Wang, Ce-doped Al_2O_3 -YAG eutectic and its application for white LEDs, *Opt. Mater.* 35 (2013) 2155–2159, <https://doi.org/10.1016/j.optmat.2013.05.035>.
- [12] Z. Wang, R. Zheng, K. Yu, C. Liu, W. Wei, The establishment and YAG:Ce-based WLED application of simulation data generation platform of light sources' color characteristics, *Opt Commun.* 434 (2019) 230–238, <https://doi.org/10.1016/j.optcom.2018.10.048>.
- [13] Z. Xia, A. Meijerink, Ce^{3+} -Doped garnet phosphors: composition modification, luminescence properties and applications, *Chem. Soc. Rev.* 46 (2017) 275–299, <https://doi.org/10.1039/c6cs00551a>.
- [14] Y.-C. Lin, M. Bettinelli, M. Karlsson, Unraveling the mechanisms of thermal quenching of luminescence in Ce^{3+} -doped garnet phosphors, *Chem. Mater.* 31 (2019) 3851–3862, <https://doi.org/10.1021/acs.chemmater.8b05300>.
- [15] M. Shang, J. Fan, H. Lian, Y. Zhang, D. Geng, J. Lin, A double substitution of $\text{Mg}^{2+}:\text{Si}^{4+}/\text{Ge}^{4+}$ for $\text{Al}(\text{I})^{3+}-\text{Al}(\text{II})^{3+}$ in Ce^{3+} -doped garnet phosphor for white LEDs, *Inorg. Chem.* 53 (2014) 7748–7755, <https://doi.org/10.1021/ic501063j>.
- [16] D. Pasiński, E. Zych, J. Sokolnicki, Relationship between structure and luminescence properties in Ce^{3+} or Ce^{3+} , Mn^{2+} -doped garnet phosphors for use in white LEDs, *J. Lumin.* 169 (2016) 862–867, <https://doi.org/10.1016/j.jlumin.2015.02.044>.
- [17] V. Gorbenco, T. Zorenko, S. Witkiewicz, K. Paprocki, A. Iskalyeva, A. M. Kaczmarek, R. Van Deun, M.N. Khaidukov, M. Batentschuk, Y. Zorenko, Luminescence of Ce^{3+} multicolors in $\text{Ca}^{2+}-\text{Mg}^{2+}-\text{Si}^{4+}$ based garnet phosphors, *J. Lumin.* 199 (2018) 245–250, <https://doi.org/10.1016/j.jlumin.2018.03.058>.
- [18] Y. Shimomura, T. Honma, M. Shigeiwa, T. Akai, K. Okamoto, N. Kijima, Photoluminescence and crystal structure of green-emitting $\text{Ca}_3\text{Sc}_2\text{Si}_3\text{O}_{12}:\text{Ce}^{3+}$ phosphor for white light emitting diodes, *J. Electrochem. Soc.* 154 (2007) J35, <https://doi.org/10.1149/1.2388856>.
- [19] N. Khaidukov, T. Zorenko, A. Iskalyeva, K. Paprocki, M. Batentschuk, A. Osvet, R. Van Deun, Ya. Zhydzaczevskii, A. Suchocki, Yu. Zorenko, Synthesis and luminescent properties of prospective Ce^{3+} doped silicate garnet phosphors for white LED converters, *J. Lumin.* 192 (2017) 328–336, <https://doi.org/10.1016/j.jlumin.2017.06.068>.
- [20] K.V. Ivanovskikh, A. Meijerink, F. Piccinelli, A. Speghini, E.I. Zinin, C. Ronda, M. Bettinelli, Optical spectroscopy of $\text{Ca}_3\text{Sc}_2\text{Si}_3\text{O}_{12}$, $\text{Ca}_3\text{Y}_2\text{Si}_3\text{O}_{12}$ and $\text{Ca}_3\text{Lu}_2\text{Si}_3\text{O}_{12}$ doped with Pr^{3+} , *J. Lumin.* 130 (2010) 893–901, <https://doi.org/10.1016/j.jlumin.2009.12.031>.
- [21] L.M. Chepyga, A. Osvet, I. Levchuk, A. Ali, Y. Zorenko, V. Gorbenco, T. Zorenko, A. Fedorov, C.J. Brabec, M. Batentschuk, New silicate based thermographic phosphors $\text{Ca}_3\text{Sc}_2\text{Si}_3\text{O}_{12}:\text{Dy}$, $\text{Ca}_3\text{Sc}_2\text{Si}_3\text{O}_{12}:\text{Dy,Ce}$ and their photoluminescence properties, *J. Lumin.* 202 (2018) 13–19, <https://doi.org/10.1016/j.jlumin.2018.05.039>.
- [22] V. Gorbenco, T. Zorenko, A.M. Kaczmarek, R. Van Deun, A. Fedorov, Y. Zorenko, Eu^{3+} multicenter formation and luminescent properties of $\text{Ca}_3\text{Sc}_2\text{Si}_3\text{O}_{12}:\text{Eu}$ and $\text{Ca}_2\text{YScMgSiO}_{12}:\text{Eu}$ single crystalline films, *Opt. Mater.* 90 (2019) 70–75, <https://doi.org/10.1016/j.optmat.2019.02.030>.
- [23] I. Levchuk, A. Osvet, C.J. Brabec, M. Batentschuk, A. Shakhno, T. Zorenko, Y. Zorenko, Micro-powder $\text{Ca}_3\text{Sc}_2\text{Si}_3\text{O}_{12}:\text{Ce}$ silicate garnets as efficient light converters for WLEDs, *Opt. Mater.* 107 (2020) 109978, <https://doi.org/10.1016/j.optmat.2020.109978>.
- [24] V. Gorbenco, T. Zorenko, S. Witkiewicz-Lukaszek, A. Shakhno, A. Osvet, M. Batentschuk, A. Fedorov, Y. Zorenko, Crystallization and investigation of the structural and optical properties of Ce^{3+} -doped $\text{Y}_{3-x}\text{Ca}_x\text{Al}_{5-y}\text{Si}_y\text{O}_{12}$ single crystalline film phosphors, *Crystals* 11 (2021) 788, <https://doi.org/10.3390/cryst11070788>.
- [25] V. Gorbenco, T. Zorenko, K. Paprocki, A. Iskalyeva, A. Fedorov, F. Schröppel, I. Levchuk, A. Osvet, M. Batentschuk, Yu. Zorenko, Epitaxial growth of single crystalline film phosphors based on the Ce^{3+} -doped $\text{Ca}_2\text{YMgScSi}_3\text{O}_{12}$ garnet, *CrystEngComm* 19 (2017) 3689–3697, <https://doi.org/10.1039/c7ce00630f>.
- [26] K.V. Ivanovskikh, A. Meijerink, F. Piccinelli, A. Speghini, E.I. Zinin, C. Ronda, M. Bettinelli, Optical spectroscopy of $\text{Ca}_3\text{Sc}_2\text{Si}_3\text{O}_{12}$, $\text{Ca}_3\text{Y}_2\text{Si}_3\text{O}_{12}$ and $\text{Ca}_3\text{Lu}_2\text{Si}_3\text{O}_{12}$ doped with Pr^{3+} , *J. Lumin.* 130 (2010) 893–901, <https://doi.org/10.1016/j.jlumin.2009.12.031>.
- [27] P.A. Tanner, L. Fu, L. Ning, B.-M. Cheng, M.G. Brik, Soft synthesis and vacuum ultraviolet spectra of YAG: Ce^{3+} nanocrystals: reassignment of Ce^{3+} energy levels, *J. Phys. Condens. Matter* 19 (2007) 216213, <https://doi.org/10.1088/0953-8984/19/21/216213>.
- [28] K. Bartosiewicz, V. Babin, K. Kamada, A. Yoshikawa, M. Nikl, Energy migration processes in undoped and Ce-doped multicomponent garnet single crystal scintillators, *J. Lumin.* 166 (2015) 117–122, <https://doi.org/10.1016/j.jlumin.2015.05.015>.
- [29] M. Tyagi, F. Meng, M. Koschan, S.B. Donnal, H. Rothfuss, C.L. Melcher, Effect of codoping on scintillation and optical properties of a Ce-doped $\text{Gd}_3\text{Ga}_3\text{Al}_2\text{O}_{12}$ scintillator, *J. Phys. D Appl. Phys.* 46 (2013) 475302, <https://doi.org/10.1088/0022-3727/46/47/475302>.
- [30] M. Kitaura, A. Sato, K. Kamada, S. Kurosawa, A. Ohnishi, M. Sasaki, K. Hara, Photoluminescence studies on energy transfer processes in cerium-doped $\text{Gd}_3\text{Al}_2\text{Ga}_3\text{O}_{12}$ crystals, *Opt. Mater.* 41 (2015) 45–48, <https://doi.org/10.1016/j.optmat.2014.12.040>.
- [31] S. Zazubovich, A. Krasnikov, Y. Zorenko, V. Gorbenco, V. Babin, E. Mihokova, M. Nikl, Chapter 6 luminescence of Pb- and Bi-related centers in aluminum garnet, perovskite, and orthosilicate single-crystalline films, nanocomposite, ceramic and thin film scintillators, 227–302, <https://doi.org/10.1201/9781315364643-7>, 2016.
- [32] Yu. Zorenko, V. Gorbenco, Ja. Vasylyk, T. Strzyzewski, A. Fedorov, R. Kucerkova, J.A. Mares, M. Nikl, P. Bilski, A. Twardak, Growth and luminescent properties of scintillators based on the single crystalline films of $(\text{Lu,Gd})_3(\text{Al,Ga})_5\text{O}_{12}:\text{Ce}$ garnets, *J. Lumin.* 169 (2016) 828–837, <https://doi.org/10.1016/j.jlumin.2014.11.040>.
- [33] Y. Zorenko, V. Gorbenco, J. Vasylyk, A. Zelenyj, A. Fedorov, R. Kucerkova, J. A. Mares, M. Nikl, P. Bilski, A. Twardak, Growth and luminescent properties of scintillators based on the single crystalline films of $\text{Lu}_{3-x}\text{Gd}_x\text{Al}_5\text{O}_{12}:\text{Ce}$ garnet, *Mater. Res. Bull.* 64 (2015) 355–363, <https://doi.org/10.1016/j.materresbull.2015.01.020>.
- [34] K. Kamada, S. Kurosawa, P. Prusa, M. Nikl, V.V. Kochurikhin, T. Endo, K. Tsutsumi, H. Sato, Y. Yokota, K. Sugiyama, A. Yoshikawa, Cz grown 2-in. size $\text{Ce}:\text{Gd}_3(\text{Al,Ga})_5\text{O}_{12}$ single crystal; relationship between Al, Ga site occupancy and scintillation properties, *Opt. Mater.* 36 (2014) 1942–1945, <https://doi.org/10.1016/j.optmat.2014.04.001>.
- [35] S.V. Nizhankovsky, A.Ya. Dan'ko, O.V. Zelenskaya, V.A. Tarasov, Yu.V. Zorenko, V.M. Puzikov, L.A. Grin', A.G. Trushkovskii, V.P. Savchin, Cathodoluminescence and scintillation characteristics of YAG:Ce crystals grown by horizontal directional crystallization in a protective atmosphere, *Tech. Phys. Lett.* 35 (2009) 964–966, <https://doi.org/10.1134/s1063785009100265>.

Article

Optical and Photoconversion Properties of Ce^{3+} -Doped $(\text{Ca}, \text{Y})_3(\text{Mg}, \text{Sc})_2\text{Si}_3\text{O}_{12}$ Films Grown via LPE Method onto YAG and YAG:Ce Substrates

Anna Shakhno ^{1,2,*} , Vitalii Gorbenko ¹, Tetiana Zorenko ¹, Aleksandr Fedorov ³ and Yuriy Zorenko ^{1,*} 

¹ Department of Physics, Kazimierz Wielki University in Bydgoszcz, 85-090 Bydgoszcz, Poland; gorbenko@ukw.edu.pl (V.G.); tzorenko@ukw.edu.pl (T.Z.)

² Mechantronics Department, Kazimierz Wielki University in Bydgoszcz, 85-074 Bydgoszcz, Poland

³ Institute for Single Crystal, National Academy of Science of Ukraine, Nauky Ave., 60, 61000 Kharkiv, Ukraine

* Correspondence: shakhno@ukw.edu.pl (A.S.); zorenko@ukw.edu.pl (Y.Z.)

Abstract

This work presents a comprehensive study of the structural, luminescent, and photoconversion properties of epitaxial composite phosphor converters based on single crystalline films of Ce^{3+} -activated $\text{Ca}_{2-x}\text{Y}_{1+x}\text{Mg}_{1+x}\text{Sc}_{1-x}\text{Si}_3\text{O}_{12}:\text{Ce}$ ($x = 0-0.25$) (CYMSSG:Ce) garnet, grown using the liquid phase epitaxy (LPE) method on single-crystal $\text{Y}_3\text{Al}_5\text{O}_{12}$ (YAG) and YAG:Ce substrates. The main goal of this study is to elucidate the structure–composition–property relationships that influence the photoluminescence and photoconversion efficiency of these film–substrate composite converters, aiming to optimize their performance in high-power white light-emitting diode (WLED) applications. Systematic variation in the $\text{Y}^{3+}/\text{Sc}^{3+}/\text{Mg}^{2+}$ cationic ratios within the garnet structure, combined with the controlled tuning of film thickness (ranging from 19 to 67 μm for CYMSSG:Ce/YAG and 10–22 μm for CYMSSG:Ce/YAG:Ce structures), enabled the precise modulation of their photoconversion properties. Prototypes of phosphor-converted WLEDs (pc-WLEDs) were developed based on these epitaxial structures to assess their performance and investigate how the content and thickness of SCFs affect the colorimetric properties of SCFs and composite converters. Clear trends were observed in the Ce^{3+} emission peak position, intensity, and color rendering, induced by the $\text{Y}^{3+}/\text{Sc}^{3+}/\text{Mg}^{2+}$ cation substitution in the film converter, film thickness, and activator concentrations in the substrate and film. These results may be useful for the design of epitaxial phosphor converters with tunable emission spectra based on the epitaxially grown structures of garnet compounds.

Keywords: Ca-Mg-Si-based garnets; Ce^{3+} dopant; liquid phase epitaxy; single crystalline films; crystal substrates; luminescence; phosphor converters



Academic Editor: Vlassios Likodimos

Received: 17 May 2025

Revised: 19 July 2025

Accepted: 28 July 2025

Published: 30 July 2025

Citation: Shakhno, A.; Gorbenko, V.; Zorenko, T.; Fedorov, A.; Zorenko, Y. Optical and Photoconversion Properties of Ce^{3+} -Doped $(\text{Ca}, \text{Y})_3(\text{Mg}, \text{Sc})_2\text{Si}_3\text{O}_{12}$ Films Grown via LPE Method onto YAG and YAG:Ce Substrates. *Materials* **2025**, *18*, 3590. <https://doi.org/10.3390/ma18153590>

Copyright: © 2025 by the authors. Licensee MDPI, Basel, Switzerland. This article is an open access article distributed under the terms and conditions of the Creative Commons Attribution (CC BY) license (<https://creativecommons.org/licenses/by/4.0/>).

1. Introduction

In recent years, the demand for high-efficiency, energy-saving light sources has significantly increased, driven by advancements in lighting and display technology. White light-emitting diodes (WLEDs) have emerged as the dominant choice due to their superior energy efficiency, long lifespan, and environmental benefits, including reduced carbon emissions and lower energy consumption compared to traditional incandescent and fluorescent bulbs [1]. Additionally, WLEDs have found applications beyond general lighting, such as in automotive headlights, backlighting for displays, and even in medical devices, further fueling the need for continuous improvements in their performance and efficiency [2,3].

A critical factor in the overall performance of WLEDs is the phosphor conversion layer, which plays a central role in color rendering and light quality. In most WLED configurations, a blue LED chip is combined with a phosphor material that converts a portion of the blue light into yellow, red, or green light, resulting in a balanced white emission. The efficiency of this conversion process directly impacts the brightness, color rendering index (CRI), and color correlated temperature (CCT) of the emitted light, all of which are crucial parameters for various applications [4–6].

The choice of phosphor material is therefore essential in the performance of the device. Among the various phosphor materials available, garnet-based materials doped with rare-earth ions, especially Ce^{3+} , have proven to be among the most effective due to their broad excitation and emission spectra, high quantum efficiency, excellent luminescent properties, and thermal stability under high-power operation [7–9]. In particular, the Ce^{3+} -doped $\text{Y}_3\text{Al}_5\text{O}_{12}$ (YAG) phosphor is widely used in the industry for producing the high efficiency and good color quality of white light. It is compatible with blue LEDs and offers advantages such as strong absorption in the blue region, stable emission characteristics, and high thermal stability, which is crucial for maintaining performance over long operating hours [10].

The most common pc-WLEDs are produced using the Volume-Casting-Conversion (VCC) design, where a blue LED and powder PC are packed with organic resins [11]. Numerous techniques, including solid-state reactions [12], hydrothermal synthesis [13], coprecipitation [14], spray pyrolysis [15], sol–gel [16], and combustion [17], can be used to make ceramic powder phosphors. The heat generated from the LED chip and PC (Stokes shift and optical losses) cannot be efficiently dissipated because of the poor thermal stability and weak thermal conductivity of the resin ($<0.5 \text{ W m}^{-1} \text{ K}^{-1}$) [1]. With the increasing demand for high-brightness lighting, the high-power wLEDs and white laser diodes (WLDs) are rapidly developing, and some limitations arise that are associated with the optical, structural, mechanical, and thermal properties of converters. The operating temperature of a color converter can reach even up to 200°C under high-power LED or laser diode excitation. The extreme heat is generated in the converter, originating from the non-radiative relaxation of phosphors and the heat transfer from high-power LED chips. With the increase in the wLED temperature, color degradation occurs because of the thermal quenching properties of the phosphor, such as luminous decay and color shifting [18]. Furthermore, this setup results in low efficiency because the diffuse phosphor reflects 60% of the total white light back onto the chip [19]. To achieve high efficiency and strong chemical and thermal stability for pc-WLEDs, downconversion phosphors have been developed from powders to plates for the Planar-Chip-Level Conversion (PCLC) approach [20].

In PCLC design, instead of powder, the ceramic, eutectics, or single-crystal phosphors based on the yellow-emitting Ce^{3+} -doped garnets are used for manufacturing high-power WLEDs under blue LED excitation. Nevertheless, glasses and ceramics have a relatively low luminescence efficiency [21], whilst the structure and optical properties of eutectic converters are hard to control. The development of single crystalline (SC) converters is much preferable to ceramics or powders, due to their higher uniformity and internal quantum efficiency (QE) than ceramics or glasses, as well as excellent thermal stability up to 300°C , and high thermal conductivity ($\sim 10 \text{ W/(m K)}$) [22–24].

It is obvious that the investigation of new types of color converters is an acute problem to be solved with the development of energy-efficient solid-state lighting sources. The minimization trend has focused attention on phosphor films that can be produced using different techniques such as sputtering deposition [25], electrochemical synthesis [26], pulsed laser deposition (PLD) [27], sol–gel [28], metal–organic chemical vapor deposition

(MOCVD) [29], and liquid phase epitaxy (LPE) as well [30,31]. Among the presented methods, the LPE technique is a versatile method for the production of SCFs for applications in optoelectronics, with thicknesses in the range of several micrometers up to 200 μm , with excellent material quality and reproducibility [32].

One of the first works in this area was by Kundaliya et al. [32] and Markovskiy et al. [33], who proposed a phosphor converter based on the YAG:Ce and LuAG:Ce garnet phosphor film epitaxially grown onto a YAG substrate, to induce yellow and green emission, respectively. Recently, the possibility of the development of $\text{Tb}_3\text{Al}_5\text{O}_{12}:\text{Ce}$ (TbAG:Ce) single crystalline film converters for wLEDs using the LPE technique was shown [34]. It is especially important to note that, according to the $\text{Al}_2\text{O}_3\text{--Tb}_2\text{O}_3$ phase diagram, the $\text{Tb}_3\text{Al}_5\text{O}_{12}$ melts incongruently, and it is difficult to grow a high-quality and large-size bulk TbAG:Ce crystal using Czochralski (Cz) or other melt-grown techniques, which is a barrier to its practical applications [35]. However, the single crystalline $\text{Tb}_3\text{Al}_5\text{O}_{12}$ matrix or $\text{Tb}_{1.3}\text{Gd}_{1.5}\text{Al}_5\text{O}_{12}$ solid solution on their base can be fabricated in the pure garnet phase using low-temperature synthesis methods such as LPE growth [34,36].

The next generation of film converters is the development of a composite color converter (CCC), based on Ce^{3+} -doped film/crystal epitaxial structures [36]. The development of CCCs suggests a few more additional tunable parameters, originating from the single-crystal substrate: (i) Ce^{3+} doping concentration in the substrate; (ii) thickness of the substrate. Finally, the combination of the emission coming from the Ce^{3+} -doped substrate and the film constituents of the color converter allows for a wide spectrum of WLEDs similar to the spectrum of natural white light to be obtained, with enhanced luminous efficacy in comparison with standard photoconverters.

Phosphors based on the Ce^{3+} -doped mixed $\{\text{Ca}_2\text{R}\}[\text{Sc,B}](\text{C,Si}_2)\text{O}_{12}$; $\text{R} = \text{Lu, Y, Gd}$; $\text{B} = \text{Sc, Ga}$, $\text{C} = \text{Ga, Al}$ silicate garnets can also be used for producing high-power WLEDs with a high color rendering index and low correlated color temperature values [37,38]. Due to the flexibility of the garnet structure, which allows for replacing ions at the dodecahedral { }, octahedral [], and tetrahedral () sites, it is possible to replace the host cations and modify the conventional $\{\text{Y}\}_3[\text{Al}]_2(\text{Al})_3\text{O}_{12}$ garnet composition for altering the Ce^{3+} spectroscopic properties to better meet the requirements for utilization in WLEDs. To date, the spectroscopic properties of Ce^{3+} in some garnets containing Si^{4+} at tetrahedral sites, namely $\text{Y}_3\text{Mg}_2\text{AlSi}_2\text{O}_{12}$, $\text{Y}_3\text{MgAl}_3\text{SiO}_{12}$, $\text{CaY}_2\text{Al}_4\text{SiO}_{12}$, $\text{MgY}_2\text{MgAl}_2\text{Si}_2\text{O}_{12}$, $\text{CaLu}_2\text{Al}_4\text{SiO}_{12}$, $\text{CaLu}_2\text{Mg}_2\text{Si}_3\text{O}_{12}$, $\text{CaY}_2\text{ZrScAl}_3\text{O}_{12}:\text{Ce}$, and $\text{Lu}_{1.5}\text{Ca}_{1.5}\text{Al}_{3.5}\text{Si}_{1.5}\text{O}_{12}:\text{Ce}$ garnets, have been investigated [39–51].

It has been shown that $\text{Ca}_3\text{Sc}_2\text{Si}_3\text{O}_{12}:\text{Ce}$ (CSSG) exhibits less thermal quenching of Ce^{3+} luminescence than YAG:Ce [37,50]. Mixed silicate garnets like $\text{Y}^{3+}\text{--Mg}^{2+}$ co-doped CSSG:Ce, e.g., $(\text{Ca,Y})_3(\text{Mg,Sc})_2\text{Si}_3\text{O}_{12}$ (CYMSSG), doped with Ce^{3+} ions, have shown also great potential as powder phosphor materials due to their broader emission spectra and absorption in the blue region than GSSG:Ce, which aligns well with the emission of blue LEDs [51,52]. However, despite the promising properties of these materials, research on the use of CYMSSG:Ce in the single crystalline films (SCF) [53] or crystals [54] as phosphor converters is limited, with even less focus on their performance in composite film–crystal structures based on the silicate garnets [55,56]. This gap hinders a complete understanding of how these materials behave under real LED excitation conditions and how variations in film structure, particularly thickness and variable cation content, influence their photoconversion efficiency.

The present study addresses this gap by investigating the structural, luminescent, and photoconversion properties of epitaxial converters based on Ce^{3+} -doped CYMSSG-based SCFs with varying cation contents. These films were crystallized using the liquid phase epitaxy (LPE) method onto YAG and YAG:Ce single-crystal (SC) substrates, allowing for

precise control over the growth process and material properties [18–24]. By systematically varying the film’s cation composition and thickness, ranging from 19 to 67 μm for Ce^{3+} -doped CYMSSG films on YAG crystals (Series A) and from 10 to 22 μm for those on YAG:Ce crystals (Series B), we thoroughly examined how these parameters influence photoconversion efficiency.

This systematic approach enabled the observation and mapping of distinct trend lines in a chromaticity or color coordinate diagram, clearly illustrating the relationship between film content, thickness, and photoconversion performance. Variations in content and thickness affected key parameters, such as emission spectra and color rendering, which are critical for optimizing the overall luminescence and efficiency of the converter. These trend lines provide valuable insights into the optimal content and film thickness required for enhanced photoconversion, highlighting the importance of precise control over all SCF parameters to achieve the desired optical characteristics in phosphor converters for WLED applications.

2. SCF Growth

Two distinct sets of thin films with nominal compositions of Ce^{3+} -doped $\text{Ca}_2\text{YMgScSi}_3\text{O}_{12}$ and $\text{Ca}_{1.75}\text{Y}_{1.25}\text{Mg}_{1.25}\text{Sc}_{0.75}\text{Si}_3\text{O}_{12}$ (Series A and B, respectively), with thicknesses ranging from 10 μm to 67 μm , were fabricated using the LPE method (Table 1). The films were crystallized within a temperature range of 975–990 $^{\circ}\text{C}$ from a supercooled melt solution composed of a $\text{PbO}:\text{B}_2\text{O}_3$ flux with a mole ratio of 12:1. The CYMSSG:Ce SCFs were grown on undoped YAG substrates for Series A and on Ce^{3+} -doped YAG substrates for Series B, with orientations close to the (111) crystallographic plane. The YAG and YAG:Ce substrates used in these experiments had a thickness of 0.5 mm. The nominal Ce concentration in the CYMSSG:Ce SCFs and YAG:Ce substrates was approximately 0.05–0.15 at. % and 0.05–0.06 at.%, respectively (Table 1). Further details about the growth process for Ca-Si-based films and the specific mole ratios used for LPE growth can be found in references [57].

Table 1. The nominal composition (in melt solution) and the measured (using EDX) composition of LPE-grown CYMSSG:Ce/YAG and CYMSSG:Ce/YAG:Ce films (Series A and B, respectively) and YAG:Ce substrates (Series C).

Sample	Nominal Content in the Melt	Measured SCF Composition	h, μm
A1	$\text{Ca}_2\text{YMgScSi}_3\text{O}_{12}:\text{Ce}$	$\text{Ca}_{1.88}\text{Y}_{1.09}\text{Ce}_{0.01}\text{Mg}_{0.9}\text{Sc}_{1.42}\text{Si}_{2.73}\text{O}_{12}$	19
A2	$\text{Ca}_2\text{YMgScSi}_3\text{O}_{12}:\text{Ce}$	$\text{Ca}_{1.83}\text{Y}_{1.08}\text{Ce}_{0.03}\text{Mg}_{0.9}\text{Sc}_{1.51}\text{Si}_{2.68}\text{O}_{12}$	34
A3	$\text{Ca}_2\text{YMgScSi}_3\text{O}_{12}:\text{Ce}$	$\text{Ca}_{1.81}\text{Y}_{1.12}\text{Ce}_{0.03}\text{Mg}_{0.93}\text{Sc}_{1.48}\text{Si}_{2.67}\text{O}_{12}$	49
A4	$\text{Ca}_{1.75}\text{Y}_{1.25}\text{Mg}_{1.25}\text{Sc}_{0.75}\text{Si}_3\text{O}_{12}:\text{Ce}$	$\text{Ca}_{1.63}\text{Y}_{1.27}\text{Ce}_{0.03}\text{Mg}_{1.19}\text{Sc}_{1.27}\text{Si}_{2.72}\text{O}_{12}$	67
B1	$\text{Ca}_2\text{YMgScSi}_3\text{O}_{12}:\text{Ce}$	$\text{Ca}_{1.92}\text{Y}_{1.08}\text{Ce}_{0.02}\text{Mg}_{0.95}\text{Sc}_{1.27}\text{Si}_{2.78}\text{O}_{12}$	10
B2	$\text{Ca}_{1.75}\text{Y}_{1.25}\text{Mg}_{1.25}\text{Sc}_{0.75}\text{Si}_3\text{O}_{12}:\text{Ce}$	$\text{Ca}_{1.65}\text{Y}_{1.35}\text{Ce}_{0.03}\text{Mg}_{1.18}\text{Sc}_{0.61}\text{Si}_{3.21}\text{O}_{12}$	11
B3	$\text{Ca}_{1.75}\text{Y}_{1.25}\text{Mg}_{1.25}\text{Sc}_{0.75}\text{Si}_3\text{O}_{12}:\text{Ce}$	$\text{Ca}_{1.68}\text{Y}_{1.32}\text{Ce}_{0.03}\text{Mg}_{1.28}\text{Sc}_{0.71}\text{Si}_{3.01}\text{O}_{12}$	22
C1	$\text{Y}_3\text{Al}_5\text{O}_{12}:\text{Ce}$	$\text{Y}_{2.99}\text{Ce}_{0.01}\text{Al}_5\text{O}_{12}$	500
C2	$\text{Y}_3\text{Al}_5\text{O}_{12}:\text{Ce}$	$\text{Y}_{2.99}\text{Ce}_{0.01}\text{Al}_5\text{O}_{12}$	500
C3	$\text{Y}_3\text{Al}_5\text{O}_{12}:\text{Ce}$	$\text{Y}_{2.988}\text{Ce}_{0.012}\text{Al}_5\text{O}_{12}$	500

The thickness of the SCF samples, denoted as **h** (in μm), was determined using a weighing method. This approach involved measuring the substrate’s mass before and after the SCF growth cycle with high-precision scales. Film thickness was then calculated using the following formula: $h = (\mathbf{m} - \mathbf{m}_s) / (2 \times \mathbf{S} \times \rho)$, where **m** is the mass of the substrate with the grown SCF (in grams), **m_s** is the mass of the substrate (in grams), **S** is the substrate area (in cm^2), and **ρ** is the film density (in g/cm^3).

The compositions of single crystals and films were analyzed using a JEOL JSM-820 electron microscope (JEOL Ltd., Akishima, Japan) equipped with an IXRF 500i LN₂ Eumex EDX detector (IXRF, Inc., Austin, TX, USA). This advanced tool provided rapid assessments and ensured the precise detection of elemental variations with an accuracy of $\pm 1\%$. The analysis revealed considerable deviations in the concentrations of Ca, Mg, Sc, and Si cations compared to the nominal (in-melt) formulas $(\text{Ca}, \text{Y})_3(\text{Mg}, \text{Sc})_2\text{Si}_3\text{O}_{12}$ and $\text{Ca}_{1.75}\text{Y}_{1.25}\text{Mg}_{1.25}\text{Sc}_{0.75}\text{Si}_3\text{O}_{12}:\text{Ce}$. Meanwhile, these deviations were consistently less than ± 0.2 formula units, as shown in Table 1. Such findings underscore the importance of precise compositional control in material synthesis. To maintain clarity and alignment with experimental results, the study consistently refers to the nominal composition of the SCFs. This approach ensures a standardized comparison while accounting for the slight variations observed during the evaluation process.

The structural quality of $\text{Ca}_{2-x}\text{Y}_{1+x}\text{Mg}_{1+x}\text{Sc}_{1-x}\text{Si}_3\text{O}_{12}:\text{Ce}$ ($x = 0-0.25$) films grown on YAG substrates was investigated using X-ray diffraction (XRD) with a DRON 4 spectrometer (Saint-Petersburg, former USSR) equipped with a $\text{CuK}\alpha$ X-ray source. For this analysis, Samples B1 and B4 with $x = 0$ and $x = 1.25$ were chosen, featuring a 0.25 Ce^{3+} concentration of 0.01 and 0.15 at.% and a thickness of 19 μm and 67 μm , respectively, as illustrated in Figure 1 and Table 1. This sample was selected for its suitability for detailed structural evaluation.

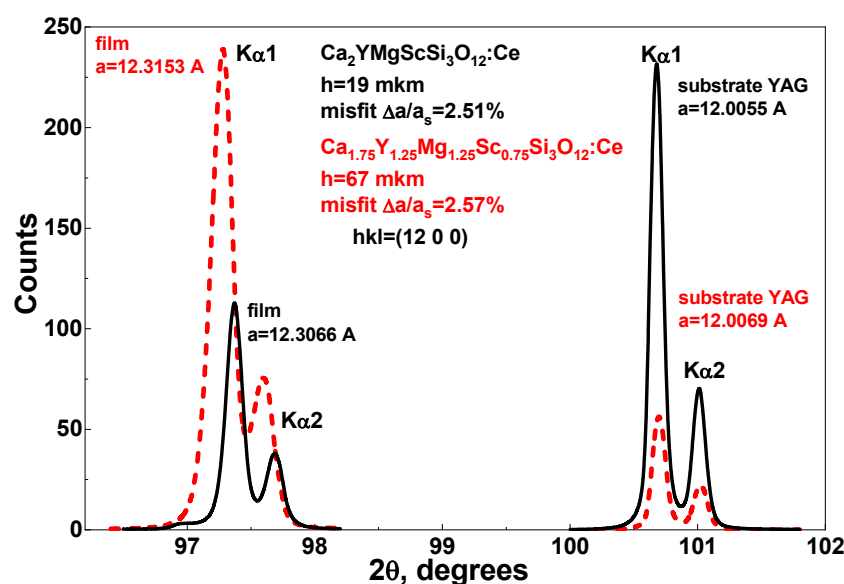


Figure 1. XRD patterns of (12 0 0) plane of $\text{Ca}_2\text{YMgScSi}_3\text{O}_{12}:\text{Ce}$ SCF (sample B1) and $\text{Ca}_{1.75}\text{Y}_{1.25}\text{Mg}_{1.25}\text{Sc}_{0.75}\text{Si}_3\text{O}_{12}:\text{Ce}$ SCFs (sample B4) grown on YAG substrate.

Typically, the single crystallinity of CYMSSG films grown on YAG substrates is confirmed using thinner samples, generally with thicknesses of less than 50–70 μm . This preference is driven by the inherent limitations associated with X-ray diffraction in thicker samples. Specifically, the garnet matrix of CYMSSG films exhibits medium X-ray absorption, which changes the relative intensity of diffraction reflections from the YAG substrate. This effect becomes more pronounced as the film thickness increases, complicating accurate structural characterization in thicker samples (Figure 1).

Therefore, thinner samples are prioritized for initial analysis to reliably confirm single crystallinity. Once verified, the growth process continues to produce thicker films (exceeding 100 μm) for further experimental studies. This sequential approach ensures that the structural integrity and quality of the CYMSSG films are thoroughly assessed before the fabrication of thicker film samples. By addressing the technical constraints of XRD analysis,

this method provides a robust framework for characterizing the structural properties of CYMSSG films on YAG substrates, paving the way for their application in advanced optical and photonic systems.

The lattice misfit between the CYMSSG SCFs and the YAG substrate was calculated using the XRD pattern corresponding to the (12 0 0) crystallographic plane of the sample (Figure 1). The standard formula for lattice misfit, expressed as $\Delta a = ((a_{\text{SCF}} - a_{\text{sub}})/a_{\text{sub}}) \times 100\%$, was used, where a_{SCF} is the lattice parameter of the film, and a_{sub} is the lattice parameter of the YAG substrate. The analysis revealed a lattice mismatch of approximately 2.51–2.57%, which indicates a significant mismatch between the SCF and substrate lattices. Meanwhile, even this degree of mismatch was found to be consistent with high-quality epitaxial growth, where strain and stress at the interface are not yet critical, maintaining the crystalline integrity of the film. This finding is particularly significant as it confirms the successful epitaxial growth of the CYMSSG ($x = 0\text{--}0.25$) film on the YAG substrate.

3. Experimental Technique

To comprehensively investigate the properties of the two sets of thin-film samples (Series A and B) and Ce-doped substrates (Series C), an extensive suite of spectroscopic techniques was employed. These techniques included absorption spectroscopy, photoluminescence (PL) emission, and excitation (PLE) spectroscopy, which together provided a detailed evaluation of the luminescent characteristics of the CYMSSG:Ce SCFs. All spectroscopic measurements were conducted under ambient conditions at room temperature (RT), ensuring their relevance to practical applications.

The absorption spectra of the SCFs were recorded using a Jasco V730 spectrophotometer (Tsukuba, Japan). For a detailed examination of the photoluminescent properties, an FS-5 spectrometer (Edinburgh Instruments, Livingston, UK) was used. Photoconversion spectra were recorded using an AvaSpec-ULS 2048-LTEC fiber-optic spectrophotometer, paired with an AvaSphere-50-IRRAD integrating sphere (Avantes, Apeldoorn, The Netherlands). These measurements enabled a comprehensive analysis of the SCFs' photoconversion performance, shedding light on their potential for advanced photonic applications. The Osram LBE 6SG ($I_f = 30$ mA, $V = 2.9$ V) blue LED 455 nm (30 mA, 2.9 V) was used as an excitation source to determine the chromaticity parameters of the samples.

4. Absorption and Luminescent Properties

4.1. Absorption Spectra

The absorption spectra of the CYMSSG:Ce SCF/YAG SCFs (Figure 2a) and CYMSSG:Ce SCF/YAG:Ce (Figure 2b) composite samples, as well as the absorption spectra of the YAG:Ce SC substrates (Figure 2c), exhibit distinct features in the 200–500 nm wavelength range, reflecting their optical properties. Notably, broad absorption bands peaking around 341 nm and within the 439–457 nm range, referred to as E2 and E1 bands, respectively, are consistently observed across all analyzed structures, confirming their successful incorporation into the CYMSSG films. These bands are characteristic for the absorption of Ce^{3+} ions in the garnet host, corresponding to the $4f^1(^2F_{5/2}) \rightarrow 5d(^2E)$ electronic transitions. Additionally, a spectral feature at 230 nm is attributed to the $4f(^2F_{5/2}) \rightarrow 5d_1(^2T_{2g})$ transitions of Ce^{3+} ions (E_3 band). These identifications align with prior studies, which highlight these transitions as key spectral signatures of Ce^{3+} ions' presence in garnet matrices [1,2].

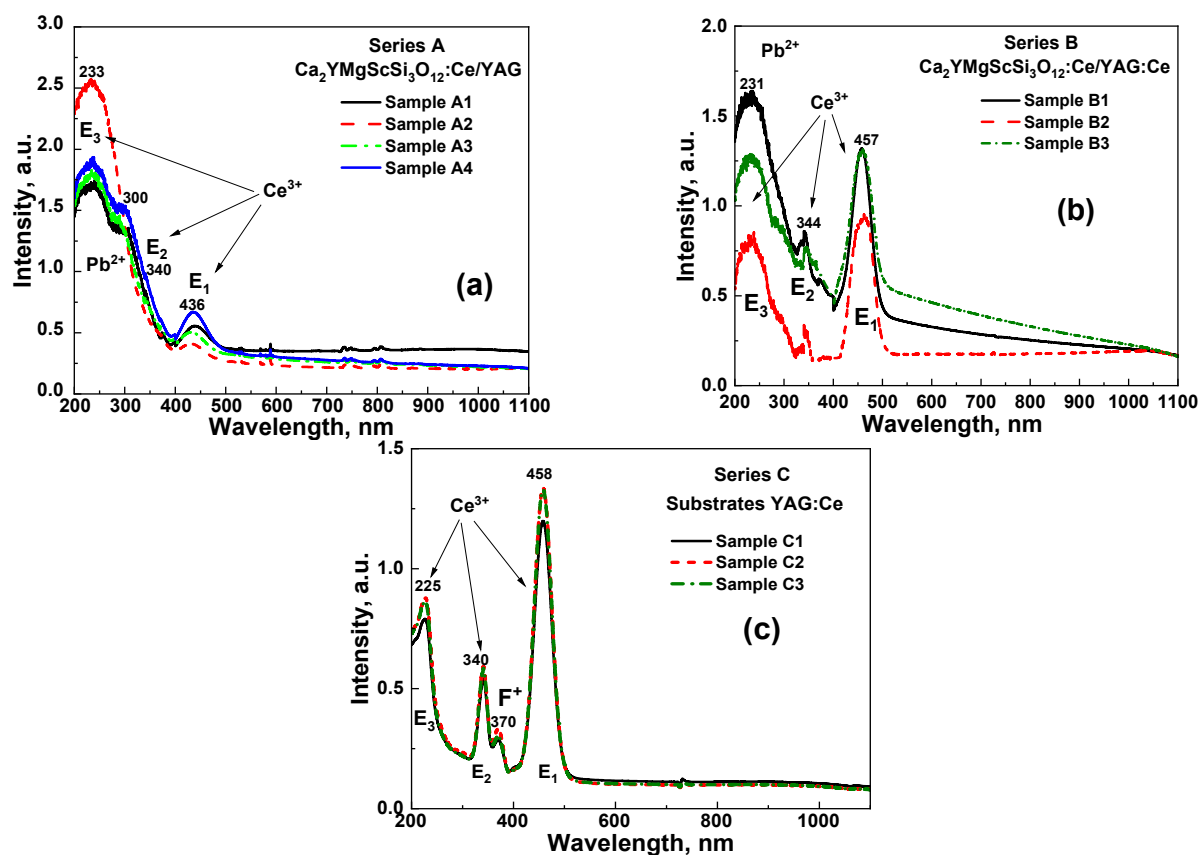


Figure 2. RT absorption spectra of CYMSSG:Ce SCF/YAG (a) and CYMSSG:Ce SCF/YAG:Ce (b) in comparison with YAG:Ce substrates (c).

Another notable feature of SCF samples is an absorption bands peaked at 300 nm and below 220 nm, corresponding to the $^1\text{S}_0 \rightarrow ^3\text{P}_1$ and $^1\text{P}_1$ electronic transitions of Pb^{2+} impurity, likely introduced into the film during LPE growth from PbO -based flux. The last Pb^{2+} -related band strongly overlapped with the E_3 band of Ce^{3+} ions. Despite being associated with trace Pb^{2+} inclusions, this feature provides valuable insights into the real material's composition and the interactions between dopants and Ce^{3+} ions [3].

In addition to these primary features, low intensive absorption bands in the UV range, peaking at 370 nm, are evident in the YAG:Ce substrates and absorption spectra of the CYMSSG:Ce SCF/YAG:Ce structure. Generally, such UV bands have been attributed to defect center absorption in garnets, grown or annealed in the reducing atmosphere [58], or containing an excess of Ca^{2+} ions [53,57], and correspond to the absorption of the F^+ center (one charged anion vacancy).

Overall, the analysis of these absorption spectra confirms the effective doping of the SCFs with Ce^{3+} ions and underscores the impact of trace impurities on their optical behavior.

4.2. PL Spectra

The PL and PLE spectra of samples from Series A and B, as well as substrates from Series C, are shown in Figure 3. The PL spectra of all SCF samples (Figure 3a,b) exhibit intense luminescence characterized by broad emission bands in the green-yellow spectral range. These bands are attributed to the $5d_1 \rightarrow 4f$ ($^2\text{F}_{5/2}$, $^2\text{F}_{7/2}$) electronic transitions of Ce^{3+} ions, which are characteristic of the luminescent behavior of cerium-doped garnets. However, it should be noted that Ce^{3+} emission bands consist of several sub-bands corresponding to non-equivalent Ce^{3+} multcenters. Specifically, Ce^{3+} ions replace the dodecahedral po-

sitions of Ca^{2+} and Y^{3+} cations, which have different local surroundings with Mg^{2+} and Sc^{3+} ions in octahedral positions and Si^{4+} in tetrahedral positions within the garnet lattice. The observed structure of the PL spectra of CYMSSG:Ce SCFs grown on a YAG substrate clearly indicates the presence of multiple Ce^{3+} emission centers in the CYMSSG host, as described in detail in our previous works [8,18].

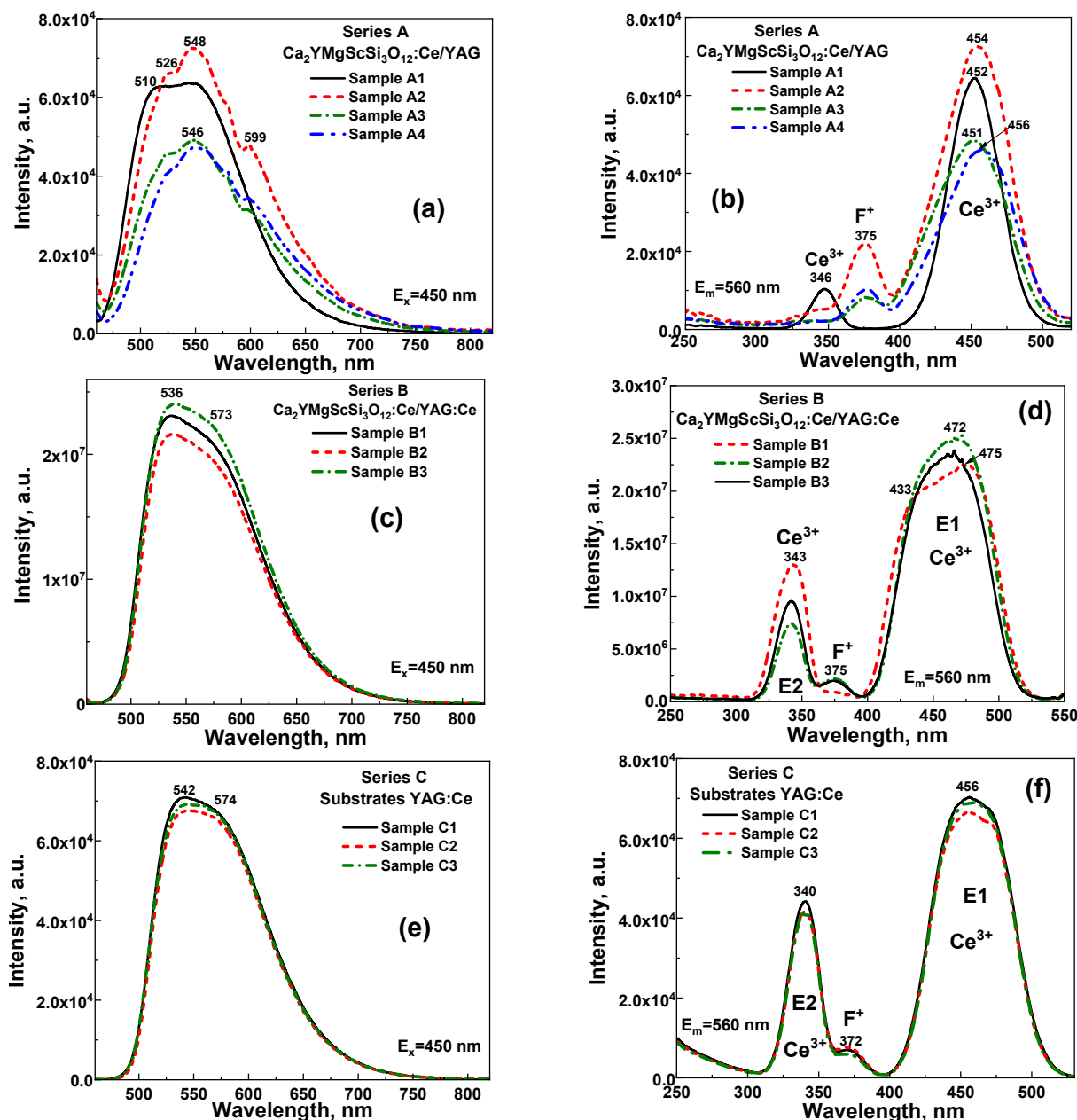


Figure 3. RT PL (a,c,e) and PLE (b,d,f) spectra of CYMSSG:Ce SCF/YAG ((a,b)—A-series) and CYMSSG:Ce/YAG:Ce ((c,d)—B series) structures in comparison with YAG:Ce substrates ((c)—series C).

The PL spectrum of samples from Series A, which were grown on an undoped YAG substrate, exhibits a broader Ce^{3+} luminescence band, with two distinct peaks at 510 nm and 548 nm. The slight blue shift in the PL emission and excitation spectra of sample A1 is caused by its lower cerium concentration, which is three times lower than that of the other samples in this set. This blue shift occurs because the reduced Ce^{3+} concentration limits the energy transfer between different Ce^{3+} multicenters, primarily affecting those emitting in the longer-wavelength range.

Conversely, the PL spectra of samples from Series B, grown on a Ce^{3+} -doped YAG substrate, display a notably broader emission band with peaks at 536 nm and 573 nm due to the overlap between the PL spectra of the YAG:Ce substrate (Figure 3c) and the CYMSSG:Ce SCFs (Figure 3a). This red shift may also result from variations in the crystal field strength or changes in the covalency of Ce^{3+} -ligand bonds within the Ca^{2+} - Si^{4+} -based CYMSSG host compared to the YAG:Ce substrate [8,18]. Specifically, increased covalency in Ce^{3+} -ligand bonds within the CYMSSG matrix reduces the energy required for Ce^{3+} electronic transitions, contributing to the observed red shift.

Interactions between Ce^{3+} ions in YAG:Ce substrates and CYMSSG:Ce films may also lead to energy transfer processes that influence the emission spectra of the epitaxial structure. Understanding these wavelength shifts is crucial for tailoring the material's properties and optimizing its emission for specific applications. These findings highlight the critical role of the substrate composition in determining the photoluminescence properties of CYMSSG:Ce films. The interactions between SCFs and substrates, particularly those involving cerium doping, significantly impact the energy transfer dynamics and luminescent behavior.

4.3. PLE Spectra

The PLE spectra of Ce^{3+} ions in YAG:Ce substrates and CYMSSG SCF/YAG and CYMSSG SCF/YAG:Ce structures are presented in Figure 3b,d,f. The $4f\ (^2F_{5/2}) \rightarrow 5d$ transitions are key characteristics of Ce^{3+} ion excitation and play a fundamental role in its luminescent behavior. The peak near 456 nm in YAG:Ce substrates is typically associated with the transition from the ground state to the lowest 5d energy level, whereas the 340 nm peak corresponds to a transition to a higher-lying 5d state. These transitions are governed by the symmetry and electronic environment of Ce^{3+} ions within the garnet matrix. The relative intensities and positions of these bands provide insights into the local crystal field and the energy splitting of the 5d states.

Furthermore, the peaks at 340 nm and 456 nm indicate that the YAG:Ce substrate and its composite structure exhibit efficient absorption capabilities at multiple wavelengths, enabling excitation in both the UV and visible regions. This dual-excitation feature enhances the material's photoluminescent properties, making it suitable for applications in lighting, displays, and optoelectronic devices.

The PLE spectra for Series A (Figure 3b) exhibit prominent maxima at 346 nm and 454 nm, corresponding to the $4f \rightarrow 5d$ electronic transitions of Ce^{3+} ions in the CYMSSG host. These peaks are typical of cerium-doped materials and indicate efficient absorption in the UV and blue regions, making them suitable for excitation by respective LEDs.

The PLE spectra of samples from Series B (Figure 3d) represent a superposition of the PLE spectra of the YAG:Ce substrate and CYMSSG:Ce SCF. These spectra feature a peak at 343 nm (E_2) and a broad complex excitation band in the blue region centered at 472 nm (E_1). The latter band is a superposition of at least two distinct peaks located at 433 nm and 476 nm. The presence of multiple peaks within the E_1 band is typically attributed to the excitation of Ce^{3+} multimers in the CYMSSG:Ce film [8,18].

The excitation peak observed at 375 nm in the PLE spectra of Ce^{3+} luminescence in CYMSSG:Ce SCFs is closely related to intrinsic electronic transitions associated with F^+ centers in garnets [1,17]. Specifically, this peak corresponds to the $^1A \rightarrow ^1B$ transition of the F^+ center, a well-known defect in many crystalline materials, including oxides. The F^+ center refers to an oxygen vacancy typically associated with a trapped electron. The presence of this excitation band at 375 nm suggests that F^+ centers play a role in the optical behavior of CYMSSG:Ce SCFs, contributing to the material's overall photonic properties. In particular, the material's ability to absorb light at this wavelength may influence the

efficiency of energy transfer processes and the overall photoluminescent behavior of Ce^{3+} ions, as interactions between F^+ centers and Ce^{3+} ions can modify emission characteristics.

5. Photoconversion Properties

Prototypes of phosphor-converted white light-emitting diodes (pc-WLEDs) were developed to assess their performance and to investigate how the content and thickness of SCFs affect the colorimetric properties of SCFs and composite converters. These pc-WLEDs were assembled by integrating epitaxial SCFs and composite converters into the OSRAM LBE 6SG blue LED chip (ams OSRAM AG, 8141, Premstaetten, Austria) with a peak emission wavelength of 450 nm. These chips operated at a fixed forward bias voltage of 2.6 V and a drive current of 20 mA.

The emission spectra of the prototypes, presented in Figure 4, correspond to converters containing CYMSSG:Ce SCFs with varying contents and thicknesses, grown on undoped (Series A) and Ce^{3+} -doped (Series B) YAG substrates, each with a thickness of 0.5 mm (see Table 1 for details). For comparison, an emission diagram of the YAG:Ce substrate (Figure 4c), used as a conventional reference sample, is also provided alongside the corresponding diagram of the composite CYMSSG:Ce/YAG:Ce structures (Figure 4b).

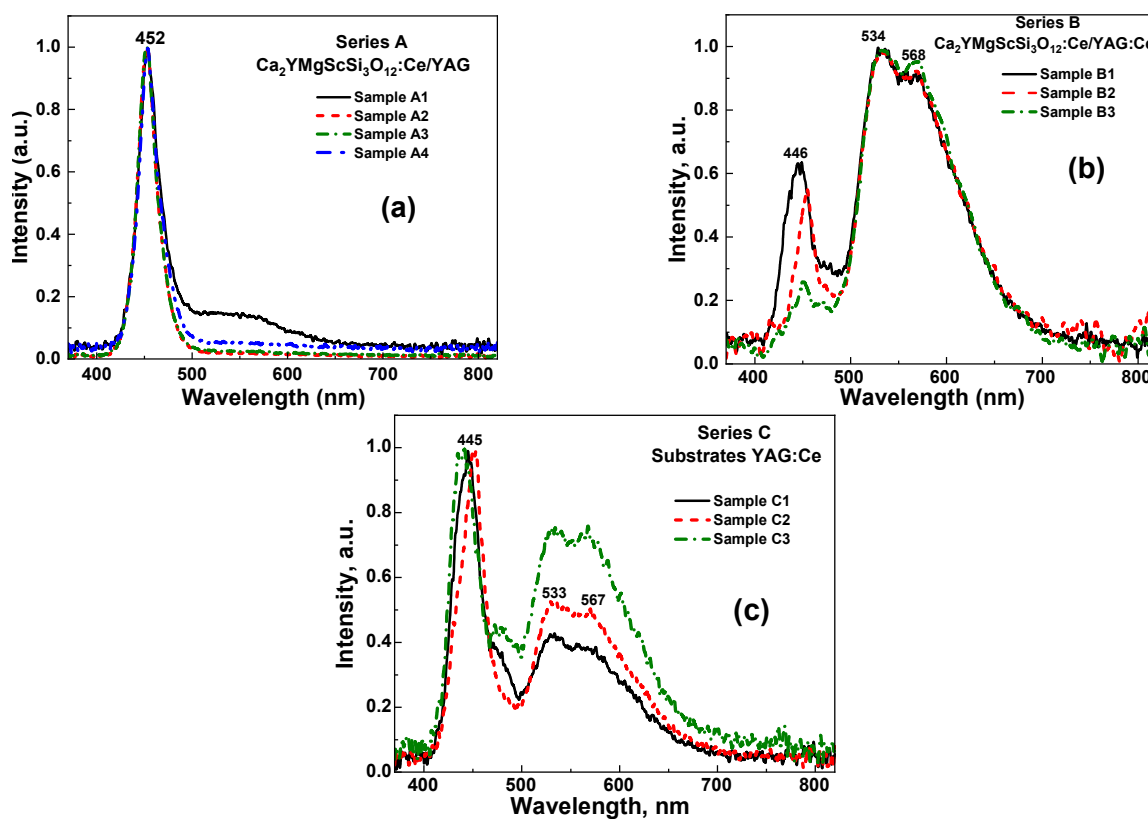


Figure 4. Normalized emission spectra of pc-WLED prototypes fabricated on the base of 450 nm LED chip and CYMSSG:Ce SCF converters grown on YAG (a) and YAG:Ce (b) substrates in comparison with converters on the base of YAG:Ce crystal substrates (c).

The emission spectrum generated by these white LED prototypes demonstrates a clear dependence of Ce^{3+} emission intensity on the thickness of the CYMSSG:Ce SCF (Figure 4a,b). As the film thickness increases, a larger number of Ce^{3+} ions are excited by the incident blue light, resulting in the stronger absorption of the blue component. This, in turn, enables the tailoring of the blue-to-yellow emission ratio (Figure 4a,b). Specifically, the addition of emission from the CYMSSG:Ce SCFs significantly reduces the blue component

and increases the yellow and red components in the total emission of the composite prototypes, compared to conventional YAG:Ce crystal converters.

For a more detailed analysis, the emission of WLED prototypes is plotted also in a CIE diagram (Figure 5). Table 2 presents the CIE chromaticity coordinates, color rendering index (CRI), correlated color temperature (CCT), and luminous efficiency (LE) of the developed WLEDs, highlighting their effectiveness in achieving desirable lighting characteristics. These parameters are critical for evaluating the lighting performance of the developed prototypes, providing insight into their color accuracy, spectral balance, and suitability for various applications.

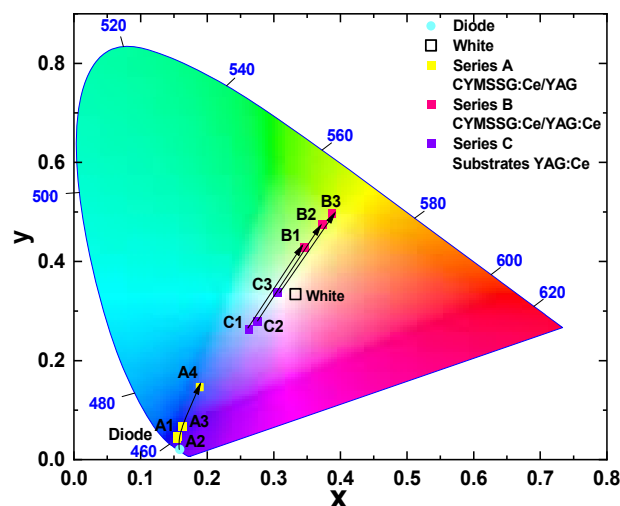


Figure 5. Chromaticity diagram of a WLED prototype fabricated on the base of 450 nm LED chip and CYMSSG:Ce SCFs grown on YAG (Series A) and YAG:Ce (Series B) substrates. The results for YAG:Ce substrates are presented for comparison.

Table 2. Comparison of the CIE coordinates, CRI, CCT, and LE of epitaxial structures based on the CYMSSG:Ce SCF samples grown on YAG (Series A, Series B) and YAG:Ce (Series C) substrates. The results for YAG:Ce substrates, as reference samples, are presented for comparison.

Samples	SCF Thicknesses, μm	Type and Thicknesses of Substrate, mm	CIE Coordinates		CCT, K	CRI	LE, lm/W
			y	y			
Series A							
A1	19	0.5	0.162	0.066		-	-
A2	34	0.5	0.155	0.043		-	-
A3	49	0.5	0.156	0.047		-	-
A4	67	0.5	0.189	0.146		-	-
Series B							
B1	10	C1; 0.5	0.346	0.428	5150	62	102
B2	11	C2; 0.5	0.374	0.475	4612	59	112
B3	22	C3; 0.5	0.388	0.496	4406	59	115
Series C							
C1	-	0.5	0.263	0.263	-	78	71
C2	-	0.5	0.276	0.278	-	75	72
C3	-	0.5	0.305	0.338	6838	70	79

CYMSSG:Ce SCF samples from Series A, grown on undoped YAG substrates, exhibited emission coordinates clustered within the blue region of the chromaticity diagram (Figure 5). Coordinates corresponding to the YAG substrates were not included here, as these substrates do not contribute to photoconversion and their emission characteristics

remain identical to those of the original blue diode. This indicates that the photoconversion behavior of the CYMSSG:Ce SCF/YAG structures is determined solely by the properties of the films, without additional contributions from the substrate. Meanwhile, the conversion efficiency of these films, with thicknesses ranging from 19 to 50 μm , is low, and only the 67 μm -thick SCF A4 sample shows a clear visible trend in CIE coordinate change with increasing thickness (yellow squares in Figure 5).

The coordinates of the YAG:Ce crystal substrates (blue squares) are also plotted on the diagram as reference samples for comparison with film and composite converters (Figure 5). As shown in Figure 5, the color coordinates of the YAG:Ce crystal converters are significantly influenced by the Ce^{3+} concentration. In particular, the YAG:Ce crystal, with 0.075% Ce^{3+} content (sample C3) and a thickness of 0.5 mm, exhibits CIE coordinates of ($x = 0.305$, $y = 0.338$) and a correlated color temperature (CCT) of 6840 K, which are very close to the standard white light reference. In contrast, samples C1 and C2, with lower Ce^{3+} contents (0.05%), show color coordinates that fall within the sky-blue region. Moreover, increasing the Ce^{3+} content in the YAG:Ce crystal converters results in a slight decrease in the CRI value, but a notable improvement in luminous efficiency from 71 to 72 for samples C1 and C2, and to 79 for sample C3 (Table 2).

In contrast, CYMSSG:Ce SCF/YAG:Ce composite converters (Series B) exhibited emission coordinates in the green-yellow region (red squares). This pronounced shift is primarily attributed to the presence of Ce^{3+} dopant in the SCF converters, which introduces additional photoluminescent features, thereby enhancing the overall emission and significantly altering the photoconversion behavior of the epitaxial structures. In this case, the color coordinates and CCT are less dependent on the properties and Ce^{3+} content of the underlying crystal substrates. Instead, the composition of the SCF converters, specifically, the ratio of Y/Mg/Sc cations as well as the film thickness, play a more dominant role in determining the photoconversion characteristics of the composites (Figure 5). These parameters can be effectively tuned to optimize the performance of the fabricated WLEDs. Notably, as the SCF thickness increases, the composite converters show a reduction in the color rendering index (CRI), with values in the range of 59–62. However, they demonstrate a significantly higher luminous efficiency, reaching 102–115 lm/W , compared to the corresponding YAG:Ce substrates (Table 2), primarily due to the enhanced absorption and emission properties of both the film and substrate converters. The highest luminous efficacy achieved is 115 lm/W for sample S3.

Thus, the proposed approach for creating composite color converters demonstrates the ability to achieve virtually any desired color coordinates within the white light region by adjusting several key parameters: (i) the Ce^{3+} concentration in the YAG:Ce substrate, (ii) the film composition, and (iii) the film thickness. The results also highlight the critical role of both the film and substrate composition, as well as the SCF thickness, in determining the photoconversion performance of these composite converters. By carefully tuning these parameters, it is possible to tailor the colorimetric properties of pc-WLEDs to meet the specific requirements of various white solid-state lighting applications. This study illustrates the potential of CYMSSG:Ce SCFs as highly versatile and effective materials for next-generation pc-WLED technologies, paving the way for further advancements in the field.

6. Conclusions

This study investigates the structural, luminescent, and photoconversion properties of Ce^{3+} -doped film–crystal composite converters based on epitaxial structures containing Ce^{3+} -doped single crystalline films (SCFs) of $\text{Ca}_{2-x}\text{Y}_{1+x}\text{Mg}_{1+x}\text{Sc}_{1-x}\text{Si}_3\text{O}_{12}:\text{Ce}$ ($x = 0\text{--}0.25$) (CYMSSG:Ce), grown using the liquid phase epitaxy (LPE) method on $\text{Y}_3\text{Al}_5\text{O}_{12}$ (YAG) and

YAG:Ce substrates. For this purpose, two series of CYMSSG:Ce SCFs with different ratios of Y, Mg, and Sc cations and varying thicknesses in the 19–67 μm range were synthesized on YAG and YAG:Ce substrates.

X-ray diffraction (XRD) analysis confirmed the presence of the epitaxial growth of high-quality SCFs, revealing a lattice misfit between the CYMSSG:Ce SCF and the YAG substrate in the range of 2.51–2.57%. Absorption spectra exhibited broad bands around 340 nm and 436–458 nm, characteristic of Ce^{3+} 4f–5d transitions, confirming the successful doping of CYMSSG:Ce SCFs. A weak absorption band below 300 nm suggests trace Pb^{2+} impurities resulting from the LPE growth process using a PbO -based flux.

Photoluminescence (PL) measurements of $\text{Ca}_{2-x}\text{Y}_{1+x}\text{Mg}_{1+x}\text{Sc}_{1-x}\text{Si}_3\text{O}_{12}:\text{Ce}$ showed broad green-yellow emission bands due to Ce^{3+} transitions. Increasing the Y and Mg content (x) in the films led to a red shift in the Ce^{3+} emission spectra, while the SCF of this garnet with a large Sc content demonstrated a more pronounced blue shift of Ce^{3+} luminescence. Excitation spectra revealed prominent peaks at 340 and 450 nm related to the 4f–5d^{1,2} Ce^{3+} transitions, while a peak near 375 nm was attributed to F^+ centers.

Prototype phosphor-converted white LEDs (pc-WLEDs) were fabricated using CYMSSG:Ce SCF/YAG substrate and CYMSSG:Ce SCF/YAG:Ce substrate structures with various SCF thicknesses placed directly onto blue-emitting InGaN chips. We found that films grown on undoped YAG substrates (Series A) displayed very low conversion efficiency, while the CYMSSG:Ce SCF/YAG:Ce substrate structures (Series B) exhibited promising characteristics for white LED applications. Chromaticity analysis of the latter structures demonstrated that both the YAG:Ce substrate and the CYMSSG:Ce SCF with different contents and thicknesses significantly affect the photoconversion performance of the WLED prototypes and can be used for the effective tuning of the tone of white light on demand. Namely, increasing the SCF thickness results in a slight decrease in the CRI value, but a notable improvement in the luminous efficiency of composite converters. The highest luminous efficacy of 115 lm/W is achieved for the $\text{Ca}_{1.75}\text{Y}_{1.25}\text{Mg}_{1.25}\text{Sc}_{0.75}\text{Si}_3\text{O}_{12}:\text{Ce}$ SCF (22 μm)/YAG:Ce (0.12%) substrate composite sample.

Author Contributions: A.S. collected and analyzed the structural and optical properties of samples and participated in the writing and preparation of the paper; V.G. perform the growth of the samples; A.F. perform XRD measurements; T.Z. participated in measurements of absorption PL and PLE; Y.Z. conceptually contributed to the research, analyzed whole experimental materials, and participated in the writing and correction of the paper. All authors have read and agreed to the published version of the manuscript.

Funding: The investigations were performed in the frameworks of the Polish National Scientific Centre (NCN) No 2022/45/B/ST8/01757 project and also supported by the Ministry of Science and High Education of Poland in the framework of Regional Excellence Initiative nr RID/SP/0048/2024/01 project.

Institutional Review Board Statement: Not applicable.

Informed Consent Statement: Not applicable.

Data Availability Statement: The original data presented in this study are included in the article as figures embedded in the Word version of the paper. These figures can be opened and accessed using any version of Origin software. For further inquiries, please contact the corresponding authors.

Conflicts of Interest: The authors declare no conflicts of interest.

References

1. Pimpulkar, S.; Speck, J.S.; DenBaars, S.P.; Nakamura, S. Prospects for LED lighting. *Nat. Photon.* **2009**, *3*, 180–182. [[CrossRef](#)]
2. Schubert, E.F.; Kim, J.K. Solid-State Light Sources Getting Smart. *Science* **2005**, *308*, 1274–1278. [[CrossRef](#)]
3. Pust, P.; Schmidt, P.J.; Schnick, W. A revolution in lighting. *Nat. Mater.* **2015**, *14*, 454–458. [[CrossRef](#)]

4. Sun, C.-C.; Chang, Y.-Y.; Yang, T.-H.; Chung, T.-Y.; Chen, C.-C.; Lee, T.-X.; Li, D.-R.; Lu, C.-Y.; Ting, Z.-Y.; Glorieux, B.; et al. Packaging efficiency in phosphor-converted white LEDs and its impact to the limit of luminous efficacy. *J. Solid State Light.* **2014**, *1*, 19. [[CrossRef](#)]
5. Schlotter, P.; Schmidt, R.; Schneider, J. Luminescence conversion of blue light emitting diodes. *Appl. Phys. A Mater. Sci. Appl. Process.* **1997**, *64*, 417–418. [[CrossRef](#)]
6. Nakamura, S.; Senoh, M.; Iwasa, N.; Nagahama, S.; Yamada, T.; Mukai, T. Superbright Green InGaN Single-Quantum-Well-Structure Light-Emitting Diodes. *Jpn. J. Appl. Phys.* **1995**, *34*, L1332. [[CrossRef](#)]
7. Meng, Q.; Zhao, G.; Zhu, Q.; Li, X.; Sun, X.; Li, J.-G. Site-selective and cooperative doping of $\text{Gd}_3\text{Al}_5\text{O}_{12}:\text{Ce}$ garnets for structural stabilization and warm WLED lighting of low CCT and high CRI. *Dalton Trans.* **2022**, *51*, 645–654. [[CrossRef](#)]
8. Lin, Y.-C.; Bettinelli, M.; Karlsson, M. Unraveling the Mechanisms of Thermal Quenching of Luminescence in Ce^{3+} -Doped Garnet Phosphors. *Chem. Mater.* **2019**, *31*, 3851–3862. [[CrossRef](#)]
9. Xia, Z.; Meijerink, A. Ce^{3+} -Doped garnet phosphors: Composition modification, luminescence properties and applications. *Chem. Soc. Rev.* **2017**, *46*, 275–299. [[CrossRef](#)]
10. Nishiura, S.; Tanabe, S.; Fujioka, K.; Fujimoto, Y. Properties of transparent $\text{Ce}:\text{YAG}$ ceramic phosphors for white LED. *Opt. Mater.* **2011**, *33*, 688–691. [[CrossRef](#)]
11. Bando, K.; Sakano, K.; Noguchi, Y.; Shimizu, Y. Development of high-bright and pure-white LED lamps. *J. Light Vis. Environ.* **1998**, *22*, 2–5. [[CrossRef](#)]
12. Lee, H.-M.; Cheng, C.-C.; Huang, C.-Y. The synthesis and optical property of solid-state-prepared $\text{YAG}:\text{Ce}$ phosphor by a spray-drying method. *Mater. Res. Bull.* **2009**, *44*, 1081–1085. [[CrossRef](#)]
13. Huang, B.; Ma, Y.; Qian, S.; Zou, D.; Zheng, G.; Dai, Z. Luminescent properties of low-temperature-hydrothermally-synthesized and post-treated $\text{YAG}:\text{Ce}$ (5%) phosphors. *Opt. Mater.* **2014**, *36*, 1561–1565. [[CrossRef](#)]
14. Zhang, S.; Zhuang, W.; He, T.; Liu, Y.; Liu, R.; Gao, W.; Hu, Y.; Long, Z. Study on co-precipitation synthesized $\text{Y}_3\text{Al}_5\text{O}_{12}:\text{Ce}$ yellow phosphor for white LED. *J. Rare Earths* **2010**, *28*, 713–716. [[CrossRef](#)]
15. Kang, Y.C.; Lenggono, I.W.; Park, S.B.; Okuyama, K. $\text{YAG}:\text{Ce}$ phosphor particles prepared by ultrasonic spray pyrolysis. *Mater. Res. Bull.* **2000**, *35*, 789–798. [[CrossRef](#)]
16. Zhang, L.; Lu, Z.; Zhu, J.; Yang, H.; Han, P.; Chen, Y.; Zhang, Q. Citrate sol-gel combustion preparation and photoluminescence properties of $\text{YAG}:\text{Ce}$ phosphors. *J. Rare Earths* **2012**, *30*, 289–296. [[CrossRef](#)]
17. Gupta, K.V.K.; Muley, A.; Yadav, P.; Joshi, C.P.; Moharil, S.V. Combustion synthesis of $\text{YAG}:\text{Ce}$ and related phosphors. *Appl. Phys. B* **2011**, *105*, 479–484. [[CrossRef](#)]
18. Bierhuizen, S.; Krames, M.; Harbers, G.; Weijers, G. Performance and trends of high power light emitting diodes. In Proceedings of SPIE; Ferguson, I.T., Narendran, N., Taguchi, T., Ashdown, I.E., Eds. SPIE: Bellingham, WA, USA, 2007. [[CrossRef](#)]
19. Allen, C.; Steckl, A.J. A nearly ideal phosphor-converted white light-emitting diode. *Appl. Phys. Lett.* **2008**, *92*, 143309. [[CrossRef](#)]
20. Kim, Y.H.; Viswanath, N.S.M.; Unithrattil, S.; Kim, H.J.; Im, W.B. Review—Phosphor plates for high-power LED applications: Challenges and opportunities toward perfect lighting. *ECS J. Solid State Sci. Technol.* **2018**, *7*, R3134–R3147. [[CrossRef](#)]
21. Fujita, S.; Sakamoto, A.; Tanabe, S. Luminescence characteristics of YAG glass—Ceramic phosphor for white LED. *IEEE J. Sel. Top. Quantum Electron.* **2008**, *14*, 1387–1391. [[CrossRef](#)]
22. Villora, E.G.; Arjoca, S.; Inomata, D.; Shimamura, K. Single-crystal phosphors for high-brightness white LEDs/LDs. In Proceedings of SPIE; Jeon, H., Tu, L.-W., Krames, M.R., Strassburg, M., Eds. SPIE: Bellingham, WA, USA, 2016. [[CrossRef](#)]
23. Arjoca, S.; Villora, E.G.; Inomata, D.; Aoki, K.; Sugahara, Y.; Shimamura, K. Temperature dependence of $\text{Ce}:\text{YAG}$ single-crystal phosphors for high-brightness white LEDs/LDs. *Mater. Res. Express* **2015**, *2*, 055503. [[CrossRef](#)]
24. Nizhankovsky, S.V.; Tan'ko, A.V.; Savvin, Y.N.; Krivonogov, S.I.; Budnikov, A.T.; Voloshin, A.V. Single crystalline $\text{YAG}:\text{Ce}$ phosphor for powerful solid-state sources of white light. The influence of production conditions on luminescence properties and lighting characteristics. *Opt. Spectrosc.* **2016**, *120*, 915–921. [[CrossRef](#)]
25. Chao, W.-H.; Wu, R.-J.; Wu, T.-B. Structural and luminescent properties of $\text{YAG}:\text{Ce}$ thin film phosphor. *J. Alloys Compd.* **2010**, *506*, 98–102. [[CrossRef](#)]
26. Hsu, C.T.; Yen, S.K. Electrochemical synthesis of thin film YAG on inconel substrate. *Electrochem. Solid State Lett.* **2006**, *9*, D9. [[CrossRef](#)]
27. Lee, Y.K.; Oh, J.R.; Do, Y.R. Enhanced extraction efficiency of $\text{Y}_2\text{O}_3:\text{Eu}^{3+}$ thin-film phosphors coated with hexagonally close-packed polystyrene nanosphere monolayers. *Appl. Phys. Lett.* **2007**, *91*, 041907. [[CrossRef](#)]
28. Bai, G.R.; Chang, H.L.M.; Foster, C.M. Erratum: “Preparation of single-crystal $\text{Y}_3\text{Al}_5\text{O}_{12}$ thin film by metalorganic chemical vapor deposition”. *Appl. Phys. Lett.* **1994**, *65*, 790. [[CrossRef](#)]
29. Díaz-Torres, L.A.; De la Rosa, E.; Salas, P.; Angeles-Chavez, C.; Arenas, L.B.; Nieto, J. Nanoparticle thin films of nanocrystalline YAG by pulsed laser deposition. *Opt. Mater.* **2005**, *27*, 1217–1220. [[CrossRef](#)]
30. Mauk, M.G. Liquid-Phase Epitaxy. In *Digital Encyclopedia of Applied Physics*; Wiley: Hoboken, NJ, USA, 2023; pp. 1–31. [[CrossRef](#)]

31. Capper, P.; Mauk, M. *Liquid Phase Epitaxy of Electronic, Optical and Optoelectronic Materials*; John Wiley & Sons: Hoboken, NJ, USA, 2007.
32. Kundaliya, D.; Raukas, M.; Scotch, A.M.; Hamby, D.; Mishra, K.; Stough, M. Wavelength Converter for an LED and LED Containing. Same. Patent 8,937,332, 20 January 2015.
33. Markovskiy, A.; Gorbenko, V.; Yokosawa, T.; Will, J.; Spiecker, E.; Batentschuk, M.; Elia, J.; Fedorov, A.; Pakuła, M.; Kaczmarek, M.; et al. Structural, luminescence and photoconversion properties of $\text{Lu}_3\text{Al}_5\text{O}_{12}:\text{Ce}$ single crystalline film phosphors for WLED application. *J. Alloys Compd.* **2022**, *929*, 167159. [\[CrossRef\]](#)
34. Markovskiy, A.; Gorbenko, V.; Zorenko, T.; Yokosawa, T.; Will, J.; Spiecker, E.; Batentschuk, M.; Elia, J.; Fedorov, S.; Zorenko, Y. LPE growth of $\text{Tb}_3\text{Al}_5\text{O}_{12}:\text{Ce}$ single crystalline film converters for WLED application. *CrystEngComm* **2021**, *23*, 3212–3219. [\[CrossRef\]](#)
35. VChani, I.; Yoshikawa, A.; Machida, H.; Fukuda, T. $(\text{Tb,Yb})_3\text{Al}_5\text{O}_{12}$ garnet: Crystal-chemistry and fiber growth by micro-pulling-down technique. *Mater. Sci. Eng. B Solid State Mater. Adv. Technol.* **2000**, *75*, 53–60. [\[CrossRef\]](#)
36. Markovskiy, A.; Gorbenko, V.; Zorenko, T.; Witkiewicz-Lukaszczak, S.; Sidletskiy, O.; Fedorov, A.; Zorenko, Y. Development of Three-Layered Composite Color Converters for White LEDs Based on the Epitaxial Structures of YAG:Ce, TbAG:Ce and LuAG:Ce Garnets. *Materials* **2023**, *16*, 1848. [\[CrossRef\]](#)
37. Setlur, A.A.; Heward, W.J.; Gao, Y.; Srivastava, A.M.; Chandran, R.G.; Shankar, M.V. Crystal Chemistry and Luminescence of Ce^{3+} -Doped $\text{Lu}_2\text{CaMg}_2(\text{Si,Ge})_3\text{O}_{12}$ and Its Use in LED Based Lighting. *Chem. Mater.* **2006**, *18*, 3314. [\[CrossRef\]](#)
38. Shimomura, Y.; Honma, T.; Shigeiwa, M.; Akai, T.; Okamoto, K.; Kijima, N. Photoluminescence and Crystal Structure of Green-Emitting $\text{Ca}_3\text{Sc}_2\text{Si}_3\text{O}_{12}:\text{Ce}^{3+}$ Phosphor for White Light Emitting Diodes. *J. Electrochem. Soc.* **2007**, *154*, J35. [\[CrossRef\]](#)
39. Katelnikovas, A.; Bettentrup, H.; Uhlich, D.; Sakirzanovas, S.; Jüstel, T.; Kareiva, A. Synthesis and optical properties of Ce^{3+} -doped $\text{Y}_3\text{Mg}_2\text{AlSi}_2\text{O}_{12}$ phosphors. *J. Lumin.* **2009**, *129*, 1356. [\[CrossRef\]](#)
40. Katelnikovas, A.; Bareika, T.; Vitta, P.; Jüstel, T.; Winkler, H.; Kareiva, A.; Žukauskas, A.; Tamulaitis, G. $\text{Y}_{3-x}\text{Mg}_2\text{AlSi}_2\text{O}_{12}:\text{Ce}_x^{3+}$ phosphors—Prospective for warm-white light emitting diodes. *Opt. Mater.* **2010**, *32*, 1261. [\[CrossRef\]](#)
41. Katelnikovas, A.; Jurkevičius, J.; Kazlauskas, K.; Vitta, P.; Jüstel, T.; Kareiva, A.; Žukauskas, A.; Tamulaitis, G. Efficient cerium-based sol-gel derived phosphors in different garnet matrices for light-emitting diodes. *J. Alloys Compd.* **2011**, *509*, 6247. [\[CrossRef\]](#)
42. Katelnikovas, A.; Ogiegło, J.M.; Winkler, H.; Kareiva, A.; Jüstel, T. Synthesis of $\text{Y}_{3-x}\text{LuxAl}_3\text{MgSiO}_{12}$ garnet powders by sol-gel method. *J. Sol-Gel Sci. Technol.* **2011**, *59*, 311. [\[CrossRef\]](#)
43. Katelnikovas, A.; Plewa, J.; Dutczak, D.; Möller, S.; Ensling, D.; Winkler, H.; Kareiva, A.; Jüstel, T. Synthesis and optical properties of green emitting garnet phosphors for phosphor-converted light emitting diodes. *Opt. Mater.* **2012**, *34*, 1195. [\[CrossRef\]](#)
44. Katelnikovas, A.; Sakirzanovas, S.; Dutczak, D.; Plewa, J.; Ensling, D.; Winkler, H.; Kareiva, A.; Jüstel, T. Synthesis and optical properties of yellow emitting garnet phosphors for pcLEDs. *J. Lumin.* **2013**, *136*, 17. [\[CrossRef\]](#)
45. Zhong, J.; Zhuang, W.; Xing, X.; Liu, R.; Li, Y.; Liu, Y.; Hu, Y. Synthesis, Crystal Structures, and Photoluminescence Properties of Ce^{3+} -Doped $\text{Ca}_2\text{LaZr}_2\text{Ga}_3\text{O}_{12}$: New Garnet Green-Emitting Phosphors for White LEDs. *J. Phys. Chem. C* **2015**, *119*, 5562. [\[CrossRef\]](#)
46. Pan, Z.; Xu, Y.; Hu, Q.; Li, W.; Zhou, H.; Zheng, Y. Combination cation substitution tuning of yellow-orange emitting phosphor $\text{Mg}_2\text{Y}_2\text{Al}_2\text{Si}_2\text{O}_{12}:\text{Ce}^{3+}$. *RSC Adv.* **2015**, *5*, 9489. [\[CrossRef\]](#)
47. Cao, L.; Li, W.; Devakumar, B.; Ma, N.; Huang, X.; Lee, A.F. Full-Spectrum White Light-Emitting Diodes Enabled by an Efficient Broadband Green-Emitting $\text{CaY}_2\text{ZrScAl}_3\text{O}_{12}:\text{Ce}^{3+}$ Garnet Phosphor. *ACS Appl. Mater. Interfaces* **2022**, *14*, 5643–5652. [\[CrossRef\]](#) [\[PubMed\]](#)
48. Huang, X.; Chan, J.; Chen, X. A well-performed green-emitting $\text{Lu}_{1.5}\text{Ca}_{1.5}\text{Al}_{3.5}\text{Si}_{1.5}\text{O}_{12}:\text{Ce}^{3+}$ garnet phosphor for high-quality pc-WLEDs. *Ceram. Int.* **2024**, *50*, 55979–55986. [\[CrossRef\]](#)
49. Khaidukov, N.; Zorenko, T.; Iskaliyeva, A.; Paprocki, K.; Batentschuk, M.; Osvet, A.; Van Deun, R.; Zhydaczevskii, Y.; Suchocki, A.; Zorenko, Y. Synthesis and luminescent properties of prospective Ce^{3+} doped silicate garnet phosphors for white LED convertors. *J. Lumin.* **2017**, *192*, 328–336. [\[CrossRef\]](#)
50. Levchuk, I.; Osvet, A.; Brabec, C.J.; Batentschuk, M.; Shakhno, A.; Zorenko, T.; Zorenko, Y. Micro-powder $\text{Ca}_3\text{Sc}_2\text{Si}_3\text{O}_{12}:\text{Ce}$ silicate garnets as efficient light converters for WLEDs. *Opt. Mater.* **2020**, *107*, 109978. [\[CrossRef\]](#)
51. Khaidukov, N.; Zorenko, Y.; Zorenko, T.; Iskaliyeva, A.; Paprocki, K.; Zhydaczevskii, Y.; Suchocki, A.; Van Deun, R.; Batentschuk, M. New Ce^{3+} doped $\text{Ca}_2\text{YMgScSi}_3\text{O}_{12}$ garnet ceramic phosphor for white LED convertors. *Phys. Rapid Res. Lett.* **2017**, *11*, 1700016. [\[CrossRef\]](#)
52. Xian, C.; Chen, X.; Huang, X. High-performance green-emitting $\text{Ca}_2\text{YScAl}_2\text{Si}_2\text{O}_{12}:\text{Ce}^{3+}$ garnet phosphors and their applications in high-quality blue-chip-pumped white LEDs. *J. Mater. Chem. C* **2024**, *12*, 12378–12388. [\[CrossRef\]](#)
53. Gorbenko, V.; Zorenko, T.; Paprocki, K.; Iskaliyeva, A.; Fedorov, A.; Schröppel, F.; Levchuk, I.; Osvet, A.; Batentschuk, M.; Zorenko, Y. Epitaxial growth of single crystalline film phosphors based on the Ce^{3+} -doped $\text{Ca}_2\text{YMgScSi}_3\text{O}_{12}$ garnet. *CrystEngComm* **2017**, *19*, 3689–3697. [\[CrossRef\]](#)

54. Shakhno, A.; Gieszczyk, W.; Bilski, P.; Witkiewicz-Łukaszek, S.; Zorenko, T.; Cieszko, M.; Szczepański, Z.; Kotlov, A.; Zorenko, Y. Luminescence and photoconversion properties of Ce-doped $\text{Ca}_3\text{Sc}_2\text{Si}_3\text{O}_{12}$ crystal. *J. Lumin.* **2024**, *266*, 120311. [[CrossRef](#)]
55. Zorenko, Y.; Batentschuk, M.; Brabec, C.; Osvet, A.; Gorbenko, V.; Levchuk, I.; Zorenko, T.; Chepyga, L.; Markovskiy, A.; Witkiewicz-Lukaszek, S. Patent Application EU EP 3831911A1 Composite Wavelength Converter. Application. EP19213887A, 5 December 2019.
56. Shakhno, A.; Witkiewicz-Łukaszek, S.; Gorbenko, V.; Zorenko, T.; Zorenko, Y. Composite color converters based on the $\text{Ca}_3\text{Sc}_2\text{Si}_3\text{O}_{12}:\text{Ce}$ single crystalline films. *Opt. Mater. X* **2024**, *22*, 100328. [[CrossRef](#)]
57. Gorbenko, V.; Zorenko, T.; Witkiewicz-Łukaszek, S.; Shakhno, A.; Osvet, A.; Batentschuk, M.; Fedorov, A.; Zorenko, Y. Crystallization and Investigation of the Structural and Optical Properties of Ce^{3+} -Doped $\text{Y}_{3-x}\text{Ca}_x\text{Al}_{5-y}\text{Si}_y\text{O}_{12}$ Single Crystalline Film Phosphors. *Crystals* **2021**, *11*, 788. [[CrossRef](#)]
58. Zhu, J.; Sidletskiy, O.; Boyaryntseva, Y.; Grynyov, B. Structure and role of carbon-related defects in yttrium aluminum garnet. *Opt. Mater.* **2021**, *11*, 110561. [[CrossRef](#)]

Disclaimer/Publisher's Note: The statements, opinions and data contained in all publications are solely those of the individual author(s) and contributor(s) and not of MDPI and/or the editor(s). MDPI and/or the editor(s) disclaim responsibility for any injury to people or property resulting from any ideas, methods, instructions or products referred to in the content.